Aus dem Institut für Molekular- und Zellbiologie der Hochschule Mannheim
Direktor: Prof. Dr. rer. nat. Mathias Hafner

Development and Application of a Proximity Ligation Assay for the Quantification of Synaptic Density in Mouse Models of Alzheimer's Disease.

Inauguraldissertation
zur Erlangung des Doctor scientiarum humanarum (Dr. sc. hum.) der
Medizinischen Fakultät Mannheim
der Ruprecht-Karls-Universität
zu
Heidelberg

vorgelegt von
Tatjana Mende

aus
Heidelberg
2022

Dekan: Prof. Dr. med. Sergij Goerdt
Referent: Prof. Dr. rer. nat. Mathias Hafner

TABLE OF CONTENTS

LIST OF ABBREVIATIONS

AB ....Antibody
AD... Alzheimer's Disease
AMPAR..................... α-amino-3-hydroxy-5-methyl-4-isoxazolepropionic acid receptor
ApoE4 .... Allele ε4 of the apolipoprotein E gene
APP..Amyloid precursor protein
Aβ ....Amyloid-beta
Aβ40..Aβ peptides with 40 amino acids
Aβ42..Aβ peptides with 42 amino acids
BACE1...β-secretase 1
BDNF .... Brain-derived neurotrophic factor
CA... Ammon's horn
Ca^{2+} ··Calcium
Camk2α ....Calcium/calmodulin-dependent protein kinase II alpha
Cdk5 .... Cyclin-dependent kinase 5
CLARITY....................................... Clear Lipid-exchanged Acrylamide-hybridized Rigid Imaging/Immunostaining/In situ-hybridization-compatible Tissue-hYdrogel
CNS .... Central nervous system
CSF...Cerebrospinal fluid
DAMPs .... Damage-associated molecular pattern molecules
DBE ....Dibenzyl ether
DCM.. Dichloromethane
EC... Entorhinal
ECi... Ethyl cinnamate
ELISA .... Enzyme-linked immunosorbent assays
EMA... European Medicines Agency
EOAD... Early onset Alzheimer's Disease
ERK .... Extracellular signal-regulated kinase
EtOH... Ethanol
FDA.. Food and Drug Association
FFPE...Formalin-fixed and paraffin-embedded
FITC... Fluorescein isothiocyanate
GD .... Gyrus dentatus
GSK3β ....Glycogen synthase kinase 3β
GWAS.. Genome-wide association studies
H$_2$O$_2$...Hydrogen peroxide
HC ....Hippocampus
HE... Hematoxylin and Eosin
HIER ....Heat-induced epitope retrieval
IF ....Immunofluorescence
IHC..Immunohistochemistry
LOAD..Late onset Alzheimer's Disease
MAPT...Microtubule-associated protein tau
MCI .... Mild cognitive impairment
MeOH ....Methanol
Methoxy-X04   .... 1,4-bis(4'-hydroxystyryl)-2-Methoxybenzene

1   INTRODUCTION

1.1   Alzheimer's Disease

Life expectancy of citizens of industrialized nations has continuously increased with a medium of 81 years in 2016 (Raleigh, 2019; Roser, Ortiz-Ospina, & Ritchie, 2013). Accordingly, the number of elderly people is augmenting as well. For instance, until 2050, more than 2 billion people will be older than 60 years. It is further assumed that with increasing age and accompanying physical decline, the number of diseases will increase as well including neurodegenerative diseases like Alzheimer's Disease (AD) (Hou et al., 2019; Wyss-Coray, 2016). Since the majority of people affected by AD is over 60 years old and with a growing and ageing population the prevalence of AD is predicted to rise from about 50 to 130 million people wordwide in only 35 years (Figure 1) (Drew, 2018).

AD is the most common cause of dementia with symptoms affecting memory, language and cognitive skills which often results in a radical loss of memory joined by mood disorders and behavioral changes. Therefore, many patients are dependent on care by relatives and / or professional caretakers and cannot live alone anymore. Thus, costs for managing AD from a social and health care perspective will also massively rise (Gaugler, Kane, & Kane, 2002; Wiley, 2021).

Therefore, a better in depth understanding of the disease is important as well as to develop more effective therapies and new drug development technologies that will lower the social and financial burden for current and future generations and help patients who suffer from AD.
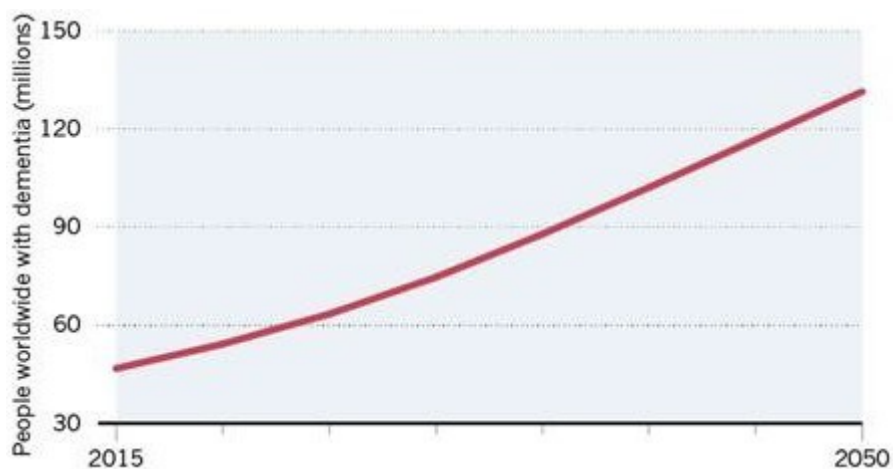
Figure 1: **Prevalence of Alzheimer's Disease**. In 2015, about 50 million people worldwide were diagnosed with AD. With growing population and life expectancy, prospectively 130 million people worldwide over the age of 60 will be affected by AD in 2050. Figure from (Drew, 2018)

AD is mostly diagnosed at a stage called mild cognitive impairment (MCI) when patients start having problems with memory, language, thinking or judgement (Wiley, 2021). However, the disease already starts years to decades before AD is diagnosed. This preclinical stage is characterized by a number of pathologic changes (Association, 2019; Sperling et al., 2011). Once a patient is diagnosed with the first symptoms, AD can be further categorized by the age of a patient, dividing patients into early-onset AD (EOAD) and late-onset AD (LOAD) at a cut-off of 65 years (Harvey, Skelton-Robinson, & Rossor, 2003). The prevalence of EOAD is lower than LOAD with only 6-16 % and differs in e.g., progression rate, heterogeneity, and the occurrence of the allele ε4 of the apolipoprotein E gene (ApoE4) (Sá et al., 2012; Wattmo & Wallin, 2017).

Another classification of AD differentiates between sporadic and familial AD. Sporadic AD applies for the majority of all cases and age represents one of the major risk factors. Other risk factors that have been recently suggested are stress-related disorders, lack of physical activity, the gut microbiome, and its regulation of the innate adaptive immune system (K. Kowalski & Mulak, 2019). It has also been hypothesized that more physical activity and a healthier lifestyle might support AD prevention (Bashiri, Enayati, Bashiri, & Salari, 2020; Tolppanen et al., 2015).

Familial or inherited forms of AD are caused by distinct genetic changes and apply for less than 5 % of all cases. Some examples for AD-related aberrations are mutations in the ε4 allele of the ApoE gene and/or in the amyloid precursor protein (APP), and the presenilin 1 and 2 genes (PSEN1 and PSEN2). The largest group within familial AD cases are patients with Down syndrome which also represents the major genetic risk factor for EOAD (Falcon et al., 2018; Wiseman et al., 2015). This is most likely because trisomy 21 and thus the typical aberration found in Down syndrome patients results in three copies of the APP coding region which is located on chromosome 21 (Sperling et al., 2011).

1.1.1 The Hallmarks of AD

AD is neuropathologically characterized by i) the aggregation of Aβ peptides and their accumulation as senile plaques, ii) the hyperphosphorylation of the tau protein which forms neurofibrillary tangles and iii) the neurodegeneration that leads to the loss of some brain areas (Figure 2) (Domingues, AB da Cruz e Silva, & Henriques, 2017). Alois Alzheimer, a German psychiatrist and the eponym of the disease, was the first to describe clinical symptoms of a fifty-year old patient named Auguste and pathological

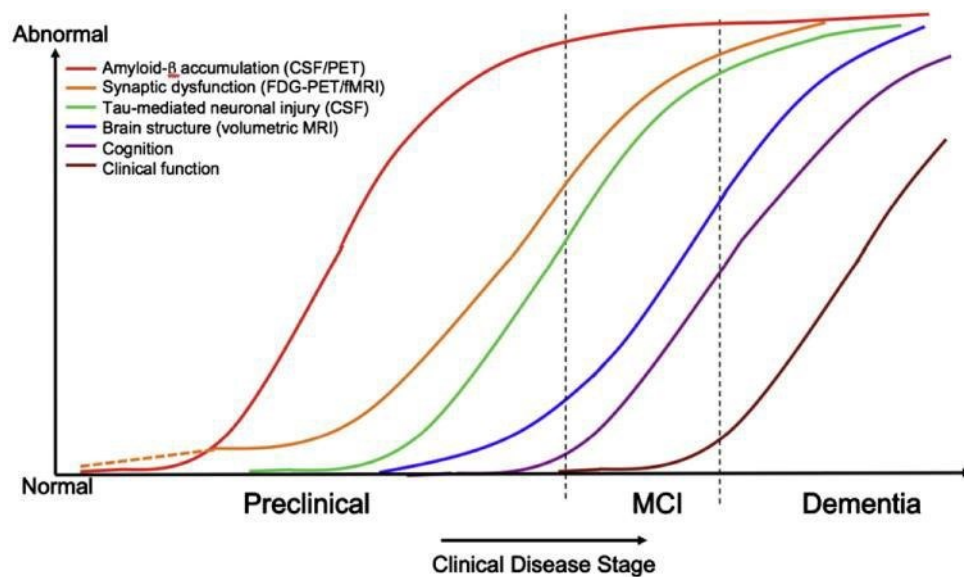abnormalities found after her death (Alzheimer, 1907; Stelzmann, Norman Schnitzlein, & Reed Murtagh, 1995).

*Figure 2: **Hypothetical biomarker model of AD**. The different biomarkers are shown as a graph of their change as a function of the clinical disease stages. Synaptic dysfunction (orange curve) is one of the earliest markers of the disease. The dotted line indicates its potential detectability in APOEε4 carriers even before Amyloid-beta (Aβ) accumulation takes place. Figure from: (Sperling et al., 2011)*

Amyloid plaques are one of the first hallmarks of the disease. They consist of Aβ peptides derived from the APP. In non-pathologic conditions, Aβ is part of the larger APP, which is a type 1 membrane glycoprotein. APP is cleaved by α-secretase between amino acids 16 and 17 of the Aβ region to function in the regulation of synaptic formation or neuronal transport (G. F. Chen et al., 2017; Dennis J Selkoe, 1996). In AD, abnormal cleavage of APP by β-secretase 1 (BACE1) and y-secretases forms Aβ peptides with 40 (Aβ40) or 42 (Aβ42) amino acids (Wang, Gu, Masters, & Wang, 2017) that are prone to aggregation and formation of senile plaques.

The second hallmark of AD are neurofibrillary tangles (NFTs) which mainly consist of the hyperphosphorylated tau protein. The microtubule-associated protein tau (MAPT) is especially expressed in neurons where it is a major part of the cytoskeleton and is involved in vesicle transportation (Bloom, 2014). The MAPT gene produces six different isoforms of tau. Isoforms that are most prevalent in AD are the three- (3R) and four-repeats (4R) of the binding domains (Figure 3) (Schonhaut et al., 2017). Abnormal hyperphosphorylation of the soluble tau protein leads to insoluble forms of tau that are prone to aggregation. These tau aggregates can be toxic for neurons as they can ultimately lead to cell death (Luna-Viramontes et al., 2020).
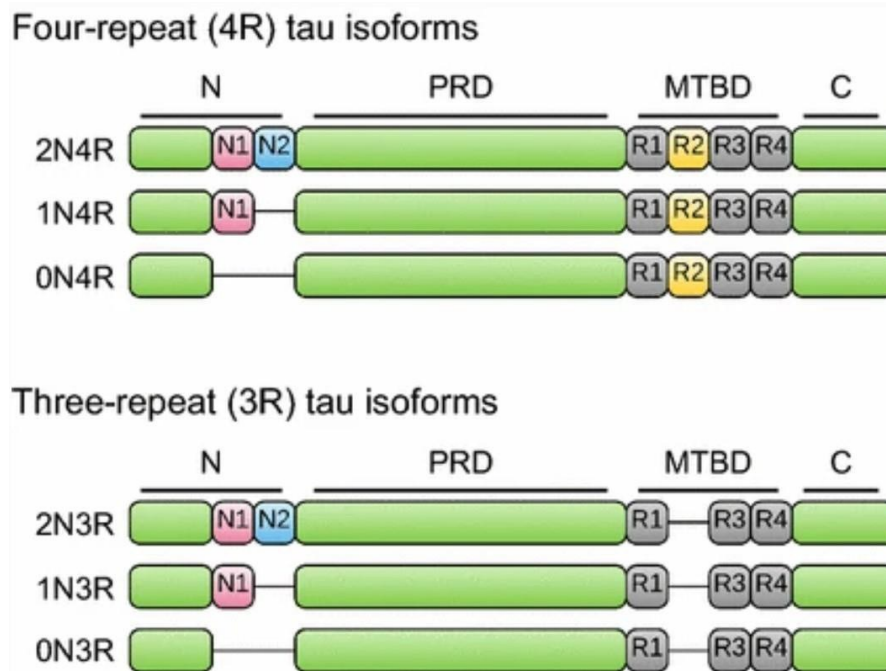
Four-repeat (4R) tau isoforms

Three-repeat (3R) tau isoforms

*Figure 3: **The six different isoforms of the protein tau** are generated through alternative splicing of the MAPT gene. At the amino (N)- terminus, distinct amino acids are excluded (0N) or included (1N, 2N) and form the different isoforms. The central part of tau is the proline-rich domain (PRD), followed by the microtubule binding domain (MTBD) which results in the 3R or 4R isoforms by alternative splicing. The C-terminal domain is the same in all six isoforms. Figure taken from (Guo, Noble, & Hanger, 2017).*

The third hallmark of AD is neuronal loss which is a result of the two pathologies, i.e., disposition of Aβ plaques in the extracellular surrounding of neurons and intracellular tau aggregates. Over time, the first Aβ plaques can be found in the area of the neocortex (Thal phase 1), followed by the hippocampus (Thal phase 2), striatum (Thal phase 3), mesencephalon (Thal phase 4), and finally the cerebellum and the pontine nuclei (Thal phase 5). Spreading of NFTs in the different brain areas during the course of the disease is categorized in the so-called Braak stages (Figure 4). First associative areas are affected, like specific nuclei of the brain stem (Braak stage I/II), followed by the entorhinal (EC) area and the hippocampus (Braak stage III/IV) and finally the neocortex (Braak stage V/VI) (Calderon-Garcidueñas & Duyckaerts, 2018; Jellinger, 2020). Only in advanced Thal phases and Braak stages, and with the onset of symptoms, AD can be diagnosed.
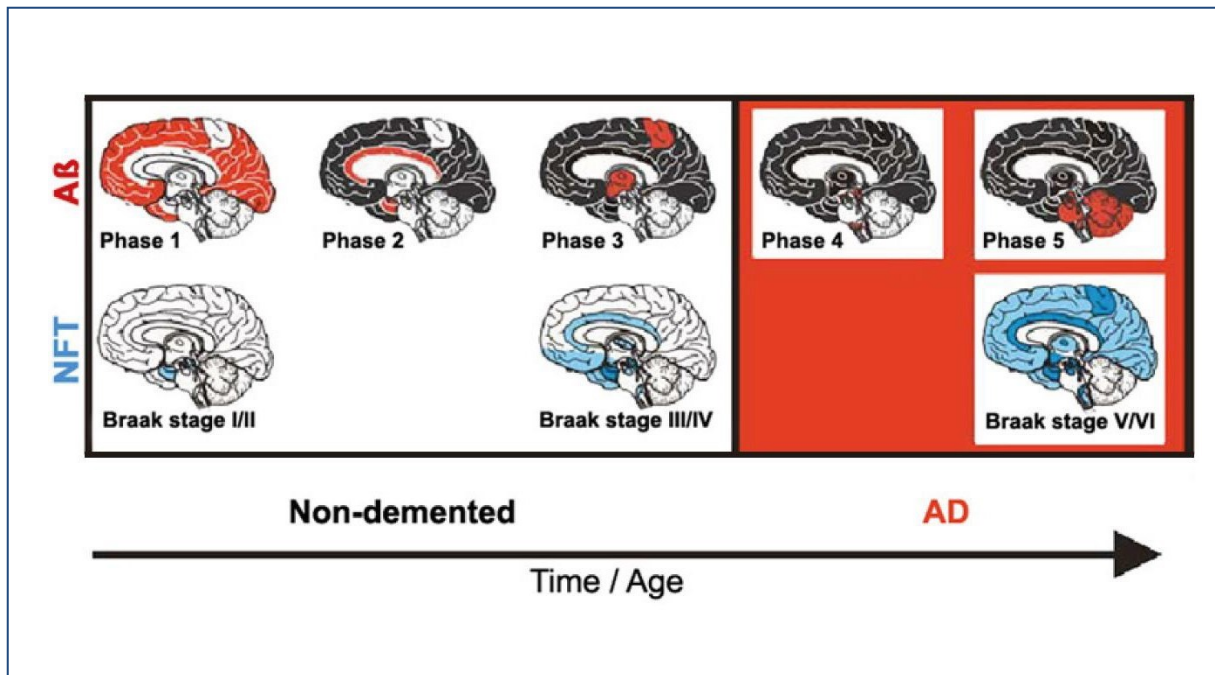
*Figure 4: **The Thal phases and Braak stages**. Brain areas affected over time and with age in AD patients by Aβagglomeration (red) and tau spreading leading to neurofibrillary tangles (NFTs, blue). Figure from (Jellinger, 2020)*

1.1.2 The Amyloid Hypothesis

Different hypotheses have been proposed for the complex AD pathology, which all revolve around Aβ and tau. How or whether tau and Aβ are connected to lead to neuronal loss and brain atrophy is still not clear. The connection between tau and Aβ has been studied for decades, and recent findings are proposing a theory where Aβ plaques enhance tau toxicity (Gomez, Morales, Maracaja-Coutinho, Parra, & Nassif, 2020).

The so-called amyloid hypothesis suggests, that due to mutations in the genes APP, PSEN1 and -2, Aβ oligomers are formed quite early in the disease progression (Makin, 2018). The accumulation of oligomers to insoluble plaques and tau tangle formation is thought to provoke a cascade of events in neuroinflammation (Scheuner et al., 1996). Under these pathological circumstances, immune cells, like activated astrocytes and microglia, participate in neuroinflammation events by producing large amounts of pro-inflammatory cytokines and chemokines which should lead to pathogen and toxin clearance (Lyman, Lloyd, Ji, Vizcaychipi, & Ma, 2014). However, these neuroinflammation events lead to neuronal dysfunction and the elimination of synaptic structures by microglia (Leng & Edison, 2021).

Aβ plaques are formed extracellularly and can be found in different brain areas as compared to NFTs (Figure 5). Recent studies have shown that in the presence of Aβ,

the tau pathology spreads from the medial temporal lobe to the neocortex and that tau development and spreading is expedited by Aβ (L. A. Gomes et al., 2019; van der Kant, Goldstein, & Ossenkoppele, 2020).

While ApoE4 is essentially involved in the Aβ deposition, it also contributes to tau-mediated neurodegeneration (Kang et al., 2021). When NFTs reach brain areas where Aβ is accumulated, Aβ serves as potentiator for tau hyperphosphorylation. AD is diagnosed at a late stage of the disease. Although cognitive symptoms of AD are more linked to the number and location of tau tangles, the disease progression aggravates when Aβ and tau converge locally in the same brain areas, which might explain why it takes so long to develop AD (Gomez et al., 2020). Animal studies have shown that tangles can build up even in the absence of Aβ plaques but not vice versa (DeVos et al., 2018). Additionally, mutations leading to Aβ aggregation, definitely worsen tau tangle formation and seem to work as a stabilizer of the environment for NFTs (Makin, 2018).
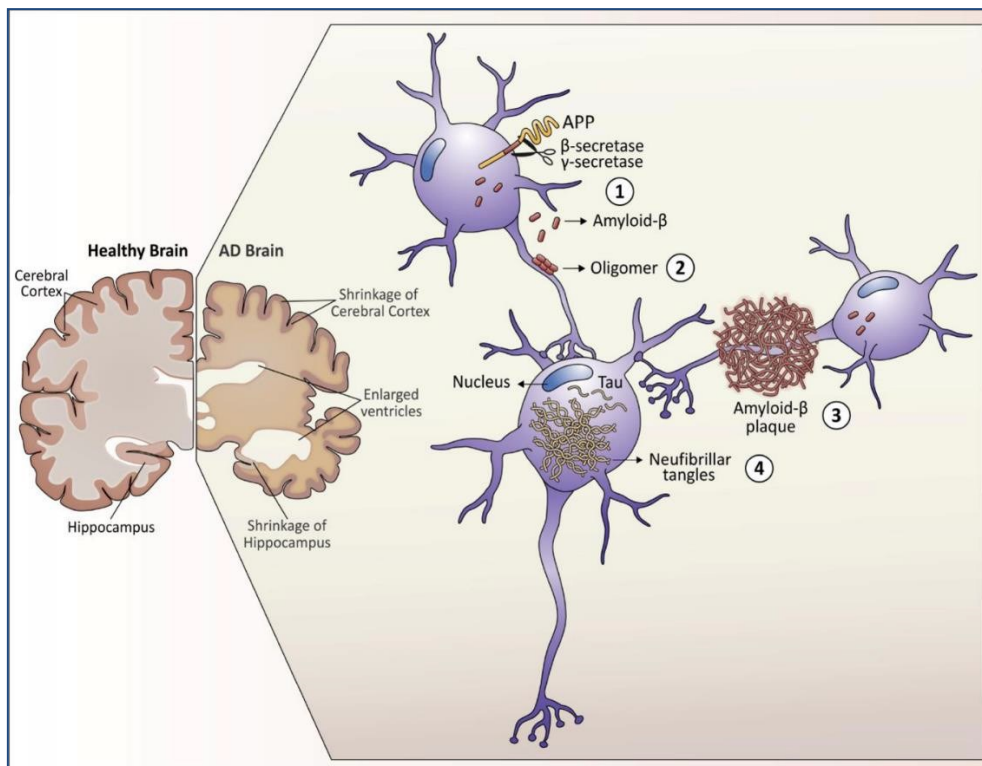
*Figure 5: **Hallmarks of Alzheimer's Disease.** As AD progresses, the brain tissue shrinks in the areas of the cerebral cortex and the hippocampus, while the volume of the ventricles enlarges. (1) In the membrane of neurons, APP is abnormally cleaved by β- and γ-secretases and accumulates as Aβ-plaques extracellularly (2) to eventually aggregate as oligomers. Here, they are thought to affect synaptic function and influence receptors on the neuron plasma membrane. (3) Aβ-plaques meddle with neuron function. (4) The hyperphosphorylation of tau leads to the formation of NFTs that interfere with intracellular organelles and cellular transport. Figure from (Gomez et al., 2020)*

Studies reported, that Aβ oligomers lead to tau hyperphosphorylation through a redirection of noradrenergic signaling and the related activation of glycogen synthase kinase 3β (GSK3β), a well-known link between Aβ and tau (Mandelkow, 1999; Zhang et al., 2020). Another reported mediator between Aβ and tau is the Src family kinase Fyn (Lau et al., 2016). In the post-synaptic compartment, Fyn builds a complex with tau post-synaptic-density protein 95 (PSD95) and N-methyl-D-aspartate receptors (NMDARs) or α-amino-3-hydroxy-5-methyl-4-isoxazolepropionic acid receptors (AMPARs). Here, Aβ could lead to the hyperphosphorylation of tau through the activation of cyclin-dependent kinase 5 (Cdk5), which is known to be deregulated in AD patients (Patrick et al., 1999). Cdk5 is dysregulated by p25 and thereby inhibits tau to bind to microtubules (H.-Y. Wu et al., 2018). In neurons depleted of tau, Fyn cannot localize to the synapse and the complex formation fails, leading to synaptic dysfunction (Yin et al., 2021).

This underpins the hypothesis that Aβ enhances the hyperphosphorylation auf tau (He et al., 2018; Sperling et al., 2011). Taken together, the amyloid hypothesis claims that Aβ is the driving force in AD leading to inflammation, NFT formation, synaptic dysfunction, and cell death in later stages.

1.2 Genome-wide Association Studies of AD

Besides known genetic risk factors like mutations in APP, PSEN1 and 2, leading to the Aβ pathology, genome-wide association studies (GWAS) were able to expand the list of AD-related aberrations. GWAS has been a powerful tool to identify genes in an unbiased way which especially play a role in AD for the more frequently occurring LOAD cases (Kamboh et al., 2012). Recent GWAS studies on the one hand support the amyloid hypothesis by identifying genes that drive the Aβ pathology in neurons but on the other hand also yield hits for mutations in genes expressed on microglia cells, which are the resident immune cells of the brain. It is assumed that microglia-related mutations result in a dysregulation of the immune response (Lemprière, 2021). In AD, activation of microglia cells are initiated by aberrantly folded Aβ, which binds to microglia receptors (G.-f. Chen et al., 2017). Failure of the activated microglia cells to clear Aβ can create a vicious cycle resulting in chronically hyper-activated microglia secreting pro-inflammatory mediators damaging neurons, which is further exacerbated by the release of damage-associated molecular pattern molecules (DAMPs) from apoptotic neurons (Norden & Godbout, 2013).
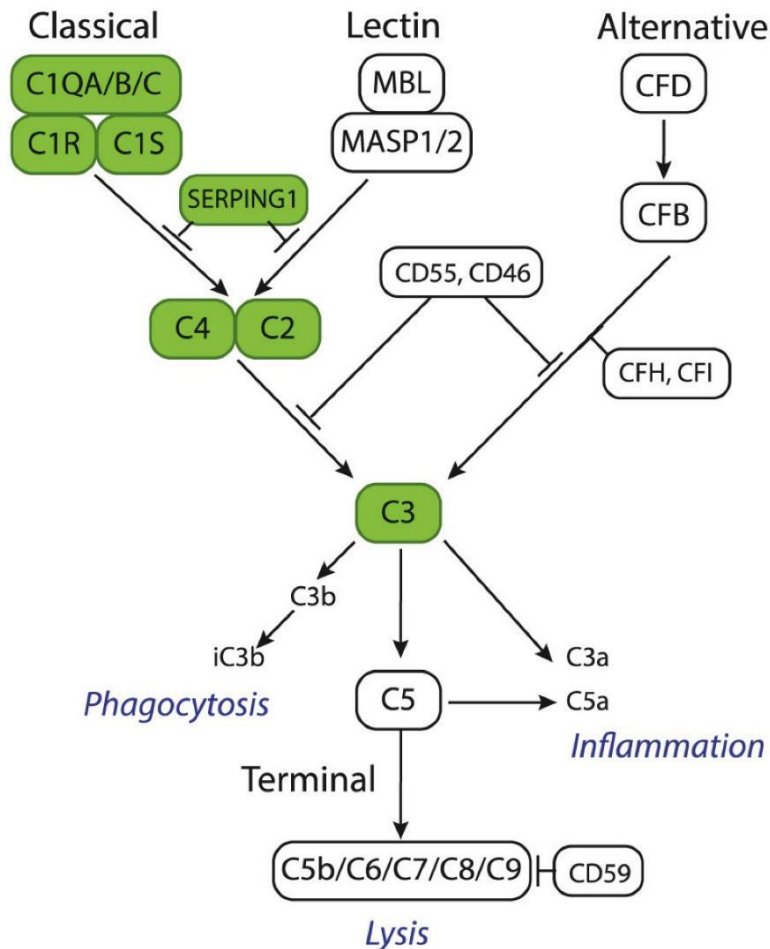
*Figure 6: **The complement system.** Highlighted in green is the classical pathway that is initiated by the binding of antigens to pathogens. The complement proteins exist as inactive zymogens and get activated by sequential cleavage. All pathways have the complement protein C3 in common, which activates the different products leading to phagocytosis, lysis, or inflammation. Figure from (T. Wu et al., 2019)*

Examples for mutations in microglia-related genes in association with an increased AD risk are the microglia receptors CD33, TREM2 and CR3. While the expression of CD33 is increased in AD patients and switches the pro-inflammatory state of microglia cells to phagocytose Aβ plaques, mutations in this gene have been shown to inhibit clearance of Aβ in AD (Zhao, 2019). A mutation in the TREM2 gene elevates the risk to develop AD by 3- to 4-fold which is similar to the high-risk of carrying allele ε4 of the APOE gene (Guerreiro et al., 2013). TREM2 is highly expressed in the hippocampus (HC), a brain area that is strongly affected by neurodegeneration in AD.

TREM2 adapts to inflammatory responses and neuroprotection, and directs myeloid cell maturation, proliferation and survival (Qin et al., 2021).

CR3 is a microglia receptor and part of the signaling cascade of the complement system and is involved in microglia-mediated synaptic pruning. Inhibition of CR3 has been shown *in vitro* to result in a reduction of the microglia phagocytotic activity to prune synapses (Abud et al., 2017; T. Wu et al., 2019). It seems not only CR3, but a dysregulation of the entire complement system plays a causal role in AD disease progression (Czirr et al., 2017). The complement system consists of three different pathways, all leading to the central component C3 (Figure 6). Interestingly, some of the complement receptors are expressed by myeloid cells (Carroll, 2004).

Altogether, GWAS studies provide a large body of evidence for an important role of neuroinflammation in AD progression, which warrants further investigation.

1.2.1 Microglia-mediated Synapse Loss

Microglia cells have been shown to present in two different morphological phenotypes: in the "resting state" microglia cells have a ramified morphology with a small soma and thin cellular processes. In this state microglia are "sensing" for threats to brain homeostasis and respond to injury and cell death. In the presence of pathogens or tissue damage, microglia cells change their morphology, become activated, display phagocytotic activity, express Toll-like receptors (TLRs) and secrete proinflammatory cytokines (Bachiller et al., 2018). In AD, activation of microglia is initiated by aberrantly folded Aβ, which binds to microglia receptors (G.-f. Chen et al., 2017). Furthermore, in the state of "microglial activation" they can actively move to a lesion or the source of an infection, are able to proliferate and thus to provide more microglia cells to restore brain homeostasis (Block, Zecca, & Hong, 2007; Colton & Wilcock, 2010; Kettenmann, Hanisch, Noda, & Verkhratsky, 2011).

In early development microglia also play an important role in synaptic pruning. In this development stage, a huge number of synaptic contacts are formed and later pruned away by microglia to leave and strengthen only the contacts that are needed (Hua & Smith, 2004; Stevens et al., 2007). This synaptic pruning by microglia is also performed in AD disease progression due to deficits in the microglia function and complement system which leads to an over-phagocytosis of synaptic spines (Paolicelli et al., 2011; Stephan, Barres, & Stevens, 2012). Studies show that the classical pathway of the complement system (Figure 6) is disturbed. For example, it tags synapses with the complement protein C1q in response to the tau pathology leading to synapse pruning by microglia (Dejanovic et al., 2018). Other studies showed that both pathologies, tau

and Aβ, lead downstream the complement cascade through C3 to an overexpression of the microglia receptor R3 (R3/CD11b-CD18/Mac-1) which results in the engulfment of synapses by microglia and their subsequent phagocytosis (Schafer et al., 2012). These findings provide convincing evidence that disturbed processes in the complement system result in microglia-mediated synaptic loss in AD which in turn is one of the earliest markers of the disease.

1.2.2 Glutamatergic Synapses Affected in AD

Over-phagocytosis of synapses by microglia during AD predominantly affects the glutamatergic neurotransmission which plays a key role in learning and memory. In a healthy neuron, the glutamatergic neurotransmission proceeds the communication from one cell to another through synapses. In glutamatergic synapses, the neurotransmitter glutamate is transported in vesicles to the presynaptic terminal, the so-called active zone. When an action potential arrives, Ca^{2+} channels open and cause the vesicle, transporting the neurotransmitter glutamate, to fuse with the cell membrane. Glutamate is then released into the synaptic cleft, a gap of 20 to 40 nm (Figure 7) (Südhof, 2012). On the post-synaptic site, glutamate binds to and activates the different glutamate receptors leading to signal transduction and thus initiation of specific cellular responses (Siddoway, Hou, & Xia, 2011). After the release of glutamate into the synaptic cleft and the activation of the post-synaptic receptors, it is continuously recaptured by reuptake transporters of neurons and astrocytes for recycling with the help of the glutamate-glutamine-cycle (Verkhratsky & Nedergaard, 2018; Yudkoff et al., 1994).

Altogether, glutamate is the most abundant neurotransmitter in excitatory neurons of the central nervous system (CNS). Corresponding glutamate receptors are expressed by neurons, astrocytes, and microglia cells and are subdivided into three different ionotropic glutamate receptors: NMDA, AMPA and Kainate receptors.

Most relevant for AD are NMDA receptors which are selectively permeable for calcium (Ca^{2+}) (Siddoway et al., 2011). For the local distribution of Ca^{2+} a correlation with Aβ and tau tangles has been described. This association indicates a link to the amyloid hypothesis, where Aβ accumulation is the driver of the disease, supporting tau hyperphosphorylation and NFT formation which ultimately leads to neuronal loss (Butterfield & Pocernich, 2003). Additionally, Aβ is also a driver of oxidative stress, resulting in an increase of extracellular glutamate due to a decreased glutamate uptake capacity by neurons and glia cells as well as to an increased glutamate release (Caraci, Nicoletti,

& Copani, 2018). This increased glutamate release accompanied with an overstimulation of the glutamate receptor NMDA with Ca^{2+} induces a change in the expression pattern of the glutamate transporter. High levels of extracellular glutamate contribute to neuroinflammation through an activation of microglia cells and by inducing a release of cytokines. This disturbed glutamate homeostasis leads to excitotoxicity in glutamatergic synapses and finally to cell death (Haroon, Miller, & Sanacora, 2017; Lewerenz & Maher, 2015).
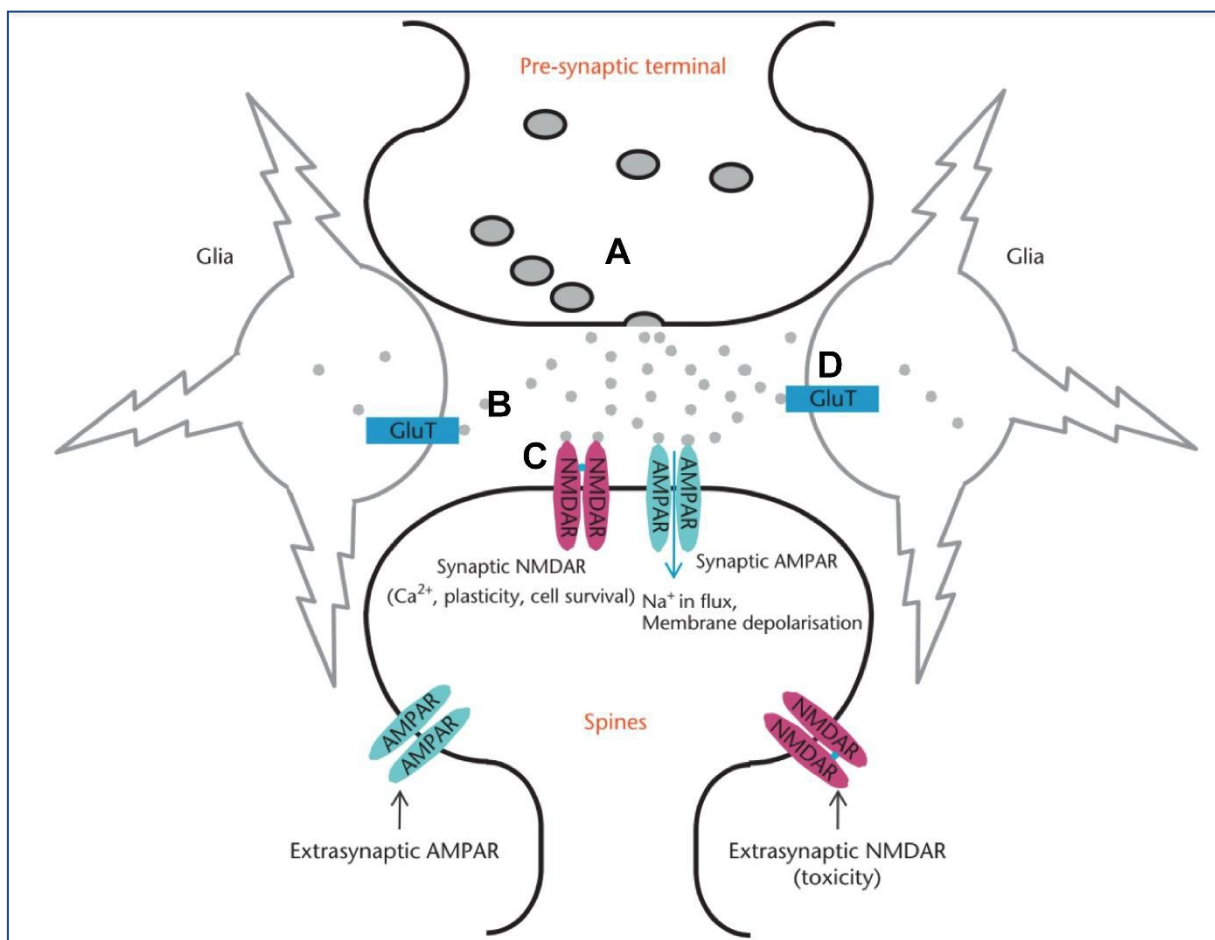
*Figure 7: **Glutamatergic synapse. (A)** At the presynaptic terminal, glutamate transporters filled with glutamate arrive. **(B)** Glutamate is released from the synaptic terminal and diffuses across the synaptic cleft. **(C)** Activation of AMPA and NMDA receptors leading to membrane depolarization. **(D)** Reuptake of glutamate by specialized glutamate transporters (Glu T) by glia cells or the pre-synaptic terminal for clearance. Figure from (Siddoway et al., 2011)*

1.3 Methods to Assess Synaptic Dysfunction in AD

Although synaptic dysfunction represents one of the earliest characteristics of AD (Morris, 2005), for the diagnosis of AD in patients and in preclinical models, neuronal markers like Aβ and tau (Duyckaerts, Delatour, & Potier, 2009; Olsson et al., 2016) and synaptic markers such as neurogranin (W. Liu et al., 2020) are considered which

can be easily measured in the peripheral blood and the CSF. It has been shown that quantification of neurogranin, a dendritic protein with an increased concentration in AD, in the cerebrospinal fluid (CSF) correlates with cognitive decline and brain degeneration (Lashley et al., 2018; Tarawneh et al., 2016).

To further assess synaptic markers in living organisms, positron emission tomography (PET) can be applied by the help of a substance that is radioactively labeled, e.g. the synaptic vesicle glycoprotein 2A labeled with the radioligand 11C-UCB-J (Figure 8 D) (Finnema et al., 2016). The advantage of imaging methods in living patients and animals consist of its high accuracy to quantify synaptic density, but the costs, the invasiveness by using radioactive substances, and the missing cellular resolution represent major drawbacks.
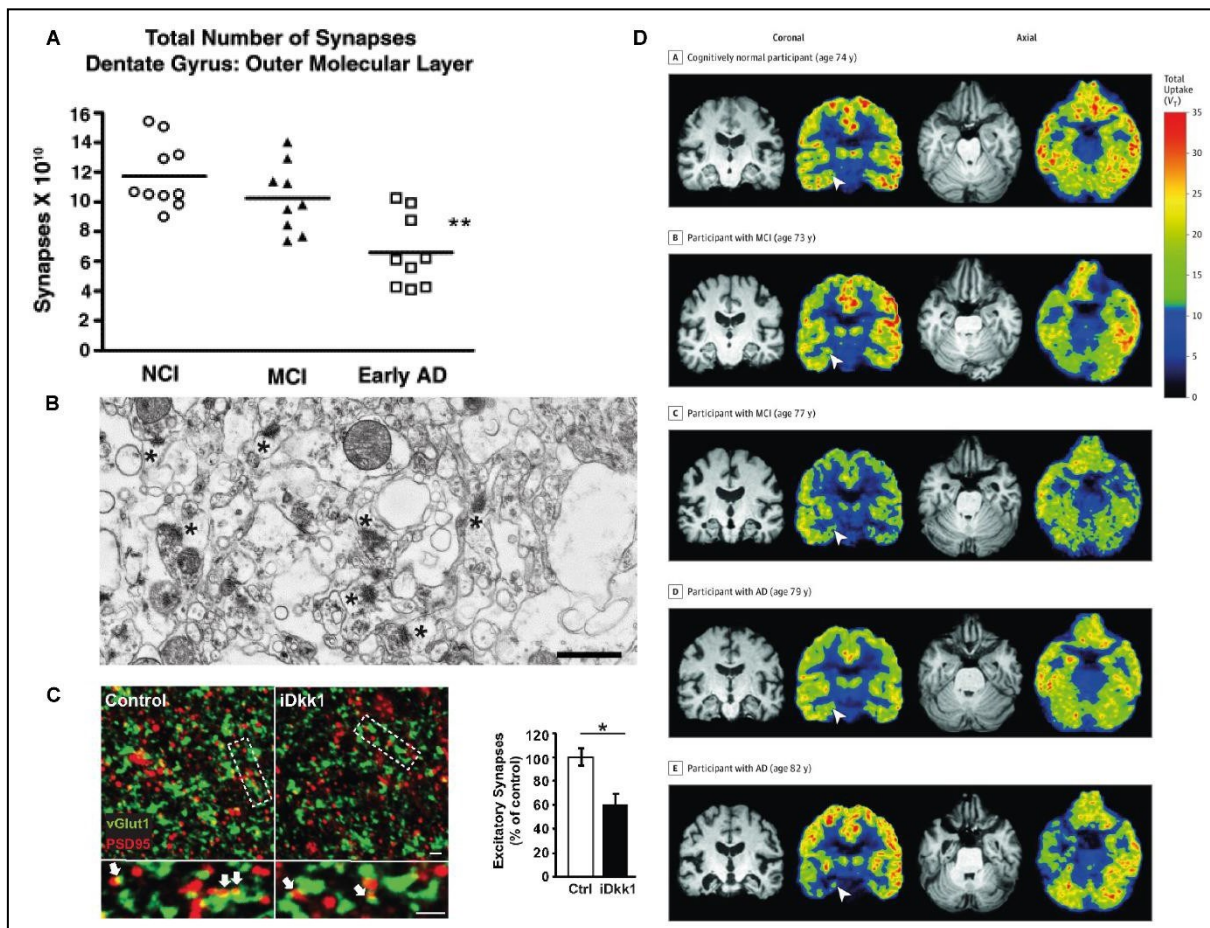
*Figure 8: **Synaptic density correlates with cognitive decline in AD**. (A) Assessment of the number of synapses in the outer molecular layer of the dentate gyrus of patients with no cognitive impairment (NCI), mild cognitive impairment (MCI) or early AD (**p>0.01). (B) Representative image taken with transmission electron microscopy in the outer molecular layer of the dentate gyrus from an early AD patient. The stars (*) indicate the synaptic density. Bar= 1 µm. Figures A and B taken from (Scheff, Price, Schmitt, & Mufson, 2006). (C) Immunohistochemistry (IHC) representative images in the area of the hippocampus, stained with primary antibodies anti-vesicular glutamate transporter 1 (vGLUT1) as pre-synaptic marker and anti-PSD95 as post-synaptic marker. The fluorescent signal of the overlay (arrows) is quantified as synaptic density. Figure taken from (McLeod, Marzo, Podpolny, Galli, & Salinas, 2017b). (D) Representative coronal and axial PET images of patients with NCI (D-A), MCI (D-B and D- and AD (D-*

D and D-E). Arrows indicate the reduction of PET-marker binding in the hippocampus. Figure taken from (M. K. Chen et al., 2018).

Moreover, synaptic dysfunction can be analyzed in post-mortem brains by different methods including transmission electron microscopy (TEM) (Scheff et al., 2006), IHC (Hong et al., 2016), enzyme-linked immunosorbent assays (ELISA) (Gottschall et al., 2010), and Western Blot (WB) (Helboe, Egebjerg, Barkholt, & Volbracht, 2017; Kopeikina et al., 2013). TEM, a more laborious technique, is mainly used for basic research and can be applied to quantify e.g., total synapse numbers in specific brain areas on thin tissue slices of AD patients (Figure 8 A and B). TEM in combination with electrophysiological methods like patch-clamp recording can be used to quantify structural changes of cells by applying currents on the post synapse (Crimins et al., 2011). The gold standard in histology for the evaluation of synapses is currently immunohistochemistry (IHC). Here, antibodies are used to investigate synaptic contacts in AD animal models by quantifying the overlay of fluorescent labels linked to the antibodies (Figure 8 C) (McLeod, Marzo, Podpolny, Galli, & Salinas, 2017a). However, there is some uncertainty that overlay of stainings accurately reflects a functional synapse.

WB or ELISA have also been used to study the expression of different synaptic proteins (Gottschall et al., 2010; Helboe et al., 2017; Kopeikina et al., 2013; Shimojo et al., 2020). Since this is an indirect and may be an incomplete measure for synaptic density it is mainly used in *in vitro* experiments.

Altogether, there is an increasing toolbox to assess synaptic dysfunction. However, when studying the pathophysiology of AD in distinct brain areas on a cellular level, methods available (EM, IHC) are accompanied by the above described limitations preventing a reliable analysis of functional synapses in large brain areas. Therefore, more sensitive, and robust techniques are needed to study synaptic loss.

1.3.1   Mouse Models and Biomarkers to Study Synaptic Dysfunction

Animal models to study AD have tremendously advanced our understanding of the molecular pathogenesis of this disorder and are indispensable for the development of effective therapies (Dawson, Golde, & Lagier-Tourenne, 2018). Although based on the "3R-concept", animals should be reduced, replaced and refined (Russell & Burch, 1959), animal models are still required because i) *in vitro* systems are not able to mirror complex responses of a living individuum, ii), only in living organisms unwanted side

effects can be determined, and iii) effectiveness of a therapeutic intervention can only be reliably assessed in a natural environment allowing the interaction of neurons with other cells of the brain (Katze, Korth, Law, & Nathanson, 2015). This is why medicine accreditation offices, like the Food and Drug Association (FDA) or the European Medicines Agency (EMA) demand preclinical toxicological, veterinary and clinical approaches (Hampshire & Gilbert, 2019). To study synaptic loss in drug development, mouse models are used that are genetically modified to carry the AD pathology (Kari, Rodeck, & Dicker, 2007; Kopeikina et al., 2013). In this work, we focused on the tau-transgenic mouse model rTG4510 and on the Aβ-transgenic APPPS1 mouse model, and a neurotoxic compound inducing neuronal loss.

The rTG4510 mouse model is bred by crossing the mouse line 4510 that carries the MAPT^{P301L} cDNA to the transactivator line (tA) which expresses a tetracycline-induced transactivator under the control of a CaMKIIα promoter (Goodwin et al., 2019). The rTG4510 model is a frequently used research model because it allows for the control of the mutant transgene expression through tetracycline administration (the prefix "r" stands for the tetracycline-dependent regulation of human tau) (Gamache et al., 2019). Characteristic for this mouse model is an early neurodegeneration and NFT formation in young animals between 2 and 7 months of age (Gamache et al., 2019). However, several studies report about mixed results regarding age-dependent synaptic loss in the TG4510 animals. While some show a progressive decline (Kopeikina et al., 2013; Rocher et al., 2010; Shimojo et al., 2020), others observe no effects or even increases in synaptic density (Crimins et al., 2011; Hoover et al., 2010). This warrants further investigation and will be addressed in the current work.

The APP mouse model is genetically modified in the transgenes APP and PSEN1 (APPPS1), under the control of a Thy1 promoter. Here, accumulation of Aβ plaques starts at six weeks of age in the neocortex (Radde et al., 2006). In 24-month-old APPPS1 animals, characteristics as volume decrease in the hippocampus as well as loss in neurons and synaptic markers are described (Gengler, Hamilton, & Hölscher, 2010; Huang et al., 2016). Strikingly, a synaptic loss in close proximity to Aβ plaques is reported (Dorostkar et al., 2014; Sauerbeck et al., 2020).

Another method to study neurodegeneration is the application of the neurotoxic compound trimethyltin (TMT) (J. Kim et al., 2013; Perretta, Righi, & Gozzo, 1993). TMT causes neurodegenerative damage in the hippocampus leading to neuronal death and microglia activation (Geloso, Corvino, & Michetti, 2011). Additionally, animals treated

with TMT show cognitive impairments and behavioral changes like amnesia, hyperactivity, aggression, and seizures (Fabrizi et al., 2016). Previous studies reported that animals treated with TMT can spontaneously recover from the clinical symptoms like stroke and seizures as well as from the TMT-induced hippocampal neuronal lesions (Sueun Lee et al., 2016). This could be due to neuroregeneration processes like the activation of the brain-derived neurotrophic factor (BDNF)/extracellular signal-regulated kinase (ERK) (Harry et al., 2008; S. Lee et al., 2016; Sandström et al., 2019; Tang et al., 2013). The TMT-induced neurodegeneration might be instrumental to study effects on markers such as synaptic density and the Neurofilament-light chain in the peripheral blood (NF-L) (Sano et al., 2021).

Currently there are only few blood biomarkers for synaptic dysfunction (Lashley et al., 2018; W. Liu et al., 2020) but the general AD-biomarker NF-L could be further evaluated for these purposes. NF-L is a major component of the cytoskeleton of axons and is released in the extracellular space when an axon is damaged. Afterwards it is found in the CFS and blood (Khalil et al., 2018; Yuan, Rao, & Nixon, 2012). As for AD, NF-L has been shown to be elevated and to correlate with cognitive decline and brain degeneration (Molinuevo et al., 2018). Furthermore, it was reported before that NF-L can be used as biomarker for peripheral nervous toxicity in rats (Sano et al., 2021). Therefore, we wanted to test if NF-L, a well-established blood biomarker for AD, can also be used as peripheral blood biomarker for neurotoxicity induced by TMT in mice.

Altogether, the use of animal models is crucial in basic research and drug development to study disease progression and toxicity or adverse reactions upon the application of drug candidates. Transgenic animals or the use of compounds that induce and mirror the complex disease progression of AD are therefore excellent models to study biomarkers such as synaptic loss *in vivo*.

1.3.2 Proximity Ligation Assay to Quantify Synaptic Density

Methods frequently used to study synaptic loss come along with various disadvantages, like high costs and laboriousness and/or an ambiguous quantification. The need for a more sensitive and reliable method to quantify synaptic density in basic research and drug development is therefore essential. The Proximity Ligation Assay (PLA) is a technique to study protein-protein or endogenous protein-cell interactions in cells and in tissues to show molecular and cellular connections and their effects (Di Maio et al., 2018; I. Gomes, Sierra, & Devi, 2016; Söderberg et al., 2006). It combines

parts of classic immunohistochemistry, in-situ hybridization, and polymerase chain re-action (PCR) techniques by first using primary antibodies that bind specifically to tar-gets of interest. The next step consists of the application of secondary antibodies tar-geted against the primary ones, coupled to affinity probe pairs. This step is based on the theory that signal transmission is carried out by different interacting molecules that are organized in modules (Fredriksson et al., 2002; Hartwell, Hopfield, Leibler, & Murray, 1999). The PLA technique applies affinity probe pairs that recognize target molecules, and only react with one another when they are in close proximity of only a few nanometers (Fredriksson et al., 2002). During the development of the technique, oligonucleotide reagents with a high affinity to a target molecule had to be identified, resulting in the so-called DNA aptamers. These aptamers have free ends in either 3' or 5' direction and thereby are able to form a proximity pair (Ellington & Szostak, 1990; Jayasena, 1999; Robertson & Ellington, 1999; Tuerk & Gold, 1990). When these ap-tamers, or probes, are close enough together, the free oligonucleotide ends are hy-bridized together by enzymatic DNA ligation. The ligated probes are then replicated by a nucleic acid amplification with the help of a PCR whereas probes that are not close enough together remain unligated and unreplicated. For the detection of the connec-tion, carboxyrhodamine (ROX) internal fluorescence standard is used to covalently bind to the DNA (Fredriksson et al., 2002).
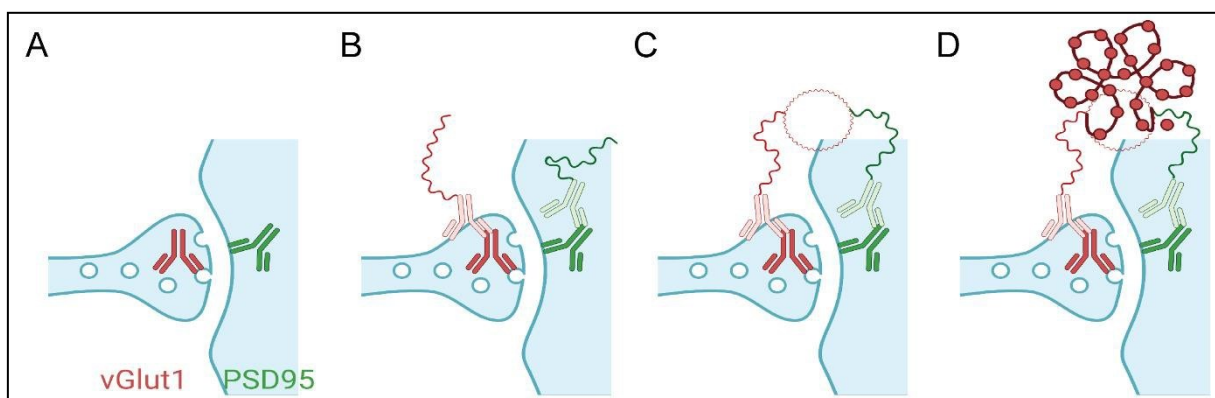
Figure 9: ***Workflow of the Proximity Ligation Assay in glutamatergic synapses. (A)*** *Anti-vGLUT1-antibody (red) to target the presynaptic vesicles carrying the neurotransmitter glutamate and the anti-PSD95 antibody (green) to bind to the post-synaptic density protein 95. **(B)** PLUS (light green) and MINUS (light red) probes labeled with oligonucleotides bind to the primary antibodies. **(C)** The free ends of the oligonucleotide labeled probes bind only to each other when they are in proximity < 40 nm. **(D)** A polymerase amplifies the signal and fluorescently labeled oligonucleotides bind to the DNA. Created with BioRender.com*

The commercially available PLA kits allow a wide range of applications with different probes to be used in cell culture and tissue experiments. The workflow (Figure 9) to quantify glutamatergic synaptic contacts uses primary antibodies (ABs) for pre- and post-synaptic targets, and probes that bind species specifically to the primary ABs. The

commercially available probes are simply called PLUS and MINUS for the 3'- or 5' direction respectively, of the free ends of the oligonucleotide reagents (Merck, 2019; Merck KGaA, accessed: 2021; Millipore, 2017). The application of the PLA to quantify synaptic contacts is highly specific due to the close vicinity of pre- and postsynaptic markers within the synaptic cleft (20-40 nm) (Südhof, 2012). This fits well to the hybridization distance of the oligonucleotide probes that is below 40 nm (Ahmari & Smith, 2002; Fredriksson et al., 2002; Widrow, Kim, Park, & Perin, 2019). It is important to select the targets wisely as they have to be in close proximity as well as near enough to the synaptic cleft to detect a functional synaptic connection. A synaptic contact (Figure 10) between two neurons is highly regulated: Before the neurotransmitter is released into the synaptic cleft, vesicles carrying the neurotransmitter, translocate to the active zone of the presynaptic neuron. Only through the activation of the SNAP/SNARE protein complex the vesicles can fuse with the membrane, so that eventually the neurotransmitter is released and can activate post-synaptic receptors (Hurst, 2013; Rudolf, Mongillo, Rizzuto, & Pozzan, 2003). In case of glutamatergic neurotransmission, it is important to choose targets that are especially involved in this process and are also in close proximity to the synaptic cleft, like the active zone of the pre-synapse or the post-synaptic density area.

Since proteins of the pre- and postsynaptic cleft are perfectly suited to generate a PLA signal, this method holds promise to quantify the synaptic density more accurate and less laboriously than as all the currently used methods.
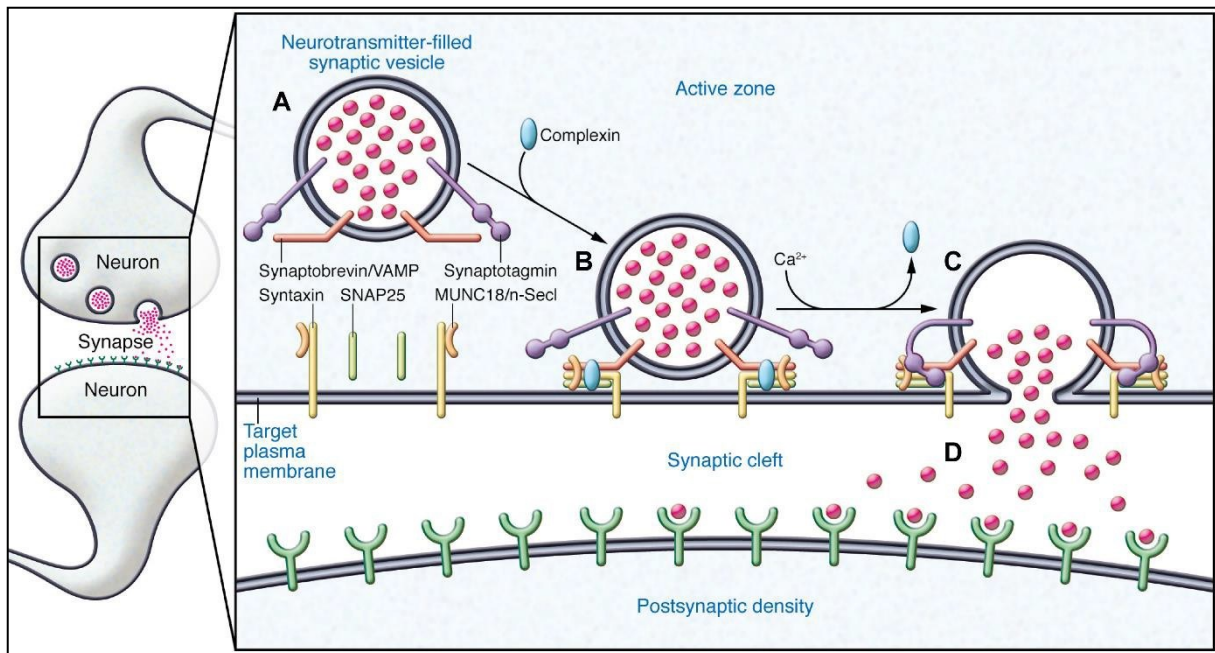
*Figure 10: **Synaptic vesicle exocytosis**. **(A)** Synaptic vesicles approaching the active zone of the pre-synapse tether to defined docking sites at the plasma membrane. **(B)** The vesicular synaptobrevin/VAMP molecules bind to the membranal SNAP25 and syntaxin for the docking maneuver. Complexin binds the previous evolved SNAP/SNARE complex to prevent a membrane fusion. **(C)** The action potential infused calcium influx results in the binding of synaptotagmin and the opening of the fusion pore. **(D)** The neurotransmitter is released and can activate receptors on the post-synaptic neuron. Figure taken from: (Hurst, 2013)*

1.4 Aim of the Study

According to the amyloid hypothesis, different mutations lead to the cleavage of the amyloid precursor protein resulting in the accumulation of Aβ plaques. This extracellular clustering of plaques promotes the hyperphosphorylation of the protein tau, which leads to the formation of neurofibrillary tangles inside of neurons and finally to neurodegeneration and the loss of brain areas. As the earliest alteration in AD consists of a synaptic dysregulation, there is an unmet need to accurately quantify changes in synaptic density in relevant brain areas and to exploit this as an alternative efficacy readout in drug development. However, current methods to quantify synaptic density are either too expensive, too laborious, or not reliable enough. Therefore, the aim of the present work was to establish a proximity ligation assay-based protocol for the quantification of synaptic contacts of general synapses as well as glutamatergic synapses in non-diseased and diseased mouse brains. Specifically, the PLA protocol had to be adapted regarding the most suitable synaptic antibody pairs, tissue preparation methods, and an optimal probe coupling. Furthermore, a robust algorithm-based quantification protocol had to be developed. By the help of this optimized PLA protocol, synaptic density was assessed in a model of TMT-induced neurodegeneration, and in two AD mouse

models representing the Aβ and the tau pathology to investigate spatiotemporal changes in large brain areas.

2 MATERIALS AND METHODS

2.1 Materials

2.1.1 Antibodies

Table 2-1: Primary antibodies

TARGETS OF PRIMARY AN-TIBODIES	VENDOR, CATALOG NUMBER	DILUTIONS USED ON			
		FREE-FLOATING	CRYO-SECTIONS	FFPE tissue	PFA-FIXED AND CLEARED TISSUE
Acetylcholines-terase	Abcam, ab183591	x	x	1:1000	x
Bassoon	Synaptic Systems,141 118	x	x	1:1000	x
DAT	Synaptic Systems, 284 003	x	x	1:500	x
HOMER1	Creative Diagnostics, CABT-BL4859	x	x	1:1000	x
HOMER1a	Synaptic Systems, 160 003	1:500	1:500	1:500	1:100
IBA1	Fujifilm, 019-19741	1:1000	1:1000	1:1000	1:500
MAP2	Merck, AB15452	1:2000	1:2000	1:2000	x
NeuN	Abcam, ab134014	1:2000	1:2000	1:2000	x
PSD95	Cell Signal, 3450S	1:200	1:200	1:200	x
PSD95	Abcam, ab12093	1:300	1:300	1:300	x
PSD95	Abcam, ab18258	1:1000	1:1000	1:1000	x
PSD95	Merck, MAB1596	x	x	1:1000	x
PSD95	Cell Signal, 3409S (D27E11)	x	x	1:1000	x
Synaptophysin (SYP)	Abcam, ab14692	1:1000	1:1000	1:1000	1:500
Synaptotagmin (SYT)	Synaptic Systems, 105 103	1:500	1:500	1:500	1:100
VAMP2	Abcam, ab215721	1:2000	x	x	1:100
VAMP2	RnD Systems, AF5136	x	x	x	1:100
vGLUT1	Synaptic Systems, 135 307	x	x	1:300	x
vGLUT1	Merck, AB5905	1:1000	x	x	1:100
vGLUT1	Merck, ABN1647	x	x	1:1000	1:500
VMAT2	Abcam, ab280364	x	x	1:1000	x

Table 2-2: Secondary antibodies

TARGETS OF SECONDARY ANTIBODIES	VENDOR NUMBER	DILUTION USED
Goat anti-Rabbit IgG (H+L) Highly Cross-Adsorbed Secondary Antibody, Alexa Fluor Plus 488	ThermoFisher A-32731	1:600
Donkey anti-Goat IgG (H+L) Cross-Adsorbed Secondary Antibody, Alexa Fluor 488	ThermoFisher A-11055	1:600
Goat anti-Guinea Pig IgG (H+L) Highly Cross-Adsorbed Secondary Antibody, Alexa Fluor 488	ThermoFisher A-11073	1:600
Goat anti-Chicken IgY (H+L) Cross-Adsorbed Secondary Antibody, Alexa Fluor Plus 488	ThermoFisher A-32931	1:600
Donkey IgG anti-Guinea Pig IgG (H+L)-Cy3	Dianova 706-165-148	1:300
Goat anti-Rabbit IgG (H+L) Cross-Adsorbed Secondary Antibody, Alexa Fluor 546	ThermoFisher A-11010	1:600
Goat anti-Mouse IgG (H+L) Highly Cross-Adsorbed Secondary Antibody, Alexa Fluor 546	ThermoFisher A-11030	1:600
Donkey anti-Rabbit IgG (H+L) Highly Cross-Adsorbed Secondary Antibody, Alexa Fluor 555	ThermoFisher A-31572	1:600
Goat anti-Guinea Pig IgG (H+L) Highly Cross-Adsorbed Secondary Antibody, Alexa Fluor 568	ThermoFisher A-11075	1:600
Goat anti-Rabbit IgG (H+L) Highly Cross-Adsorbed Secondary Antibody, Alexa Fluor Plus 647	ThermoFisher A-32733	1:600
Goat anti-Mouse IgG (H+L) Cross-Adsorbed Secondary Antibody, Alexa Fluor 647	ThermoFisher A-21235	1:600
Goat anti-Rabbit IgG (H+L) Cross-Adsorbed Secondary Antibody, Alexa Fluor 700	ThermoFisher A-21038	1:600
Goat anti-Mouse IgG (H+L) Highly Cross-Adsorbed Secondary Antibody, Alexa Fluor 790	ThermoFisher A-11357	1:600
Donkey anti-Mouse IgG (H+L) Highly Cross-Adsorbed Secondary Antibody, Alexa Fluor Plus 800	ThermoFisher A32789	1:600
Donkey anti-Rabbit IgG (H+L) Highly Cross-Adsorbed Secondary Antibody, Alexa Fluor Plus 800	ThermoFisher A32808	1:600

Table 2-3: Instruments

INSTRUMENTS	COMPANY
PT Module	Thermo Fisher
Hybaid Shake 'N' Stack	Thermo Fisher
InSlide Out™ Hybridization Apparatus	Boekel Scientific
LSM 700	Zeiss
Axioscan.Z1	Zeiss
Pannoramic Midi II	3DHistech
Ultra-microscope II	Miltenyi Biotec
ASP300s	Leica
VIP® 6 AI	Tissue-Tek
Pannoramic 1000 (p1000)	3DHistech
Para Trimmer	Thermo Scientific
HistoStar	Thermo Scientific
Tissue-Ek Prisma Plus Automated Slide Stainer	Sakura
Tissue-Tek Glas	Sakura
Oven	Memmert

Tissue-Tek Autosection	Sakura
PFM Rotary 3006 Em	PFM
CM305S Kryostat	Leica
Array Scan	Thermo Fisher
Pherastar FSX	BMG Labtech
Frigomobil	Leica
Wacom Cintiq 16 With Pro Pen 2	WACOM
Ipad Pro (11 Zoll) With Pencil	Apple
X-Clarity Polymerization System C20001	Logos Bio
X-Clarity Tissue Clearing System C30001	Logos Bio
ELLA (Fully Automated ELISA)	Protein Simple

2.1.2 Kits

KIT	VENDOR NUMBER
Duolink® In Situ PLA® Probe Anti-Rabbit PLUS	DUO92002-100RXN
Duolink® In Situ PLA® Probe Anti-Rabbit MINUS	DUO92005-100RXN
Duolink® In Situ PLA® Probe Anti-Mouse PLUS	DUO92001-100RXN
Duolink® In Situ PLA® Probe Anti-Mouse MINUS	DUO92004-100RXN
Duolink® In Situ PLA® Probe Anti-Goat MINUS	DUO92006-100RXN
Duolink® In Situ PLA® Probe Anti-Goat PLUS	DUO92003-100RXN
Duolink® In Situ Probemaker PLUS	DUO92009-1KT
Duolink® In Situ Probemaker MINUS	DUO92010-1KT
Duolink® In Situ Wash Buffers, Fluorescence	DUO82049-20L
Duolink® In Situ Detection Reagents Far Red	DUO92013-100RXN
Duolink® In Situ Detection Reagents Orange	DUO92007-100RXN
Duolink® In Situ Mounting Medium with DAPI	DUO82040-5ML
Duolink® In Situ Microplate Nuclear Stain, Anti-Fade	DUO82064-1KT
Mouse-on-Mouse (MoM) Blocking Kit, 1mL	VEC-MKB-2213
Pierce™ BCA Protein Assay Kit	23227
X-CLARITY Hydrogel Solution Kit	C1310X
Electrophoretic Tissue Clearing Solution	C13001

2.1.3   Reagents

Table 2-4: Reagents

REAGENT	DISTRIBUTOR	VENDOR NUMBER
DPBS, no calcium, no magnesium	Gibco	14190169
DPBS, calcium, magnesium	Gibco	14040174
Tween 20 Solution	Biorad	161-0781
Donkey Serum	Sigma Aldrich	D9663
35% BSA in DPBS	Sigma Aldrich	A7979
Hydrochloride acid	Sigma Aldrich	320331-500ML
Sodium hydroxide (NaOH) pellets	Sigma Aldrich	S8045
Paraformaldehyde	Sigma Aldrich	158127
Ketamine 10%	WDT	FS1670044WDD
Rompun 2% Injektionslösung	BAYER	(01)04007221031017
Sevoflurane	AbbVie	PZN: 01974365
Isotonic saline solution 0,9%	Braun	PZN: 03239121
Wash Buffer for IHC (20X)	Medac	B1-30A
Gelatine	VWR	24350262
TritonX-100	Sigma Aldrich	X100-100ML
Saponin	Sigma Aldrich	S4521-25G
Sodium azide	Sigma Aldrich	S2002-5G
Ethanol 70 %	VWR	83801.360
Ethanol 80 %	VWR	85828.440
Ethanol 96 %	VWR	83804.360
Ethanol absolute	VWR	83813.360
Xylene	VWR	28973.363
Formalin 10 %	VWR	11699404
Hematoxylin 7211	Thermo Scientific	10034813
Eosin	Morphisto	18277.01000
Pertex®	Medite	UN 1993
Salzsäure Alkohol (0,25 % / 70 %)	Morphisto	14473.02500
Surgipath Paraplast Bulk	Leica	39602012
Sudan Black B	Sigma Aldrich	199664-25G
Proteinase K		
Sucrose	Sigma Aldrich	1076511000
OCT	Thermo Scientific	LAMB/OCT
Fluorescence Mounting Medium	Dako	GM304
ToPro3	Thermo Fisher	T3605
Acridine Orange	Sigma Aldrich	A6014-10G
SYTOX Deep Red	Thermo Fisher	S11380
HOECHST	Thermo Fisher	62249
SYTOX Blue	Thermo Fisher	S11348
Methoxy-X04	Tocris	4920
Tris-EDTA Buffer 10X pH9 (PT Module)	Medac Diagnostica	MAD-004070R/D
Citrate Buffer 10X pH6 (PT Module)	Medac Diagnostica	MAD-004071R/D
Trimethyltin chloride	Sigma Aldrich	146498
X-CLARITY Mounting Solution	Logos Bio	C13101
Pierce 20X PBST Tween 20 Buffer (PBST)	Thermo Scientific	28352
Simple Plex Wash Buffer A	Protein Simple	896055
Simple Plex Sample Diluent SD13	Protein Simple	896098

2.1.4 Equipment

Table 2-5: Equipment

EQUIPMENT	DISTRIBUTOR	VENDOR NUMBER
Rocking shaker	neoLab	7-0952
Tube rotator	VWR	444-0500
StainTray Objektträger-Färbungssystem	Sigma Aldrich	Z670146-1EA
Slide box for humidity chamber (self-made)	VWR	631-0737
Coverslips (24 x 50 mm, Menzel Gläser #1 Spezial)	NeoLab	E4136
BRAND® staining tray, black	Sigma Aldrich	BR471400-5EA
Pap Pen (liquid blocker)	Abcam	ab2601
Clear nail polish	Maybelline	B001IDZ8TG
Kimtech wipes	Kimberly-Clark	107281
BOND covertiles	Leica Biosystems	S21.2001
Hot plate with magnetic stirrer	VWR	OHAU30500523
Filter paper	VWR	515-5009
Venofix A	Braun	PZN 05039567
AGANI Needle	Terumo	AN*2623R1
Dissecting scissors	VWR	HAMMHSB028-15
Adult Mouse Brain Slicer Matrix	ZIVIC Instruments	BSMAS001-1
Injekt® Luer Lock Solo 2 ml	Braun	4606701V
Omnifix®	Braun	4617053V
Reglo ICC digital peristaltic pump	ISMATEC	IDX1798-PD-IS
Microvette® 500 K3 EDTA	Sarstedt	20.1341
Tissue-Tek Ausgießformen	Sakura	7055
Uni-Cassette Biopsiekassette weiß/gestapelt/mit Deckel	Sakura	8086
Water bath	Sakura	1451
Adhäsionsobjektträger, SuperFrost Plus	VWR	631-0446
WÄGESCHÄLCHEN QUADRATISCH 7 ML WEISS	VWR	611-0093
PolarChuck™ Circular Pattern, 40mm Thin St	Leica	70171-04
KimTECH SCIENCE precision wipes	Kimberly-Clark	05511
Adhesive cement Blu Tack	Bostik	30811745
Freezer block COOLRACK M15 GRAY	Corning	479-1853
Microcon-30kDa Centrifugal Filter Unit with Ultracel-30 membrane	Merck	MRCF0R030
VACUSAFE	Integra Bioscience	391-2094
Orbital shaker	OHAUS	OHAU30391900
TPP®-Gewebekulturplatten	Merck	Z707783-72EA
Nunc® Cell Culture Inserts in 12-well Nunclon Delta surface plate	Nunc	TMO140652
Mouse Brain Slice Holder	Logos Bio	C12004
Holder for 6 Mouse Brains	Logos Bio	C12013
72-well ELLA Cartridges	Protein Simple	SPCKB-PS-002448

2.1.5 Mice

Immunofluorescence (IF) and PLA staining, TMT study and clearing experiments were performed on adult wild-type C57BL/6 mice at a weight of 22-25 g/mouse. In addition,

fifteen day old (P15) wild-type C57BL/6 mice were used to study age-related synaptic density by PLA.

The rtg4510 (TG4510) mouse line expresses human tau and bears the P301L mutation that leads to frontotemporal dementia (Gamache et al., 2019; Ramsden et al., 2005). Mice were 2-, 6-, and 10-month-old.

C57/bl_CaMKII-tTA (tA) transgenic mice are the transactivator line of the transgenic tg4510 mice and were used as control animals to the rtg4510 mouse line. Animals express the mouse calcium/calmodulin-dependent protein kinase II alpha (Camk2α) promoter that drives Cre recombinase expression in the forebrain (Tsien JZ, 1996). Mice were 2-, 6- and 10-month-old.

The APP/PS1 mice contain transgenes of human APP and human PSEN1 (Maia et al., 2013; Radde et al., 2006). Mice were 2-, 6- and 10-month-old.

All animals were housed in microisolator cages type II in groups of 1-3 animals per cage at a temperature of 20-24 °C, a humidity of 50-60 %, and a 12 h light-dark-cycle. Wood shavings were provided for bedding and sizzle nest as nesting material. Food and water were provided ad libitum.

All experiments were conducted in accordance with appropriate guidelines and approved by the regional ethics committee in Rhineland-Palatine, Germany.

2.1.6 Freshly Prepared 4 % Paraformaldehyde Solution

For 1 L of a freshly prepared paraformaldehyde (PFA) solution, 800 ml of 1x Phosphate buffered saline (PBS) was added into a glass beaker on a stir plate in a ventilated hood and heated up to 60 °C. 40 g of Paraformaldehyde powder was added. To dissolve the powder, pH of the solution was increased with sodium hydroxide (NaOH) pellets until the solution clears. Once paraformaldehyde was dissolved, the solution was filtered into a bottle placed on ice. Adjust the volume to 1 L with 1x PBS. Once the solution was cooled down, pH was adjusted to 6.9 with drops of a hydrochloride acid solution. The solution was then aliquoted and frozen at -20 °C or stored at 4 °C for 1 month.

2.1.7 IHC Wash Buffer

IHC wash buffer concentrate (Medac) was diluted 1:20 in deionized (VE) water.

2.1.8 Antibody Dilution Stock Buffer

To prepare the antibody dilution stock buffer being used for blocking and antibody dilution, 1 % (v/v) of BSA was added to PBS and mixed.

2.1.9 Blocking Buffer

The blocking buffer, used to prevent cross-reactions and reduce background staining, as well as for permeabilization, was generated by adding 5 % (v/v) donkey serum and 0,1 % (v/v) Tween-20 to the antibody dilution stock buffer.

2.1.10 Antibody Dilution Buffer

For primary and secondary antibody dilutions, 1 % (v/v) donkey serum was added to the antibody dilution stock buffer.

2.1.11 Buffers A and B

Buffers A and B (Merck, Millipore) were commercially purchased and were dissolved in MilliQ water. They served as washing buffers for the PLA.

2.1.12 PBSGT Solution

To prepare the PBS with Gelatin and Triton (PBSGT) solution which was used as blocking and permeabilization solution of the ethyl cinnamate (ECi)-Clearing, 0.2 % gelatin and 0.5 % TritonX-100 were added to PBS.

2.1.13 PBSGT+S Solution

The PBSGT with Saponin (PBSGT+S) was used as antibody dilution solution. Therefore, 10 mg/ml Saponin were added to the PBSGT solution.

2.2 Methods

2.2.1 Perfusion Surgery

Mice were sedated and anesthetized with a mixture of Ketamine/Xylazin (120 + 20 mg/kg) via intraperitoneal injection. After 5 min, the toe pinch-response method was used to determine depth of anesthesia. Animal must be unresponsive before continuation of the procedure. Then, a small incision in the diaphragm was made. The incision was continued along the entire length of the rib cage. The sternum was lifted away and

clamped to the side. A perfusion needle was passed through the ascending aorta. A clamp was used to fix the needle to the heart. An incision was made in the animal's right atrium. A pump connected to the needle started to infuse PBS buffer running at 4.6 ml/min for 8 min. Clearing of the liver served as an indicator for a good perfusion. Usually, after 8 min a sufficient clearing level was reached. In case of insufficient clearing, PBS was run until the liver was clear. Then, a 4 % PFA solution was infused for 8 min. As an indicator for successful perfusion, fixation tremors should be observed after a short time. After fixation, the head was removed with scissors, and a midline incision of the scull was performed from the nose to the neck. Remaining neck muscle was removed. The scull was carefully peeled away from the brain to finally place it in a 4 % PFA solution. Post-fixation of the brain was done at 4 °C while shaking overnight to let the formaldehyde integrate and to denature the proteins. Finally, brains were placed in PBS/0.1 % sodium azide (NaN_3) until further use.

2.2.2 IF Protocol on Free-Floating Tissues

After the perfusion described in 2.2.1 free-floating tissue sections were prepared by soaking a hemisphere of the brain from wt C57Bl6/J animals in a 30 % sucrose in PBS solution overnight. A water droplet was placed on the freezing plate of a Frigomobil. To prepare coronal sections the tissue was placed on the droplet with the side down (cerebellum) of the second cut as indicated in Figure 11 before the water droplet could freeze. With a pipette, the tissue was surrounded with water droplets to produce a matrix of ice around the tissue. Then the tissue was frozen on the freezing block for 20 min under a small glass beaker. Afterwards, 40 µm sections were cut and the slices were collected in a 6-well plate filled with PBS/0.1 % NaN_3.

2.2.3 IF Protocol on Cryosections

2.2.3.1 Tissue Processing of Cryosections

According to the perfusion surgery protocol described in 2.2.1, a hemisphere of the brain from wildtype (wt) C57Bl6/J animals was soaked in a 30 % sucrose in PBS solution overnight. This was done prior to embedding of the tissues in order to decrease cell destruction and to limit the swelling of the tissue (Bahr, Bloom, & Friberg, 1957). For embedding of tissues in OCT medium, tissues were placed in small weighing

bowls. Due to the opaque color of the medium after freezing, an area was painted on the bottom of the bowl before to indicate where the tissue was placed. The bowl was placed on an even surface at -20 °C overnight. Subsequently, the frozen OCT block was taken out of the bowl, cut along the before painted area, to receive a small frozen block with the mounted brain hemisphere inside. The mounted hemisphere was then transferred into the cryostat. On a Polar Chuck (ThermoFisher), a little amount of liquid OCT Medium was placed to freeze the OCT tissue block on the chuck by the help of the integrated fast freezing station. With a cryostat, 10 µm sections were cut and every 2nd slice was mounted. Slides were collected and stored until staining at -20 °C. Before staining, slides were allowed to adjust to room temperature (RT) over 2 h.

2.2.3.2 IF Protocol for Cryosections

For immunohistochemistry stainings on cryosections the tissue was processed as described before (2.2.3.1). Washing steps of cryosections was performed on the slides with a volume of 500 µl/slide. Excess liquid was aspirated and not tapped off to prevent tissue damage, and was solely aspirated. All incubations were performed in a moisture chamber.

After the initial washing with PBS, 3x for 5 min, slides were dried with Kim wipes around the tissue and then encircled with a PAPpen. For blocking and permeabilization, the antibody dilution buffer and blocking buffer were prepared. Blocking buffer was added (350 µl/slide) and incubated for 60 min at RT Afterwards, primary antibodies were thawed, briefly vortexed and spun down, to prepare the primary antibody solution mix. Blocking buffer was aspirated, and 350 µl/slide of primary antibody solution mix was added and incubated overnight at 4 °C in a moisture chamber. For the secondary antibody incubation step, primary antibody solution was 2x washed off with IHC wash buffer for 5 min. Secondary antibody solution mix was prepared. PAPpen was renewed if needed under a fume hood. 350 µl/slide of the secondary antibody solution was added to the slides and incubated for 2 h at RT. Then, secondary antibody solution was 2x washed off with IHC wash buffer for 5 min. For nuclear staining and mounting, excess wash buffer was aspirated by using Kim wipes to dry the slides around the tissue. Slides were mounted with 70 µl/slide DAKO Fluorescence Mounting Medium. Mounting Medium was allowed to dry in the dark for 15 min before imaging.

2.2.4 IF on FFPE Tissue

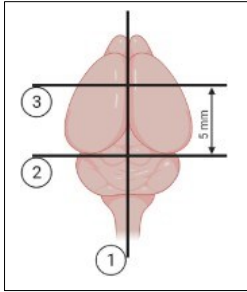### 2.2.4.1 Formalin-fixed and Paraffin-embedded (FFPE) Tissue Processing

Figure 11: Tissue processing.

First, a razor blade was placed through the midline of the mouse brain matrix to separate the brain hemispheres. The second blade was positioned through the midbrain. The third cut was placed in a distance of 5 mm through the cortex.

The tissue was trimmed with the help of a mouse brain matrix. The brain was located with the cortex to the top in the matrix. If not otherwise stated, brains were cut into two hemispheres along the longitudinal fissure. The first cut to separate the hemispheres was done along the midline of the brain (Figure 11). In caudal direction, the second cut was placed before the cerebellum, through the midbrain. The next cut was positioned 5 mm rostral, through the cortex. The tissue section was then placed into a cassette and in a beaker filled with either 70 % ethanol (EtOH) or 10 % formalin, depending on the tissue processing automat used. The remaining tissue of the cerebellum and the olfactory bulbs were collected in a solution of PBS with 0.01 % NaN_3 and stored at 4 °C for further use. The following tissue processing protocols are summarized in Table 2-6 according to the processing automat used. If not otherwise stated, usually protocol A on the Leica ASP300S was performed. After execution of the processing steps, tissue was positioned into metal forms in which hot paraffin wax was filled in. With the help of the cooling plate of the HistoStar Embedding Workstation, the tissue was embedded into paraffin blocks. The bottom of the cassette was put on top of the paraffin block for identification. Afterwards, excess wax was melted away from the cassette with the heated plate of the PARA Trimmer.

Table 2-6: Tissue Processing Steps

A. Leica ASP300S		B. Tissue-Tek VIP 6 AI	
Reagent	Duration [min]	Reagent	Duration [min]
Ethanol 70 %	60	Formalin 10 %	5
Ethanol 80 %	60	Ethanol 50 %	30
Ethanol 96 %	45	Ethanol 70 %	30
Ethanol 96 %	30	Ethanol 80 %	30
Ethanol Absolute	10	Ethanol 96 %	30
Ethanol Absolute	10	Ethanol 96 %	30
Ethanol Absolute	10	Ethanol Absolute	30
Xylene	30	Ethanol Absolute	30
Xylene	30	Xylene	30
Xylene	30	Xylene	30

Paraffin Wax	60	Paraffin Wax	25
Paraffin Wax	60	Paraffin Wax	25
Paraffin Wax	60	Paraffin Wax	25
		Paraffin Wax	25

2.2.4.2 FFPE Slide Selection Strategy

FFPE brain tissue was cut using a rotation microtome or an auto-sectioning microtome. Serial slices were generated by cutting 4 µm thick tissue slices. Every second slice was mounted on a slide. Excess paraffin was melted away from the slides in an oven at 72 °C for 20 min. After cooling down, every 25th slide from a slide series of the same tissue block was stained with hematoxylin and eosin (HE). This was done according to the steps described in Table 2-7 and performed by an automated slide stainer in combination with a mounting apparatus for coverslips. After mounting with Pertex mounting medium and drying overnight, the slides were scanned with a P1000 slide scanner. Scanned and digitized slides were then compared to the Allen Brain Atlas "Mouse, P56, Coronal" / "Mouse, P14, Coronal" / "Mouse, E16.5, Coronal" (Science, 2020a, 2020b, 2021) to classify the regions of interest (ROI).

Table 2-7: HE-staining Steps

Reagent	Duration [min]
Xylene	3
Xylene	3
Xylene	3
Ethanol Absolute	2
Ethanol Absolute	2
Ethanol 96 %	1
Ethanol 96 %	1
Running water	3
Hematoxylin	8
Running water	5
0,25 % HCl alcohol	1
Running water	1
Running water	1
Running water	4
Ethanol 96 %	0,5
Eosin	1
Ethanol Absolute	1
Ethanol Absolute	1

Ethanol Absolute	1
Xylene	2
Xylene	1

2.2.4.3 Heat-Induced Epitope Retrieval (HIER) on FFPE Tissues

To access the epitope in formalin-fixed tissues, heat-induced epitope retrieval was used to unfold crosslinked proteins and restore antigenicity. The Pre-Treatment (PT) Module (ThermoFisher) for simultaneous dewaxing and antigen retrieval was used, that holds the temperature for 30 min at 98 °C. Buffers used for the antigen retrieval were adjusted to pH 6, 8 or 9 according to the antibody used.

2.2.4.4 Autofluorescence Quenching with Sudan Black on FFPE Tissues

Sudan Black (SB) was used as additional treatment of IF stainings on FFPE tissue to reduce background signal. Therefore, a 0.1 % SB solution in 70 % EtOH was produced and applied on FFPE tissues after staining with the secondary antibody. Slides were incubated for 30 min at RT. Afterwards, SB solution was washed off with PBS 3x for 5 min.

2.2.4.5 Enzymatic Pre-Treatment of FFPE Tissue with Proteinase K

Proteinase K was used as an additional pre-treatment of IF stainings on FFPE tissue to reduce background signal by inactivation of endogenous nucleases. Therefore, pro-teinase K reagent was diluted 1:30 with PBS. Slides were incubated with Proteinase K solution for 20 min at RT after heat-induced epitope antigen retrieval and washing. Wash solution was removed with IHC wash buffer for 3x, 5 min each.

2.2.4.6 IF protocol on FFPE Tissues with PAPpen

For immunohistochemistry stainings on FFPE slides were used that have been pro-cessed as described before (2.2.4.1). Antigen retrieval as described in 2.2.2, 2.2.4.4, and 2.2.4.5 was performed as required. Washing steps for FFPE slides were

performed in a staining tray on a rocking shaker. All incubations were performed in a moisture chamber.

After the initial washing of FFPE slides with PBS, 3x for 5 min, slides were dried with Kim wipes around the tissue and then encircled with a PAPpen. For blocking and permeabilization, the antibody dilution buffer and blocking buffer were prepared. Blocking buffer was added (350 µl/slide) and incubated for 60 min at RT Afterwards, primary antibodies were thawed, briefly vortexed and spun down, to prepare the primary antibody solution mix. Blocking buffer was tapped off, and 350 µl/slide of primary antibody solution mix was added and incubated overnight at 4 °C in a moisture chamber. For the secondary antibody incubation step, primary antibody solution was 2x washed off with IHC wash buffer for 5 min. Secondary antibody solution mix was prepared. PAPpen was renewed if needed under a fume hood. 350 µl/slide of the secondary antibody solution was added to the slides and incubated for 2h at RT. Then, secondary antibody solution was 2x washed off with IHC wash buffer for 5 min. For nuclear staining and mounting, excess wash buffer was tapped off and Kim wipes were used to dry the slides around the tissue. Slides were mounted with 70 µl/slide DAKO Fluorescence Mounting Medium. Mounting Medium was allowed to dry in the dark for 15 min before imaging.

2.2.4.7 IF protocol on FFPE Tissues with Covertiles

To minimize the amount of material used and to improve the staining quality, Covertiles were used for FFPE tissues instead of a PAPpen as liquid barrier. Covertiles can be used up to 25 times. To ensure a proper use with low discoloring and damaging, Covertiles were washed after every use with 70 % EtOH for at least 15 min and no longer than 24 h. Afterwards, Covertiles were washed 2x with VE water and 1x with MilliQ water and then dried with Kim wipes. Before antigen retrieval was performed as described in 2.2.2, all FFPE washing steps were done in a staining tray on a rocking shaker. Initial washing of tissue slides after antigen retrieval was performed 3x with 1x PBS for 5 min. For blocking of unspecific staining and for permeabilization, antibody dilution buffer and blocking buffer were prepared. 200 µl blocking buffer per slide was added, and a Covertile per slide was applied as described in Figure 12 followed by an incubation for 60 min at RT in a moisture chamber. Afterwards, primary antibodies were thawed, briefly vortexed and spun down, to prepare the primary antibody solution

mix. After tapping off the blocking buffer 200 µl primary antibody solution mix per slide were added, a coverslip was applied, and the slides were incubated overnight at 4 °C in a moisture chamber. For the secondary antibody incubation step, primary antibody solution was washed off 2x with IHC wash buffer for 5 min. Covertiles were washed in a beaker filled with MilliQ water. Afterwards, the Covertiles were dried with Kim wipes for further use. Secondary antibody solution mix was prepared and if necessary, antibodies were thawed, briefly vortexed and spun down. Then, the Covertile was applied again, 200 µl secondary antibody solution was added per slide, and incubated for 2h at RT in a moisture chamber. Secondary antibody solution was washed off 2x with IHC wash buffer for 5 min. For nuclear staining and mounting, excess wash buffer was tapped off and Kim wipes were used to dry slides around the tissue. Slides were mounted with 70 µl DAKO Fluorescence Mounting Medium per slide. Mounting Medium was allowed to dry in the dark for 15 min before imaging.
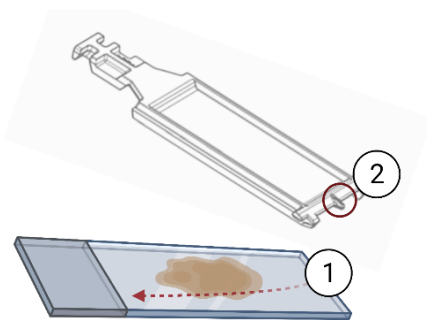

*Figure 12: **Positioning of Covertiles on a slide and application of liquids. (1)** The Covertiles were placed with the narrow side on the end of a microscope slide. **(2)** Liquids were applied through a little hole in the Covertile and were passively distributed through capillary forces on the entire slide.*

2.2.4.8 Methoxy-X04 Staining for Aβ Plaques

For the staining of Aβ plaques, the brain-permeable and fluorescent dye 1,4-bis(4'-hydroxystyryl)-2-Methoxybenzene (Methoxy-X04) was used (Alexander, 2018; Klunk et al., 2002). Therefore, a 5 mg/ml Methoxy-X04/PBS stock solution was prepared and homogenized in an ultrasound bath for 1.5 h at RT. For staining, tissue sections were washed in PBS for 5 min at RT. A 100 µM Methoxy-X04 solution was prepared with 40 % ethanol and MilliQ water. pH was adjusted to 10 with sodium hydroxide pellets. Then, sections were incubated for 10 min at RT. Reaction was stopped by dipping the sections 5x in tap water. Thereafter, a 0.2 % sodium hydroxide solution was prepared

with 80 % ethanol and MilliQ water. Slides were incubated for 2 min. Then slides were washed in tap water for 10 min.

2.2.5 Tissue Clearing

For the evaluation of the synaptic density in a whole mouse brain, different tissue clearing methods were applied and tested.

2.2.5.1 Antibody Validation for Solvent Tissue Clearing

To make sure that an antibody is suitable for solvent tissue clearing, an antibody validation assay was performed. Therefore, PFA-fixed tissue sections were collected on adhesive microscope slides. Non-methanol (MeOH) treated slides were used as positive control. The sections were then incubated for 3 h in 100 % MeOH at RT. Afterwards, the samples were rehydrated in PBS for 5 min. Thereafter, the IF protocol as stated in 2.2.4.6 followed.

2.2.5.2 Ethyl Cinnamate (ECi) Clearing protocol

Samples were perfused and dissected as previously described in 2.2.1. The samples were either cut in 2 mm with the help of a mouse brain matrix or an entire brain hemisphere was used. Then the following protocol was applied: samples were dehydrated in a series of 50 %, 80 % and 100 % MeOH/PBS (without calcium and magnesium) for 1h in the case of 2 mm slices or 1.5 h for bigger samples, at RT with shaking in an overhead shaker. Samples were transferred into a solution of 6 % hydrogen peroxide (H_2O_2) in MeOH to bleach the sample and incubate overnight at 4 °C and protected from light. After bleaching, the samples were rehydrated in 2x 100 % MeOH for 1h/1.5 h at RT while shaking. Further the samples were rehydrated under rotation in an 80% followed by a 50 % MeOH/PBS mixture for 1 h and 1.5 h, respectively. A final rehydration step was performed at RT under rotation in PBS for 1 h and 1.5 h, respectively. The sample could now be stored optionally in PBS with 0.01 % NaN_3 at 4 °C until further use. For blocking of unspecific staining, a PBSGT solution was prepared to incubate the sample for 2 days under rotation at RT. Then the immunolabeling was performed by preparing PBSGT solution with 10 mg/mL saponin. Primary antibodies were diluted in the solution and the samples were incubated in primary antibody

solution for 7 days at 37 °C and rotation. The solution was rinsed off by washing the sample 6x for 1h each in PBSGT at RT under rotation. PBSGT was prepared with 10 mg/mL saponin. To avoid secondary antibody precipitates, the secondary antibodies were diluted in PBSGT with saponin and filtered through a 0.22 µm filter. Then, the samples were incubated for 2 days at 37 °C and under rotation in the secondary antibody solution. The samples were rinsed 6x in PBSGT for 1 h each at RT under rotation. At this step, the samples can be optionally stored in PBS with 0.01 % NaN_3 at 4 °C until further use. For nuclear staining of the samples see Table 2-8 for incubation times and dilution. Before clearing, the samples were dehydrated in a series of 20 %, 40 %, 60 %, 80 %, 2x 100 % MeOH/PBS⁻ ⁻ for 1 h each at RT under rotation. For clearing, the samples were subjected to a mixture of 66 % Dichloromethane (DCM) and 33 % MeOH overnight at RT. To wash out MeOH, the samples were incubated in 100 % DCM for 30 min. Then, the samples were transferred into Dibenzyl ether (DBE) until transparent. Before imaging, the samples were placed in ECi in the imaging room for acclimatization. For imaging, the imaging chamber filled with ECi was prepared and samples were imaged with an UltraMicroscope II, Miltenyi with a LVMI-Fluor 4X/ 0.3WD6 objective.

2.2.5.3 X-CLARITY Protocol

Samples were perfused and dissected as previously described in 2.2.1. The samples were either cut in 2 mm slices with the help of a mouse brain matrix or one entire brain hemisphere was used. Then the following protocol was applied: Hydrogel-initiator solution was prepared by adding 25 % X-CLARITY polymerization initiator (w/v) to X-CLARITY hydrogel solution. The samples were incubated in the solution at 4 °C for 24 h. Noteworthy, it needed to be ensured that samples were submerged. Polymerization was initiated by using the X-CLARITY Polymerization System by running the system at 37 °C and -90 kPa for 3 h to efficiently expose the tissue to the solution. Then, the samples were taken out and gently shaken for 1 min after polymerization. Thereafter, the samples were rinsed several times with PBS⁻ ⁻. At this point, the sample can be stored at 4 °C in PBS until further use. The tissue clearing was performed by using the X-CLARITY Tissue Clearing System and the Mouse brain slice holders for electrophoretic clearing with a current of 1 A at 37 °C. The pump was set to 50 rpm and the system run for 8 h. If transparency was not sufficient, clearing was continued until the

sample was clear. Subsequently, the samples were washed several times in PBST. Then, samples were transferred into a 50 ml falcon tube filled with PBST and incubated overnight at RT while shaking to wash out the clearing solution. Before immunolabeling, samples were treated in blocking solution for 2 days at 37 °C under rotation. For immunolabeling, primary antibodies had to be labeled appropriately in PBST and incubated in total for 5 days. Primary antibody solution was refreshed after 2 and 4 days by adding half of the antibody dilution volume. Thereafter, the sample was washed in PBST at RT while shaking several times for one day. Then, the sample was incubated with secondary antibody solution for 5 days at 37 °C under rotation. Therefore, secondary antibodies coupled to fluorophores in PBST were diluted appropriately and protected from light. Afterwards, samples were washed several times in PBST for one day. For the following nuclear staining, see Table 2-8. Then, the samples were washed 3x in distilled water for 5 min in the dark with gentle agitation. For the refractive index homogenization, samples were incubated in X-CLARITY mounting solution at RT in the dark for 1 h. Mounting solution was replaced with fresh solution and the sample was acclimated in the imaging room for at least 1 h. For imaging, the imaging chamber was filled with X-CLARITY mounting solution and the sample was imaged with an UltraMicroscope II, Miltenyi with a LVMI-Fluor 4X/ 0.3WD6 objective.

Table 2-8: Nuclei dyes used for tissue clearing techniques

CLEARING METHOD	NUCLEI DYE	DILUTION	SOLUTION	DURATION/ TEMPERATURE
ECi	ToPro3	1-600	PBS⁻⁻	1 h/RT
ECi	Acridine Orange	1%	PBSGT	1 h/RT
ECi	SYTOX Deep Red	0,5 µM	PBSGT	2 h/RT
ECi	HOECHST	0,10%	PBSGT	2 h/RT
ECi	SYTOX Blue	1 µM	PBSGT	1 h/RT
X-CLARITY	ToPro3	1-600	PBS⁻⁻	1 h/RT

2.2.5.4 Combination of ECi Tissue Clearing and PLA

To study synaptic loss in large samples, the PLA protocol was combined with CLARITY clearing. Samples were perfused and dissected as previously described in 2.2.1. The samples were cut in 2 mm slices with the help of a mouse brain matrix. For incubation, the samples were placed in 5 ml tubes, filled with 3 ml solution. EtOH solutions with 50 % and 80 % EtOH with an pH adjusted to 9 were prepared (with MilliQ water since distilled water could absorb carbon dioxides from the atmosphere and become acidic

(Klingberg et al., 2017)). EtOH solutions were stored at 4-8 °C. Samples were dehydrated first in 50 % ethanol followed by 80 % ethanol for 1 h each with overhead rotation at RT. Samples were then dehydrated in 100 % MeOH for 1 h with overhead rotation at RT. Samples were transferred to a solution of 6 % H_2O_2 and MeOH for bleaching, incubated at 4 °C overnight and protected from light. Then, the samples were rehydrated with first 2x 100 % MeOH, followed by 80 % MeOH/PBS, 50 % MeOH/PBS and PBS for 1 h each with overhead rotation at RT. At this point, samples can be stored in PBS with 0.1 % NaN_3 at 4 °C. For blocking and permeabilization, PBSGT solution (2.1.12) was prepared. Samples were then incubated in PBSGT solution for 2 days with overhead rotation at RT. For primary antibody incubation, antibodies were incubated in PBSGT + 10x saponin (2.1.13) solution for 2 days at 37 °C with rotation. Afterwards, the samples were washed 2x in Buffer A for 1 h each with overhead rotation at RT. For probe incubation, probes were diluted 1:5 in PBSGT + 10x saponin solution. Samples were incubated in probe solution for 24 h at 37 °C with rotation. The samples were then washed 2x in Buffer A for 1 h each with overhead rotation at RT. For ligation, ligation buffer was diluted 1:5 in MilliQ water. The ligase was added shortly before sample incubation 1:40 into the prepared buffer. Samples were then incubated in the ligation mix for 30 min at 37 °C with rotation. The samples were then washed 2x in Buffer A for 1 h each with overhead rotation at RT. The amplification mix was prepared by diluting the amplification buffer 1:5 in MilliQ water (protected from light). Amber tubes were used from now on. Shortly before sample incubation, polymerase was added to the buffer (1:80 dilution). Then, samples were incubated in the amplification mix for 100 min at 37 °C under rotation. Afterwards, samples were washed 2x in Buffer B for 1 h each, followed by rinsing in 0.01x Buffer B for 30 min. Nuclear staining was performed by incubating the samples in a mixture of ToPro3 diluted 1:600 in PBS for 1 h with overhead rotation at RT. Then, samples were rinsed 2x in PBS for 1 h each. Clearing was performed in 5 ml TPP conical tubes (amber). A dehydration series with 20 %, 40 %, 60 %, 80 % and 2x 100 % MeOH/PBS was performed for 1 h each at RT and with overhead rotation. Then the samples were incubated in a mix of 2/3 DCM and 1/3 MeOH overnight at RT and shaking. Subsequently, the samples were incubated in 100 % DCM to wash out MeOH for 30 min at RT. Final clearing step was performed in DBE until the samples were transparent. For acclimatization, the samples were transferred into ECi for at least 1 h at RT in the imaging room. For imaging, imaging chamber

was filled with ECi. Samples were imaged with an UltraMicroscope II, Miltenyi with a LVMI-Fluor 4X/ 0.3WD6 objective.

2.2.5.5 Combination of CLARITY and PLA

To study synaptic loss in large samples, the PLA protocol was combined with CLARITY clearing. Samples were perfused and dissected as previously described in 2.2.1. The samples were cut in 2 mm slices with the help of a mouse brain matrix. Then the following protocol was applied: Hydrogel-initiator solution was prepared by adding 25 % X-CLARITY polymerization initiator (w/v) to X-CLARITY hydrogel solution. Samples were incubated in the solution at 4 °C for 24 h. It had to be ensured that the samples were submerged. The polymerization was initiated by using the X-CLARITY Polymerization System by running the system at 37 °C and -90 kPa for 3 h to diffuse the tissue with the solution. Samples were taken out and shaken gently for 1 min after polymerization. Samples were rinsed several times with PBS^{--}. At this point, the samples can be stored at 4 °C in PBS until further use. The tissue clearing was performed by using the X-CLARITY Tissue Clearing System and the Mouse brain slice holders for electrophoretic clearing with a current of 1 A at 37 °C. The pump was set to 50 rpm and the system run for 8 h. If transparency was not sufficient, clearing was continued until the sample was clear. Subsequently, the samples were washed several times in PBST. Samples were transferred into a 50 ml falcon tube filled with PBST and incubated the overnight at RT while shaking to wash out the clearing solution. For the PLA staining, samples were treated in blocking buffer (2.1.9) for 2 days at 37 °C with gentle rotation to prevent unspecific binding and to permeabilize them. Afterwards, primary antibodies were diluted in antibody dilution buffer (2.1.10) for 5 days at 37 °C with gentle rotation. Primary antibody was refreshed 3x in 5 days. Then, samples were washed 3x in Buffer A for 1 h each at RT with gentle rotation. Probes were diluted 1:5 in antibody dilution buffer (2.1.10) and incubated for 3 days at 37 °C under rotation. Then, samples were washed 3x in Buffer A for 1 h each at RT with gentle rotation. Ligation mix (MilliQ water, ligation buffer 1:5, ligase 1:40) was prepared and the samples were incubated for 2 days at 37 °C under rotation. Then samples were washed 3x in Buffer A for 1 h each at RT with gentle rotation. Amplification mix (MilliQ water, amplification buffer 1:5, polymerase 1:80) was prepared and samples were incubated for 4 days at 37 °C under rotation and in the dark. For nuclear staining, ToPro3 was used as indicated in Table

2-8. Afterwards, samples were washed 3x in MilliQ water for 5 min each at RT with rotation in the dark. For the refractive index homogenization, samples were incubated in X-CLARITY mounting solution at RT in the dark for 1 h. Mounting solution was replaced with fresh solution and acclimated in the imaging room for at least 1 h. For imaging, imaging chamber was filled with X-CLARITY mounting solution and samples were imaged with an UltraMicroscope II, Miltenyi with a LVMI-Fluor 4X/ 0.3WD6 objective.

2.2.5.6 Data Analysis of 3D Samples

Data analysis of the 3D data stacks was performed with arivis Vision 4D (version 3.3.0, arivis AG, Munich, Germany) software. Mosaic and tile scans were sorted with the help of the tile sorter function. To quantify colocalization of pre-and post- synaptic markers, the background correction, Blob Finder, and Compartment operation of the arivis Vision 4D Analysis Pipeline were used.

2.2.6 PLA Protocol

To overcome the hurdle of classic immunohistochemistry such as the highly subjective and hardly quantifiable overlay-quantification of a double staining of two targets labeled with fluorescent markers, the commercially available PLA kit of DUOLINK was used in this work. This allowed quantification of functional synaptic contacts. When performing the PLA, the same primary antibodies were used as for the previous IF staining. However, a next, crucial step consists of the linkage of oligonucleotide probes to the primary antibody. An important feature of this method is that only probes that are in close proximity to one another can be ligated. Accordingly, hybridization of herein used probes can be used to indicate functional synaptic contacts due to the requirement of a proximity below 40 nm which represents the distance of a synaptic cleft.

2.2.6.1 Direct Labeling of Probes to Primary Antibodies

Whenever PLA probes could not be applied due to the species of the primary antibody used (e.g., guinea pig), primary antibodies were directly conjugated to a probe. In this case the DUOLINK® Probemaker kit was used, and the conjugation was performed according to the supplier's instructions (Jarvius et al., 2007; Merck, 2019). To

exchange the buffer of a primary antibody, a spin column was pre-equilibrated with 1x PBS by first spinning the column at 3000 rpm for 1 min. Then, 400 µl 1x PBS were added and spun again for 1 min. This was repeated 4 times. Thereafter, the column was placed in a new microfuge tube. Antibody (12–50 µl) was added to the column and spun again for 2 min at 3000 rpm. The concentration of the collected antibody was verified by optical density (OD). 1 mg/ml should have an OD at 280 nm of 1.4. To determine the concentration, a Pierce BCA protein kit was used. Therefore, a dilution series of BSA was prepared: c = 2 mg/ml, 1 mg/ml, 0.5 mg/ml, 0.25 mg/ml, 0.125 mg/ml, 0.625 mg/ml, 0.3125 mg/ml, PBS. Reagent A was mixed with reagent B at a ratio of 1:50. 9 µl of the dilutions were pipetted in a 96 well-plate in wells 1 A-H. 91 µl of the BCA solution was added. In column B, 3 µl of the sample was pipetted in doublets followed by the addition of 97 µl BCA solution. Plate was covered with foil and incubated at 37 °C and 8 % CO_2 for 30 min. Absorbance assay was performed in the microplate reader PHERAstar and data were analyzed with the MARS software.

2.2.6.2 PLA Protocol on FFPE Tissues

Quantification of synaptic density by PLA on FFPE-processed mouse tissue was primarily done according to the supplier's protocol (Millipore, 2017) with some adjustments as described in the following. All wash buffers should be kept at RT before use. Deparaffinization without a PT module using a solution for dewaxing and simultaneous HIER, was performed by melting off excess paraffin for 30 min at 50 °C in an incubator. Afterwards, slides were immersed in 100 % xylol for 10 min, followed by 100 % xylol, 2x 100 % ethanol, 96 % ethanol, 80 % ethanol, 70 % ethanol solutions and finally in a water bath for 2 min. In the following steps sections were prevented from drying out. All washing steps were performed in a beaker on a rocking shaker. Then, antigen retrieval was done in antigen retrieval buffer (citrate buffer, pH6) for 30 min at 95 ° C. Afterwards, cuvettes with slides were taken out into a beaker filled with tap water and cooled down to RT for 30 min. After antigen retrieval, slides were washed 2x in PBS for 5 min. Then, tissue was circled with a hydrophobic PAPpen followed by the addition of 325 µl Blocking solution (PBS++, 5% DS, 0.1% Tween) per slide and an incubation time of 60 min at RT in a moisture chamber. Thereafter, blocking solution was tapped off and if primary antibodies used on mouse tissues were produced in the same species, a mouse-on-mouse (MoM)-blocking step was added by applying 325 µl MoM-

blocking buffer for 15 min. Then, blocking buffer was tapped off, and the antibody diluent (PBS^{++}, 1 % DS) was prepared. After dilution of primary antibodies in the antibody diluent solution, 325 µl per slide were applied, and incubated overnight at 4 °C in a moisture chamber. Thereafter, slides were washed 2x in Buffer A for 5 min. PLA probes were diluted 1:5 in antibody diluent. Wash buffer was tapped off, and 325 µl diluted PLA probe solution per slide was applied and incubated in a moisture chamber at 37 °C in an oven. Subsequently, slides were washed 2x in Buffer A for 5 min. Meanwhile, ligation mix was prepared (MilliQ water, ligation buffer 1:5, ligase 1:40). Noteworthy, it is of fundamental importance to add the ligase to the mix only before adding it immediately to the sample. Moreover, it had to be ensured that the ligation buffer was fully thawed and properly vortexed before use. Then, 325 µl were added per slide and incubated for 30 min at 37 °C in a moisture chamber in an oven. This was followed by 2 washing steps in Buffer A for 5 min. While washing amplification mix (MilliQ water, amplification buffer 1:5, polymerase 1:80) was prepared and polymerase was added shortly before applying it on the sample. It had to be considered that the amplification buffer contains fluorophores and is therefore light-sensitive. Wash buffer was removed and 325 µl amplification mix was added to the slides for an incubation time of 100 min at 37 °C in a moisture chamber in an oven. Afterwards, the mix was washed off 2x in Buffer B for 10 min followed by a washing step in 0.01x Buffer B for 1 min. If a counterstain was performed, tissue was again treated with blocking solution, and incubated for 60 min at RT. Incubation steps of primary and secondary antibodies were performed according to the IF protocol described in 2.2.4.6. Slides were protected from light to preserve the PLA signal. Again, wash buffer was removed, and slides were allowed to dry completely in the dark at RT for 20 min. Slides were mounted by adding 75 µl mounting medium per slide and by putting a cover glass on top. After 15 min at RT in the dark coverslips were circled with clear nail polish and kept in the dark for further hardening. After imaging, slides were stored in the dark at 4 °C for up to 4 days or at -20 °C for up to 6 months.

2.2.6.3 Improved PLA Protocols on Tissues

Based on the original protocol and the adjusted protocol in 2.2.6.2, further improvements and changes have been applied to the protocol:

(A) Optimized PLA on FFPE Tissues

For FFPE tissue, deparaffinization and antigen retrieval steps were merged with the help of the PT Module as described in 2.2.2. Washing steps, either with PBS, Buffer A or B, were performed in a beaker to ensure that all excessive compounds were washed away. Additionally, PBS without calcium and magnesium was used to further reduce background (Burgey, 2019). Antibody Dilution Stock Buffer was prepared as described in 2.1.8 to prepare the Blocking buffer (2.1.9) and the antibody dilution buffer (2.1.10). Addition of BSA to the antibody dilution stock buffer was introduced to further reduce background. A volume of 325 µl was applied to the slides into the liquid barrier around the tissue to prevent a drying out of the tissue. A volume of 70 µl Duolink® PLA Mounting Medium with DAPI was applied as a minimum volume.

(B) PLA on FFPE Tissues with Covertiles

An improvement to version A was done by using BOND Covertiles (see 2.2.4.7) which replaced PAPpens. Specific advantages were i) no need to work under a fume hood because of the toxicity of the pen, ii) an equal liquid distribution over the tissue and iii) a reduction of the volume used from about 325 µl to only 200 µl per slide.

(C) PLA on FFPE Tissues with Covertiles and Hybridization Oven

Further optimization steps were introduced to achieve a more homogeneous signal distribution by using metal boxes for a better heat distribution during the incubation steps requiring an increased temperature. Moreover, a hybridization oven (BOEKEL) was used where the slides, covered with Covertiles, were directly put on the aluminum plate of the oven. For these implementation experiments, a moisture chamber needed to be prepared to compare a PLA signal with PAPpen or Covertiles (Figure 13).

Figure 13: Slides with Covertiles (top) or a moisture chamber in an aluminum tray of the hybridization oven with PAPpen as liquid barrier (bottom).

2.2.7 Analysis of IF and PLA Stainings

2.2.7.1 Image Acquisition

Image acquisition was done on different microscope platforms as described in the following.

Image acquisition with a confocal microscope was conducted with a Zeiss LSM 700. For a 63x magnification a Plan-Apochromat 63x/1.40 Oil DIC M27 objective was used. Images were acquired as single planes.

For fluorescent whole slide images, two different systems were used: First, we used the 3DHISTECH Pannoramic MIDI II with a PLAN Apochromat 40x/1.60 objective was used. For a whole slide scan, the scanning areas were manually defined. Fluorescence parameters, as extended focus was set to maximum, exposure time for the DAPI channel was set to 400 ms, for the fluorescein isothiocyanate (FITC) channel to 200 ms, and for the Cy5 channel to 500 ms.

The second fluorescent whole slide scanner used, was the Zeiss Axio Scan.Z1 system with a Plan-Apochromat 40x/0.95 Korr M27 objective. For the DAPI channel, a LED-module 385 nm was used as light source at 50 % intensity and 10 ms exposure time. For the Alexa Fluor 647 channel, a 630 nm LED-module was used as light source at 100 % intensity and an exposure time of 420 ms. For the AF488 channel, the 475 nm

LED-module was used at an intensity of 50 % and an exposure time of 100 ms. The image area was defined manually.

For light microscopy and whole slide imaging, the 3D Histech P1000 was used. A Plan-Apochromat 20x/1.6 objective was applied, and the scan area was defined manually.

2.2.7.2 Line Profile Analysis

The data analysis for IF double stainings and PLA puncta was performed with the Zeiss ZEN 2.3 lite software to quantify the signal to background ratio (S/B). In the "Profile"-application a line was drawn in ROI, preferably through the cortex and the corpus callosum. The software then delivers the signal intensity data along the drawn line for all imaged channels. Intensity data of the imaged fluorophores and respective antibodies were then transferred into an excel sheet. Here, the intensity values were sorted in increasing and decreasing orders. Then the highest and lowest 10 % of each channel were calculated and a S/B ratio determined:

$$\frac{S}{B} = \frac{mean\ 10\ \%\ highest\ values\ on\ line\ profile}{mean\ 10\ \%\ lowest\ values\ on\ line\ profile}$$

2.2.7.3 HALO Data Analysis

The Indica Labs HALO software was used to quantify PLA puncta. With the annotation tool and by the help of a Wacom tablet and pen or an iPad and pencil, ROIs were drawn in specific brain areas. For analysis, the Indica Labs – FISH v2.1.10 algorithm was used and modified for the PLA puncta analysis. Analysis magnification was set to 1, and the settings were adjusted for the Alexa Fluor 647 channel (PLA puncta) and applied on every image. Obtained results were exported into an Excel sheet. For the quantification of the PLA puncta in a specific ROI, Copies/µm² x100 were analyzed.

2.2.7.4 Data Analysis of PLA Results

To evaluate the PLA data[1], a quality control and an experimental unit consideration of the data by comparing the means and medians was performed of every single group and ROI. Further, a quality check of each group and ROI was applied by comparing the PLA data (median Copies/µm²x100) to the technical control (vGLUT1-only CTRL). Per strain and age group, data was assessed regarding an age-dependent synaptic loss using an ANOVA effect test in the different ROIs.

For future studies, a power analysis was performed. For a hypothetical treated group of TG4510, scenarios of mean levels of synaptic density measured with PLA were assumed to increase 20 %, 40 %, and 60 % compared to tA mice group.

2.2.8 Trimethyltin-Induced Neurotoxicity

To quantify synaptic density after a neurotoxic insult by exposure to trimethyltin (TMT), the following study was designed: Trimethyltin (TMT, CAS number: 1066-45-1, Pub-Chem Substance ID: 24848783, M=199,27 g/mol) was diluted in a 0.9 % saline stock solution at a concentration of 0.01 M. Identification of the mice was done by a tail mark. Detailed observations of the physical condition and behavior was recorded daily approximately 1 to 2 hours after dosing from the day of administration until day 10.

*Table 2-9: **TMT study design** (a. Trimethyltin chloride formulated as solution in vehicle (0.9 % saline). Control animals received the vehicle only. B. C57BL6/J)*

Test group	Test item [a]	Dosage (mg/kg/day)	Concentration (mg/mL)	Dose volume (mL/kg)	Number of males [b]
1-3	Control	0	0	5	9
4-6	TMT	1.2	0.24	5	9
7-9	TMT	2	0.4	5	9

Table 2-9 summarizes the study design with 9 different groups with 3 male animals per group. Three different dosages were administered (control, 1.2 mg/kg and 2 mg/kg). Mice were sacrificed at three different time points (24 h, 72 h and 10 days after TMT application).

The administration of the compound TMT occurred once and was administered intra-peritoneally. Clinical observations were taken 3 and 6 h post-dosing and before each necropsy. Figure 14 illustrates the workflow of the study: Blood samples for biomarker

---

[1] Statistics performed by Yulia Mordashova, Senior Research Statistician, RDCD-Pharma Development, AbbVie Deutschland GmbH & Co. KG

analysis were taken one week before dosing (Baseline), 1 h after dosing (t_{max}), and before the necropsy of the three different necropsy timepoints.
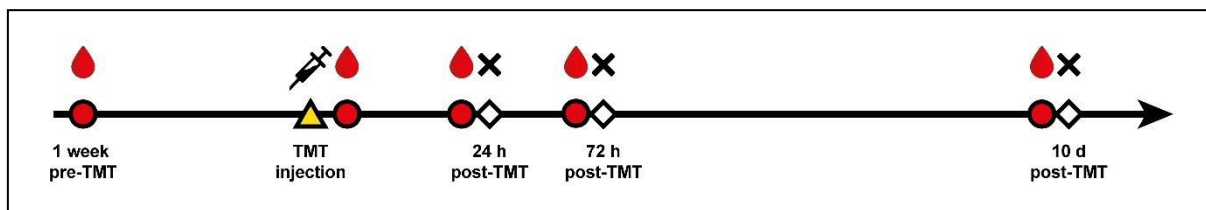

*Figure 14: **TMT model workflow.** 1 week before administration of TMT the first blood sampling was done from the vena saphena (Baseline). After intraperitoneal administration (i.p.) of the compound the next blood sample (t_{max}) was taken. 24 h after TMT injection, blood was collected before the first necropsy of groups 1, 4 and 7 took place. The next blood sampling was done 72 h after administration and the necropsy of groups 2, 5 and 8. The last blood sample was taken 10 days after administration. The last necropsy of groups 3, 6 and 9 also occurred 10 days post TMT injection. (●blood sampling; ▲TMT administration; ◇ necropsy).*

2.2.8.1 PLA to Measure Synaptic Density after Neurotoxic Events

Necropsy was conducted 24 hours post dose (groups 1, 4, 7), 72 hours post dose (groups 2, 5, 8) and 10 days post dose (groups 3, 6, 9). Mice received 0.1 mg/kg buprenorphine subcutaneous (s.c.) 30 min prior induction of inhalant anesthesia with sevoflurane and perfusion (2.2.1). Brain and sciatic nerve samples were collected in 4 % PFA and incubated for 1 h at 4 °C. The rest of the mouse body was preserved in 10 % formalin. Samples were prepared and processed as described earlier in 2.2.4.1. Then, HE-staining (Table 2-7) was performed for slide selection of the brain samples and for the morphological assessment of the sciatic nerves. Finally, quantification of synaptic density was assessed by the PLA (2.2.6.3 C).

2.2.8.2 Neurofilament-Light (NF-L) Chain Assay

In AD, NF-L is elevated and correlates with cognitive decline and brain degeneration (Molinuevo et al., 2018). With the application of the neurotoxic compound TMT in C57BL6J mice, apart from quantifying the synaptic density in the brain, the blood biomarker NF-L was measured after TMT injection in plasma samples. Therefore, whole blood samples (60 µl) were collected from the vena saphena in tubes containing EDTA (1.) one week before dosing (baseline), (2.) 1h after dosing (t_{max}), (3.) 24 h after dosing and before necropsy of groups 1, 4 and 7, (4.) 72 h after dosing of groups 2, 5 and 8, and (5.) 10 days after dosing of groups 3, 6 and 9 (Figure 14). The blood samples were centrifuged for 15 min at 1000 rpm (112 rcf) within 30 min of collection. Plasma aliquots of at least 25 µl were prepared, put immediately on dry ice, and were then transferred to a -80 °C freezer. Mouse plasma samples were then analyzed with the help of a fully

automated ELISA (ELLA, Protein Simple). ELLA machine was started, and the calibration cartridge was run. Afterwards, the plasma samples were vortexed and centrifuged at 13'000 rcf before dilution (1:5) in SD13 sample diluent. 50 µl of a sample was pipetted into a 72-well ELLA cartridge, and 1 ml wash buffer was added in all buffer slots [2].

2.2.8.3 Statistical Analysis of TMT Study

HALO annotations were drawn with the help of the Allen Brain Atlas in areas of the hippocampus (Allen Institute for Brain Science (2011) Allen Mouse Brain Atlas, Mouse, P56, Coronal. Available from mouse.brain-map.org. Allen Brain Institute (2022)). Sub-regions were drawn in the Ammon's horn (CA) subregions CA1, CA2, CA3 and gyrus dentatus (GD). Sub-subregions were drawn in the stratum oriens (so), pyramidal layer (sp), stratum radiatum (sr) and stratum lacunosum-moleculare (slm) of the CA-regions. Sub-subregions in the gyrus dentatus were drawn in the molecular layer (mo), granule cell layer (sg) and polymorph layer (po). PLA puncta quantification was performed with HALO, statistical analysis of PLA data of TMT study was performed with JMP software (version 14.1.0)[3]. Data were analyzed in log scale using 2-way ANOVA with interaction: Group and treatment timepoint and their interaction followed by post-hoc Dunnett's test comparing control to both dose groups for each timepoint.

For a power analysis, the following assumptions were made for a sample size calculation required for future studies: Calculations were based on the data available of PLA quantification in HC and diverse subregions. Effect sizes were based on observed differences between control and 2mg/kg treatment group in all regions. No covariates (sex, body weight etc.) were included. The variability of the groups was assumed similar to the ones observed during the pilot study, the Power was fixed at 80%, and alpha was 5%. Sample sizes will be presented assuming the effect size to be detected as the equivalent of the differences between control and 2 mg/kg treatment group (100% effect size), using 2-sided, two-group Satterthwaite t-test. Noteworthy, the Variability in control and treated group might be different comparing to assumed variability, no adjustments were made for multiple comparison and for possible further covariates (sex, bodyweight, etc.).

---

[2] ELISA measurement was performed by Sabine Weiss, Scientist, RDDI-Discovery Research, AbbVie Deutschland GmbH & Co. KG.
[3] Statistics performed by Yulia Mordashova, Senior Research Statistician, RDCD-Pharma Development, AbbVie Deutschland GmbH & Co. KG

3   RESULTS

3.1   Staining of Different Pre- and Post-Synaptic Markers

The analysis of synaptic contacts on rodent brain slices is challenging. The quantification of synaptic contacts with current methods like classic immunohistochemistry or electron microscopy can be highly subjective, lack sensitivity and thus are difficult to interpret (M.-K. Chen et al., 2018; McLeod et al., 2017a; Scheff et al., 2006). For a better understanding of synaptic loss in AD mouse models, we sought to establish a proximity ligation assay-based system to quantify functional synapses by assessing pre- and post-synaptic markers in close vicinity.

Therefore, different antibodies targeting pre- and post-synaptic markers were tested on free-floating tissue, cryosections, FFPE slides, as well as PFA-fixed and cleared slices.

3.1.1   IF for Synaptic Markers on Free-Floating Tissue Sections

Immunohistochemistry for the visualization of protein localization cannot only be applied on tissue sections adhered to glass slides, but also on free-floating tissue sections. A major advantage is that thicker tissue slices can provide more three-dimensional information. Additionally, a better antibody penetration can be achieved from all sides of a tissue slice as they are surrounded by the antibody solution (Potts, Coppotelli, & Ross, 2020). Furthermore, since no fixation was used, no antigen retrieval is needed.

To analyze glutamatergic synapses, 40 µm thick tissue slices of wt C57BL6/J (n = 3) mice were used. Species of the primary and secondary antibodies were chosen according to the availability of commercial PLA kits. As technical control, no primary antibody was applied. IF stainings for anti-vGLUT1 (AB5905) coupled to a goat anti-guinea pig secondary antibody labeled with Alexa Fluor 488 (A-11073) and anti-PSD95 (ab18258) linked to goat anti-rabbit secondary antibody labeled with Alexa Fluor 647 (A32733) were performed. IF imaging (Zeiss LSM700) was done under identical conditions with constant exposure and color map in areas of the HC and gyrus dentatus (Figure 15).
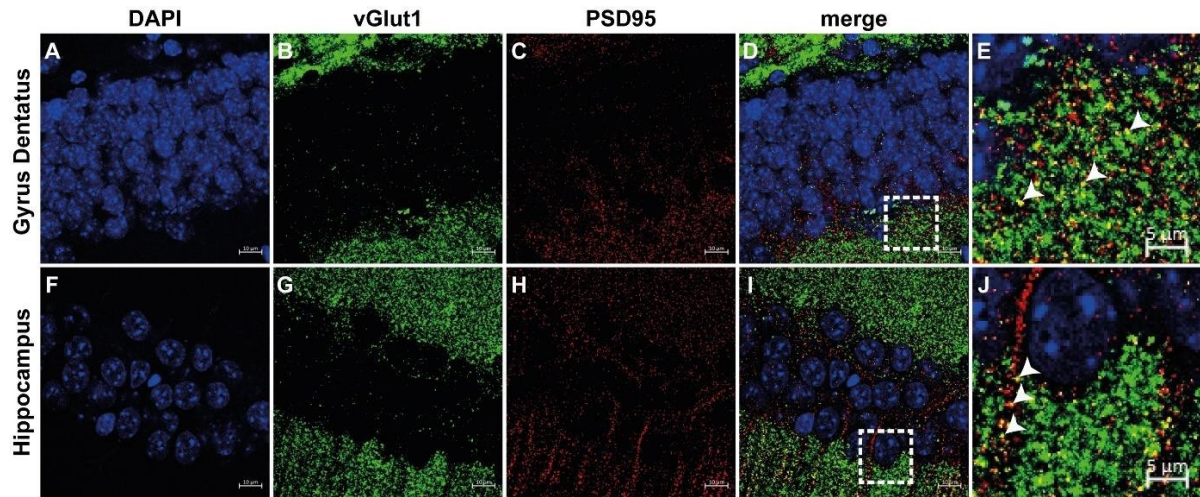
Figure 15: **Staining on free-floating tissue slices resulted in a very good immunoreactivity for vGLUT1 and PSD95.** Gyrus dentatus (GD): **(A)** DAPI, **(B)** vGLUT1 **(C)** PSD95 and **(D)** merge. **(E)** Zoom into dotted square of (E): Arrows indicate overlay of pre- and post-synaptic signals. Hippocampus (HC): **(F)** DAPI **(G)** vGLUT1 **(H)** PSD95 staining, and **(I)** merge. **(J)** zoom into rectangle in (I). Arrows indicate signals of synaptic contact. Scale bars 10 µm (A-D, F-I) and 5 µm (E, J)

Immunoreactivity on the free-floating slices for vGLUT1 and PSD95 revealed a highly specific co-localized punctate-like staining for both antibodies with low background reactions. However, for most slices it was impossible to mount them on microscope slides. Furthermore, mounting of the slices could also lead to folds and wrinkles of the tissue which may result in a loss of information when crucial ROIs are affected. Finally, it could not be excluded that an overlap in the 2D image was false positive due to an optical overlap but not a real close proximity of two signals. Due to these technical challenges and limitations, the free-floating method was not further pursued for the implementation of PLA stainings.

3.1.2   IF for Synaptic Markers on Cryosections

Next, we tested the suitability of IF stainings on cryosections to visualize synaptic density. Therefore, wt (C57Bl6, n = 3) mice were perfused with a PFA solution as described before (2.2.1). IF stainings were performed on 10 µm cryosections for various pre- and post-synaptic, neuronal (NeuN) and microglial (IBA1) markers as described in 2.2.3. IF imaging (3D HISTECH MIDI2) was performed under identical conditions with constant exposure and color map.

The IF signal on cryosections was sparse, weak, and inconsistent for most IF stainings. For example, when staining NeuN, a high background and low immunoreactivity was observed. In higher magnifications, the cryosections appeared to be damaged which might have contributed to the low signal quality (Figure 16 D). Additionally, control stainings (no primary antibody used) resulted in a marked background and unspecific

puncta staining (Figure 16 E). Therefore, application of cryosections to assess synaptic density was not further pursued.
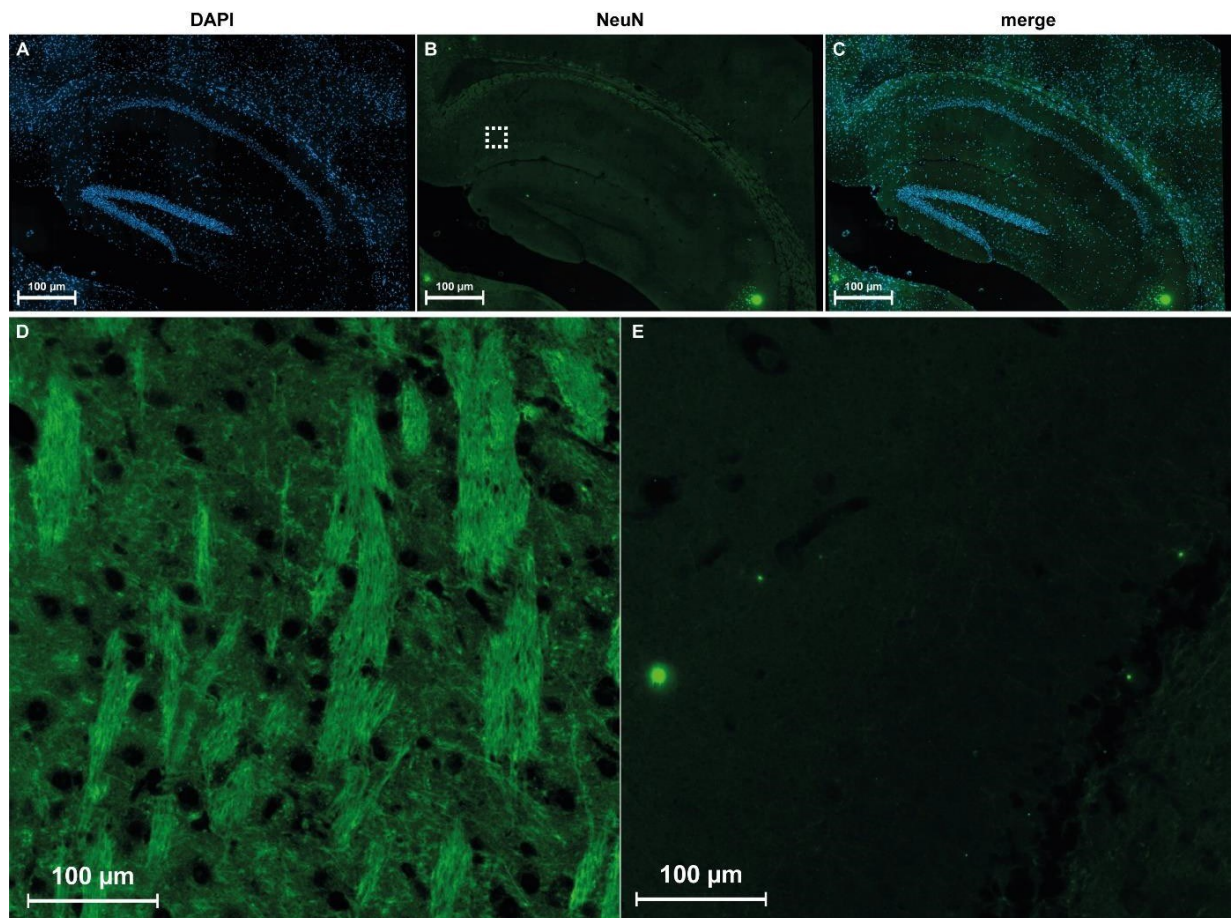

*Figure 16: **IF staining on cryosections. (A)** DAPI, **(B)** NeuN and **(C)** merge. **(D)** Higher magnification of dotted square in (B) and **(E)** higher magnification of control staining without primary antibody.*

3.1.3 IF for Synaptic Markers on FFPE Slides

Next, we tested the applicability of FFPE tissue slides to visualize pre- and post-synaptic structures. For FFPE tissues, a heat-induced antigen retrieval (HIER) was performed to allow antibodies to access their target. Therefore, buffers differing in their pH were tested and a simultaneous dewaxing in the PT-module to find the best pre-treatment for pre- and post-synaptic antibodies was performed.

First, an anti-vGLUT1 antibody (AB5905) was used for IF stainings on FFPE tissue of wt C57BL6/J (n = 3, 3 slides per animal, processing according to Table 2-6 B), coupled to a goat anti-guinea pig secondary antibody linked to Alexa Fluor 488 (A-11073). For AB5905 a HIER treatment in the presence of buffers with either pH 8 or 9 and without any other pre-treatment was tested. This was followed by IF imaging (Zeiss LSM700) under identical conditions with constant exposure and color map. A Line Profile

analysis for the vGLUT1 channel (green fluorescence) resulted in higher maximum intensity values (MIV) for pH 9 compared to pH8 (10 MIV vs. 2 MIV, Figure 17).
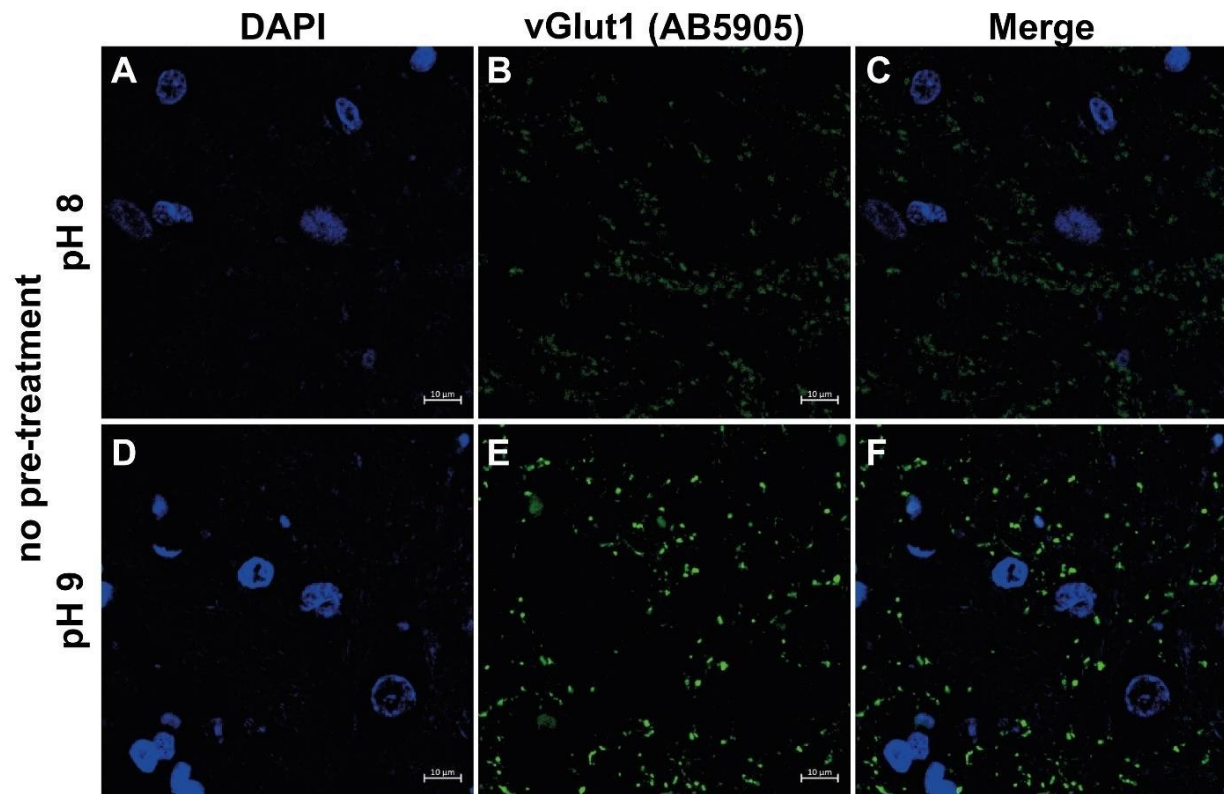

*Figure 17: **Comparison between different PT-module buffers for heat-induced antigen retrieval with simultaneous dewaxing.** Two buffers differing in their pH were compared for vGLUT1 (AB5905) IF staining. Images from layer V of mouse somatosensory cortex were acquired with Zeiss LSM700. **(A)** DAPI and **(B)** vGlut IF after pH 8-adjusted HIER **(C)** merge. **(D)** DAPI **(E)** and vGLUT1 IF after pH 9 HIER **(F)** merge. pH 9 HIER resulted in higher intensity values than pH 8. Scale bars 10 µm.*

For PSD95 (3450S), a HIER with a buffer at pH 9 was recommended and therefore not tested for any additional pre-treatments (Ageta-Ishihara et al., 2015; Danielson et al., 2021).

Next, Proteinase K was used as an additional pre-treatment to unmask antigens on FFPE tissue and thereby to enhance the staining intensity of the antibodies. A HIER pre-treatment in the presence of a buffer adjusted to pH 8 followed by a Proteinase K pre-treatment before incubation with an anti-vGLUT1 antibody (AB5905) had a MIV of 127 as compared to a buffer adjusted to pH 9 at 86 MIV. However, this was mainly due to a high background signal for pH 8. Although for pH 9 the background signal was low, a dot-like signal was not achieved which would have allowed a proper quantification (Figure 18 A-F).
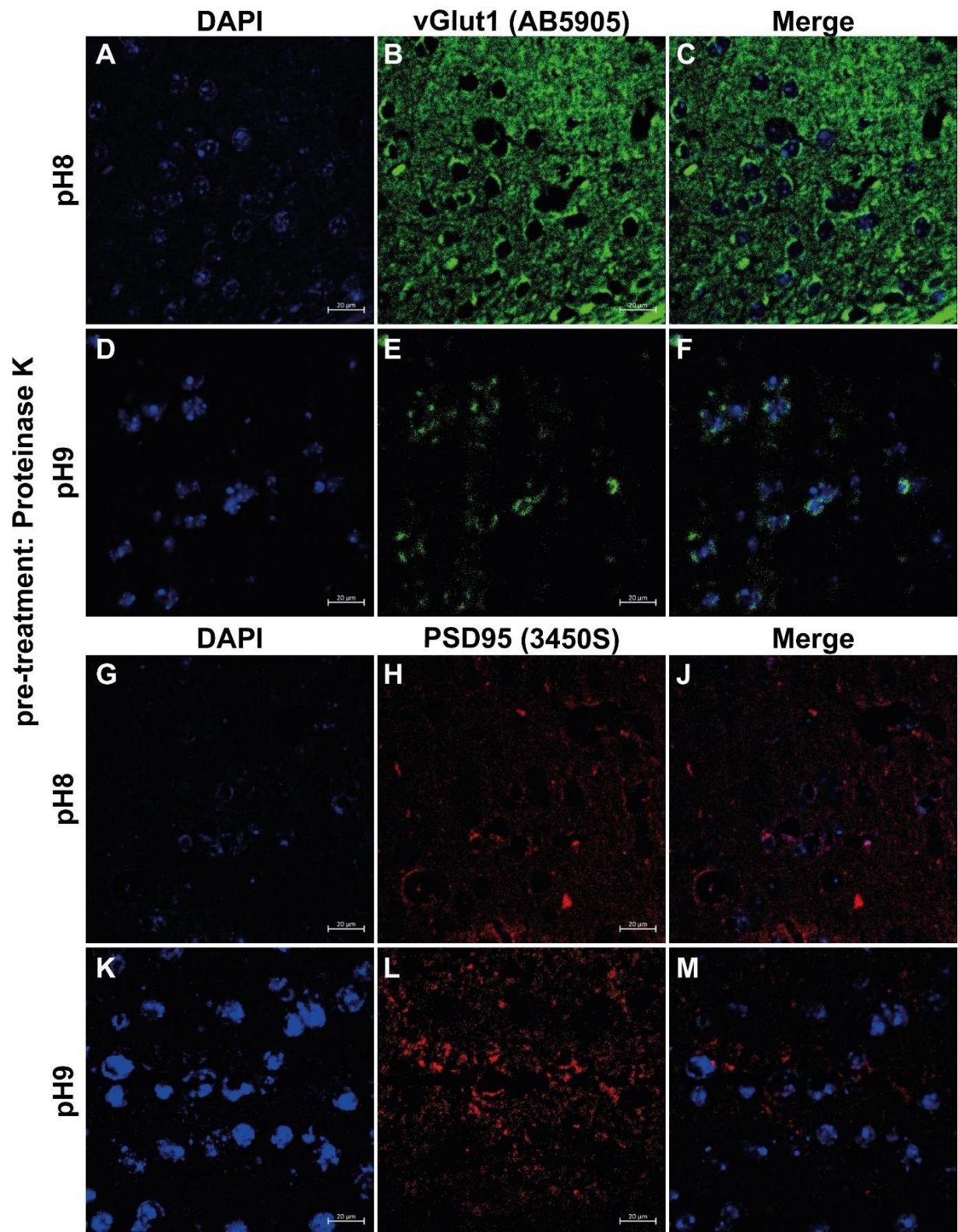
Figure 18: **Comparison of a combination of HIER and Proteinase K pre-treatment for IF of anti-vGLUT1 and anti-PSD95 antibodies in the presence of buffers adjusted for either pH 8 or pH 9.** *Two different PT-module buffers at pH 8 and pH 9 were used. (A) DAPI and (B) vGLUT1 IF resulting in a high background after additional with Proteinase K and HIER pre-treatment in the presence of a pH 8 adjusted buffer, (C) merge. (D) DAPI and (E) vGLUT1 IF with low signal intensity and immunoreactivity after additional Proteinase K and HIER pre-treatment in the presence of a pH 9 adjusted buffer, (F) merge. (G) DAPI and (H) PSD95 IF with low signal intensity and immu-noreactivity after additional Proteinase K and HIER pre-treatment in the presence of a pH 8 adjusted buffer, (J) merge. (K) DAPI and (L) PSD95 IF resulting in a high background after additional Proteinase K and HIER pre-treatment in the presence of a pH 9 adjusted buffer, (M) merge. Scale bars 10 µm.*

For anti-PSD95 (3450S) antibody staining, HIER pre-treatment followed by a Proteinase K treatment led to similar MIV for pH 8 and 9 (51 MIV vs. 55 MIV) (Figure 18 G-M).

According to Erben et al., a combination of HIER and Sudan Black (SB) was tested for anti-vGLUT1 and PSD95 IF stainings to reduce the background signal (Erben, Ossig, Naim, & Schnekenburger, 2016). The line profile analysis in layer V of the somatosensory cortex for anti-PSD95 IF after SB treatment revealed a higher MIV for pH 8 than for pH 9 (178 MIV vs. 79 MIV). For anti-vGLUT1 IF, MIV was higher at pH 9 than pH 8 after SB treatment (64 MIV vs. 111 MIV). The implementation of the anti-vGLUT1 and anti-PSD95 antibodies resulted in unspecific immunoreactivity for both antibodies.

Moreover, further antibodies were tested for synaptic targets to have a variety of different pre- and post-synaptic markers (Table 3-1). All antibodies were tested comparing their performance after HIER treatment in the presence of buffers adjusted to pH 8 or pH 9, as well as additional Proteinase K or SB treatment. In general, antibodies performed better with HIER treatment with buffers adjusted to pH 9 and without any other additional pre-treatment. Detailed information on antibodies tested and pre-treatment conditions is given in Table 3-1. Additionally, pre- and postsynaptic antibodies were tested together as marker pairs as summarized in Table 3-2.

RESULTS

Table 3-1: Antibody dilutions and tested pre-treatments for IF stainings on FFPE tissue. X = not recommended; [K] = in combination with Proteinase K; [SB] = in combination with Sudan Black

ANTIBODY TARGET	CATALOG NUMBER	DILUTION USED FOR IF ON FFPE TIS-SUE	HIER BUFFER pH 8	HIER BUFFER pH 9	PROTEINASE K	SB
Acetylcholinesterase	ab183591	1:1000	X	pH 9	X	X
Bassoon	141 118	1:1000	X	pH 9	X	X
DAT	284003	1:500	X	pH 9	X	X
HOMER1	CABT-BL4859	1:1000	X	pH 9	X	X
HOMER1a	160 003	1:500	pH 8 [K]	pH 9	X	X
IBA1	019-19741	1:1000	X	pH 9	X	X
MAP2	AB15452	1:2000	X	pH 9	X	X
NeuN	abab134014	1:2000	X	pH 9	X	X
PSD95	3450S	1:200	pH 8 [K, SB]	pH 9	X	X
PSD95	ab12093	1:300	X	pH 9	X	X
PSD95	ab18258	1:1000	X	pH 9	X	X
PSD95	MAB1596	1:1000	X	pH 9	X	X
PSD95	3409S	1:200	X	pH 9	X	X
SYP	ab14692	1:1000	X	pH 9	X	X
SYT	105103	1:500	X	pH 9	X	X
VAMP2	ab215721	1:2000	X	pH 9	X	X
vGLUT1	135 307	1:300	X	pH 9	X	X
vGLUT1	AB5905	1:1000	pH 8 [K]	pH 9	X	X
vGLUT1	ABN1647	1:1000	X	pH 9	X	X
VMAT2	ab280364	1:1000	X	pH 9	X	X

Table 3-2: Established synaptic marker pairs

PRE-SYNAPTIC MARKERS			POST-SYNAPTIC MARKERS			
ANTIBODY	VENDOR, CATALOG NUMBER	DILUTION FFPE	ANTIBODY	CATALOG NUMBER	DILUTION FFPE	SYNAPSE TYPE
Synaptophysin	Abcam ab14692	1-1000	PSD95	Merck MAB1596	1-1000	general
Synaptotagmin	SySy 105 103	1-500	PSD95	Merck MAB1596	1-1000	general
VAMP2	Abcam ab215721	1-2000	PSD95	Merck MAB1596	1-1000	general
vGLUT1	Merck ABN1647	1-1000	PSD95	Merck MAB1596	1-1000	glutamatergic
vGLUT1	Merck AB5905	1-1000	HOMER1	SySy 160 003	1-500	glutamatergic
Synaptophysin	Abcam ab14692	1-1000	PSD95	Merck MAB1596	1-1000	general
Synaptotagmin	SySy 105 103	1-500	PSD95	Merck MAB1596	1-1000	general
VAMP2	Abcam ab215721	1-2000	PSD95	Merck MAB1596	1-1000	general
VAMP2	Abcam ab215721	1-2000	PSD95	Abcam ab12093	1-300	general
vGLUT1	Merck ABN1647	1-1000	PSD95	Merck MAB1596	1-1000	glutamatergic
vGLUT1	Merck AB5905	1-1000	HOMER1	SySy 160 003	1-500	glutamatergic
vGLUT1	Merck ABN1647	1-1000	PSD95	Abcam ab12093	1-300	glutamatergic
vGLUT1	SySy 135 307	1-200	PSD95	Abcam ab18258	1-1000	glutamatergic
vGLUT1	SySy 135 307	1-200	HOMER1	SySy 160 003	1-500	glutamatergic
vGLUT1	SySy 135 307	1-300	PSD95	Cell Signal 3409S	1:200	glutamatergic
Bassoon	SySy 141 118	1-1000	HOMER1	Creative Diagnostics CABT-BL4859	1-1000	general
VAMP2	Abcam ab215721	1-2000	HOMER1	Creative Diagnostics CABT-BL4859	1-1000	general

3.1.4 Tissue-Clearing and 3D Imaging to Quantify Synaptic Density

For the 3D quantification of synaptic density, recently established clearing techniques (Alexander, 2018) were used in combination with lightsheet microscopy. Therefore, different primary and secondary antibodies were tested for their applicability in the solvent-based ethyl cinnamate (Klingberg et al., 2017) and the water-based X-CLARITY clearing protocol (Simon-Chica et al., 2022). For solvent tissue clearing, antibodies were tested additionally on their applicability with methanol solutions as described in 2.2.5.1 and applied as stated in 2.1.1.

Antibody stainings for synaptic contacts were performed with VAMP2 and PSD95 (MAB1596) on 2 mm thick brain slices. Comparing the X-CLARITY and the ECi clearing protocols, a puncta-like signal was achieved by ECi clearing but not with X-CLARITY. Additionally, immunoreactivity varied for these antibodies especially in the area of the gyrus dentatus (Figure 19). Immunoreactivity in X-CLARITY-cleared samples was comparable to IF stainings on FFPE tissue.

Quantification of a colocalization of pre- and post-synaptic markers was performed with arivis software for general synaptic marker pairs VAMP2 (AF5136) and HOMER1 of ECi-cleared tissue samples (n = 6 C57Bl6/J, Figure 19 G). For X-CLARITY-cleared tissues a high background was observed on stainings with both antibodies and for the respective controls (no primary antibodies, data not shown, Figure 19).

Staining of ECi-cleared tissues appeared to be more specific. For instance, a puncta-like signal was observed in the CA1 region of the HC. However, the strong background in the gyrus dentatus did not disappear (Figure 19 A-C). Quantification of colocalized 25fluorescent signals did not show a significant difference between IF stainings for VAMP2 and HOMER1 or vGLUT1 and HOMER1 vs controls, respectively. A higher dot count was observed for the synaptic marker pair VAMP2-HOMER1 as compared to the vGLUT1-HOMER1 glutamatergic synaptic marker pair (Figure 19 H+I).

Altogether, when comparing IF staining quality on free-floating sections, cryosections, FFPE slides, and PFA-fixed and cleared slices for pre- and post-synaptic markers, stainings on free-floating sections and FFPE slides were superior to the other methods in terms of signal to background ratio, immunoreactivity, and a precise punctate-like staining. However, since for stainings on free-floating sections a high default rate was observed and since the method was technically challenging and laborious, we continued with the use of FFPE slides for the implementation of the PLA protocol.
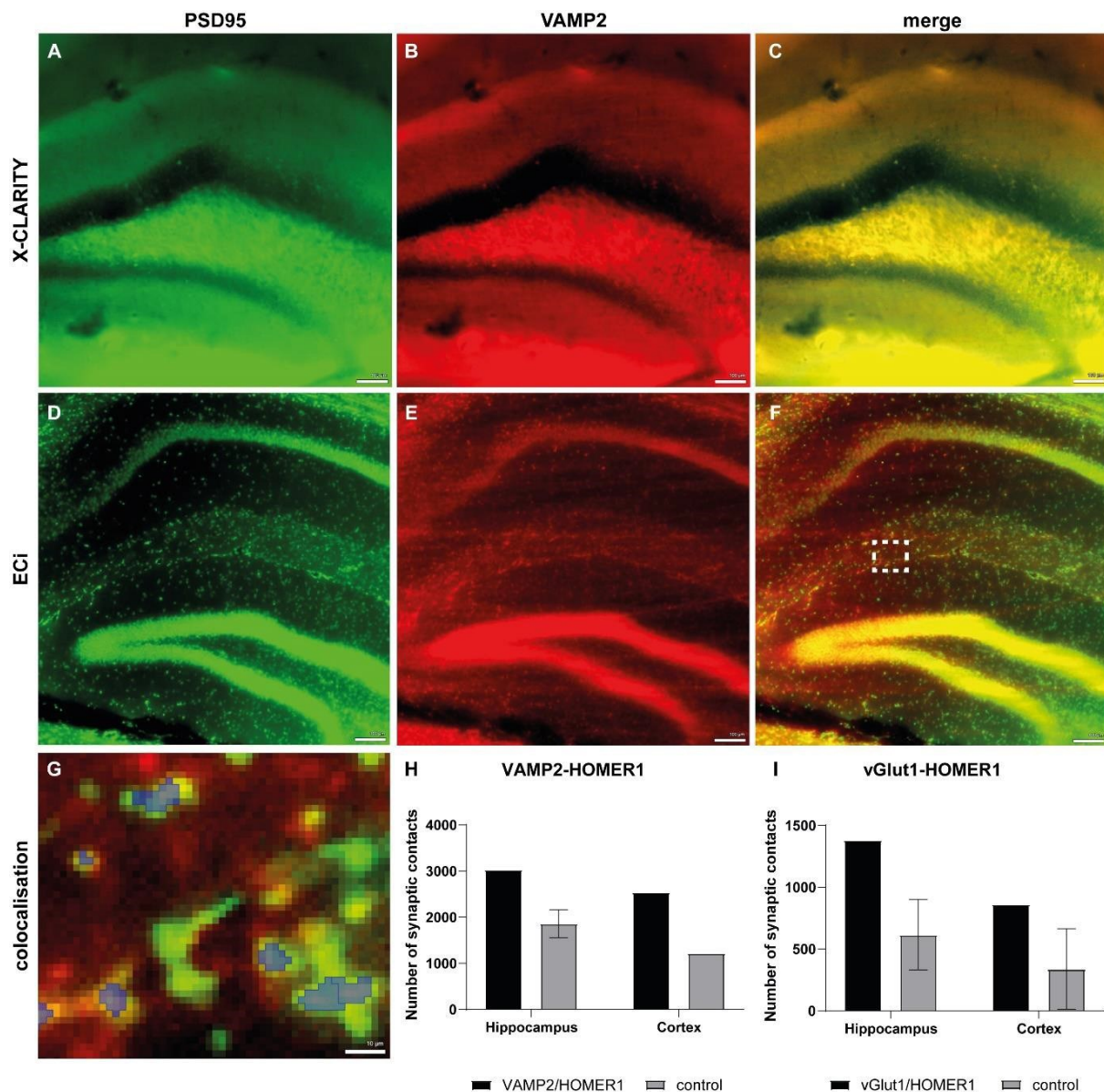
*Figure 19: **IF staining of synaptic contacts in cleared tissue samples.** Representative images of single planes of cleared wt mouse brain tissue samples stained with anti-VAMP2 **(B, E, red)** and anti-PSD95 **(A, D, green)** antibodies applied with X-CLARITY **(A-C)** and ECi **(D-F)** clearing techniques. Analysis of colocalized signals (blue) of synaptic contacts in ECi-cleared tissue (higher magnification of dotted box in (F)) in the hippocampus was performed **(G)**. Quantification of a synaptic marker pair with VAMP2 as pre-synaptic marker and HOMER1 as post-synaptic marker **(H)** and quantification of glutamatergic synaptic contacts with vGLUT1 and HOMER1 **(I)** of ECi-cleared wt brain samples. Scale bars 100 µm **(A-F)** and 10 µm **(G)**. Data represent means with SD.*

3.2 Establishment of PLA protocol

3.2.1 Implementation and Optimization of Commercial PLA Protocols

Implementation of the PLA protocol to quantify synaptic density was based on previous results on the staining quality of antibodies recognizing different pre- and post-synaptic markers (see 3.1). Therefore, FFPE-processed tissue slides were used to apply and

optimize the PLA workflow regarding buffers used, application methods for different solutions, controls, image analysis, and mounting.

3.2.1.1 Application of PLA on FFPE Tissue with Different Pre- and Postsynaptic Markers

In a first attempt to visualize synaptic contacts with PLA, stainings were performed on FFPE tissue of CD1 wt mouse brains (n = 4, male, 1 section per animal). The tissue was FFPE processed according to the protocol described in 2.2.6.2. Anti-SYP (ab14692), anti-SYT (105103) and anti-VAMP2 (ab215721) antibodies were used as general pre-synaptic markers, while anti-vGLUT1 (AB5905, coupled directly to PLUS-probe) served as glutamatergic pre-synaptic marker. Regarding the post-synaptic site, anti-PSD95 (MAB1596) and anti-HOMER1 (160 003) antibodies were used. In general, PLUS (+) -probes were coupled to the pre-synaptic antibodies, whereas MI-NUS (-) -probes were coupled to post-synaptic antibodies. As negative controls no primary antibodies were applied (data not shown). IF imaging (Zeiss LSM700) was performed under identical conditions with constant exposure and color map in the area of the gyrus dentatus (granule cell layer, Figure 20). The pre-synaptic marker SYP in combination with the post-synaptic marker PSD95 (SYP(+)PSD95(-)) resulted in a clear puncta signal in the area of the granular cell layer of the gyrus dentatus. For SYT(+)PSD95(-) (Figure 20 D-E), also a clear PLA puncta signal was achieved, but there was an unexpected immunoreactivity in the nuclei of GD cells. PLA stainings of VAMP2(+)PSD95(-) (Figure 20 G-I) resulted in a high puncta density in the gyrus dentatus. In contrast, a less dense puncta-like staining was observed in GD cells for glutamatergic markers vGLUT1 and HOMER1 (Figure 20 J-L).
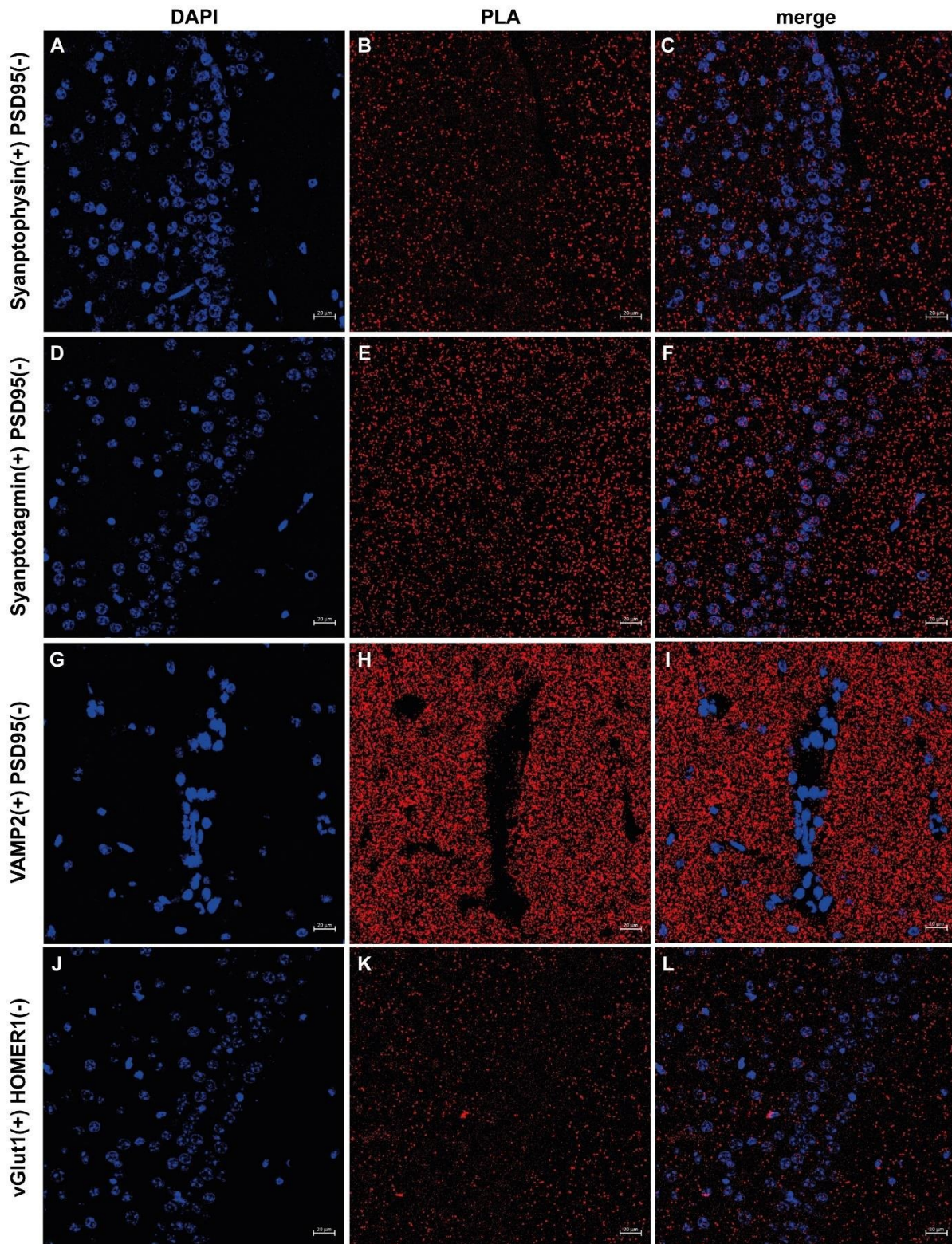
Figure 20: **PLA of different synaptic targets leads to a clear puncta signal of synaptic contacts. (A)** *DAPI channel of pre-synaptic marker synaptophysin (SYP) and PSD95,* **(B)** *PLA of SYP(+) and PSD95(-) staining, and* **(C)** *merge of SYP(+)PSD95(-) with DAPI staining show clear puncta-like signal around the granular cell layer of the gyrus dentatus.* **(D)** *DAPI channel of synaptotagmin (SYT) and PSD95 staining,* **(E)** *PLA of SYT(+) and PSD95(-) shows clear puncta signal of synaptic contacts, and* **(F)** *merged channels of DAPI and PLA of SYT-PSD95.* **(G)** *DAPI channel of VAMP2-PSD95-PLA in gyrus dentatus area,* **(H)** *PLA channel of VAMP2(+)PSD95(-) staining, and* **(I)** *merged channel of DAPI for nuclei staining together with VAMP2(+)PSD95(-)-PLA for general synaptic contacts around the granular cell layer of the gyrus dentatus shows high synaptic density.* **(J)** *DAPI channel for nuclei staining from* **(K)** *vGLUT1(+)-PSD95(-)-PLA staining.* **(L)** *Merged channel of vGLUT1(+) PSD95(-) staining with DAPI shows lower density in the gyrus dentatus granular cell layer for glutamatergic synapses than general synaptic marker pairs. Scale bars 20 μm.*

3.2.1.2 Analysis of PLA Signal Using HALO

In a next step, the aim was to quantify puncta-like stainings as a surrogate for synaptic density in different brain areas. Therefore, a reference data set of C57BL6/J wt mice (n = 9) was used for the implementation of the HALO (Indica Labs, Corrales, NM) analysis. Different settings in the digital image analysis software HALO were compared on PLA stainings for the synaptic targets VAMP2(+)PSD95(-) and vGLUT1(+)PSD95(-). Three sections per brain per animal (200 µm intersectional distance) were stained and scanned. Scanning was performed with a Zeiss Axioscan.Z1 whole slide scanner under identical conditions with constant exposure and color map. HALO analysis was always performed on raw images on annotated areas of the somatosensory cortex (SS CTX), hippocampus (HC) and entorhinal cortex (EC).
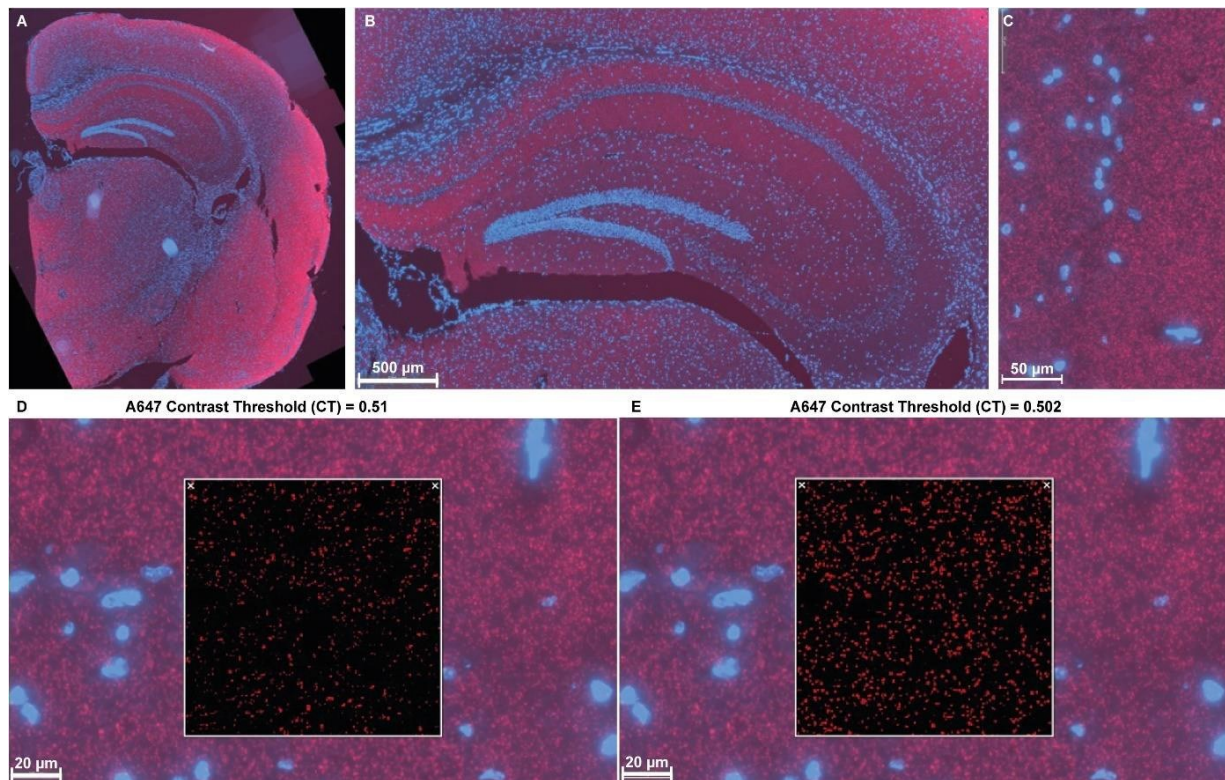
Figure 21: ***Comparison between different contrast threshold settings of HALO dot count analysis of PLA VAMP2(+) and PSD95(-) stainings. (A)*** *Representative images of an overview of a brain hemisphere stained with PLA VAMP2(+) PSD95(-).* ***(B)*** *Represents a zoom into the hippocampus. Scale bar 500 µm.* ***(C)*** *Higher magnification of the representative image in the hippocampus. Scale bar 50 µm.* ***(D)*** *Real-time Tuning window shows mark-up of the HALO analysis settings with contrast threshold (CT) at 0.51. Scale bar 20 µm. In comparison,* ***(E)*** *a representative image of the same image with a Real-time Tuning window showing the mark-up of HALO analysis settings with CT of 0.502, where the PLA puncta get detected more specifically. Scale bar 20 µm.*
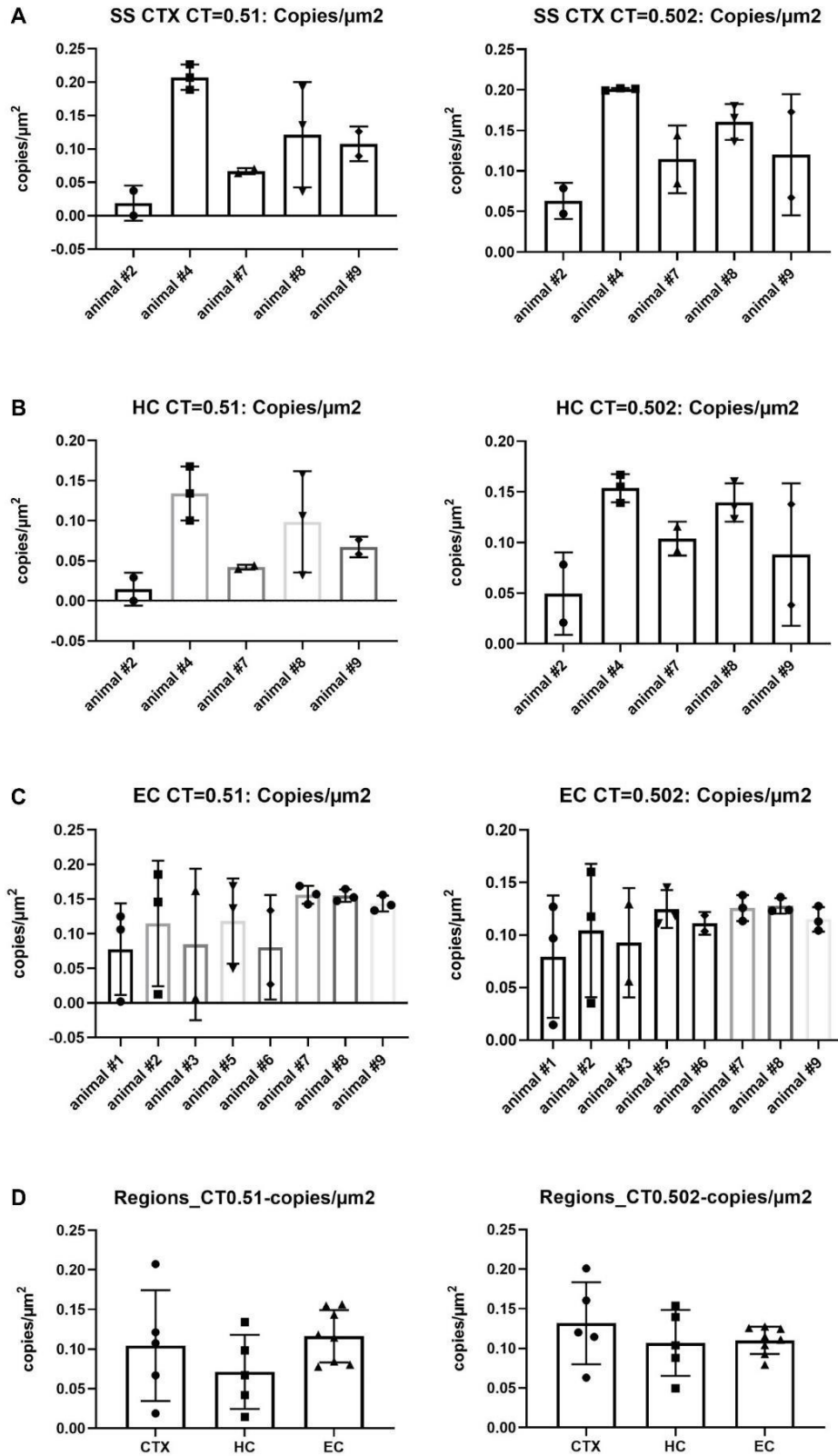
Figure 22: **HALO quantification between different contrast threshold (CT) settings of PLA VAMP2(+) and PSD95(-) stainings. (A)** *Quantification of the PLA dots analyzed with the two different CT settings in the soma-tosensory cortex (SS CTX).* **(B)** *PLA puncta quantification with two different CT settings at 0.51 compared to 0.502 in the area of the entorhinal cortex (EC).* **(C)** *PLA dot quantification in the area of the hippocampus (HC) compared again with the two different CT values.* **(D)** *The different regions (CTX, HC and EC) analysis shows the different PLA copies/µm² values with two different CT settings.*

To implement HALO analysis settings for future experiments, we focused on the contrast threshold (CT) settings, because this markedly influenced the dot count detection (Figure 21 - Figure 24). All other variables (minimum signal intensity, spot size, copy intensity and spot segmentation aggressiveness) for the Alexa Fluor 647 (PLA) channel were set identical. Due to scanner problems, some slides had a bad scan quality and were excluded (therefore, not all animals (n = 9) or slides per animal (n = 3 slides per animal stained) could be analyzed).

PLA stainings for general synaptic contacts VAMP2(+) and PSD95(-) (MAB1596) were compared with two different CT settings in the HALO Real-time Tuning window, where the respective HALO analysis settings are shown in a mark-up image (Figure 21 D, E). Settings with CT 0.502 generally detected more specifically the PLA dots (Figure 22) which also showed the quantification of synaptic contacts in the different animals in the SS CTX, HC, and EC. A high variability between the animals resulted in the comparison of the PLA copies per µm² for CT 0.51, which could be lowered with CT 0.502. Lowest variability was found in the EC area (Figure 22 D).
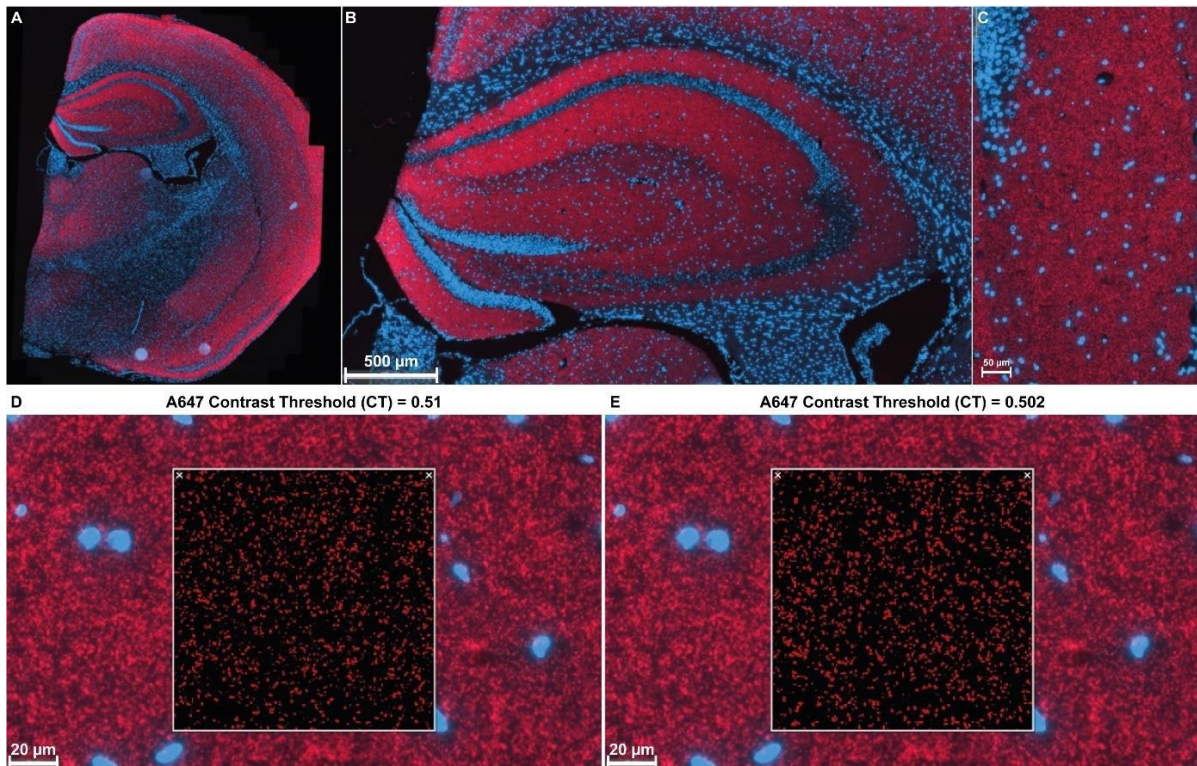
Figure 23: **Comparison of two different contrast threshold settings in HALO dot count analysis of vGLUT1(+)PSD95(-) PLA. (A)** *Representative image of a brain hemisphere stained with glutamatergic markers vGLUT1(+) and PSD95(-) PLA.* **(B)** *Representative image with a higher magnification in the hippocampus (HC). Scale bar 500 µm.* **(C)** *Zoomed further into the hippocampal region shows PLA puncta signal. Scale bar 50 µm.* **(D)** *The Real-time Tuning window shows the mark-up of the PLA puncta signal (A647 channel) detection with contrast threshold (CT) set to 0.51. Scale bar 20 µm.* **(E)** *Compared with CT settings at 0.502 shows a higher and more specific signal detection of the PLA puncta.*
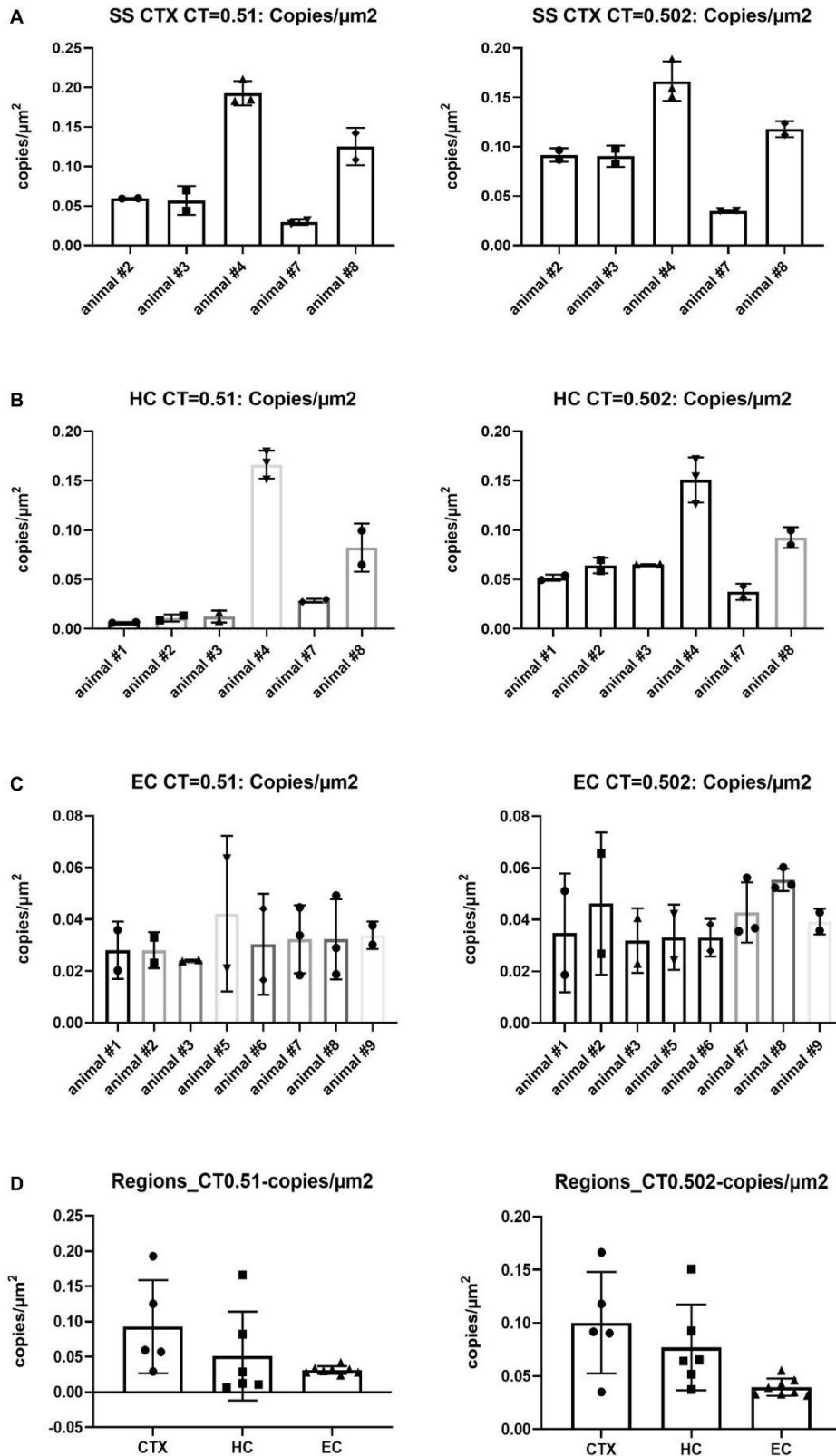
*Figure 24: **HALO quantification between different contrast threshold settings of PLA vGLUT1(+) and PSD95 (-) stainings. (A)** PLA copies/µm² quantification compared the two CT settings in the somatosensory cortex (SS CTX), **(B)** entorhinal cortex (EC), and **(C)** hippocampus (HC). **(D)** The three regions compared to one another show the lowest variability for both CT settings in the EC ROI.*

The same comparison of CT values was performed for a PLA staining with the glutamatergic synaptic markers vGLUT1(+) (ABN1647) and PSD95(-) (MAB1596) (Figure 23, Figure 24). Again, quantification was performed in the SS CTX, EC, and HC areas. The glutamatergic stainings resulted in the HALO PLA dot count quantification with both CT settings demonstrating a high variability between animals. Overall, the CT 0.502 led to a more specific detection of the PLA dots in the mark-ups of the Real-time Tuning windows and also in the quantification of the copies/µm² in the respective areas (Figure 24).

Altogether, the CT 0.502 settings revealed the lowest variability for both antibody combinations and were chosen for further analysis.

3.2.1.3 Alternate Coupling of PLA Probes

Next, we wanted to quantify the synaptic density of the stainings established in 3.2.1.1 with different probe conjugations (+/- or -/+) and in different brain areas. Tissue processing and conditions were described before (3.2.1.1). Brain areas which are usually affected in AD such as cortex, HC including gyrus dentatus (GD), pons (PO), cerebellum (CB) and hypothalamus (HY) were chosen for imaging (Pikuleva, 2006).

PLA staining was performed on FFPE tissue of C57BL6/J wt animals (n = 4, 3 slides per animal, which was processed as described in 2.2.4.1). The pre-synaptic anti-vGLUT1 (AB5905) antibody was directly coupled to the probes (+ or -). Omission of primary antibodies served as negative control. IF imaging (Zeiss LSM700) was performed under identical conditions with constant exposure and color map.

A general synaptic PLA staining with SYP and PSD95 showed significantly higher copies per µm² as a surrogate for synaptic density for the (+/-) probe conjugation of all ROIs compared to the (-/+) coupling (Figure 25 A, ****p<0.0001, two-way ANOVA).

PLA staining of the second general pair of synaptic markers (SYT and PSD95) also evidenced that (+/-) probe conjugation detects more synaptic contacts than (-/+) probe conjugation (Figure 25 B, ****p<0.0001, two-way ANOVA).

The third general synaptic marker pair VAMP2 and PSD95 also resulted in a higher number of copies per µm² for the (+/-) probe configuration than the (-/+) probe configuration (Figure 25 C, ****p<0.0001, two-way ANOVA).
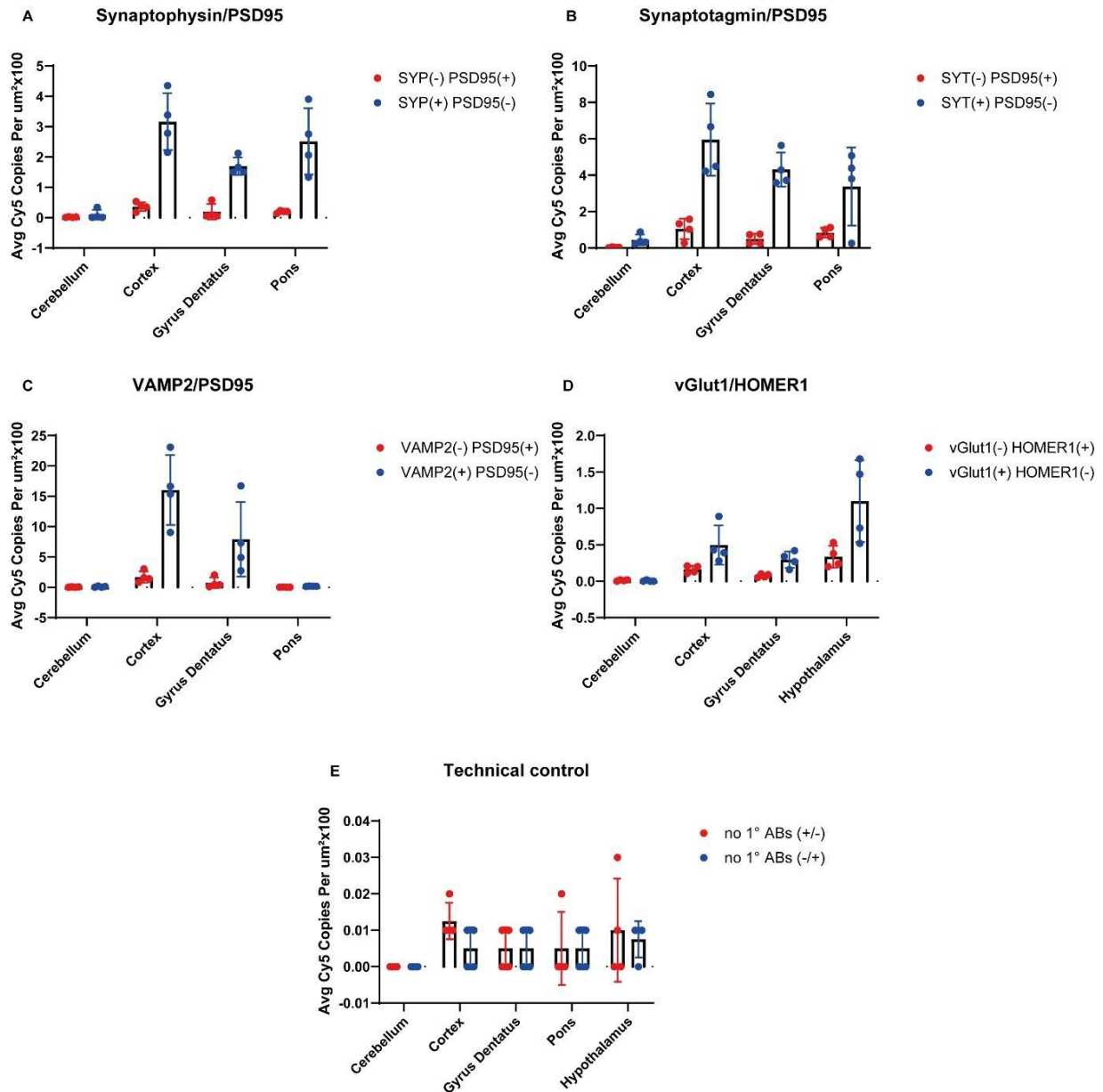
*Figure 25: **Quantification of synaptic density depending on probe conjugation and brain areas with PLA stainings for different marker pairs.** General marker pairs for **(A)** synaptophysin (SYP) and PSD95 with alternate probe coupling (+/-) or (-/+), **(B)** synaptotagmin (SYT) and PSD95 and **(C)** VAMP2 and PSD95 show in general a higher dot count (Avg Cy5 Copies Per µm² x100) than glutamatergic synaptic markers **(D)** vGLUT1 and HOMER1. **(E)** Controls with no primary antibodies (no 1° ABs) with alternating probe configuration.*

As expected, staining for the synaptic marker pair for glutamatergic synaptic contacts (vGLUT1 and HOMER1) resulted in a generally lower dot count for glutamatergic synapses. In addition, as compared to the (-/+) coupling the (+/-) probe configuration resulted in a significantly higher number of detected synapses (Figure 25 D, ***$p<0.0005$ two-way ANOVA).

With regards to the brain location, highest dot counts were observed in the cortex for all general synaptic marker pairs (SYP/SYT/VAMP2 and PSD95) coupled to the (+/-) probe configuration. For the glutamatergic staining with vGLUT1(+) and PSD95 (-), the

highest dot count was detected in the area of the hypothalamus (Figure 25). Lowest dot counts were found for all (+/-) stainings in the area of the cerebellum (granular layer).

3.2.1.4 IF Mounting Medium for PLA Staining

In a next attempt we tested if the Duolink mounting medium of the PLA kit can be replaced by the less expensive mounting medium used in 3.1.2 (DAKO) for IF stainings. However, use of IF mounting medium resulted in a high signal loss. For the (-/+) probe conjugation, a maximum intensity value of only up to 3 was observed (Figure 26 A-D). For the (+/-) probe configuration, maximum intensity values of only 30 - 41 as compared to approx. 3000 MIV for a "full PLA" with the DUOLINK medium were measured with a line profile analysis (Figure 26 E-H). Additionally, a high background for both conditions and no clear PLA puncta were seen (Figure 26). Furthermore, an unspecific immunoreactivity of the PLA signal occurred in the nuclei. Therefore, the IF mounting medium was not further used.
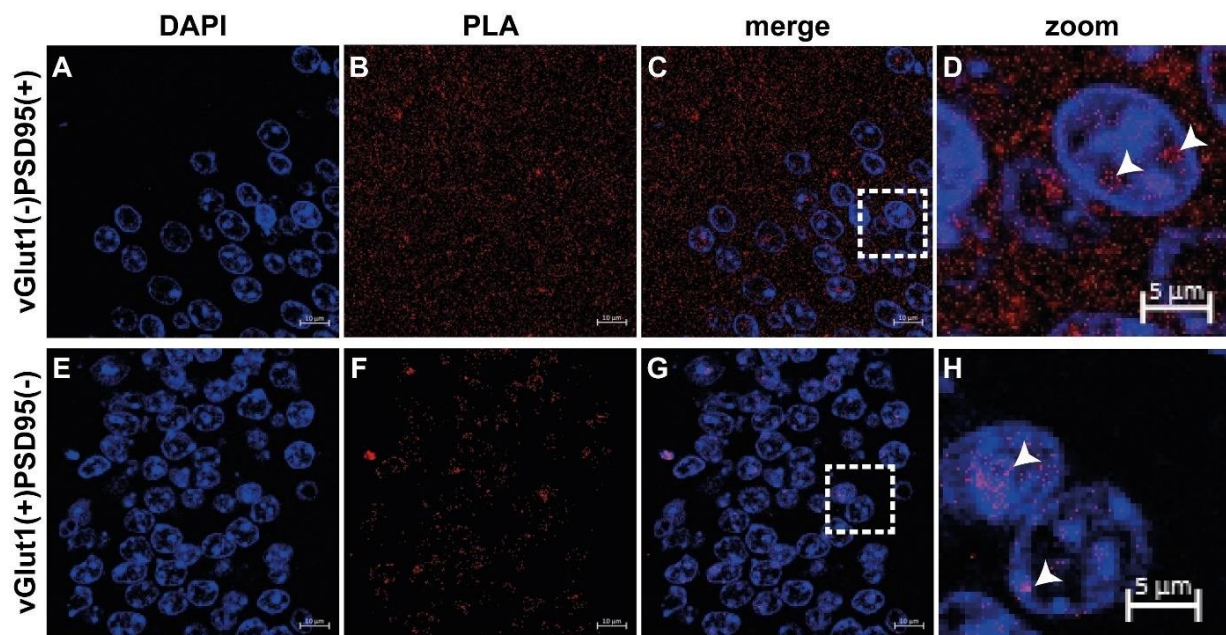
*Figure 26: **IF mounting medium leads to unspecific PLA signal.** (A) DAPI, (B) vGLUT1(-) PSD95(+) PLA, and (C) merge. (D) Zoom into rectangle shown in (C) where an unspecific PLA signal was found in nuclei (arrowheads). Scale bar 5 µm. (E) DAPI, (F) vGLUT1(+) PSD95(-) PLA, and (G) merge. (H) Zoom into rectangle of (G) where unspecific PLA puncta are found in the nuclei. Scale bar 5 µm. Scale bars 10 µm (A-C, E-G).*

3.2.1.5 Technical Negative Controls

As a further control of the specificity of the PLA signal, only one (vGLUT1-only; PSD95-only) or none (probes-only) of the respective primary antibody pairs was used. This was done on FFPE tissues of wt C57Bl6/J animals (n = 4 animals).

*Figure 27: **Technical controls to assess specificity of the PLA staining.** Representative image of wt brain hemisphere with **(A)** no primary (1°) antibody control, **(E)** PSD95-only-control, **(I)** vGLUT1-only control and **(M)** PLA with vGLUT1(+) and PSD95(-) as a positive control. Scale bar 1 mm. Representative image with higher magnification in the hippocampus **(B, F, J, N)** and cortex **(C,G,K,O)** of the respective stainings. Scale bar 50 µm. HALO analysis of copies/µm² x100 in regions of isocortex, somatosensory (SS) cortex, hippocampus, and entorhinal cortex of the respective control or PLA staining **(D,H,L,P)**. vGLUT1-only control resulted in highest number of copies/µm² x100 false positive detection. **(L,P)** Dotted squares indicate the comparison between a "full PLA" with both primary antibodies **(P)** and vGLUT1-only control detecting the false positive copies/µm²x100 in the respective regions resulting in the highest quantification window.*

Controls with no primary antibodies resulted in almost undetectable false positive sig-nals (Figure 27 A-C). Leaving out one of the primary antibodies, using both (+) and (-) probes, showed a slightly increased signal detection of false positive dots which was more prominent for vGLUT1 (Figure 27 I-K). A fold-change analysis of PLA vGLUT1(+) PSD95(-) copies/µm² x100 divided by the copies/µm² x100 of the vGLUT1-only con-trols revealed a 14.5x higher fold change in the positive control as compared to the highest false positive values seen for vGLUT1 only in the isocortex. This was even 18.3x higher in the somatosensory cortex, 5.5x higher in the hippocampus, and 12.4x higher in the entorhinal cortex (Figure 27 L, P). To account for the highest possible numbers of false positive copies/µm²x100, vGLUT1 only was used in further experi-ments as a technical negative control.

3.2.1.6 Clearing Combined with PLA

Next, we tested the combination of the two clearing protocols with the PLA technique in order to get a more detailed 3D information on synaptic contacts. Quantification of synaptic density in 3D tissue samples was performed as described in 2.2.5.4 by com-bining ECi clearing and the PLA for synaptic stainings with VAMP2(+) (AF AF5136) and HOMER1(-) and for glutamatergic synapses with vGLUT1(+) (ABN1647) and HOMER1(-).

Furthermore, when combining X-CLARITY with PLA (2.2.5.5) antibody pairs VAMP2(+) (ab215721) and HOMER1(-), and for glutamatergic staining vGLUT1(+) (ABN1647) and HOMER1(-) were used.

However, no PLA signal was observed for either of the clearing methods under a light-sheet microscope, while the nuclear staining (ToPro3) was present (data not shown). Accordingly, this approach was not further pursued.

3.2.2 Age-dependent Assessment of Synaptic Density by Using PLA

To further challenge the robustness of the PLA, we sought to quantify the change in synaptic density in mouse brain slices in an age-dependent manner. This was based on the observation that at postnatal day 15 (P15) synaptic development shows a peak in synapse numbers (Fan et al., 2018; Li et al., 2010) while in adult mice (P180) syn-apses are known to be reduced through synaptic pruning to only necessary contacts (Stevens et al., 2007).

3.2.2.1 Validation of HALO Quantification of PLA on P15 Mouse Brain Tissue Slices

On 4 µm-thick and FFPE-processed CD1 (P15, n = 4) brain tissue slices, a PLA with synaptic markers VAMP2(+) and PSD95(-) (MAB1596) (Figure 28 A-C) and vGLUT1(+) (ABN1647) and PSD95(-) (MAB1596) (Figure 29 A-C) was performed. Scanning was done with a whole slide scanner (Zeiss Axioscan.Z1) under identical conditions with constant exposure and color map. HALO annotations were set for ROIs in SS CTX, HC and EC and analyzed for contrast threshold settings at 0.51 and 0.502. Three slides per animal/ROI were analyzed.

A quantification of VAMP2(+) PSD95(-) PLA stainings in the ROI SS CTX and HC with both CTs revealed no significant differences among the animals (Figure 28 A-F, $p>0.05$, Ordinary one-way ANOVA). However, for EC animal #2 presented with significantly increased values at a CT of 0.502 (Figure 28 F, *$p<0.05$, Ordinary one-way ANOVA). When comparing values of different regions, for a CT of 0.502 a significant difference was found for the SS CTX region while a CT of 0.51 revealed significantly higher numbers for HC (Figure 28 G, $p<0.001$; Ordinary one-way ANOVA).

A quantification of vGLUT1(+) PSD95(-) PLA stainings in the ROI SS CTX revealed no significant differences among the animals for a given brain area for both CTs (Figure 29 A-F, $p>0.05$, Ordinary one-way ANOVA). When looking at different regions, a significant difference was found for HC with CT 0.502 (Figure 29 G, ***$p<0.001$; ordinary one-way ANOVA).

Altogether, a CT of 0.502 appeared to be less prone to varying results in samples of the same animal as demonstrated by a lower standard deviation for both synaptic contacts stainings for all ROIs analyzed.
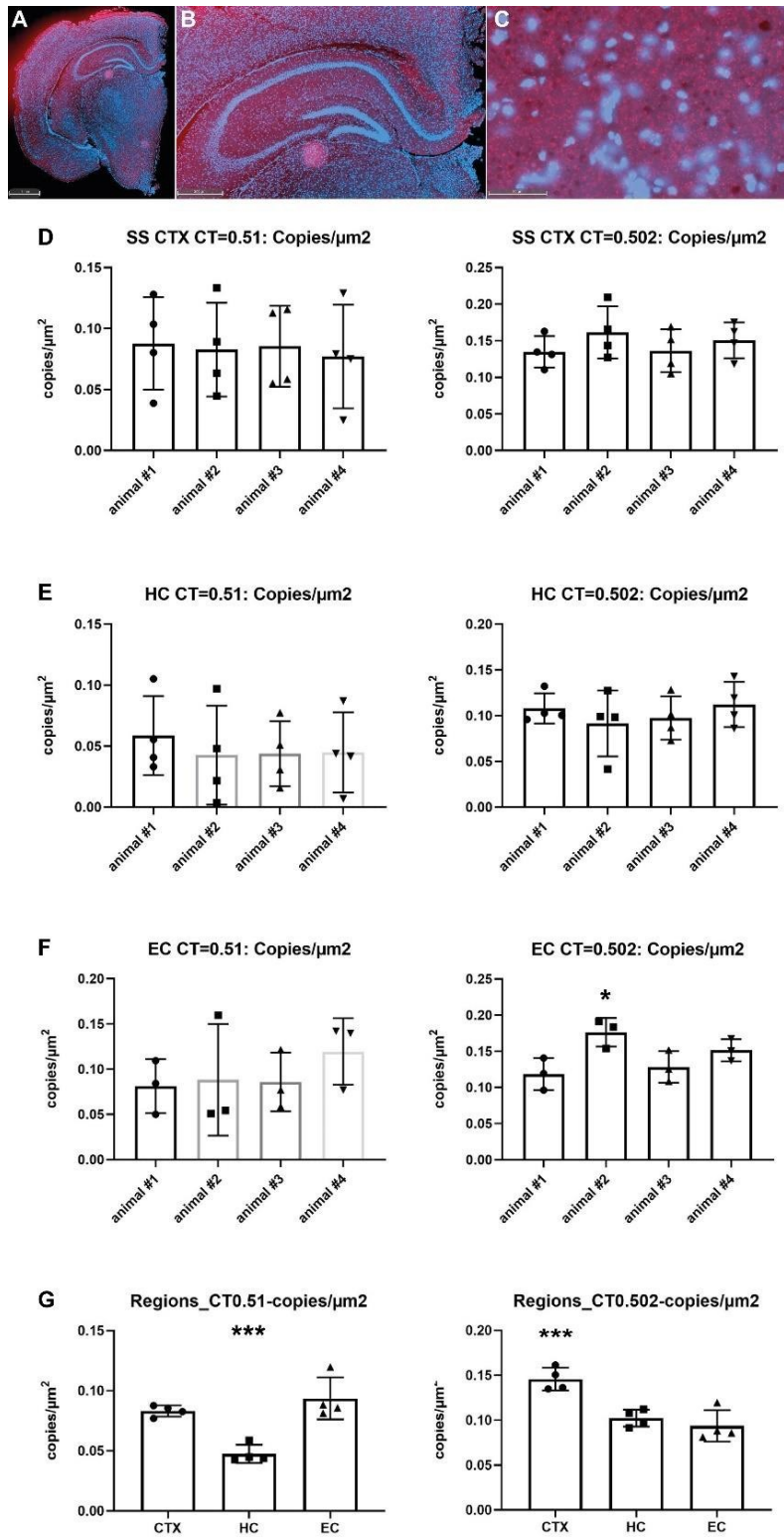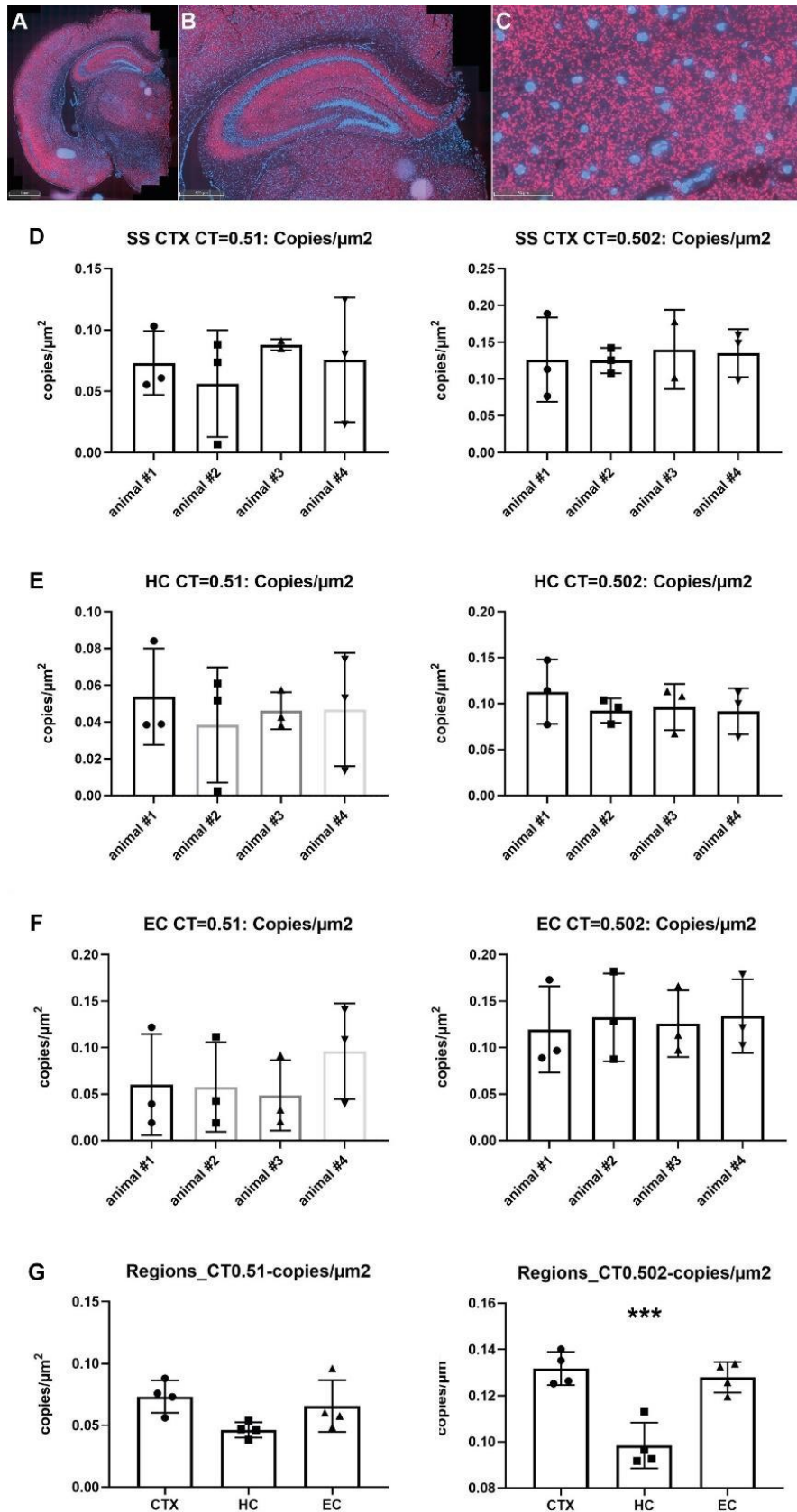
Figure 28: **Comparison of different contrast threshold settings for VAMP2(+) PSD95(-) PLA dot count analysis in HALO of P15 mice for general synaptic contacts. (A)** Representative image of a VAMP2(+) PSD95(-) PLA staining on a brain hemisphere of a 15-day-old CD1 mouse. Scale bar 1 mm. **(B)** Higher magnification in hippocampus (HC). Scale bar 500 μm. **(C)** Higher magnification in the HC shows PLA dots visualizing synaptic contacts. Scale bar 50 μm. Comparison between CT settings 0.51 and 0.502 in areas **(D)** somatosensory cortex (SS CTX), **(E)** HC, **(F)** entorhinal cortex (EC) where for CT 0.502 a significant difference between animal #2 and all other animals was found and **(G)** in the regions analyzed. A highly significant difference between the regions was found for CT 0.51 in the HC and for CT 0.502, a significant difference was found between the cortex area (CTX) and other regions (*p<0.5, ***p<0.001, ordinary one-way ANOVA).

*Figure 29: **Comparison of different contrast threshold settings for vGLUT1(+) PSD95(-) PLA dot count analysis in HALO of P15 mice for glutamatergic synaptic contacts. (A)** Representative image of a vGLUT1(+) PSD95(-) PLA staining on a brain hemisphere of a 15-day-old CD1 mouse. Scale bar 1 mm. **(B)** Higher magnification in hippocampus (HC). Scale bar 500 µm. **(C)** Higher magnification in the HC shows PLA dots visualizing synaptic contacts. Scale bar 50 µm. Comparison between CT settings 0.51 and 0.502 in areas **(D)** somatosensory cortex (SS CTX), **(E)** HC, **(F)** entorhinal cortex (EC), and **(G)** in the regions analyzed. A highly significant difference between the HC and the other regions was found for CT 0.502 (***p<0.001, ordinary one-way ANOVA).*

3.2.2.2 Validation of HALO Quantification in P15 vs. P180 Mice

According to the current literature, synaptic density should be highest in young animals, as the synaptic contact formation matures (Fan et al., 2018). Therefore, we compared the PLA copies/µm² of P15 with the stainings in adult wt mice.

For the PLA staining of general synaptic contacts VAMP2(+) PSD95(-), no significant differences could be observed between young and adult mice in the different ROIs (Figure 30 A, p>0.05, Two-way ANOVA followed by Tukey's multiple comparison). Furthermore, this was independent of the chosen CT.

The same was seen for the vGLUT1(+) PSD95(-) PLA analysis except a significant difference in the EC ROI between adult and P15 animals for a CT of 0.502 (Figure 30, ***p<0.001, Two-way ANOVA, followed by Tukey's multiple comparison) in favor of P15 animals which show a higher synaptic density.
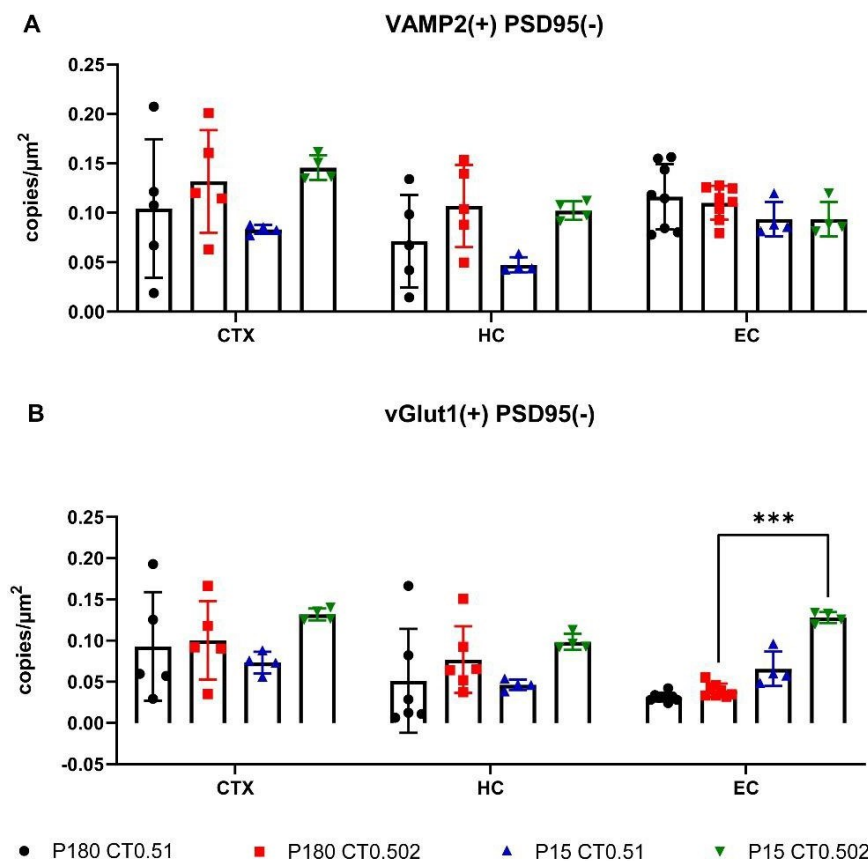
Figure 30: **Comparison of PLA dot copies per µm² of P15 and adult (P180) wt mice with PLAs for general and glutamatergic synaptic contacts**. *(A) VAMP2(+) PSD95(-) PLA for general synaptic contacts of P180 and P15 mice data points with different contrast threshold (CT) analysis settings to detect PLA dots. (B) Comparison of the same animals with PLA for glutamatergic synaptic contacts vGLUT1 (+) PSD95(-).*

3.2.2.3 Synaptic Density in P15 vs. P180 wt Mice

To test if a new scanner set-up (Zeiss Axioscan.Z1) would be more suitable to unravel age-dependent differences for synaptic contacts we re-analyzed the same samples as in 3.2.2.2. Therefore, we changed settings in the Focus Map regarding Focus point strategy, Noise Filter, Bleaching Settings, and Exposure time for AF647 (PLA) channel in the Zeiss imaging software. We compared the synaptic density of P15 (CD1, n = 4) brains of wt mice with adult mice at postnatal day 180 (P180, C57BL6/J, n = 4). PLA stainings with vGLUT1(+) (ABN1647) and PSD95(-) (MAB1596) were re-analyzed. Scans of the adult P180 wt animals showed relatively high PLA signal variability comparing different sections. Comparing the mean values in the chosen ROIs show a low variability (Isocortex: mean 5.386 ± 0.796, n = 4; SS CTX: mean 4.451 ± 1.090, n = 4; HC: mean 2.678 ± 0.833, n = 4) except for the entorhinal cortex (EC: mean 5.612 ± 2.325, n = 4).
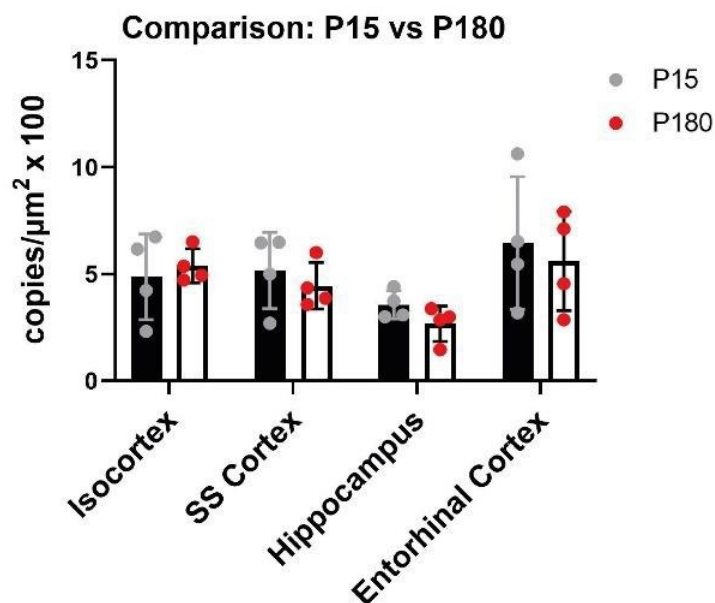
*Figure 31: **Numbers of glutamatergic synapses in P15 and P180 wt mice after newly implemented scanner setup**. (A) No significant differences could be observed in the different analyzed brain regions between P15 and P180 wt mice.*

For P15 animals, slides were re-scanned with the new scanner set-up. A high PLA signal variability between the sections was optically observed, potentially due to rescanning and thus subsequent signal bleaching (Isocortex mean 4.866 ± 2.008, n = 4; SS CTX mean 5.165 ± 1.784, n = 4; HC mean 3.562 ± 0.658, n = 4; EC mean 6.452 ± 3.111, n = 4).

Altogether, adjustments in the scanner set-up did not reveal any age-dependent differences in any of the analyzed regions when comparing P15 to P180 animals (Figure 31, p>0.5, Two-way ANOVA).

3.2.2.4 Usability of the Corpus Callosum as Negative Control

As another option to test the specificity of the PLA, we looked for a brain area in which no or a greatly reduced density of synaptic contacts can be expected. Therefore, the corpus callosum was chosen as potential negative control because it is mostly composed of myelinated fiber tracts connecting the brain hemispheres (Evans, Bury, Huang, & Sabo, 2019).
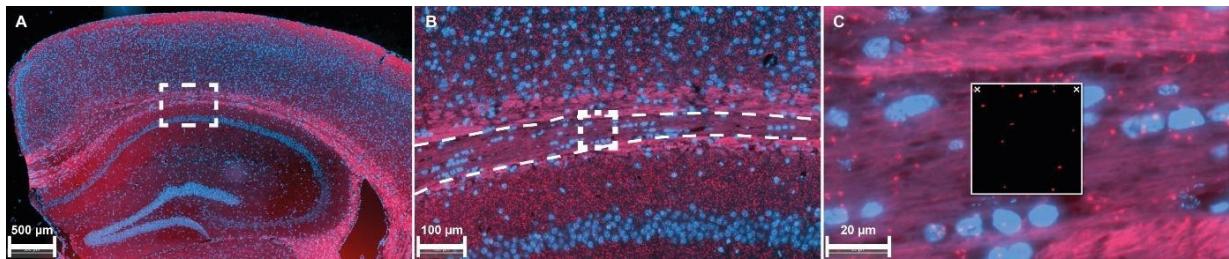
Figure 32: **Corpus callosum with low synaptic density serves as biological negative control. (A)** *Representative image of a PLA vGLUT1(+) PSD95(-) on a wt mouse. Scale bar 500 µm.* **(B)** *Higher magnification image in the area of the corpus callosum (rectangle in* **(A)***). Scale bar 100 µm.* **(C)** *Higher magnification of rectangle in* **(B)** *shows low PLA puncta detection in corpus callosum with Real-time Tuning window in HALO. Scale bar 20 µm.*

As expected, PLA dot detection with established HALO settings (CT 0.502) showed no to only sparse signal detection in Real-time Tuning window (Figure 32).

3.2.3 Further Optimization of PLA Protocol on FFPE Tissue

Results of 3.2.2, the unexpected outcome regarding the comparison of P15 and adult animals and the observed high signal variability, forced us to aim for further improvements of the PLA protocol with regard to primary antibody selection (mouse on mouse staining), signal distribution (liquid barrier, heat distribution) and scanning parameters. Since the signal distribution of a whole slide scan was inconsistent, so that many slides were not analyzable, a focus was set on the improvement of the liquid- and heat-distribution and -stabilization. Here, the images of whole slide scans showed "edge effects" with a higher signal on the edges than in the middle of a tissue slice. The same was true for large tissue slices where a gradient from one end to the other was observed (Figure 33).
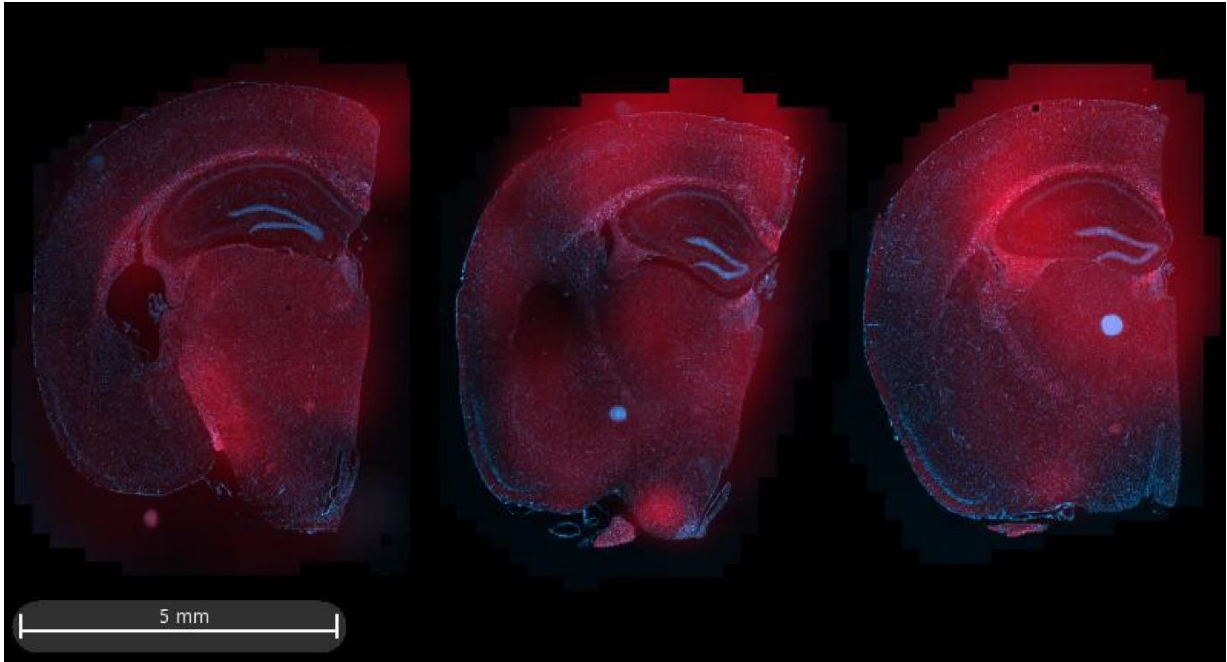
*Figure 33: **Inconsistent vGLUT1(+)PSD95(-) PLA signal distribution on a whole slide scan.** Signal of red channel (PLA) showed a gradient from left to right.*

Therefore, we hypothesized that the heat distribution and stability during the 37 °C incubation steps could be inconsistent when using a HYBAID hybridization oven with a comparatively large inner volume compared to the moisture chambers. Here, a temperature discrepancy between the moisture chamber and the oven could occur resulting in a long heating period until the inner temperature in the moisture chamber achieves 37 °C. In this case, the incubation time would be too short. Additionally, a heat drop could occur during loading and unloading of the moisture chamber containing the slides resulting in an even higher temperature discrepancy. Another test to optimize the PLA signal, were substitutions for liquid barriers. Since the liquid barrier of a PAPpen was easily washed off and broke during incubation steps resulting in tissue that dried-out and a signal loss.

Besides, we further used only primary antibodies which were not raised in mice and of host animals for which probes were commercially available. Since mouse-on-mouse stainings produced high dot counts for the negative pre-synaptic antibody-only controls, despite using blocking solution to block endogenous mouse Immunoglobulin G (IgG), we excluded antibodies for mouse-on-mouse stainings in future experiments. Also, we excluded the direct labeling of primary antibodies, since for the directly coupled vGLUT1 antibody (AB5905), a variability in signal intensity was observed. Primary antibodies were selected depending on the availability of commercially available probes. Furthermore, we reduced the intersectional distance between consecutive

sections from 200 µm to 50 µm in order to obtain a better comparability of a given area in the same animal.

3.2.3.1 Testing Primary Antibody Distribution with IF Staining for Equal Signal Distribution

First, we wanted to exclude the possibility of the primary antibodies being the source of an unequal signal distribution. Therefore, IF stainings with primary antibodies VAMP2 (ab215721), vGLUT1 (ABN1647) and PSD95 (MAB1596) were performed on wt C57BL6/J animals (n = 3). Whole slide scans were scanned (Zeiss Axioscan.Z1) under identical conditions with constant exposure and color map.

Signal was equally distributed on the entire slide without any gradient, so that the primary antibodies could be excluded being the cause of an unequal signal distribution (Figure 34).
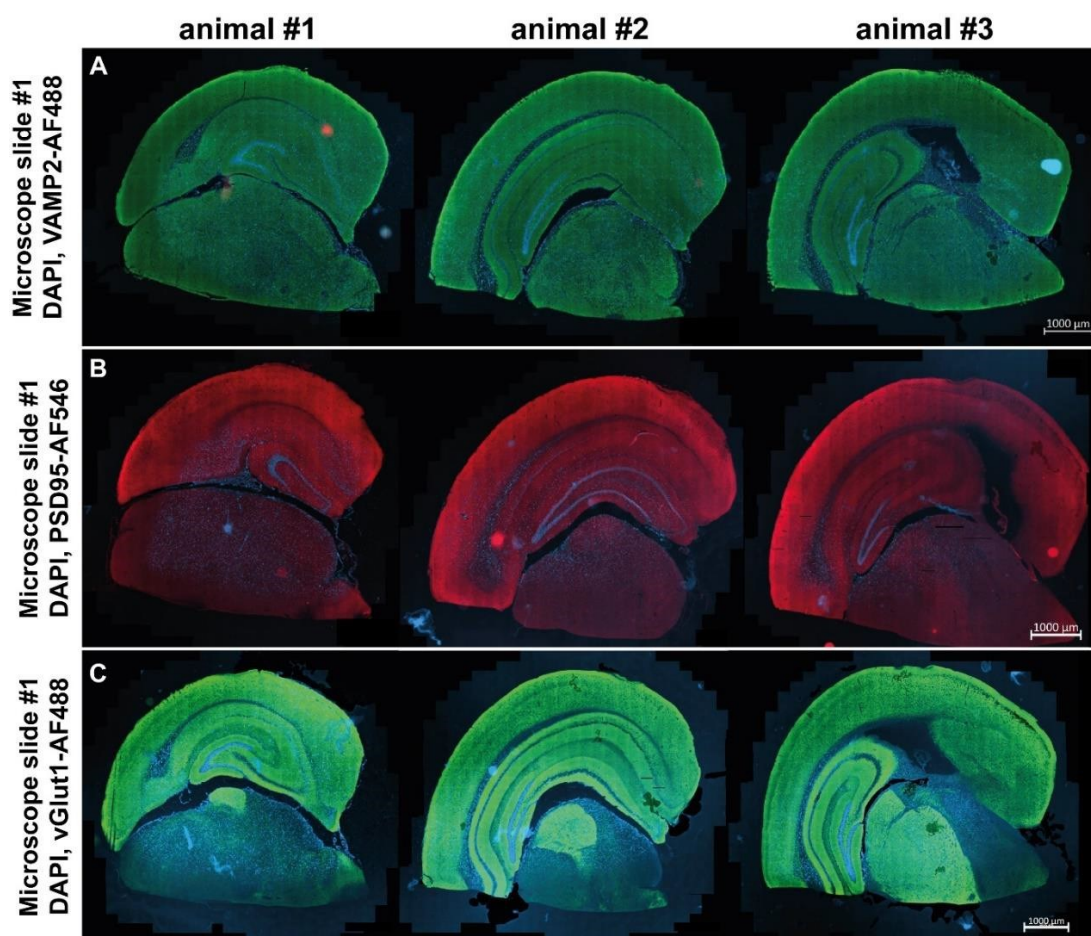
*Figure 34: **Immunofluorescence stainings of VAMP2, PSD95 and vGLUT1 with DAPI show equal signal distribution on the entire scan**. (A-C) Representative images show IF stainings of the primary antibodies of three animals on a microscope slide. The signal distribution of the fluorophore (AF488 or AF546) is equally distributed for each primary antibody over the whole slide.*

3.2.3.2 Test of Replacement Options for PAPpen

To avoid an unintentional leakage of the liquid barrier, we tested potential substitutions for the PAPpen and performed IF stainings on C57BL6/J wt animals (n = 3). First, we tested different liquid barrier pens (Hölzel, Abcam, agar scientific) from other distributors, which also frequently broke during washing steps.

Next, we tested iSpacers (SunjinLabs, IS203) and CoverWells (ThermoFisher, C18151 and C18150) which were both glued around the tissue onto the microscope slides. Due to their fixed size, iSpacers were partly too small to surround already prepared tissue slices. Additionally, they repeatedly detached during washing steps, as the glue was not strong enough. We also observed the opposite phenomenon that iSpacers could not be removed before mounting of the slides with coverslips. Then the removal led to a destruction of the tissue. In contrast, CoverWells adhered well to the microscope slides during the whole procedure and could easily be peeled off before mounting. However, a major disadvantage of both systems was the requirement of large amounts of solution (up to 500 µl/slide) that had to applied to the slides to cover the area surrounded by iSpacers and CoverWells. This would have a tremendous impact on material amounts and costs to perform the PLA and was therefore not further pursued.

Covertiles (Leica) represented another glue-less option to replace the use of a PAPpen. According to the supplier, this system facilitates an even reagent flow and minimizes the required amounts of fluids used during staining procedures. Therefore, we compared PLA stainings prepared with PAPpen, where 325 µl per slide needed to be applied, with Covertiles requiring a volume of 200 µl per slide. The Covertiles were tested i) by applying the liquid as described in Figure 12 or ii) by placing them upside down before adding the liquid and a positioning of the microscope slide on top of the Covertile. Therefore, PLAs with vGLUT1(+) (ABN1647) and PSD95(-) (MAB1596) and respective controls (vGLUT1-only) on C57BL6/J wt animals (n = 4, 3 slides per animal and condition) were performed. Whole slide scans (Zeiss Axioscan.Z1) were done under identical conditions with constant exposure and color map. Scans of the three different experimental conditions showed optically huge differences regarding the PLA signal intensity which was highest for the PAPpen condition and lowest for the Covertile upside down condition. Accordingly, the HALO analysis of the copies/µm²x100 showed significantly higher dot counts for the PAPpen condition in the somatosensory cortex (Figure 35 G, **p<0,01, ordinary one-way-ANOVA followed by Dunnett's multiple comparisons test) while this was not the case in the area of the hippocampus

(Figure 35 H, ns, p>0.5, one-way ANOVA). However, for the PAPpen condition an unwanted gradient in signal intensity was observed on each of the three slides stained (Figure 35 A) but not for any of the Covertile conditions.
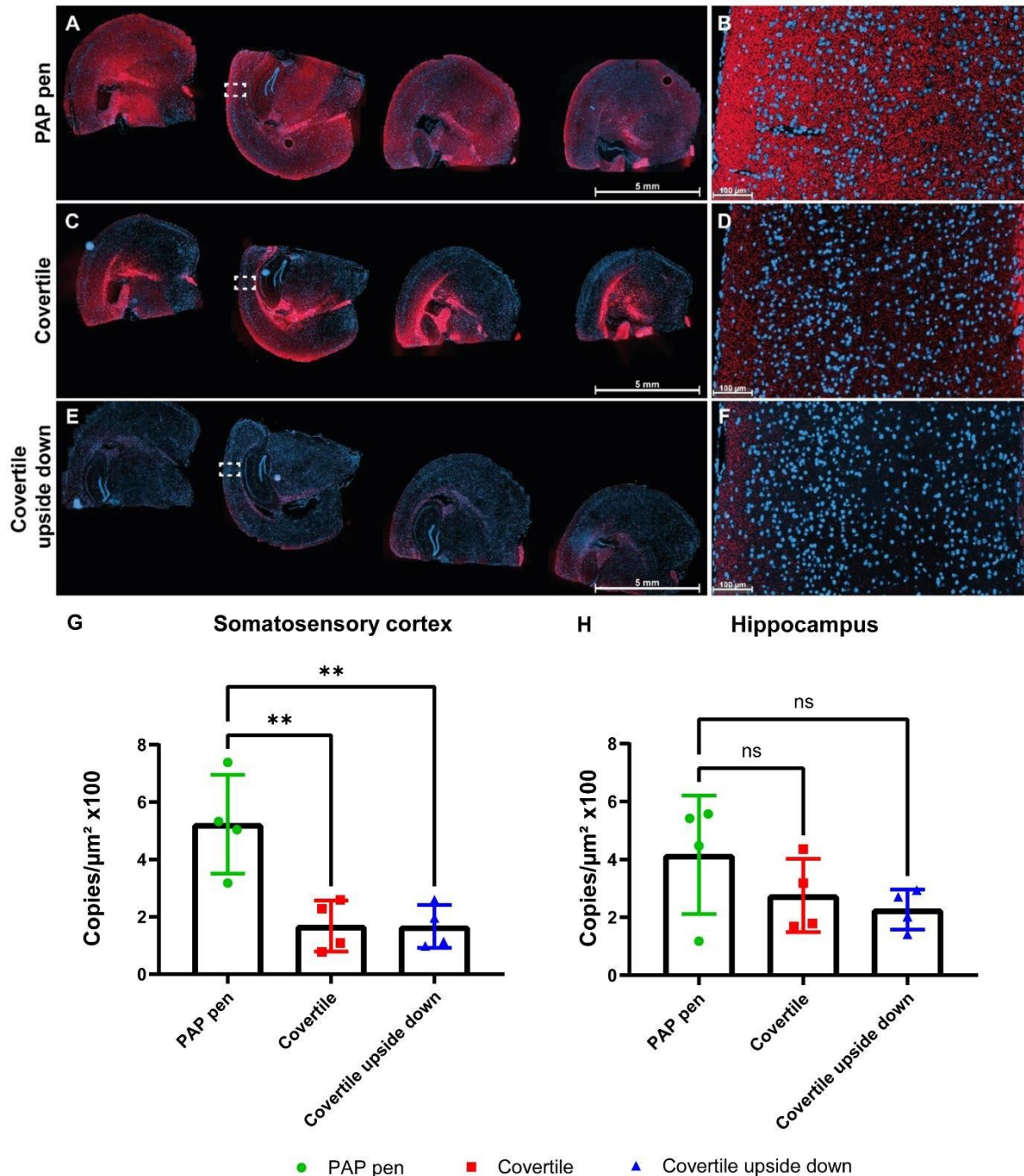

*Figure 35: **Comparison of PLA vGLUT1(+) PSD95(-) prepared with a standard liquid barrier, Covertile and Covertile placed upside down.** Representative images of whole slide scans **(A, C, E)** with 4 animals on one microscope slide show a decrease in PLA signal. Additionally, a PLA signal gradient is observed from left to right with the PAP pen condition **(A)**. Scale bar 5 mm. **(B, D, F)** Representative images of higher magnification of the second animal from left (rectangles in **A, C, E**) in the area of the somatosensory cortex, show the PLA puncta of synaptic contacts with a decreasing signal intensity from **B** to **F**. Scale bars 100 µm. **(G)** The decreasing signal intensity is also shown with the HALO quantification of the different conditions in the somatosensory cortex of the means with SD. **(H)** A decrease in PLA copies/µm²x100 with decreasing tendency of the means with SD is observed in the hippocampus.*

Altogether, important advantages of Covertiles were an easy handling, a cost-effective lower volume to cover slides, no exposure to toxic chemicals, no drying out of the slides during incubations, no re-drawing of the liquid barrier, a lower variability between the slides, and finally a gradient-free distribution of the PLA signal (Figure 35 C-D). This was especially the case for conventional Covertiles since the upside down Covertile condition was too cumbersome to handle and revealed a somewhat lower signal intensity. Although the PAPpen seemed to result in a higher signal intensity and dot count, due to the even and therefore less-biased distribution of the signal intensity on the whole slide we decided to continue with the Covertiles for further experiments.

3.2.3.3 Metal Boxes to Improve Heat Distribution

Another approach to minimize a potential uneven distribution of the PLA signal and to improve the quality of the signal consisted of the use of metal boxes. We hypothesized that heat-sensitive incubation steps with enzymes (ligation and amplification) could have an effect on both, signal distribution and quality. Therefore, we tested a PLA staining placing the slides directly on a metal surface (box for surgical instruments, Holtex) during the 37 °C incubations. Again, we compared Covertile and PAPpen conditions. We performed PLAs with vGLUT1(+) (ABN1647) and PSD95(-) (MAB1596) and respective controls (vGLUT1-only) on TG4510 animals (10-moth-old, n = 4, sagittal, 3 slides per animal and condition). Whole slide scans were (Zeiss Axioscan.Z1) performed under identical conditions with constant exposure and color map.

The HALO quantification of the PLA copies/μm^2x100 did not reveal significant differences for both liquid barrier conditions in the somatosensory cortex as well as the hippocampus (Figure 36 E-F, p>0.05, Two-tailed unpaired t-test). However, the whole slide scans resulted in a higher but mostly unspecific PLA signal for the PAPpen condition, and a marked staining gradient (Figure 36 A, B). A contribution of a non-even surface could not be excluded. As for the Covertiles a high variability of PLA dots was observed. Therefore, we decided to test the same conditions in the hybridization oven (BOEKEL) in order to reduce the inner volume for a more optimal and equal heat transfer as a possible reason for the limitations observed when using the metal box.
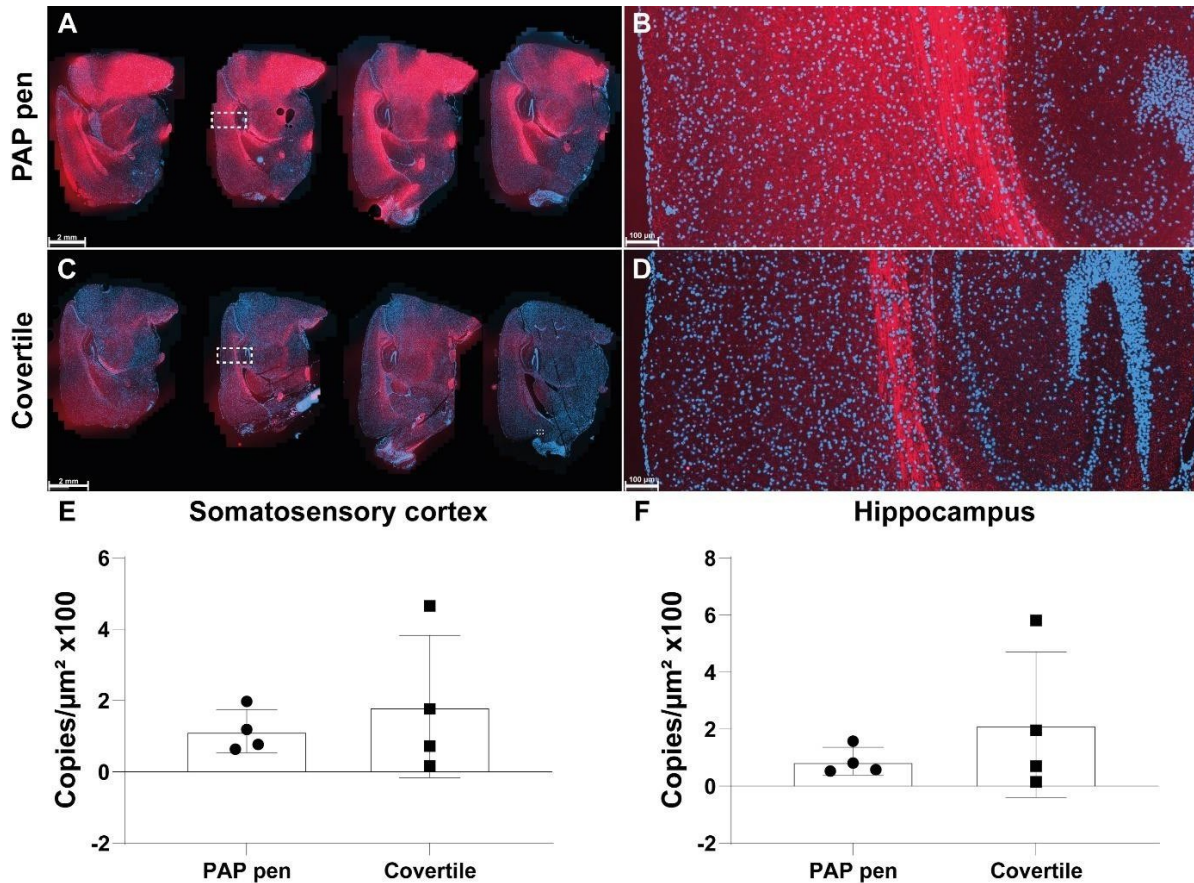
*Figure 36: **Comparison of PLA vGLUT1(+) PSD95(-) staining on TG4510 animals with PAPpen or Covertiles incubated on a metal plate.** Representative images of DAPI and PLA staining prepared with PAPpen **(A, B)** or Convertible **(C, D)** show a higher signal intensity for the PAPpen condition with a decreasing gradient from left to right. Scale bar 2 mm. **(B, D)** Representative images with higher magnification of animal #2 (rectangles in A, C) show a high background in the 647 channel for the PAPpen condition. Scale bar 100 μm. **(G, H)** HALO quantification of PLA copies/μm²x100 show a higher mean for the Covertile condition in the areas of the somatosensory cortex **(G)** and hippocampus **(H)**.*

3.2.3.4 PLA Signal Obtained in Hybridization Oven

To test the Covertile and PAPpen conditions in a hybridization oven (BOEKEL), the same tissue and stainings were performed as described in 3.2.3.3. The slides processed with Covertiles were placed directly on the aluminum tray. For the PAPpen condition, a moisture chamber was prepared (2.2.6.3 C).

Although the PLA stainings with vGLUT1(+) PSD95(-) showed a higher signal intensity for the PAPpen condition, a high variability in signal distribution over the slide accompanied by an inacceptable high background was observed (Figure 37 A, B). In contrast, the PLA staining with Covertiles showed an evenly distributed signal on the whole slide scans and clearly differentiable puncta in the somatosensory cortex (Figure 37 C, D). Interestingly, HALO quantification of the PLA copies/μm²x100 was significantly higher for the PAPpen than the Covertile condition in the somatosensory cortex (Figure 37 E,

**p<0.01, Two-tailed unpaired t-test) and in the hippocampus (Figure 37 F, ***p<0.001, Two-tailed unpaired t-test).

Although the HALO quantification gave a significantly higher dot count of PLA copies/µm^{2}x100 for the PAPpen condition, we decided to move on with Covertiles for future experiments, due to the even PLA signal distribution, a lower volume (200 µl) required and due to the favorable signal/background ratio.
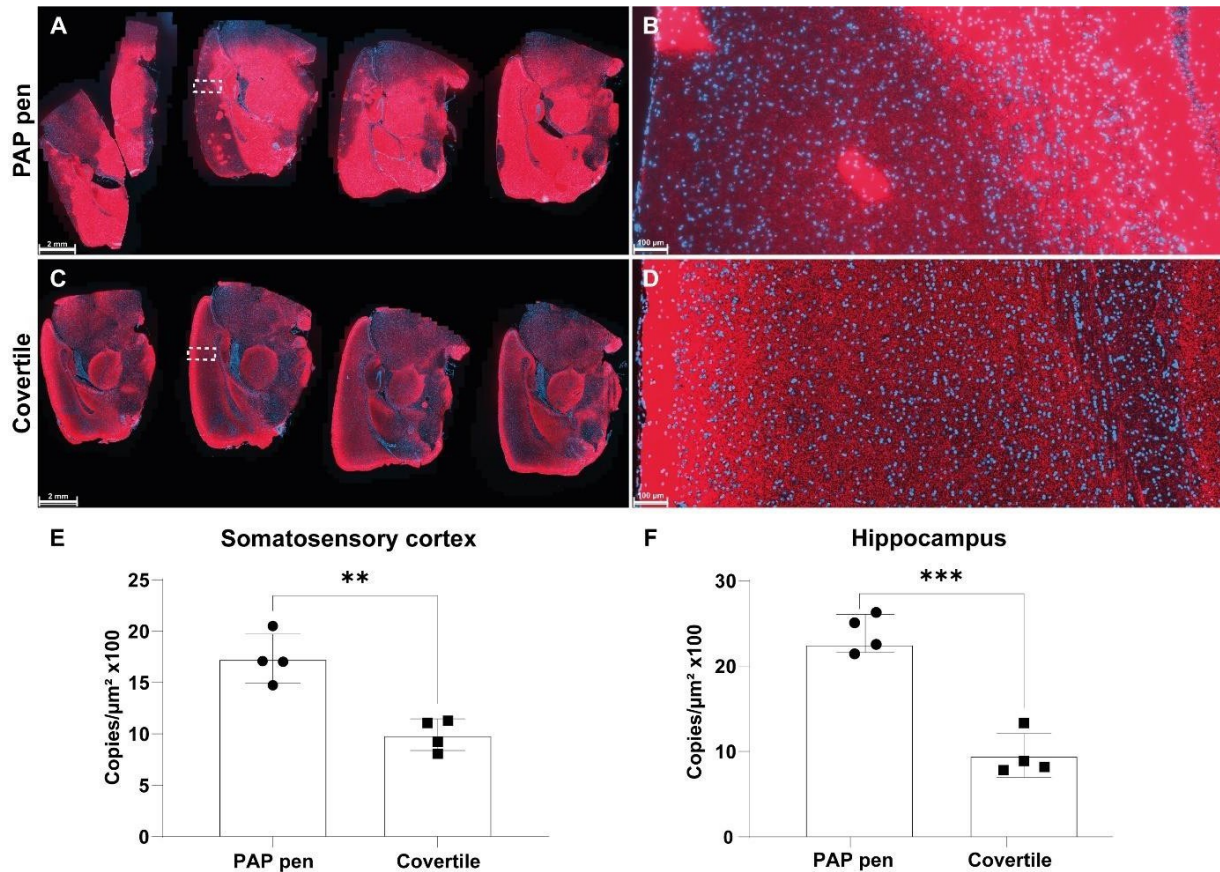

*Figure 37: **Comparison of PLA vGLUT1(+) PSD95(-) staining on TG4510 animals with PAPpen or Covertiles in a hybridization oven.** Representative images of DAPI and PLA staining prepared with PAPpen **(A,B)** or Covertiles **(C,D)** show a higher but less specific signal intensity for the PAPpen condition and a high variability of the signal distribution. Scale bar 2 mm. **(B,D)** Representative images with higher magnification of animal #2 (rectangles in A,C) show a high background in the 647 (PLA) channel for the PAPpen condition with unidentified puncta. Scale bar 100 µm. **(G,H)** HALO quantification of PLA copies/µm²x100 show a higher mean for the PAPpen condition in the areas of the somatosensory cortex **(E)** and hippocampus **(F)** with a significant difference (**p<0.01, Unpaired t test; ***p<0.001, Unpaired t test).*

3.2.3.5 Establishment of New vGLUT1-PSD95 Antibody Pair

To reduce background staining caused by using a mouse antibody for PSD95 (MAB1596) on mouse tissues, we went on to establish a new vGLUT1-PSD95 antibody pair with antibodies that were not produced in mice. We made use of goat-anti-vGLUT1 (135307) and rabbit-anti-PSD95 (3409S) antibodies for IF staining on coronal

brain sections of C57Bl6 wt mice (n = 4, Figure 38). The 10 % highest and lowest signal intensity values for PSD95 and vGLUT1 (Figure 38 G) resulted in acceptable S/B ratios indicating a good immunoreactivity and low background signal. Furthermore, we tested whether using the blocking and antibody dilution buffers included in the assay kit (Duolink buffers) would further elevate the signal quality. The resulting signal intensity values for the self-made buffers (2.1.10) showed slightly higher signal intensity values and S/B ratios compared to the Duolink buffers (Figure 38 H).
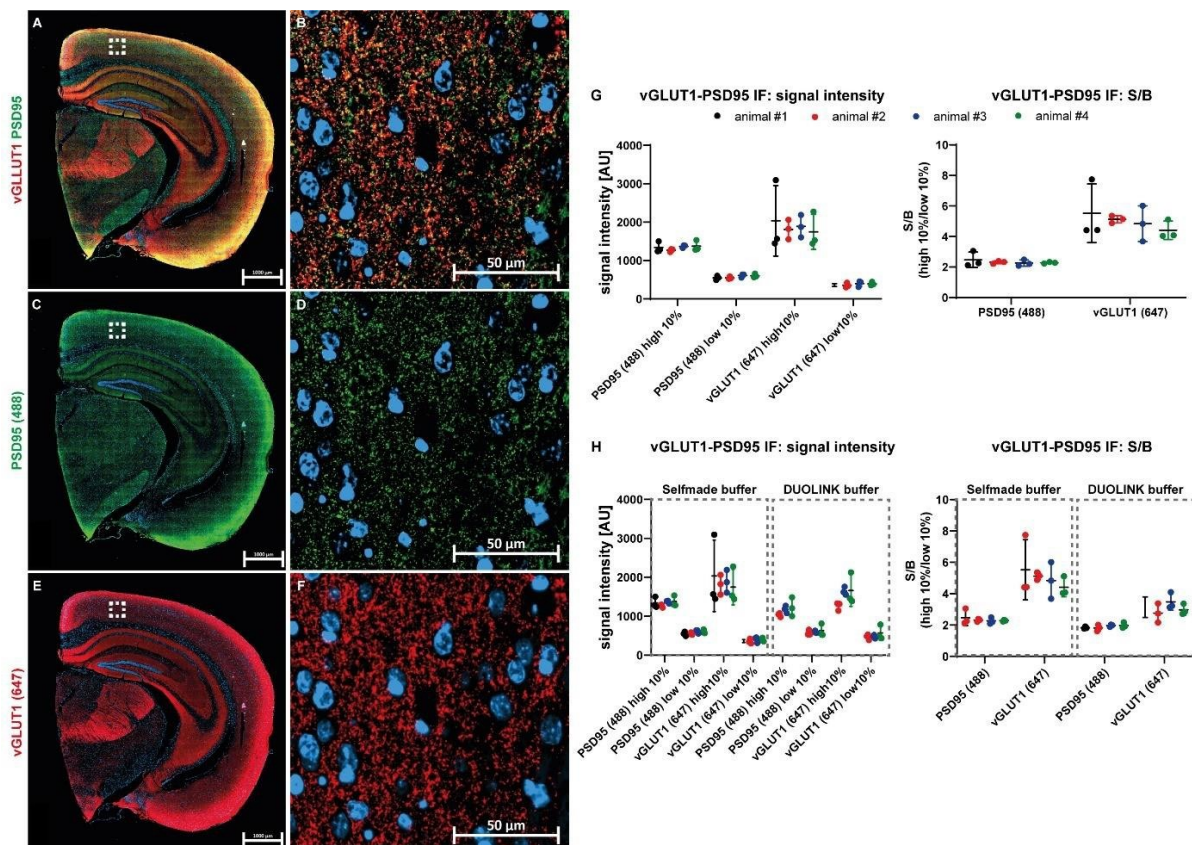
Figure 38: **Representative images of IF double stainings of new glutamatergic synaptic contacts antibody pair vGLUT1 and PSD95.** *IF stainings with both primary antibodies **(A, B)** and single stainings anti-vGLUT1 **(red, E, F)** and anti-PSD95 **(green, C, D)** of a whole brain hemisphere **(A, C, E)** and a higher magnification in the cortex **(B, D, F)**. **(G)** Signal intensity analysis of IF double staining with vGLUT1 and PSD95 in the cortex. The resulting Signal to background (S/B) ratio is calculated by dividing the highest and lowest 10 % of the signal intensities. **(H)** Comparison of the signal intensities and resulting S/B-ratios of IF-stainings with self-made buffer and DUOLINK buffer.*

Next, we tested this new glutamatergic antibody pair regarding its usability for PLA staining. We started with the technical validation (as implemented in 3.2.1.5) by comparing the PLA signal with reactions in which either one (vGLUT1-only; PSD95-only) or both primary antibodies (probes-only) were omitted (Figure 39 A-H). As expected, signals using both primary antibodies in the PLA reaction showed higher signal intensity and favorable S/B ratios compared to the technical negative control conditions (Figure 39 I). In fact, quantification of the puncta confirmed this result showing

significantly higher counts for the PLA reaction with pre- and postsynaptic antibodies in the cortex (Figure 39 J) indicating high sensitivity for the detection of synaptic contacts. Interestingly, omitting PSD95 from the PLA reaction yielded the highest false positive rate whereas basically no signal was observed and quantified when no primary antibodies were used (Figure 39 I-J). We again investigated whether S/B ratios could be further improved by using a self-made instead of the Duolink buffers (Figure 39 A-H). In line with the immunofluorescence staining (Figure 38 H), using Duolink buffers, worsened the overall signal intensity which also translated into a lower puncta count (Figure 39 J).
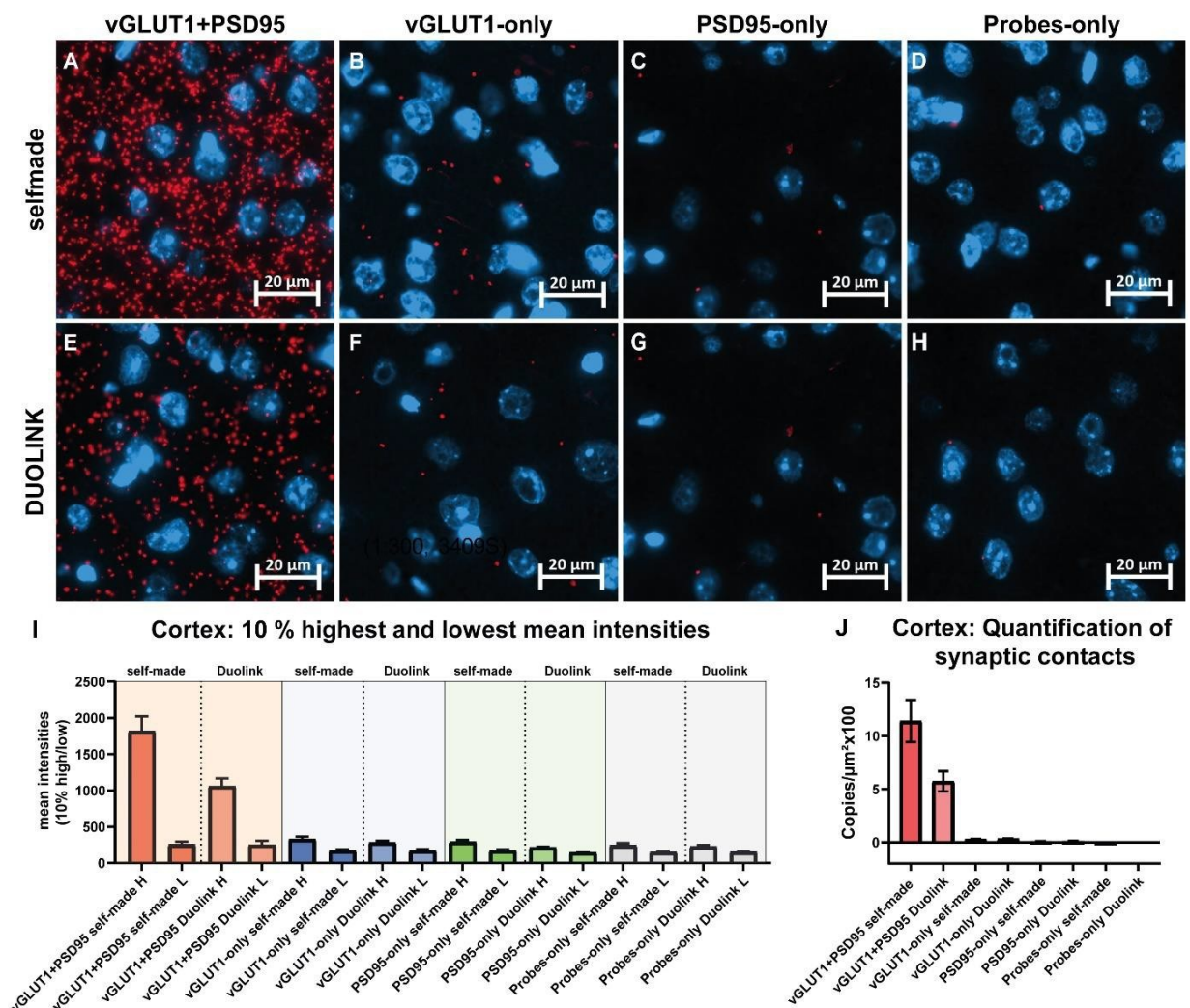

Figure 39: **New antibody pair for the detection of glutamatergic synaptic contacts.** *PLA staining with vGLUT1(+) and PSD95(-)* **(A, E)** *compared to signal with reactions in which only one primary antibody, vGLUT1-only* **(B, F)** *and PSD95-only* **(C, G)**, *or both primary antibodies (probes-only)* **(D, H)** *were omitted with either self-made* **(A-D)** *or Duolink buffer* **(E-H)**. *Evaluation of the 10 % highest and lowest mean intensity values in the cortex of PLA staining* **(I)** *and quantification of PLA signal in the cortex* **(J)** *of the different combinations with self-made or DUOLINK buffer.*

Then we assessed whether there is a difference in coupling the probes to the primary antibodies for the new primary antibodies (similar to 3.2.1.3). We analyzed PLA stainings with vGLUT1 and PSD95 as pre- and post-synaptic markers on FFPE tissue slices of C57BL6/J wt mice. PLA stainings with vGLUT1 coupled to PLUS-probes and PSD95 coupled to MINUS-probes (Figure 40 A) compared to PLA stainings with vGLUT1 coupled to MINUS-probes and PSD95 coupled to PLUS-probes (Figure 40 B) showed a reduction in signal intensity and dot number. To quantify the signal intensity, a Line Profile analysis with Zeiss ZEN 2.3 software was performed. The mean of the 10 % highest and lowest intensity values were plotted. For both probe configurations (+/-) or (-/+), the full PLA with pre- and post-synaptic antibodies (vGLUT1(+/-) and PSD95 (-/+)) showed a superior signal over controls (Figure 40 I, J). Mean intensity values of the highest 10 % of a full PLA stood in contrast to the lowest 10 % of a full PLA and the respective controls vGLUT1-only, PSD95-only, or no primary antibody (probes-only). Intensity values of controls stayed at a baseline level whereas a decrease of mean intensity values.

Next, a quantification of synaptic contacts of full PLAs and respective controls was performed in before annotated areas in the cortex (Figure 40 K-M). HALO analysis confirmed the signal intensity analysis (line profile) in detecting a higher number of copies/µm²x100 in a full PLA condition compared to controls. HALO analysis showed a decrease in the copies/µm²x100 of the controls in the same order as in the line profile analysis (vGLUT1-only < PSD95-only < probes-only). Using the PLUS probe on the pre- and the MINUS probe on the post-synaptic site performed better in terms of signal intensity and copies/µm². The vGLUT1-only control showed the highest rate of false positives (Figure 40 K, L). The probe configuration with PLUS probe on pre- and MINUS probe on post-synaptic site (+/-) gave a larger quantification window and is significantly higher than a (-/+) probe configuration (Figure 40 M, ****p<0.01, two-way ANOVA). Therefore, the vGLUT1-only control of the (+/-) probe configuration was used to calculate a fold change of full PLAs to negative controls. Additionally, the vGLUT1-only control of the (+/-) probe configuration was used as technical control in the following experiments.
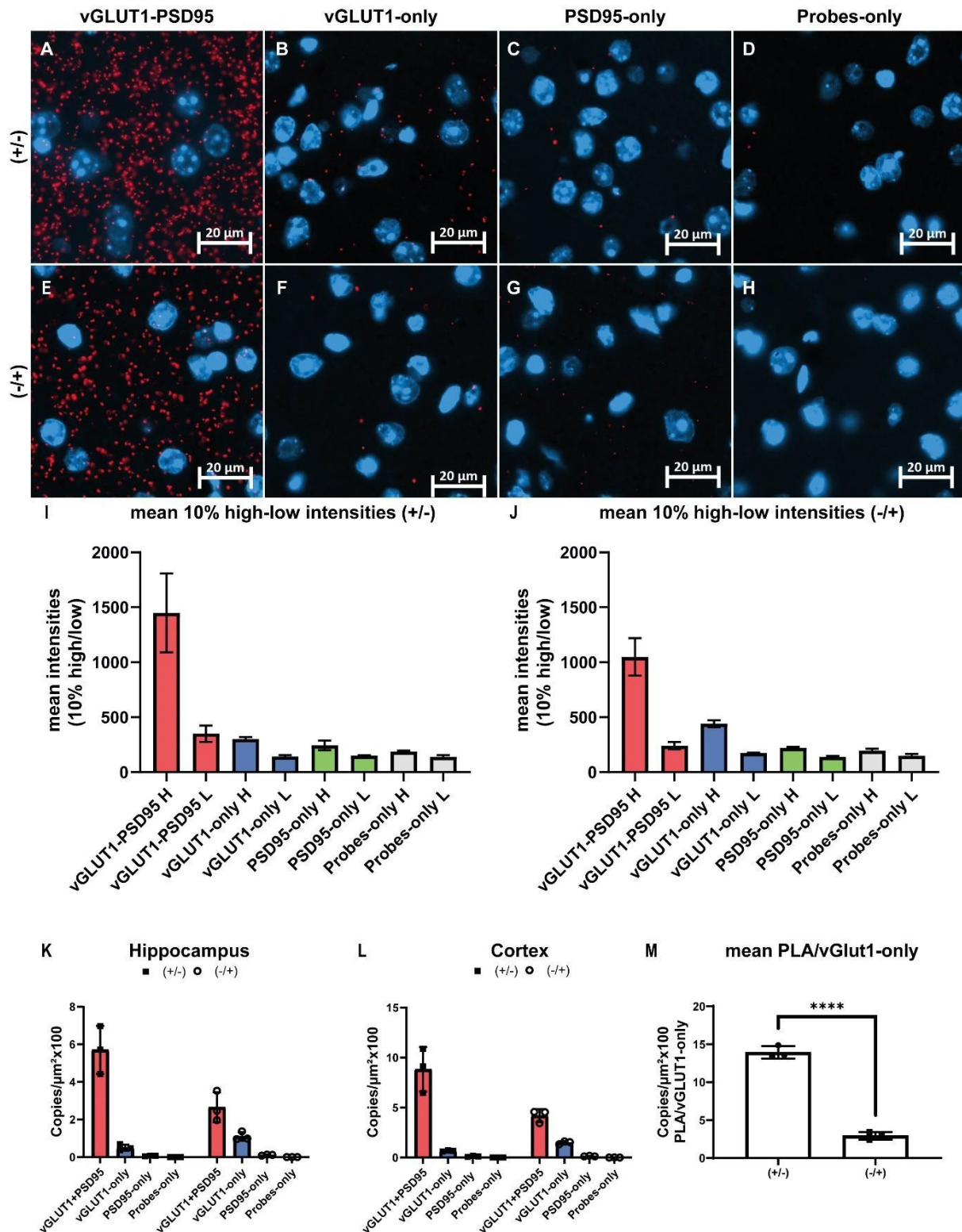
*Figure 40: **Comparison of reverse probe coupling to identify favorable combinations. (A, E)** Full PLA for different vGLUT1 and PSD95 probe couplings and respective controls **(B-D, F-H)** to assess signal intensity and PLA puncta quantities. Comparing the highest and lowest 10 % mean intensity values showed higher signal intensity values for the (+/-) probe coupling **(I)** than for the (-/+) variation **(J)**. A quantification of the PLA copies/µm² x100 in the hippocampus **(K)** and cortex **(L)** also showed higher dot counts for the (+/-) probe coupling, as well as higher dot counts of full PLAs with both primary antibodies used compared to the controls with only one (vGLUT1-only, PSD95-only) or no primary antibody (Probes-only) used. Among controls, the vGLUT1-only control with both probe couplings resulted in the highest number of false positives. Therefore, the vGLUT1-only control of the (+/-) probe configuration was used to calculate the fold change of the full PLA as compared to negative controls (****p<0.0001, Two-way ANOVA) **(M)**.*

3.2.3.6 Synaptic Density in Cortical Layers I to VI in wt Animals

Having confirmed the new antibody pair for glutamatergic synaptic contacts for PLA, we next investigated its biological validity. To reliably analyze pathological changes in synaptic density using PLA, we hypothesized that this assay should be able to identify biologically known differences in synaptic density. Therefore, we took advantage of the reduction in glutamatergic synapses from cortical layer I to VI in healthy brains (Zhou & Roper, 2010; Zhu et al., 2018). Cortical layers in brain sections of C57Bl6/J wt mice (n = 3) were identified using the Allen Brain Atlas (Figure 41 A) (Allen Institute for Brain Science (2011) Allen Mouse Brain Atlas, Mouse, P56, Coronal. Available from mouse.brain-map.org. Allen Brain Institute (2022)). In line with previously reported cortical synaptic density changes (M.-K. Chen et al., 2018; Michiels et al., 2021), we quantified the highest density in cortical layer I with the PLA using antibodies to vGLUT1 and PSD95. A significant reduction of PLA puncta was observed when comparing layer I with all other cortical layers (Figure 41 B; $*p<0.05$ for layer I vs. layer II-III; $**p<0.01$ for layer I vs. layer IV; $***p<0.001$ for layer I vs. layer V; $****p<0.0001$ for layer I vs. layer VI; two-way ANOVA and Fisher's post hoc comparison). These results indicate that PLA can detect changes in synaptic density demonstrating sufficient sensitivity to also analyze pathological alterations in synaptic density.
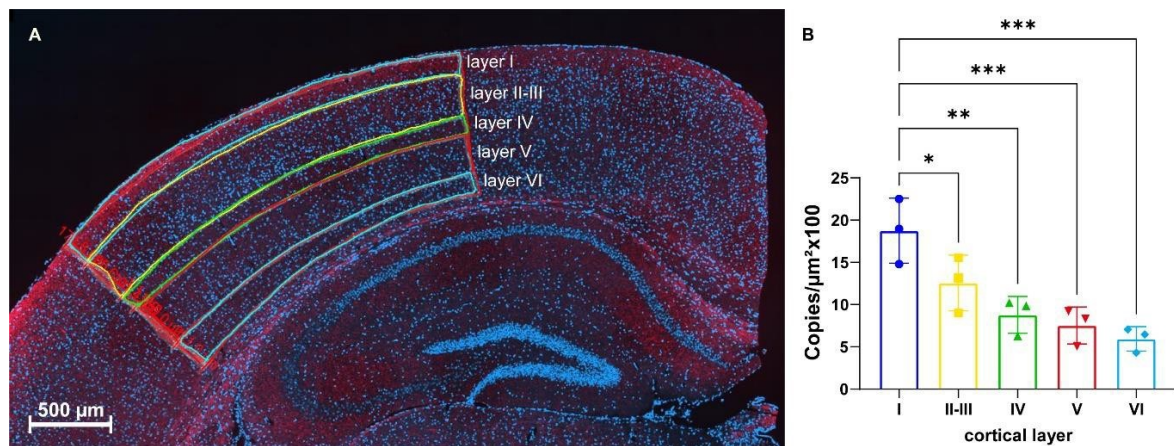

*Figure 41: **PLA quantification in cortical layers I to VI in somatosensory cortex of wt animals**. **(A)** Representative image of the cortex and hippocampus of a wt mouse with annotations drawn of the cortical layers I-VI in the somatosensory cortex. PLA vGLUT1(+) and PSD95(-) staining (red) with DAPI (blue) was performed to quantify the synaptic density in the different layers. Scale bar 500 µm. **(B)** The quantification of the PLA copies/µm²x100 in the single cortical layers of wt mice (n = 3, three sections per animal) showed a decrease in synaptic density from layer to layer (* p<0.05, ** p<0.01, *** p<0.001; Two-way ANOVA and Fisher's post hoc comparison).*

3.3   Density and Distribution of Functional Synapses by PLA in AD Mouse Models

3.3.1   Functional Synapses in Aβ-Transgenic Mouse Model

3.3.1.1   Implementation of Methoxy-X04 to Visualize Aβ-Plaques in Combination With the PLA

The aim of this experiment was to visualize Aβ plaques and synaptic contacts at the same time. Therefore, MethoxyX04 stainings were performed pre and post PLA stainings in APPPS1 mice as a model for AD. For the PLA, we used a combination of vGLUT1(+) (ABN1647) and PSD95(-) (MAB1596). This was done on three sections per animal of 6-month-old APPPS1 mice (n = 3). Whole slide scans (Zeiss Axioscan.Z1) were performed under identical conditions with constant exposure and color map and evaluated optically (Figure 42).
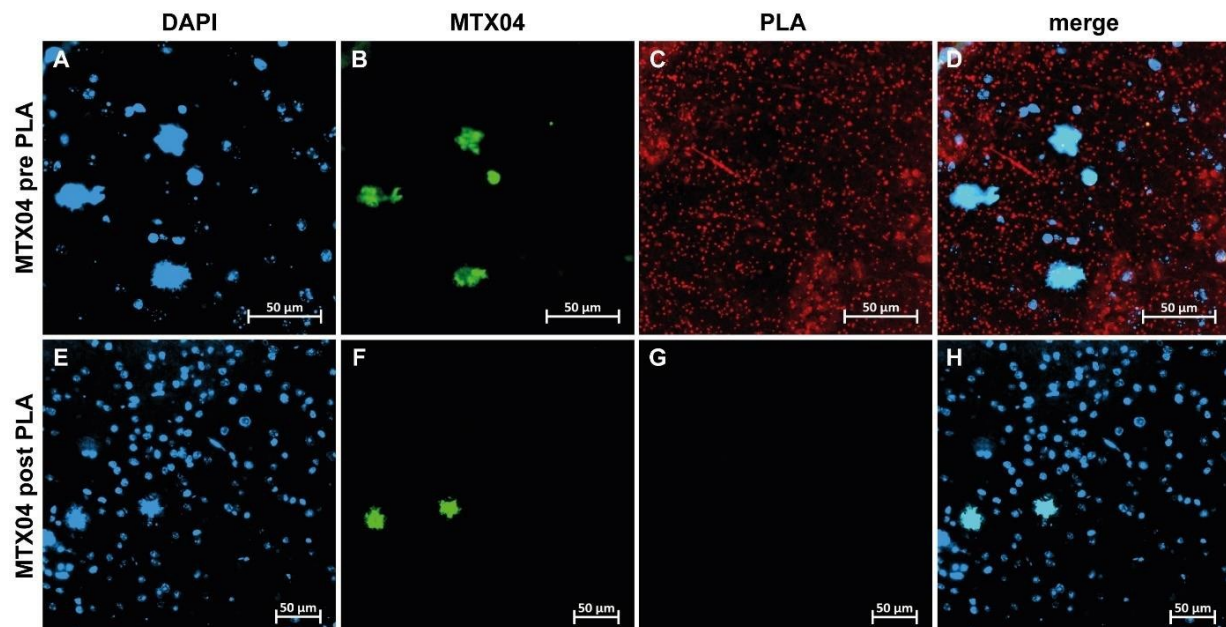

*Figure 42: **MethoxyX04 stainings in the cortex of APPPS1 mice before and after PLA stainings.** Representative images in the cortical layer II-III of the somatosensory cortex of a 6-month-old APPPS1 animal with Methoxy X04 staining pre PLA **(A-D)** and post PLA **(E-H)**. **(A)** DAPI, **(B)** MethoxyX04 (MTX04) stains Aβ plaques, **(C)** PLA staining with vGLUT1(+) and PS95(-) for glutamatergic synaptic contacts, and **(D)** merge. **(E)** DAPI, **(F)** MTX04 staining **(G)** no detection of PLA puncta in 647 channel and **(H)** merge shows that PLA signal gets lost with followed MTX04 staining. Scale bars 50 µm.*

PLA signal was only detectable when MethoxyX04-staining was performed before the PLA staining. In contrast, no signal was observed on slides where MethoxyX04 staining was performed after the PLA. Therefore, in the following experiments, MethoxyX04 co-stainings had to be performed prior to PLA stainings.

3.3.1.2 Plaque Based Analysis in APPPS1 and wt Mice

The goal of this experiment was the analysis of synaptic density in the brain of APPPS1 animals relative to the occurrence of Aβ plaques. Therefore, we processed three animals per genotype (6-month-old C57BL6/J wt and APPPS1). HE-stainings were performed to allocate different brain regions by the help of Allen Brain Atlas and to facilitate slide selection (Allen Institute for Brain Science (2011) Allen Mouse Brain Atlas, Mouse, P56, Coronal. Available from mouse.brain-map.org. Allen Brain Institute (2022)).

In a first attempt, we focused on the area of the cortex and selected randomly 20 plaques per section (Figure 43). Three sections per animal were analyzed. An automatic plaque detection did not work with the HALO software for the 488 channel. Therefore, plaques were analyzed in the DAPI channel (as shown in Figure 43 E, F). With the HALO annotation tool, plaques were encircled. Concentric circles were placed around the plaques with a distance of 5 µm from the plaque edge and then from circle to circle. Ten circles were drawn with a total distance of 50 µm from the plaque edge. Then, the HALO dot count analysis of PLA puncta was performed on APPPS1 animals (n = 2). First, the data were analyzed per section of an individual animal.

When comparing the number of copies per circle, the area of a circle increased, whereas the copies/µm²x100 per circle did not show an effect. Additionally, not all plaques had the same size, so that the circles surrounding the plaques differed in their size (Figure 44 A-F). Therefore, a fold-change of the copies/µm²x100 of the mean values over the plaques per animal was calculated from circle to circle (Figure 44 G+H). No significant difference among means was determined (Figure 44 A-F, $p > 0.05$, Ordinary one-way ANOVA). A moderate non-significant increase could be observed with increasing distance to the plaques, followed by a plateau of copies/µm²x100 of synaptic contacts.
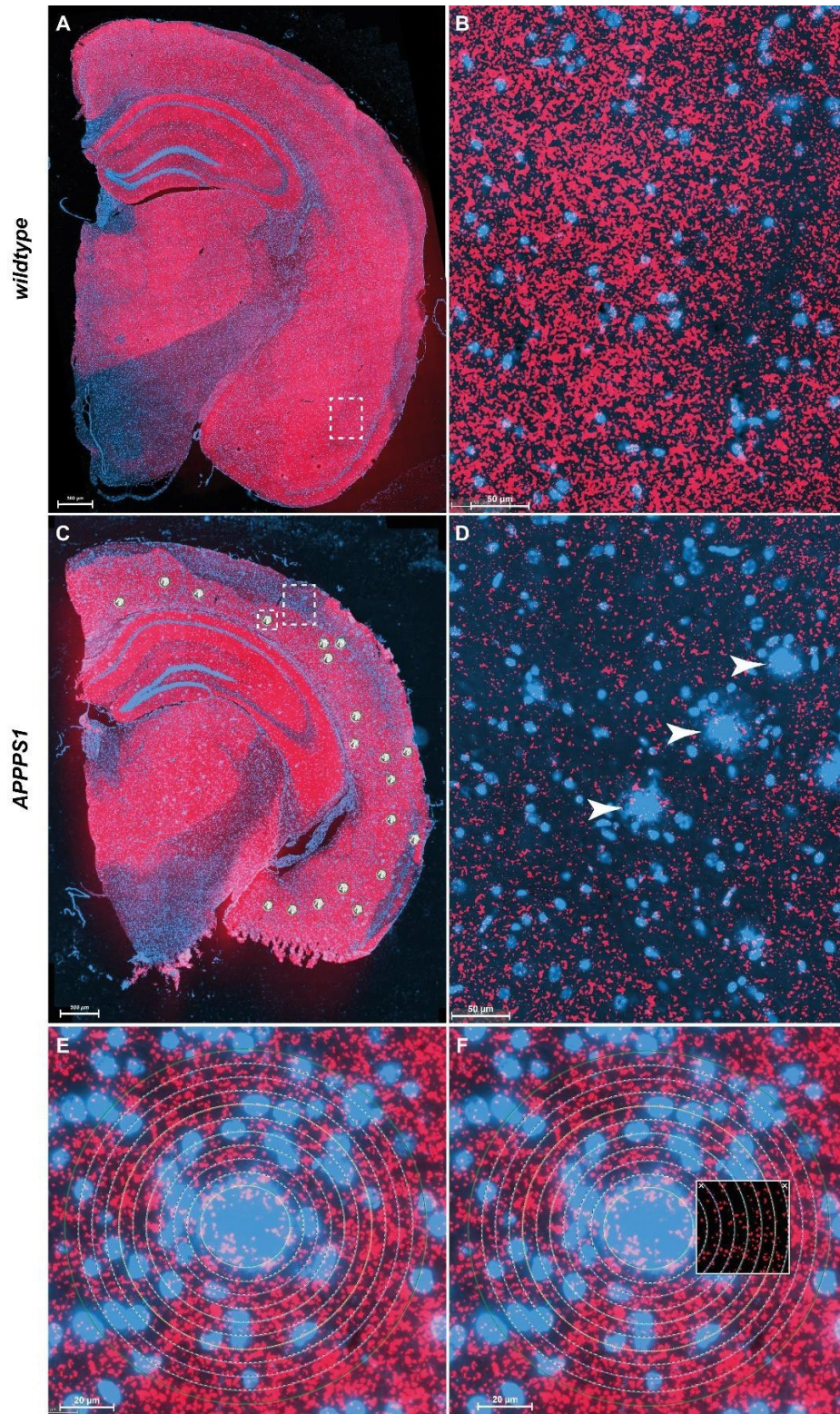
*Figure 43: **Methoxy-X04 staining on 6-month-old APPPS1 and wt animals. (A)** Representative image of a PLA vGLUT1(+) PSD95(-) (red), DAPI (blue) and Methoxy-X04 (MTX) staining of a wt animal. Scale bar 500 µm. **(B)** Higher magnification of rectangle in **(A)** in the area of the entorhinal cortex showing no diffuse plaques. Scale bar 50 µm. **(C)** PLA vGLUT1(+) PSD95(-) (red), DAPI (blue) and MTX (blue) staining of a 6-month-old APPPS1 animal. Scale bar 500 µm. **(D)** Higher magnification of rectangle in **(C)** showing diffuse Aβ plaques (arrow heads) stained with MTX04 in layer II-III of the somatosensory cortex. Scale bar 50 µm. **(E)** Higher magnification of dotted square in (C) of an Aβ plaque in layer V of the somatosensory cortex with concentric circles drawn in the HALO annotation tool. The first circle is placed on the edges of an Aβ plaque. The following circles have a distance of 5 µm until a total distance of 50 µm. Scale bar 20 µm. **(F)** Real-time Tuning window in HALO showed PLA puncta mark-up of detected synaptic contacts. Scale bar 20 µm.*
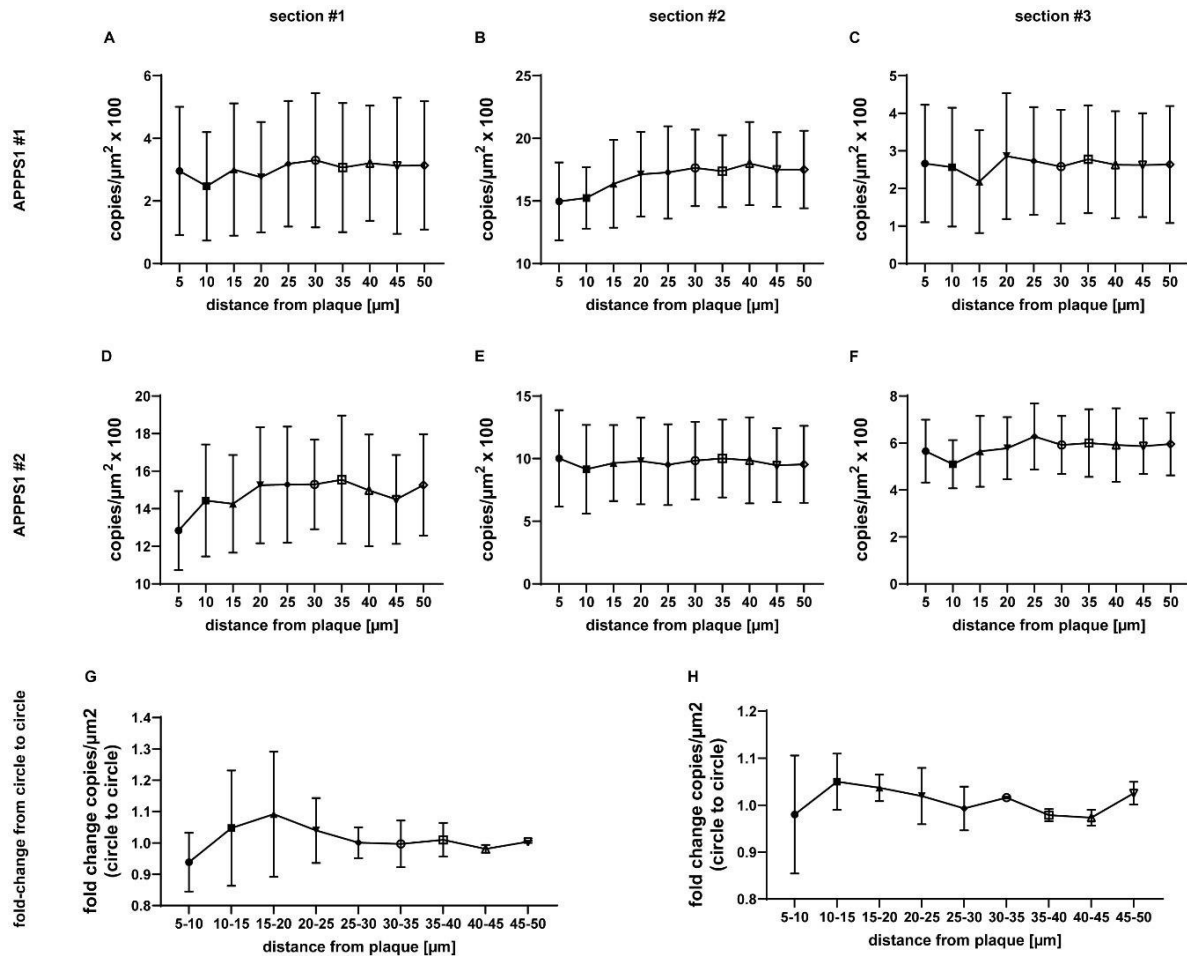
*Figure 44: **Plaque-based analysis in 6-month-old APPPS1 animals. (A)** Copies/µm²x100 in distance to Aβ plaque edge in first section of animal 1 (#1), **(B)** second section and **(C)** third section. The same analysis was performed in animal #2 on three different sections **(D, E, F)** were as well as in animal #1 the plaques differ in size. To overcome this hurdle, a fold-change analysis was performed: Fold-change of copies/µm²x100 from circle to circle of mean of 20 plaques per sections of **(G)** animal #1 and **(H)** animal #2. Here no significant difference could be determined, though a lower numbers of copies/µm²x100 closer to the plaque edge is observed.*

3.3.2 Functional Synapses in Tau-transgenic Mouse Model

Next, we aimed to elucidate tau-derived effects on synaptic density in a tau-transgenic mouse model. TG4510 mice overexpress the frontotemporal dementia-linked P301L tau mutation and have previously been described to show an age-dependent loss of glutamatergic synapses (Kopeikina et al., 2013; Spires-Jones & Knafo, 2011).

The hippocampus and somatosensory cortex of 2-, 6- and 10- months old animals (n = 6 males/age) were analyzed for glutamatergic synaptic density using PLA. rTg(tau P301L)4510 (TG4510) mice are produced by the crossing of a tetO-MAPT*P301L re-sponder line and the activator line Tg(Camk2a-tTA)1Mmay (tA). To exclude additional transgene effects, tA mice served as controls.

3.3.2.1 Application of the PLA to Assess Synaptic Density in the TG4510 AD Mouse Model

In TG4510 animals, an age-dependent synaptic loss has been suggested as compared to tA (Kopeikina et al., 2013). In a first attempt, we aimed to explore if we can reproduce this tau pathology-driven effect with the help of the innovative PLA system.

Therefore, we compared synaptic density in 2- (2m) and 10- (10m)-month-old TG4510 mice and in the control transactivator line CaMKIIα-tTA (tA) mice. We used FFPE-processed 4 µm thick tissue slices of 2-month-old Tg4510 (n = 3, male), 2-month-old tA (n = 3, male) animals, and 10-month-old TG4510 (n = 3, male) animals. PLA staining with pre-and post-synaptic markers vGLUT1(+) (ABN1647) and PSD95(-) (MAB1596) was performed with 4 sections per animal with an intersectional distance of 50 µm. Technical controls were performed with vGLUT1-only on 3 sections per animal. Slides were selected by the help of HE-stainings which were selected on Allen Brain Atlas position 75 (Allen Institute for Brain Science (2011) Allen Mouse Brain Atlas, Mouse, P56, Coronal. Available from mouse.brain-map.org. Allen Brain Institute (2022)), to ensure a similar coronal plane.

PLA staining for glutamatergic synaptic contacts resulted in a lower number of synaptic contacts in 10-month-old as compared to 2-month-old TG4510 animals in all analyzed areas including the isocortex, somatosensory cortex (Figure 45), hippocampus and entorhinal cortex (Figure 46). However, a significant decrease in synaptic numbers was only seen in the somatosensory and entorhinal cortex (Figure 46 B-D, *$p<0.05$, one-way ANOVA followed by Dunnett's multiple comparison test). Interestingly, 2-month-old Tg4510 animals showed higher numbers of synaptic contacts than age-matched control animals (tA) in all areas analyzed (Figure 46). Like before, a high intersectional variability of the PLA signal was observed among animals.
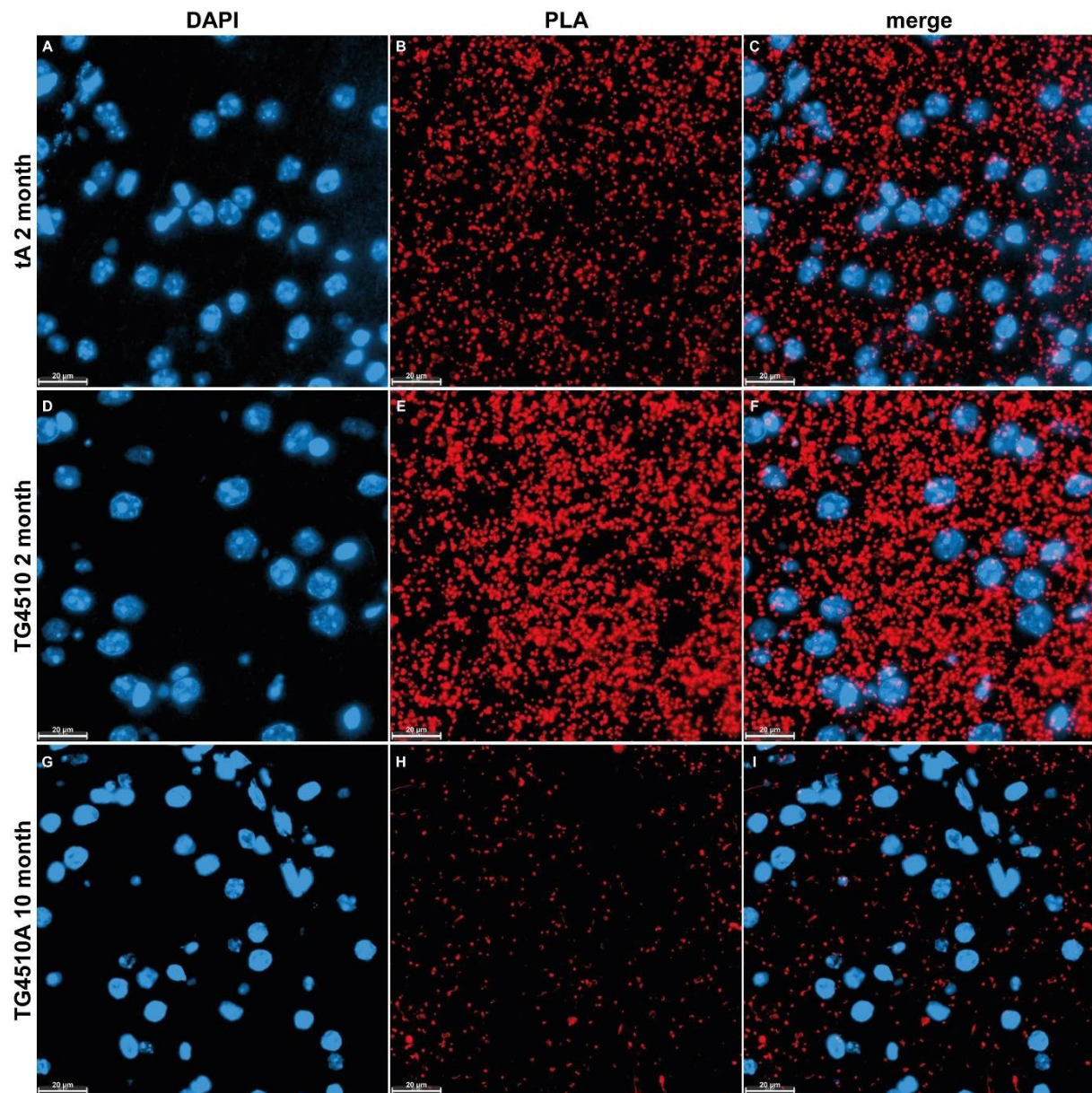
Figure 45: **PLA vGLUT1(+) PSD95(-) on 2-month-old CaMKIIα-tTA (tA) and TG4510 compared to 10-month-old TG4510 animals**. *Representative images all taken in layer II-III of the somatosensory cortex.* **(A)** *DAPI,* **(B)** *PLA vGLUT1(+) PSD95(-) puncta and* **(C)** *merge of a representative image of a 2-month-old tA animal. Compared to an age matched TG4510 animal:* **(D)** *DAPI,* **(E)** *PLA and* **(F)** *merge.* **(G)** *DAPI,* **(H)** *PLA and* **(I)** *merged of a of 10-month-old TG4510 animal showed a greatly reduced PLA signal and dot count. Scale bars 20 µm.*
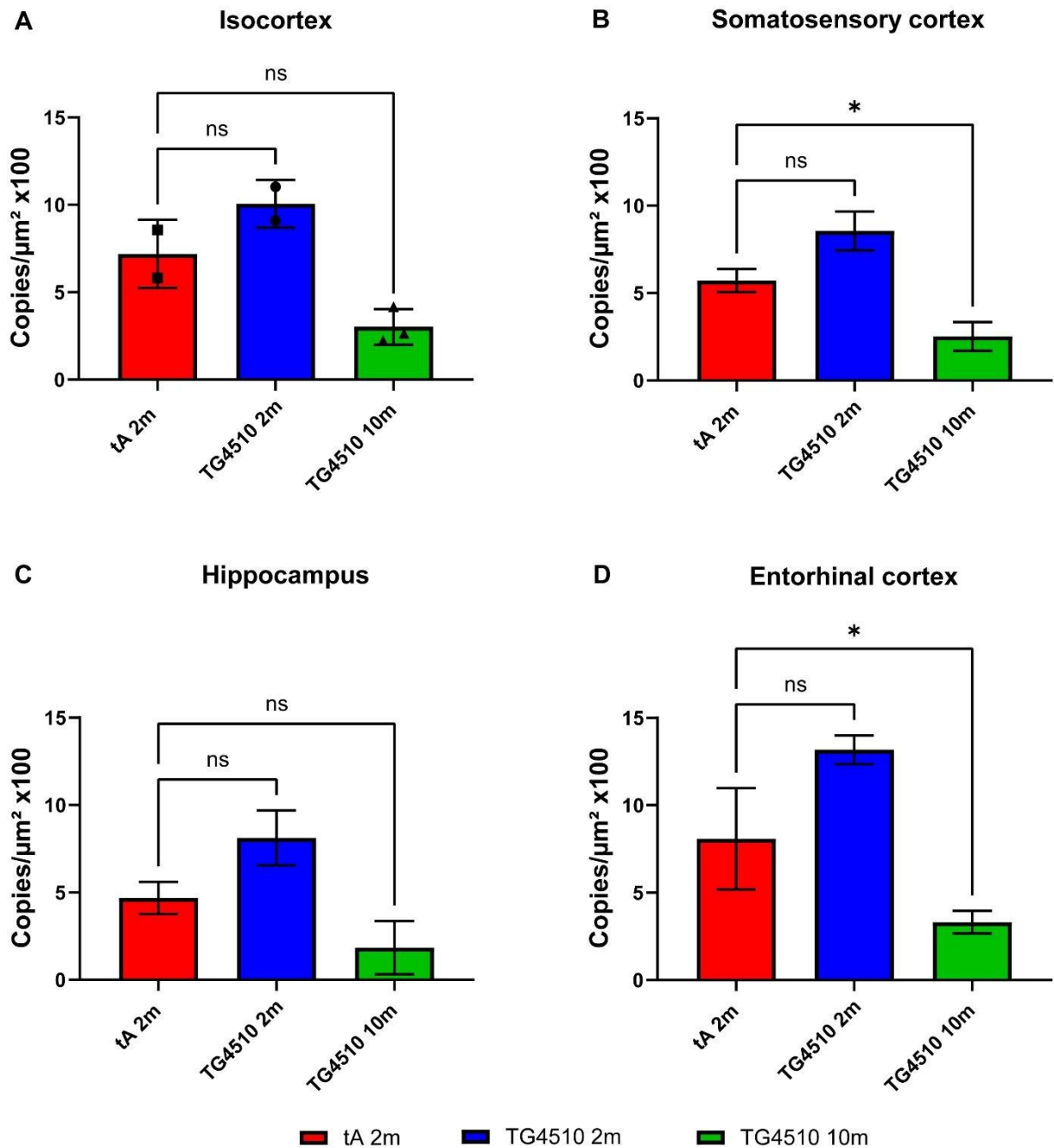
*Figure 46: **Comparison of PLA vGLUT1(+) PSD95(-) copies/µm²x100 in of 2-month-old tA and TG4510 and 10-month-old TG4510 in different brain areas.** The comparison of the means of the different animals in the areas of the **(A)** isocortex, **(B)** somatosensory cortex, **(C)** hippocampus and **(D)** entorhinal cortex show a high variability in 2-month-old animals. A reduction in synaptic density comparing 2- and 10-month-old TG4510 animals can be observed in all regions.*

3.3.2.2 Quantification of Age-dependent Synaptic Density in Transgenic TG4510 and Age-matched Control tA Animals

Due to the observation of an age-dependent synaptic loss in tau-transgenic mice, while young Tg4510 animals showed an unexpected increased synaptic density at an age of 2 months as compared to controls, we aimed to perform a more in-depth analysis

by adding further timepoints, increasing the number of animals, and by controlling the observed effects by the help of respective age-matched controls.
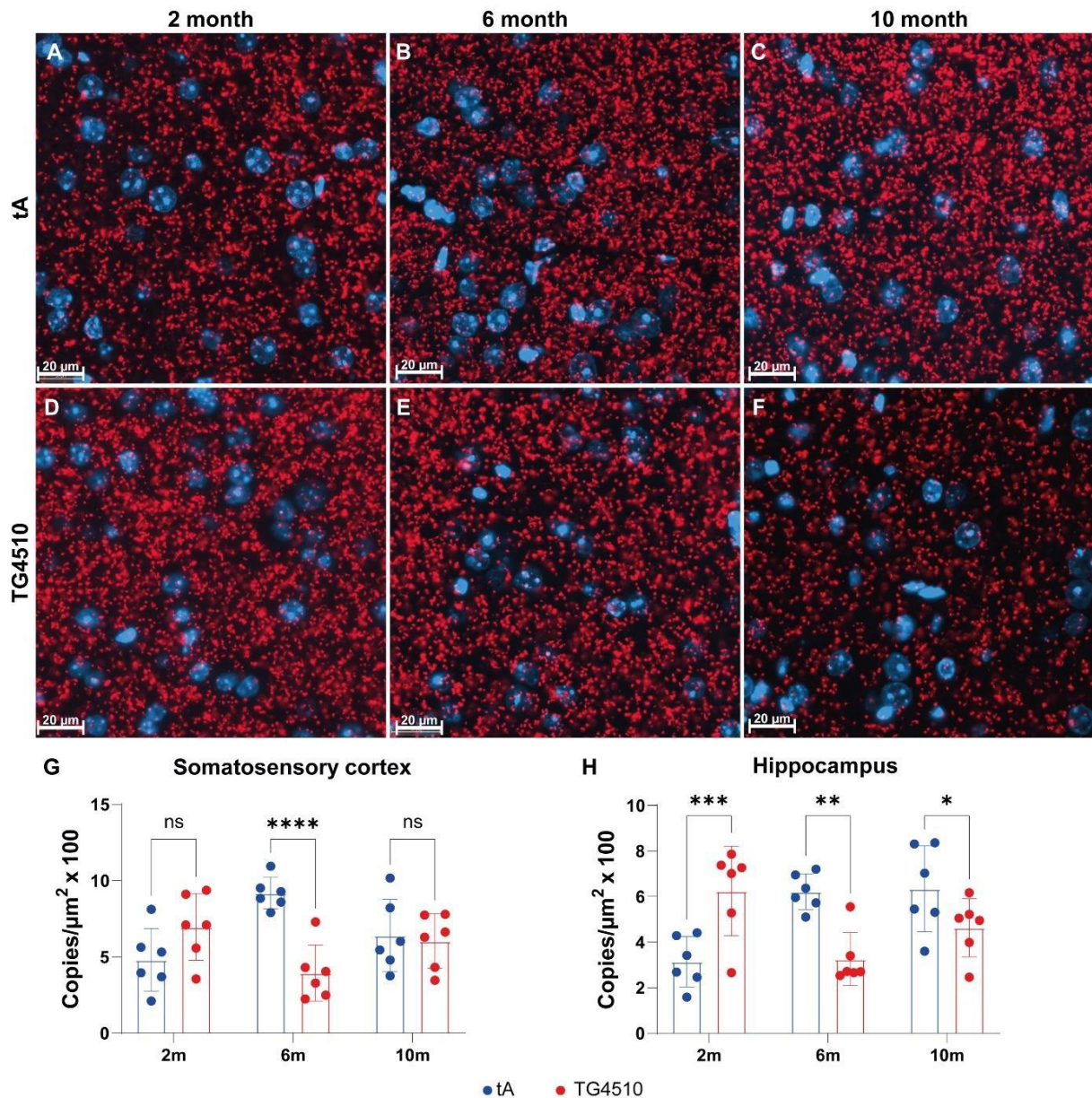

*Figure 47: **Age-dependent PLA puncta quantification in large ROIs.** Representative images in layer II-III of the somatosensory cortex of TG4510 and tA animals at 2-, 6- and 10-months of age **(A-F). (G)** In the hippocampus, a significant increase in synaptic density was observed in 2-month-old TG4510 mice compared to age-matched tA controls (***p<0.001, Two-way ANOVA followed by post-hoc Tukey's multiple comparison). A reduction was observed in 6- and 10- month-old Tg4510 animals compared to age-matched tA animals. **(H)** In the somatosensory cortex, only a significant reduction was observed in 6-month-old TG5610 animals compared to age-matched tA controls (***p<0.001, Two-way ANOVA followed by post-hoc Tukey's multiple comparison).*

The hippocampus and somatosensory cortex of 2-, 6- and 10- months old Tg4510 and tA animals (n = 6 male/age) were analyzed for glutamatergic synaptic density using the PLA. To ensure analysis of similar brain levels, tissue sections were chosen based on the Allen Brain Atlas (Allen Institute for Brain Science (2011) Allen Mouse Brain

Atlas, Mouse, P56, Coronal. Available from mouse.brain-map.org. Allen Brain Institute (2022)).

PLA with vGLUT1(+) (135307) and PSD95(-) (3409S) optically revealed no clear age-dependent synaptic loss in TG4510 compared to tA animals (Figure 47 A-F). Quantification of PLA puncta in 2-month-old TG4510 compared to tA animals confirmed the initial upregulation of synaptic density in the somatosensory cortex and hippocampus for tau-transgenic mice (Figure 47 G-H). This was again followed by a strong decrease in older TG4510 mice. As compared to age-matched controls this effect was most pronounced in 6-months old mice for both brain areas analyzed (Figure 47 G-H). At 10 months age, decrease in synaptic density was only significant in the hippocampus area (Figure 47 H, *$p<0.05$, two-way ANOVA and Fisher's post hoc comparison).

3.3.2.3 Age-dependent Quantification of Synaptic Density in Cortical Layers in tA and TG4510 Animals

To finally perform a more detailed analysis of locoregional changes in synaptic density at different timepoints, we analyzed age-dependent synaptic loss in cortical layers. We performed a cortical layer analysis on the same data set as in 3.3.2.2, since a decrease of vGLUT1 and PSD95 from layer I to VI was reported before (Zhou & Roper, 2010; Zhu et al., 2018). In line with wildtype animals (Figure 41 in 3.2.3.6), quantification of PLA puncta in tA animals indicated that the highest synaptic density is found in cortical layer I of all ages and a significant reduction comparing layer I to all other layers was observed (Figure 48 A-C, ****$p<0.0001$,***$p<0.001$, **$p<0.01$, *$p<0.05$, two-way ANOVA followed by Tukey's multiple comparisons test). In contrast, a significant reduction of layer I compared to all other layers was only observed for 2- and 6-month-old TG4510 animals (Figure 48 A-C, ####$p<0.0001$, two-way ANOVA followed by Tukey's multiple comparisons test), but not for 10-month-old animals. 6-month-old TG4510 animals showed a reduction in synaptic density in layer I to V compared to age-matched tA controls (Figure 48 B, TG4510 layer I vs tA layer I, ****$p<0.0001$; TG4510 layer II-III vs. tA layer II-III, ***$p<0.001$; TG4510 layer IV vs. tA layer IV, **$p<0.01$; TG4510 layer V vs. tA layer V, *$p<0.05$; Two-way ANOVA followed by Tukey's multiple comparisons test). 10-month-old TG4510 animals showed a reduction in synaptic density only in layer I compared to age-matched tA controls (Figure 48 C,

TG4510 layer I vs tA layer I, ****p<0.0001 Two-way ANOVA followed by Tukey's multiple comparisons test). The highest reduction was observed in layer I of TG4510 animals with a significant reduction of 2-month-old animals compared to 6-month-old animals (Figure 48 D, ***p<0.001, Two-way ANOVA followed by Tukey's multiple comparisons test) and 2-month-old animals compared to 10-month old animals (Figure 48 D, ****p<0.0001, Two-way ANOVA followed by Tukey's multiple comparisons test). In age-matched tA control animals, a significant increase in synaptic density from 2-month of age to 6-month of age was observed (Figure 48 D, **p<0.01, Two-way ANOVA followed by Tukey's multiple comparisons test).

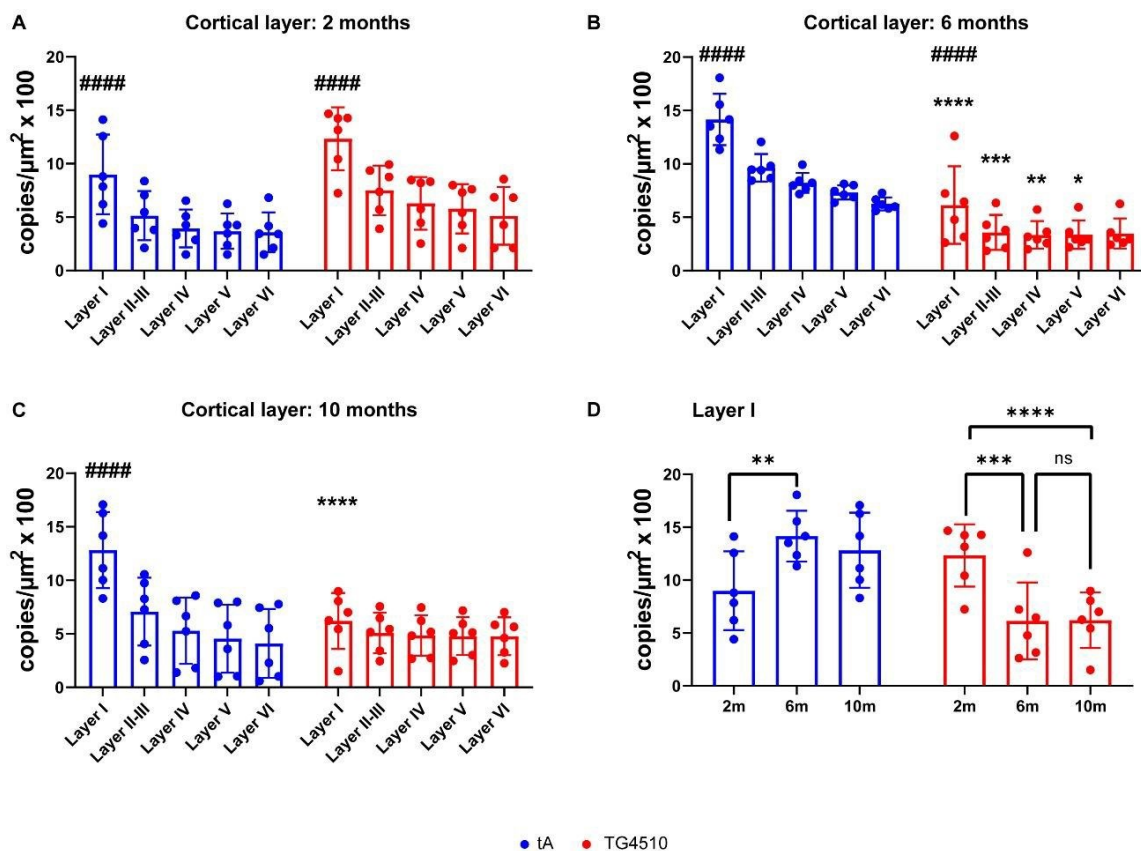*Figure 48: **Age-dependent cortical layer analysis in tA vs TG4510 animals. (A)** Cortical layer analysis in 2-month-old animals shows no age-dependent effects. **(B)** Cortical layer analysis in 6-month-old animals shows age-dependent effects in TG4510 mice in layer I to V compared to tA animals. **(C)** Cortical layer analysis in 10-month-old-animals shows extreme significance in the difference between tA and Tg4510 animals in layer I. **(D)** PLA puncta quantification in cortical layer I of tA vs TG4510 animals shows age-dependent effect in layer I in TG4510 animals. 2way ANOVA followed by post-hoc Tukey's multiple comparison for layer I vs all other layers: ####p<0.0001; 2way ANOVA followed by post-hoc Tukey's multiple comparison within a group (2m vs. 6m, 2m vs. 10m, 6m vs. 10; tA vs. TG4510): ****p<0.0001, ***p<0.001, **p<0.01, *p<0.05, nsp>0.05.*

3.3.2.4 Power Analysis for Sample Size Calculation for Future Studies

The generated data of the quantification of synaptic density in the cortical layers of tA and TG4510 mice of the pilot study (3.3.2.3) was used for a power analysis to calculate

the sample size for future studies and potential compound effects[4]. The data were analyzed in age-dependent groups of 2-, 6, and 10-month-old tA and TG4510 (n = 6, male per group). Future studies are planned for PLA analysis in 6-month-old mice since in this age-group the highest probability to observe an effect in a treated group is expected. Using the pilot data in layers I and II-III, we calculated an effect size of 6-month-old TG4510 compared to tA animals (Figure 49). For a hypothetical treated group of TG4510, scenarios of mean levels of synaptic density measured with PLA were assumed to increase 20 %, 40 %, and 60 % compared to tA mice group. Variability was assumed to be the same as in pilot study for untreated TG4510 and tA mice as well as for the hypotheticalyl treated TG4510 group. Power analyses were conducted assuming the use of same gender (male) in the future studies.
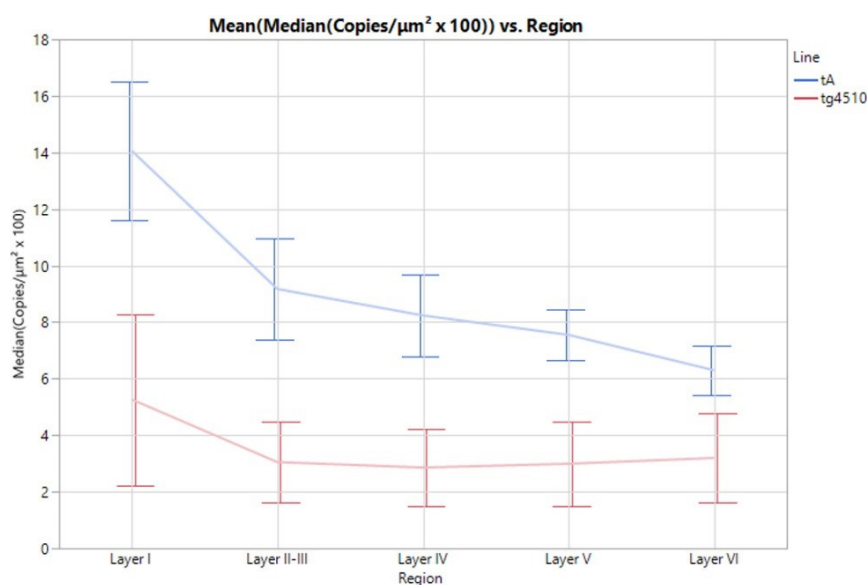

*Figure 49: **Mean of Median Copies/µm²x100 for 6-month-old tA and TG4510 animals.** Data from pilot study of PLA quantification of synaptic density in cortical layers I to VI of 6-month-old tA (blue line) and TG4510 (red line) animals.*

Table 3-3: Assumed effect sizes of 6-month-old TG4510 mice in cortical layers I and II-III

INCREASE OF SYNAPTIC DENSITY IN TREATED TG4510 GROUP	MOUSE LINE	ROI	ASSUMED EFFECT SIZE
20 %	TG4510	Layer I	2.556
40 %	TG4510	Layer I	2.208
60 %	TG4510	Layer I	1.861
20 %	TG4510	Layer II-III	3.107
40 %	TG4510	Layer II-III	2.763
60 %	TG4510	Layer II-III	2.419

---

[4] The analysis was performed by statistician Yulia Mordashova and calculated as described in 2.2.7.4.

For layer I, we assumed that the calculated effect size is based on the data from the pilot study (Figure 49 and Table 3-3). Used was a two-sided t-test with adjusted alpha significance level. Required power was assumed to be 80 % and a two-sided significance level of 0.025 was taken. With these assumptions, a sample size of 7 animals will be required to show an increase of 60 % in synaptic density level in treated TG4510 animals compared to tA animals (effect size 1.861, see Table 3-4).
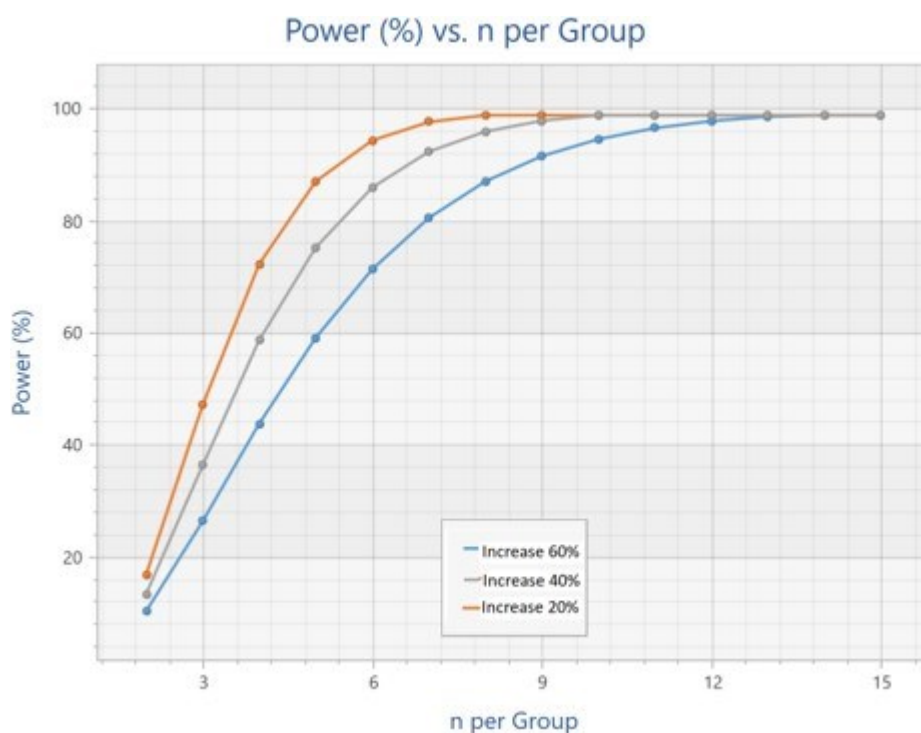

*Figure 50: **Power analysis for layer I.** An increase in synaptic density level measured with PLA with an assumed effect size (Power) and the required sample size (n per group).*

Table 3-4: Effect size in layer I

INCREASING SYNAPTIC DENSITY LEVEL IN TREATED TG4510 IN LAYER I	REQUIRED SAMPLE SIZE
20 %	5
40 %	6
60 %	7

For layer II-III, the following assumptions were made to calculate the sample size in treated TG4510 mice: The effect size was calculated based on the data from the pilot study (Figure 49). A power of 80 % was required and a two-sided significance level of 0.025 was taken. These assumptions led to a result of a sample size of 5 animals to detect an increase of 60 % in synaptic density in treated TG4510 compared to tA group (effect size 2.419, see Table 3-5).
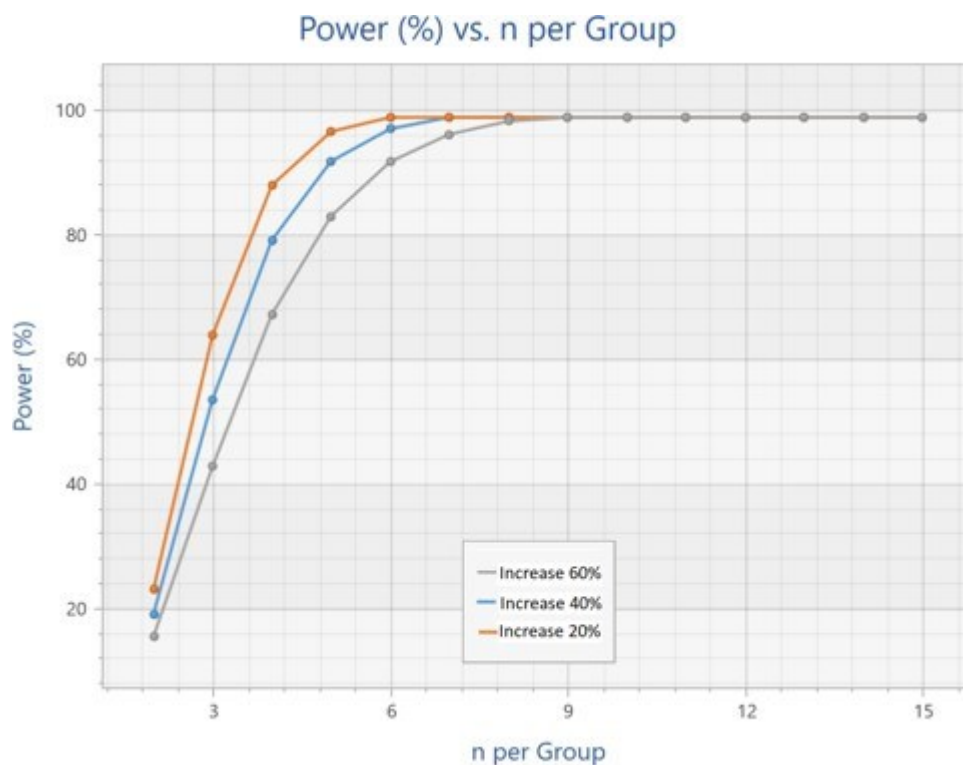
Figure 51: **Power analysis for layer II-III.** An increase in synaptic density level measured with PLA with an assumed effect size (Power) and the required sample size (n per group).

Table 3-5: Effect size in layer II-III

INCREASING SYNAPTIC DENSITY LEVEL IN TREATED TG4510 IN LAYER II-III	REQUIRED SAMPLE SIZE
20 %	4
40 %	4
60 %	5

Important to state is, that the variability of the treated group may not be the same as assumed according to different scenarios. This calculation doesn't take in account potential dropouts. And the sample size required for each group is accounted for one gender (male).

3.4 Application of PLA after TMT-induced Neurotoxic Injury

To finally monitor changes in synaptic density upon a neurotoxic insult, the PLA was used in TMT-treated mice. The study was designed as described in 2.2.8 using a control group and two different TMT doses.

3.4.1 Clinical Symptoms and Histological Evaluation of Mice after TMT-Induced Neurotoxicity

Clinical observations were performed at different timepoints and showed anomalies on day 2 (48 h post TMT treatment), where mice of group 9 were found being lethargic. On day 10 post TMT before necropsy, we observed skin lesions on mouse #27 of group 9.

For histology, mouse brains were processed as described in 2.2.4.1. To ensure analysis of similar brain levels of the hippocampal layers in brain sections of wt mice, respective HE-stained slides were identified using the Allen Brain Atlas (Allen Institute for Brain Science (2011) Allen Mouse Brain Atlas, Mouse, P56, Coronal. Available from mouse.brain-map.org. Allen Brain Institute (2022)). Histopathological analyses were performed on HE-stained tissue slices of animals 24 h, 72 h and 10 days post TMT treatment. Whole slide scans (P1000, Plan-Apochromat 40x, 1.6x on DAPI) were assessed under identical conditions with constant exposure and color map. Histological findings showed no significant changes of control or TMT-treated animals under low magnification (not shown). Under high magnification, TMT-treated mice show single cell necrosis in CA1 region of the hippocampus (Figure 52 B, C, E, F). Eosinic cytoplasm, nuclear pyknosis and nuclear karyolysis were found in the CA1 and gyrus dentatus of TMT-treated mice after 24 h and 72 h post TMT application. Lesions were recovered in TMT-treated animals after 10 days (Figure 52 H, I). In control mice, no anomalies were observed (Figure 52 A, D, G).
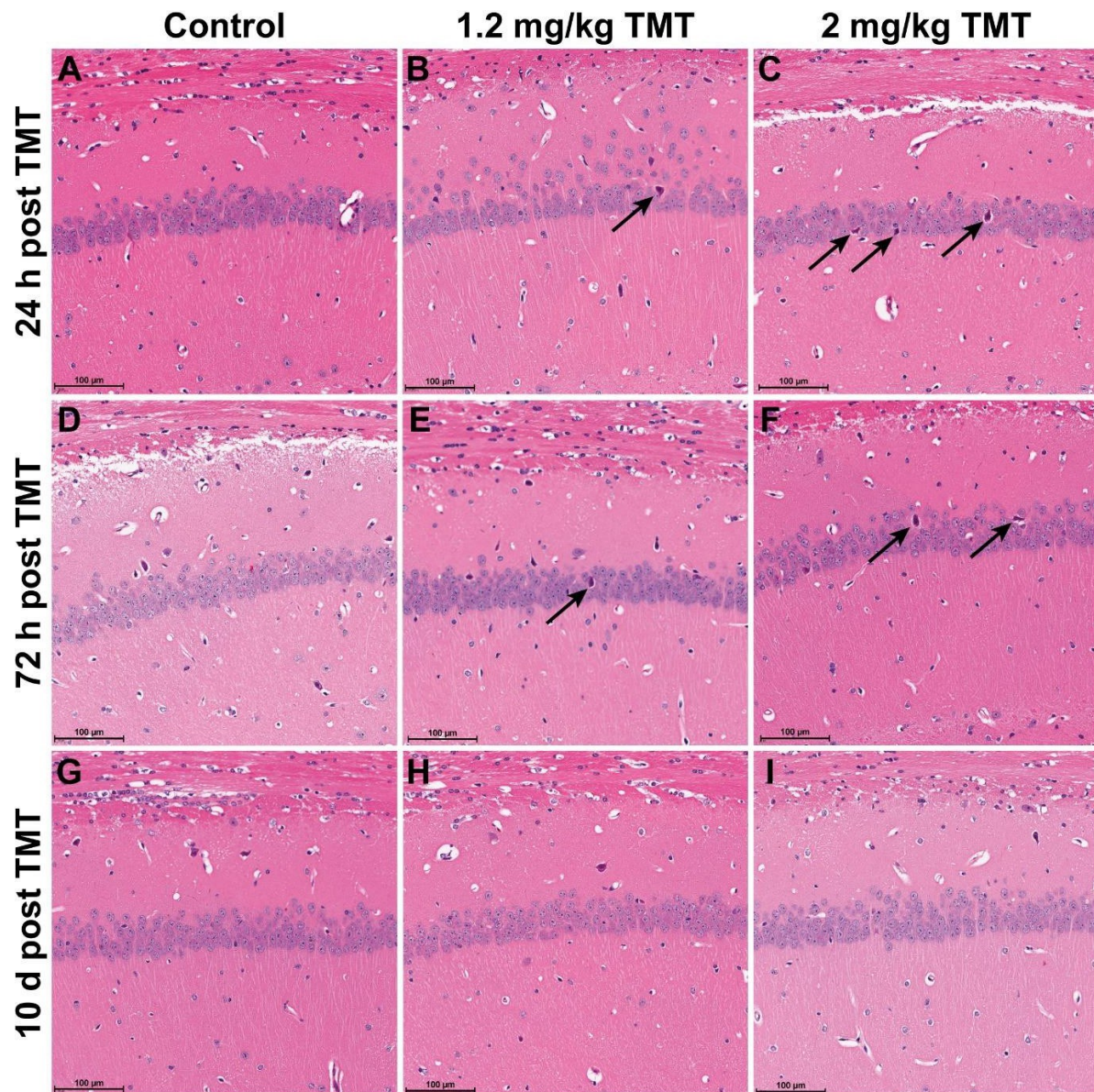
*Figure 52: **Histopathological analysis was performed using HE-staining at 24 h, 72 h and 10 days post TMT treatment.** Representative images with high magnification taken in the CA1 region of the hippocampus. Single cell necrosis (arrows) was observed in TMT treated animals after 24 h and 72 h post TMT **(B, C, E, F)**. A recovery was observed in TMT treated animals after 10 days **(H, I)**.*

3.4.2 Evaluation of Synaptic Density with PLA after TMT-Induced Neurotoxicity

Based on reported effects of TMT on glutamatergic neurons (Sandström et al., 2019), we performed a PLA staining with vGLUT1 (135 307) and PSD95 (3409S). Whole slide scans (Zeiss Axioscan.Z1) were assessed under identical conditions with constant exposure and color map. With the help of the Allen Brain Atlas (Allen Institute for Brain Science (2011) Allen Mouse Brain Atlas, Mouse, P56, Coronal. Available from mouse.brain-map.org. Allen Brain Institute (2022)), annotations were drawn with HALO in the hippocampus and subregions for a detailed analysis of the brain areas affected

by TMT injury. Optically, no synaptic loss in PLA puncta was observed in TMT-treated animals or over time (Figure 53). Analysis of PLA copies/µm²x100 showed in the area of the HC an unexpected increase in synaptic density over time.

A significant increase in synaptic density was observed in TMT-treated animals 72 h post medication as compared to controls (Supplementary Figure 1 A, dose group 1.2 mg/kg, *p<0.05; dose group 2 mg/kg, **p<0.01, two-way ANOVA followed by post-hoc Dunnett's test). 10 days post TMT treatment differences between the study groups disappeared (Supplementary Figure 1 A).
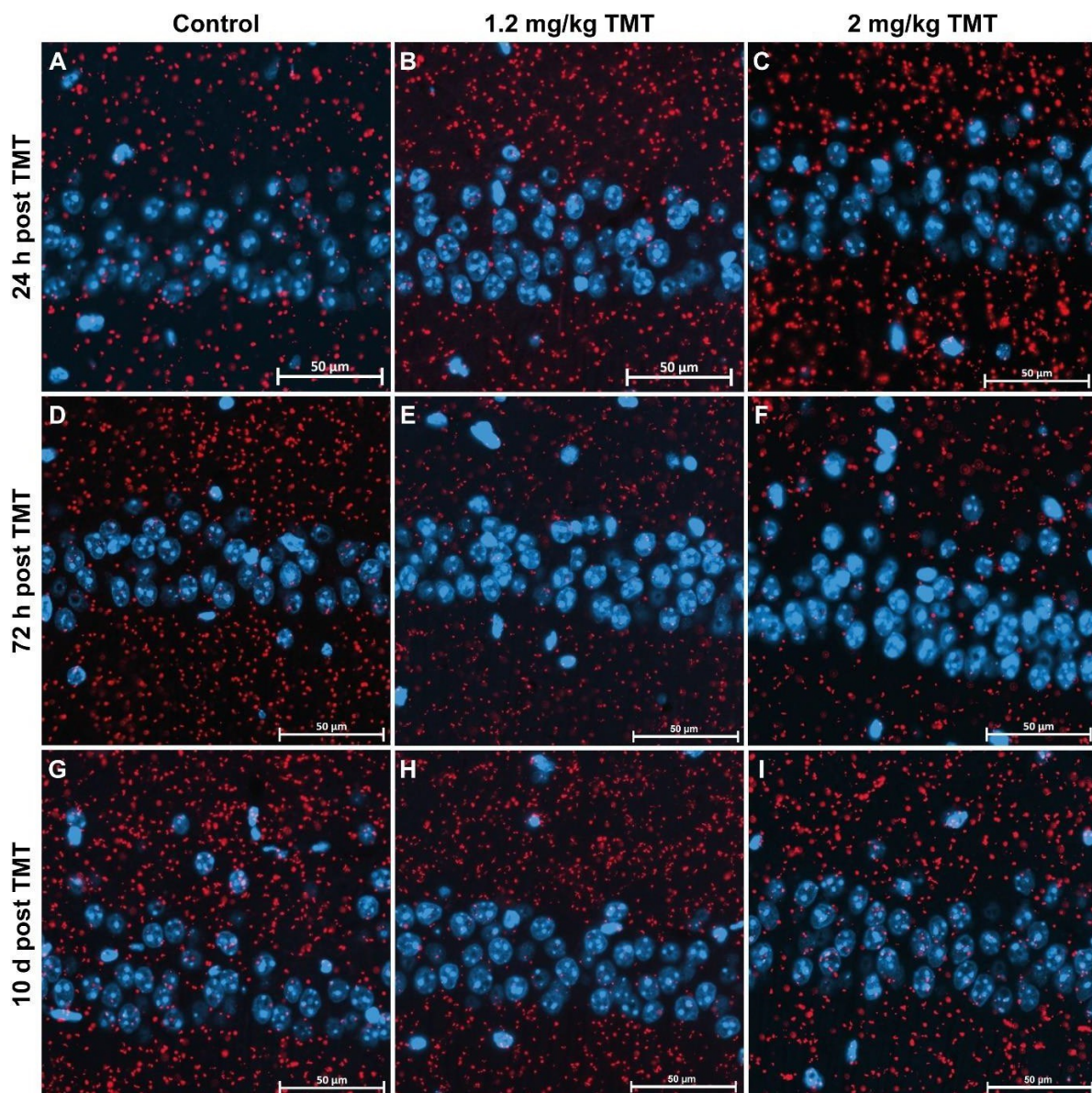
Figure 53: **Quantification of synaptic density with PLA vGLUT1(+) PSD95(-) of control and TMT-treated mice.** *Representative images with high magnification in the hippocampal CA1 region at 24 h* **(A, B, C),** *72 h* **(D, E, F)** *and 10 days* **(G, H, I)** *after TMT application. Control mice* **(A, D, G)** *vs. animals treated with 1.2 mg/kg TMT* **(B, E, H)** *and 2 mg/kg TMT* **(C, F, I)** *show optically no differences in the CA1 region.*

When looking more detailed at the subregions of the hippocampus, at 72 h we found a significant increase of the synaptic density in the CA1, CA2, and CA3 region for the higher dose group only (Supplementary Figure 1 B-D, *p<0.05, **p<0.01, and ***p<0.001, respectively, two-way ANOVA followed by post-hoc Dunnett's test) which disappeared at 10 days post treatment. For the lower dose group, a significant increase of the synaptic density was only determined at 10 days post treatment for the CA2 and CA3 subregions (**p<0.01, two-way ANOVA followed by post-hoc Dunnett's test).

In the stratum oriens of the CA1 subgroup, PLA puncta quantification for glutamatergic synaptic density, showed no significant difference between the different dose groups 24 h and 10 days post TMT treatment. However, at 72 h post TMT injection, a significant difference was observed between the control (G1) and 2 mg/kg (G3) dose group (Figure 54 A, *p<0.05, two-way ANOVA followed by post-hoc Dunnett's test), which was not the case for the 1.2 mg/kg TMT treatment group.

As for the pyramidal layer, stratum radiatum, and the stratum lacunosum-moleculare of CA1, a significant increase in the synaptic density was observed for both treatment groups at 72 h exclusively (Figure 54 B-D). At 24 h and 10 days post treatment no differences were observed among the study groups.

In the stratum oriens, pyramidal layer, stratum radiatum and the stratum lacunosum-moleculare of the CA2 subregion, a significant increase in synaptic density was observed at 72 h in the high dose group only (Supplementary Figure 2 A-D) while for the lower dose a delayed significant increase 10 days post treatment was detected for the stratum oriens, and the pyramidal layer (Supplementary Figure 2 C-D).

Regarding the different layers of the CA3 region of the HC, we observed similar changes, which consisted of a significant increase in the synaptic density at 72 h in all layers in the high dose group only (Supplementary Figure 3 A-D). For the low dose group, only in the stratum oriens significantly increased numbers of puncta-like stainings were found 10 days after TMT treatment (Supplementary Figure 3 A).

As for the GD region and its sublayers, again a significant increase of synaptic density was only found for the high dose treatment and only at 72 h post medication (Supplementary Figure 4 A-D). Low dose application of TMT did not result in any significant changes.

Altogether, these results demonstrate a marked increase of synaptic density in different areas of the HC upon TMT-induced neurotoxic injury which predominantly occurred at 72 h for the high dose group and at 10 days post treatment for the low dose group.

CA1 subgroups
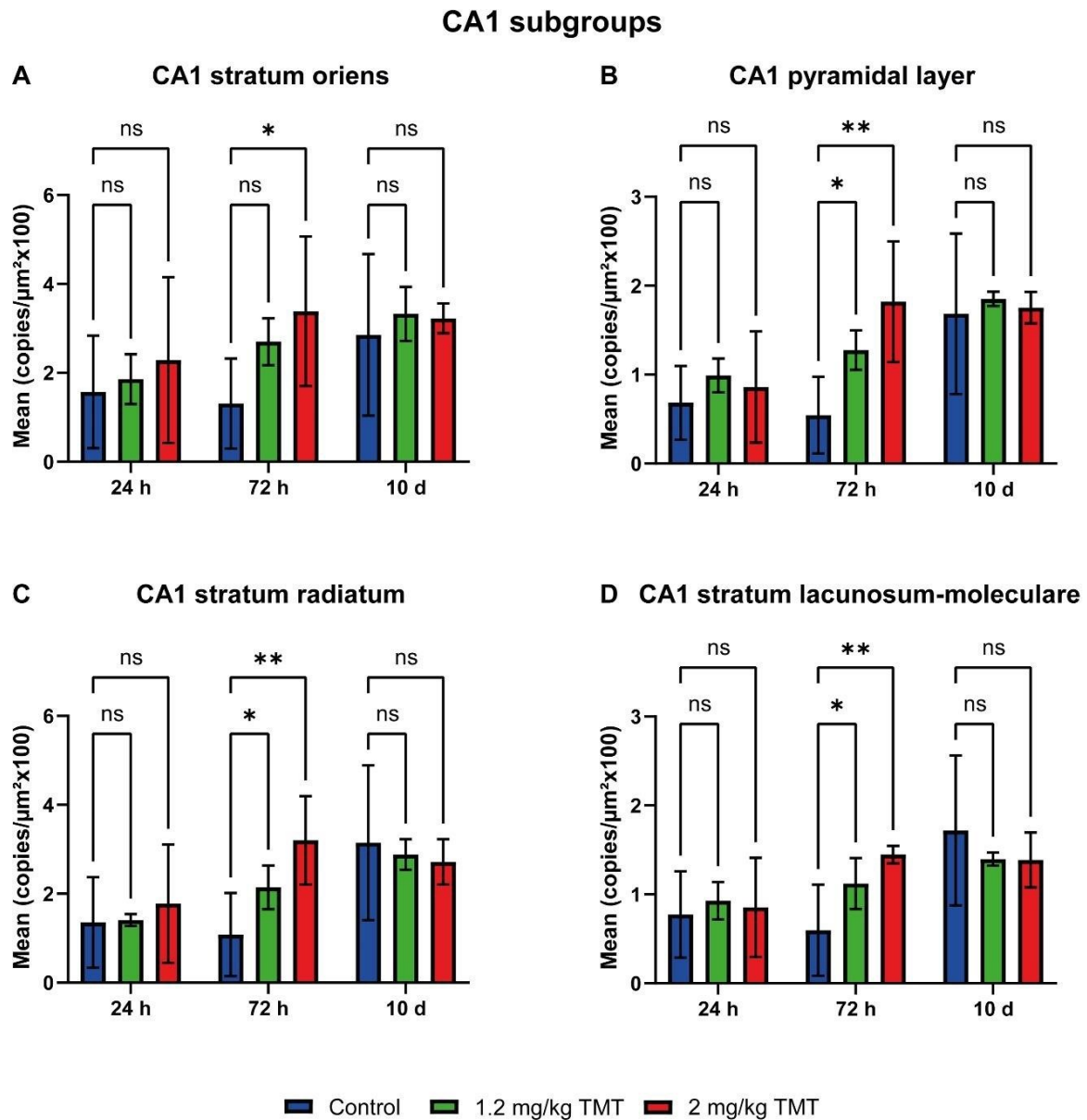
*Figure 54: **Synaptic density quantification after TMT treatment in CA1 sub-areas.** PLA puncta quantification for synaptic density in control (blue) and TMT-treated animals with low (green) and high dose (red) after 24 h, 72 h and 10 days in the sub-areas stratum oriens **(A)**, pyramidal layer **(B)**, stratum radiatum **(C)** and stratum lacunosum-moleculare **(D)** of the CA1 region of the hippocampus.*

3.4.2.1 Power Analysis for Future Studies of Synaptic Density Based on TMT-induced Neurotoxicity Studies

Assumptions for the sample size calculation for future studies were described in 2.2.8.3. Based on the observed differences between control and 2 mg/kg TMT treatment group (Figure 54, Supplementary Figure 1, Supplementary Figure 2,

Supplementary Figure 3, and Supplementary Figure 4), effect sizes were calculated as summarized in Table 3-6.

Table 3-6: Sample size calculations for future studies of synaptic density after TMT-induced neurotoxicity

AREA ANALYZED	SAMPLE SIZE 24 H	SAMPLE SIZE 72 H	SAMPLE SIZE 10 D
HC	163	3	118
CA1	157	6	88
CA2	1224	3	48
CA3	705	3	32
GD	2717	5	545
CA1 so	80	9	1024
CA1 sp	141	5	149
CA1 sr	125	5	68
CA1 slm	672	6	60
CA2 so	406	3	9
CA2 sp	348	5	1183
CA2 sr	1519	3	38
CA2 slm	537	3	72
CA3 so	144	3	216
CA3 sp	323	3	28
CA3 sr	2170	3	123
CA3 slm	11053	3	10112
GD mo	348	5	1183
GD sg	161	4	78
GD po	33	10	67

3.4.3 Findings in NF-L Plasma Levels of TMT Treated Mice

In rats, synaptic density and plasma levels of Neurofilament-light chain (NF-L) have been identified as biomarkers for TMT-induced neurodegeneration (Sano et al., 2021). Therefore, we also assessed NF-L plasma levels as described in 2.2.8.2.

Interestingly, baseline plasma NF-L levels, taken from all mice one week before TMT treatment, showed elevated levels for group 9 (Supplementary Figure 5 A, mice #25: m=864.612 ± 25.114, n=3; #26: m=572.604 ± 9.979, n=3; #27: m=304.616 ± 1.890, n=3). Upper and lower limits of all other baseline NF-L levels of replicates/animal (n = 3 replicates/animal) were between 23.885 pg/ml and 302.827 pg/ml. Plasma NF-L levels 1 h post TMT application showed no significant difference among the different study groups (Supplementary Figure 5 B). 24 h after TMT treatment and before necropsy of

groups 1, 4 and 7 the plasma NF-L levels showed a significant decrease between control group and the high dose 2 mg/kg TMT group (Figure 55 A, **p>0.01, two-way ANOVA followed by Dunnett's multiple comparison test). After 72 h, a significant increase was observed between control group and the high dose 2 mg/kg TMT group (Figure 55 B, *p>0.05, two-way ANOVA followed by Dunnett's multiple comparison test). 10 d after TMT application, no significant difference among means was observed between control and TMT treated groups (Figure 55 C). A high variability between the means/animal was observed for the highest dosing groups at 10 d post TMT application, similar to the elevated baseline plasma NF-L levels of group 9 (2 mg/kg TMT, necropsy 10 d post TMT) but not of group 8 (2 mg/kg TMT, necropsy 72 h post TMT, mice #16, 17, 18).
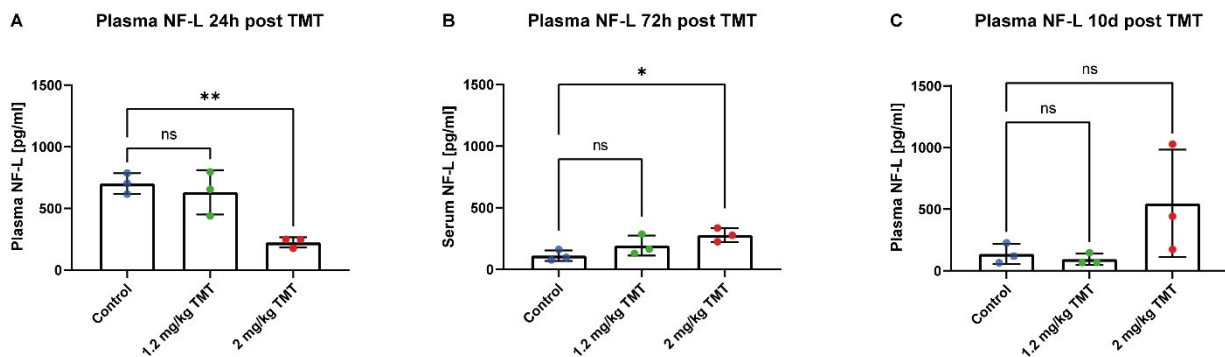
*Figure 55: **Plasma NF-L levels at different time points**: (A) Plasma NF-L levels 24 h post TMT treatment shown as mean/animal per group show only a significant decrease between control and dosing group 2 mg/kg TMT. Plasma NF L levels 72 h (B) and 10 d (C) after TMT treatment show no significant differences among the means of control compared to TMT-treated mice. A high variability of the means/animal in the highest dosing group was observed (*p<0.05, **p<0.01, Two-way ANOVA followed by Dunnett's multiple* comparison test).

4   DISCUSSION

Measurement of the synaptic density is one of the most important parameters in AD to study treatment responses, since synaptic loss is one of the earliest biomarkers in AD and has a well-known negative correlation with cognitive performance (Bancher, Jellinger, Lassmann, Fischer, & Leblhuber, 1996; DeKosky & Scheff, 1990; Terry et al., 1991). Therefore, a reliable, fast, and cost-efficient assay to study synaptic density is of utmost importance and its development and application in different types of mouse models has been a major aim of the current work.

4.1   Development of a Robust Assay for the Quantification of Synaptic Density

4.1.1   Current Methods to Evaluate Synaptic Density

Methods for the quantification of synaptic density include electron microscopy (EM), positron emission tomography (PET), and immunohistochemistry (IHC). While EM is highly sensitive, it requires an expensive equipment, is laborious, does only allow the evaluation of rather small brain areas, and cannot be used in a high throughput format (Scheff et al., 2006). In contrast, one of the major advantages of PET is that it exclusively enables *in vivo* imaging. However, tracers binding to synaptic proteins are expensive and a resolution on the cellular or subcellular level is not possible (M.-K. Chen et al., 2018). Therefore, it is mainly used to monitor patients at risk to develop AD (O'Dell et al., 2021). Preclinically, IHC is the most commonly used method to investigate synaptic contacts in mouse models of AD. It makes use of antibodies for pre- and postsynaptic structures which are co-localized in brain tissues. Major advantages are cost-effectiveness, and that the analysis of synaptic contacts in many samples is possible in an automatable easy-to-handle approach (Romoli et al., 2019). However, synaptic density quantification by IHC can be highly subjective since a seemingly colocalization of pre- and postsynaptic markers does not ensure the necessary proximity of less than 40 nm to form a synapse. Furthermore, IHC does not account for the intensity of a staining and therefore quantification of synaptic density and interpretation of results remain difficult (3.1 and Figure 34) (McLeod, Marzo, Podpolny, Galli, & Salinas, 2017).

4.1.2 PLA as a Reliable Alternative to Measure Synaptic Density

None of the before described methods offers the necessary sensitivity, scalability, and cost-effectiveness to study synaptic contacts in a reliable way in disease-relevant AD mouse models. To address these requirements the proximity ligation assay (PLA) might be a promising alternative approach. It detects protein-protein interactions by specifically targeting distinct structures with two separate primary antibodies. Species-specific secondary antibodies coupled to oligonucleotide probes can only be hybridized when the target structures are in a close vicinity (less than 40 nm). Since the synaptic cleft has a size of about 20-40 nm, pre- and postsynaptic targets are perfectly suited to detect a functional synapse by the PLA. After the incubation with secondary antibodies, oligonucleotide probes are hybridized, and the signal gets amplified by a rolling circle amplification resulting in quantifiable puncta (Fredriksson et al., 2002). Finally, the detected amplified signal corresponding to synaptic contacts, can be easily quantified in large tissue areas.

Recently, PLA has been successfully applied to sensitively detect protein-protein-interactions, like Ser1292 phosphorylation of LRRK2 (Di Maio et al., 2018), to quantify inter-organelle contact sites, namely mitochondria-endoplasmic reticulum (ER) and mitochondria-late-endosomes, in mammalian optic nerve tissues (Ching, Osborne, Eva, Prudent, & Yu-Wai-Man, 2021). Furthermore, there are first indications in neuronal cell cultures (Almandoz-Gil et al., 2018; Dore et al., 2020; Eagleson, Milner, Xie, & Levitt, 2013; Hromadkova et al., 2020; Lundgren et al., 2015; Verstraelen et al., 2020), rat (Di Maio et al., 2018) and mouse tissue (Amadeo et al., 2021; Orlandi et al., 2018) that the PLA might be suitable to quantify synaptic density.

Since at the beginning of this work, data on mouse tissue were not available and the protocol descriptions for the other applications were quite undetailed, a thorough establishment of suitable antibody combinations, tissue processing methods, buffers, mounting medium, probe coupling, persistent liquid barriers, an optimal heat distribution, and PLA signal analysis were necessary before applying the PLA successfully in AD mouse models.

4.1.3 Synaptic Markers Suitable for PLA

To use the PLA for the visualization of synaptic contacts, we first looked for suitable synaptic targets which are in close neighborhood to the synaptic cleft (20-40 nm)

(Südhof, 2012). Since synapses accommodate a unique proteome for which a plethora of antibodies have been developed, not all synapse markers can be used for the quantification of synaptic contacts. As shown before (Hurst, 2013; Verstraelen et al., 2020), pre-and post-synaptic targets need to be located near the synaptic cleft.

For general pre-synaptic markers, we selected proteins of the SNAP/SNARE complex in the active zone, like VAMP2, Synaptophysin, and Synaptotagmin playing an important role in vesicle fusion with the membrane close to the synaptic cleft (Hurst, 2013). As glutamatergic synapses are highly affected in AD, we also searched for glutamatergic markers (Caraci et al., 2018). In a presynaptic neuron, the neurotransmitter glutamate is transported in synaptic vesicles to the active zone. The most abundant of the three existent glutamate transporters is vesicular glutamate transporter 1 (vGLUT1). When vGLUT1 reaches the active zone and fuses with the pre-synaptic membrane to release glutamate, it serves as a target close to the synaptic cleft on the presynaptic site (Du et al., 2020).

As post-synaptic markers, the well-studied post-synaptic density protein 95 (PSD95) and HOMER1 were used for which a variety of antibodies exist. PSD95 and HOMER1 are both proteins localized at the post-synapse and play a key role for the interaction between receptors, ion channels and the related signaling proteins (Hayashi et al., 2009; Mahoney, 2007).

Specificity and staining intensity of 20 antibodies recognizing the targets described before had been tested on mouse tissues by IF. Altogether, 9 antibody pairs to detect general synapses and 8 antibody pairs to detect glutamatergic synapses could be successfully established regarding optimal dilution and staining specificity (Table 3-1) as summarized in Table 3-2.

4.1.4   Tissue Processing Methods

Since staining quality depends on fixation, preservation, and thickness of a tissue, we compared staining results for antibodies recognizing different synaptic markers on tissues varying substantially in the tissue processing method. This included staining on cryo-frozen, free-floating, FFPE and cleared tissues.

IF stainings on free-floating tissue sections revealed an excellent staining quality and colocalization of synaptic markers vGLUT1 and PSD95, antigen retrieval was not required and thicker tissue slices could provide more information (Figure 15) (Potts et al., 2020). However, this method harbored a series of disadvantages such as i) a

marked risk of false positive signals due to an optical but not real colocalization of synaptic markers in thick tissue slices (Figure 15), ii) mounting of the slices was time-consuming and challenging, iii) mounting of the slices frequently resulted in folds and wrinkles of the tissue during the mounting process which led to a loss of information if crucial ROIs were affected. Therefore, the free-floating method was not further pursued for the implementation of PLA stainings.

The use of cryosections to visualize markers for synaptic contacts, often led to a high deterioration rate of the samples. Furthermore, immunoreactivity and staining quality of IF signal in cryosections was sparse, weak, and inconsistent for the antibodies tested (Table 2-1 and Figure 16). Furthermore, the density of puncta-like signals for pre- and post-synaptic markers did not reach the expected density of one billion synaptic contacts in a cubic millimeter of a mouse brain (Deweerdt, 2019). Therefore, this approach was abandoned.

Another unsatisfactory approach consisted of the clearing of tissue samples followed by whole-volume 3D imaging. In theory, this should enable imaging of large tissue samples and therefore a quantification of synaptic density in whole brain areas. Based on the initial invention of Spalteholz, modern tissue clearing techniques can be divided in aqueous- and solvent-based methods, both removing light-scattering lipids by simultaneously obtaining the protein structure (Alexander, 2018; Spalteholz, 1914). In this work we utilized the solvent-based ECi- and the water-based X-CLARITY-clearing techniques on mouse brain tissue. Although ECi-clearing resulted in a quantifiable puncta-like staining (Figure 19 D-I) and yielded a higher number of synaptic contacts for a general synaptic marker pair than for a glutamatergic synaptic marker pair (Figure 19 H-I), a high background was observed for the ECi stainings. Therefore, no significant differences between IF stainings and negative controls (no primary antibodies used, Figure 19 H-I) was observed. As for the X-CLARITY protocol, results obtained were even worse since in cleared samples a puncta-like signal was almost invisible (Figure 19 A-C). Although the CLARITY method has been proposed to enhance clearing through increasing the pore size by embedding the tissue in a hydrogel-monomer solution (Choi, Guan, & Chung, 2021; Yang et al., 2014), neither the clearing result nor the following IF staining quality were convincing (Figure 19).

Finally, on FFPE tissues a series of antigen retrieval (Proteinase K, HIER-buffers differing in pH), and background reduction (Sudan Black) protocols were tested with the aim to get a convincing visualization of synaptic contacts. Best signal intensity was

achieved with a pre-treatment HIER-buffer at pH9 for all antibody pairs tested, while Sudan Black (SB) reduction only led to slight improvements of the IF signal and therefore was neglected (Table 3-1). In addition, FFPE tissues had several advantages like storage at room temperature, cost-effectiveness, long-term and good preservation of cell structures due to fixation and wax, and a well-preserved immunoreactivity and staining quality for IF stainings. Therefore, FFPE tissue processing was the favored technique used for the establishment of PLA stainings and its optimization.

4.1.5 PLA Protocol Optimization

After having identified synaptic marker pairs, which performed well in regard to specificity and sensitivity, low background, and a well-quantifiable puncta-like staining and after assessing the most optimal tissue processing protocols, we based our PLA approach to determine functional synapses on these antibodies, tissue, and pretreatment conditions. The commercially available PLA protocol (Millipore, 2017) describes many vulnerable steps which had to be optimized to obtain a highly specific and sensitive PLA signal quality on FFPE tissues. This included buffers used, mounting medium, probe coupling, liquid barrier, heat distribution and a standardized algorithm to analyze the PLA signal.

An intact and stable liquid barrier is one of the most important requirements to successfully perform a PLA. Among the methods of choice (PAPpens, CoverWells, iSpacers, and Covertiles), Covertiles were superior to all the other approaches since they yielded a better and even signal distribution (Figure 36, Figure 37) over whole slides and in addition reduced the volume per slide from 325 µl to 200 µl and reduced material costs substantially.

Negative controls are important to benchmark the PLA signal. Accordingly, further improvements of the assay included the introduction of several technical negative controls by omitting either one of the two primary antibodies or applying no primary antibody at all (probes-only). Interestingly, the pre-synaptic antibody-only control always led to the highest detection of false positive signals (Figure 27, Figure 39, Figure 40) and was therefore chosen as the most relevant negative control. Others have used negative controls by omitting one (Almandoz-Gil et al., 2018; Amadeo et al., 2021; Dore et al., 2020; Eagleson et al., 2013; I. Gomes et al., 2016) or both antibodies (Hromadkova et al., 2020; Lundgren et al., 2015), using knockouts of one of the targets (Amadeo et al., 2021; I. Gomes et al., 2016; Orlandi et al., 2018) and quantifying the

PLA signal in areas where biologically no signal would be expected (Orlandi et al., 2018). As positive controls, others used areas in which a high PLA signal would be detected (Amadeo et al., 2021) and IF co-stainings with one of the PLA targets (Verstraelen et al., 2020).

Besides, we compared the Duolink buffers from the commercially available kit to self-made buffers. The latter contained BSA which acts as an antioxidant, binds components such as various molecules, fatty acids, hormones, etc. Additionally, BSA blocks unspecific binding sites for proteins (A. Kowalski, 2019). By using this self-made buffer to perform PLA stainings we were able to improve the signal intensity markedly (Figure 39).

Alternate probe coupling turned out to have a major impact on the staining quality. Coupling of PLUS-probes to the pre-synaptic markers and MINUS-probes to the post-synaptic markers resulted in a higher dot count quantification (Figure 25, Figure 40). This might be due to steric effects of the probes which influences the reactivity of the molecules for the (-/+) combination (Gait, 1984). Moreover, the direct coupling of the probes to a guinea-pig anti vGLUT1 antibody showed a high variability in signal intensity. Therefore, direct coupling of probes to primary antibodies was neglected.

Moreover, as previously described by Nielsen at al. and Darby et al. the use of a hybridization oven (BOEKEL) with a smaller interior space and the direct positioning of the microscope slides on metal (aluminum tray), significantly improved the staining quality (Figure 35, Figure 37) (Darby & Hewitson, 2006; Nielsen, 2012).

Additionally, the complementary Duolink mounting medium emerged to be essential for the PLA signal since the use of the more cost-effective IF mounting medium (DAKO) did not result in a proper PLA signal but an unspecific signal in the nuclei (Figure 26). In contrast, PLA stainings with the Duolink Mounting medium resulted in clear PLA dots (e.g., Figure 20).

A reliable and standardized quantification of PLA dots represented an important step in the assay development. With the use of HALO software, we were able to quantify the PLA signal as copies/μm² to calculate the synaptic numbers in a ROI (Figure 21 and Figure 23). The settings especially for the contrast threshold (CT) had a great influence on PLA dot detection and resulting variability between the animals (Figure 22 D and Figure 24 D). Others mostly used FIJI (NIH) for the detection and quantification of the PLA signal (Almandoz-Gil et al., 2018; Amadeo et al., 2021; Dore et al., 2020; I. Gomes et al., 2016; Hromadkova et al., 2020; Orlandi et al., 2018), however,

using FIJI can be cumbersome by needing additional plugins whereas the software has its limitations with large image sizes of whole slide scans. Additionally, no batch processing was possible with large image files. Other softwares used to quantify PLA puncta were Acapella software (Perkin Elmer) (Verstraelen et al., 2020) used for the analysis of cell images, Duolink Image Tool (Merck) (I. Gomes et al., 2016) or Adobe Photoshop (Eagleson et al., 2013). However, comparing the above mentioned softwares to HALO, the HALO FISH algorithm to quantify the PLA dots, was easy to handle, a batch processing could be performed, and an effect of settings on the variables (Contrast threshold, Signal Minimum Intensity, Spot Size, Copy Intensity, Spot Segmentation Aggressiveness) could be directly assessed on the detected PLA signal (and background) with the help of the Real-time Tuning window.

Altogether, the before described assay improvements laid the foundation to employ the PLA reliably for the quantification of synaptic contacts in a series of healthy and diseased mouse models.

4.2   Synaptic Density in Healthy Brains

Since the PLA is a highly sensitive method to quantify synaptic contacts, we tested if we could reproduce the known synaptic distribution in the different brain areas of wt C57Bl6/J mice and at different ages with the PLA. Synaptic contacts are excessively formed during the first postnatal days of mice peaking at P15. Then, they get pruned away by microglia to leave and strengthen only needed synaptic contacts in adult mice (Hua & Smith, 2004; Stevens et al., 2007). Therefore, we compared the synaptic density in ROIs of large brain areas at P15 and adult (P180) mice followed by a more detailed assessment of the synaptic distribution in the cortical layers of the somatosensory cortex of adult mice.

In line with the current literature, for P15 we observed a significantly lower number of glutamatergic synapses in the hippocampus compared to the SS CTX and EC (Figure 29) (El Mestikawy, Wallén-Mackenzie, Fortin, Descarries, & Trudeau, 2011). In contrast, we identified highest synaptic density in the CTX for general and glutamatergic synaptic marker pairs, respectively (Figure 28, Figure 29).

As for P180, in accordance with previous findings synaptic density decreased from cortical layer I to VI (Zhou & Roper, 2010; Zhu et al., 2018). However, since the PLA allows a resolution of synaptic density on the cellular level and the identification of functional synapses rather than the expression of single proteins as a surrogate, our

findings surpass previous Western Blot analyses and thus provide novel information on the spatial distribution of synaptic density.

When finally comparing synaptic density in young and adult mice, unexpectedly, we did not find an age-dependent discrepancy in CTX, HC and EC for general synaptic numbers. For glutamatergic stainings of CTX and HC, we also did not observe age-dependent synaptic density differences (Figure 31). However, for glutamatergic synapses in the EC we were able to reproduce the expected higher numbers of synaptic contacts in P15 as compared to P180 mice (Figure 30 B) (Gonzalez-Lozano et al., 2016). Recent data from Jawaid and colleagues might provide an explanation for the lack of age-dependent differences in the assessment of synaptic contacts between P15 and P180 (Jawaid et al., 2018). As shown in Figure 56, highest increase in synaptic density was observed on postnatal day 21 while the level observed on postnatal day 15 resembled that of P41 and thus an advanced age.
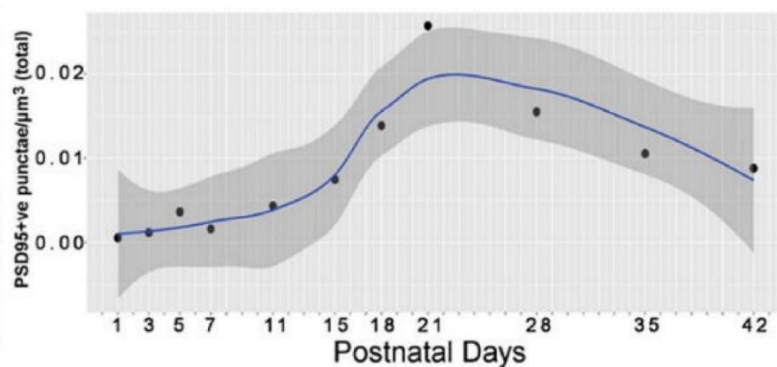

Figure 56: Quantification of post-synaptic marker PSD95 in postnatal days of C57Bl6/j wt mice suggesting highest synaptic density at day 21. Figure taken from (Jawaid et al., 2018).

Another group reported an even more delayed peak for synaptic density in C57Bl6 mice at P40 (Paolicelli et al., 2011). Therefore, it cannot be excluded that P15 could be a too early timepoint to achieve opposing values as compared to adult P180 mice. Altogether, our data strongly suggest that synaptic density assessed by the PLA provides novel and more detailed information on the spatial and temporal distribution of synaptic contacts and therefore can be used as an innovative tool to determine synaptic density changes during the development of neurodegenerative disorders or upon neurotoxic insult.

4.3 Synaptic Density in AD Models

4.3.1 Synaptic Density in Aβ-transgenic AD Mouse Model

Based on technical improvements of the PLA protocol which led to a reliable and specific detection of functional synapses in general as well as glutamatergic synapses, we were finally able to make use of the PLA in AD mouse models. Meanwhile, there is a substantial number of transgenic mouse models to study the mechanisms of cerebral amyloidosis of AD pathology which are also used to develop therapeutic strategies (D. J. Selkoe & Schenk, 2003). Many of these mouse models are limited in a late onset of the pathology, mixed genetic backgrounds, breeding difficulties, gender differences in pathology and a high variability in Aβ levels (Radde et al., 2006). Therefore, in this work the APPPS1 mouse model was used to study synaptic density dependent on Aβ pathology, because the APPPS1 model co-expresses the mutated presenilin 1 (PS1) and APP genes, respectively. Furthermore, it harbors high levels of neuron-specific transgene expression and low genetic variability, and Aβ deposition starts at 6 weeks of age (in the CTX) (Radde et al., 2006). In addition, dendritic spine loss was reported to start approx. 4 weeks after plaque formation in 4- to 5-month-old animals (Bittner et al., 2012).

First, we established a protocol to visualize simultaneously Aβ plaques by Methoxy-X04 staining and synaptic density by the PLA on 6-month-old APPPS1 animals harboring Aβ pathology. Noteworthy, to determine synaptic density successfully, it was important to perform the Methoxy-X04 staining prior to the PLA protocol (Figure 42). Subsequent HALO analysis revealed a decrease of synaptic contacts in close vicinity to Aβ plaques (Figure 43 and Figure 44). This is in good accordance with the current literature describing that in 18-month-old APPPS1 a proximity-dependent loss of synapses (colocalization of IF stainings with SYN and PSD95 on 15 μm thick cryosections) was revealed in < 25 μm from the plaque core (Sauerbeck et al., 2020).

Nevertheless, in future studies HALO analysis should be further improved by including the real shape of a plaque rather than defining plaques by concentric circles. This would lead to an even better representation of synaptic density data in the vicinity of Aβ plaques. Furthermore, synaptic density should be assessed at different ages of the animals to determine age-dependent changes of synaptic contacts relative to the Aβ pathology.

Altogether, the implementation of the co-staining of Aβ plaques and synaptic contacts with the PLA, as well as the successful plaque-based analysis with HALO represents

an important basic data set for future experiments in Aβ-transgenic mouse models and drug development.

4.3.2 Synaptic Density in Tau-transgenic AD Mouse Model

We challenged the usability of the PLA to quantify age-dependent synaptic changes in tau transgenic mice (TG4510) and thus another AD model. Several studies reported mixed results regarding an age-dependent synaptic loss in the TG4510 animals ranging from a progressive decline (Kopeikina et al., 2013; Rocher et al., 2010; Shimojo et al., 2020) to no effects or even an increased synaptic density (Crimins et al., 2011; Hoover et al., 2010). In the current work, the application of the PLA in tau-transgenic mice revealed for the SSCTX and HC an initial increased synaptic density in 2-months-old TG4510 mice as compared to controls (tA) followed by a significant decline at 6 months for both localizations. At 10 months, decreased synaptic density stayed only significant for HC (Figure 47). Especially the increased synaptic density at 2 months of age could be a result of an increased bouton stability which decreases with age (Rochefort & Konnerth, 2012). Furthermore, it cannot be excluded that this unexpected finding is caused by small but significant fractions of synapses responsive to cognitive function, injury or disease that therefore underlie a constant addition and removal of synaptic contacts (Cruz-Martín, Crespo, & Portera-Cailliau, 2010; Grillo et al., 2013; Holtmaat, Wilbrecht, Knott, Welker, & Svoboda, 2006; Majewska, Newton, & Sur, 2006; Murmu, Li, Holtmaat, & Li, 2013; Trachtenberg et al., 2002) (Schafer & Stevens, 2010). Altogether, our data are in line with Jackson et al., who reported the same initial increase of synaptic density (in 4-month-old TG4510 mice) by *in vivo* two-photon imaging following expression of the fluorescent protein in superficial cortical layers revealing a more rapid turnover of postsynaptic spines whereas presynaptic boutons are stabilized which led to a progressive decrease in spine density in 5.5-month-old TG4510 mice compared to wt animals (Jackson et al., 2017). Noteworthy, while data of Jackson and colleagues were obtained on small, circumscribed areas, the PLA used in the current work allowed for assessing synaptic density in large brain areas and thus provides an even more robust information.

Furthermore, we performed and in-depth analysis of the temporegional synaptic density changes in the different cortical layers of SSCTX, which revealed a significant synaptic loss in layer I to V at 6 months, while at 10 months only layer I showed a significant decrease of the synaptic density as compared to control animals (Figure 48 A-C). Other

studies on individual neurons describe a tau-dependent synaptic loss in 8.5- (Rocher et al., 2010) and 9-month-old (Crimins et al., 2011) TG4510 animals in the SSCTX by whole cell patch clamp analysis, as well as by *in vivo* imaging of dendritic spine density of apical dendrites of pyramidal neurons where a significant loss of spine density in 9-month-old TG4510 was demonstrated (Kopeikina et al., 2013). However, in the same study and similar to our results in 3.3.2.2, array tomography detecting all synapses, was performed revealing no difference in the colocalization of synaptic markers SYP and PSD95 in the SSCTX of 5.5- and 8.5-month-old TG4510 and age-matched controls (tA) (Kopeikina et al., 2013).

Another important outcome of this study consists of the results of the power analysis. This was based on synaptic density data obtained at different timepoints and different localizations in the TG4510 model. These calculations predicted the necessary number of animals required in the frame of a treatment approach which would have effects on synaptic contacts. Furthermore, it specifically allows to determine those localizations (layer I and II-III) and timepoints where the lowest number of animals is needed due to the observed effect size (3.3.2.4).

However, a potential limitation of the current study may be that the TG4510 mouse model has been questioned as a model for the complex pathogenesis of AD, since it has not been undoubtedly proven that the overexpression of mutant human tau P301L alone causes the phenotype in the mouse model and also it is unclear if tau is the driver of synaptic loss (Gamache et al., 2019). We tried to account for this limitation by using the tA model as control with only the activator transgene, which do not overexpress tau (Kopeikina et al., 2013).

In summary, assessment of synaptic density in the TG4510 tau model provides an important data set for future treatment approaches in terms of synaptic density kinetics, spatial distribution of synaptic density changes and animal study designs. To the best of my knowledge, this is the first detailed analysis of synaptic density in this AD model accounting for changes in different layers of the SSCTX.

4.4 Synaptic Density Upon Neurotoxic Insult

An exposure to the organotin compound TMT fosters neurodegeneration specifically in the HC and thus a region which is of major importance for learning and memory functions (S. Lee et al., 2016; Sueun Lee et al., 2016; Tang et al., 2013). Based on the

literature, we used a low dose of 1.2 mg/kg (Sandström et al., 2019) and a higher dose of 2 mg/kg TMT (Harry et al., 2008). After applying these two concentrations, we observed dose-dependent alterations in neurons including eosinophilic cytoplasm, nuclear pyknosis and nuclear karyolysis of the CA1 region of the HC with fewer anomalies for the low dose than for the high dose, as well as a recovery after 10 days (Figure 52), concomitant with the clinical observations 48 h after TMT application where mice showed abnormalities like lethargy (3.4.1). Although, we were able to reproduce neurotoxic effects after TMT insult (Figure 52 B-C, E-F), PLA-based synaptic density quantification in the hippocampus revealed an unexpected dose-dependent synaptic increase after 72 h, and a plateau 10 days post TMT application, similar to the neuronal recovery (Supplementary Figure 1, Figure 52 H, I), showing a presumed compensatory effect in synaptic numbers. This was also the case for HC sublayers CA1 (Figure 54), CA2 (Supplementary Figure 2), CA3 (Supplementary Figure 3), and GD (Supplementary Figure 4).

Our findings are contrasted by others describing in the same mouse model and after application of the same or similar TMT concentrations a decreased expression of glutamatergic neuronal markers (Sandström et al., 2019), an impaired energy metabolism (Z. Liu et al., 2021), and in another mouse model after application of the highest dose a distinct neuronal loss (Kraft, McPherson, & Harry, 2016). Noteworthy, these studies may not be entirely comparable with our approach since others focused on expression levels of i) different and ii) single neuronal markers, while the PLA visualizes a co-localization of pre- and postsynaptic markers after several rounds of amplification and thus would inform about the functionality of a synapse rather than changes in expression levels. Yet in line with our findings, after TMT treatment of neuronal stem cells Casalbore et al. reported an elevated expression of the general postsynaptic marker PSD95 which has also been analyzed in our study (Casalbore et al., 2010). Furthermore, authors provided evidence that overexpression of brain-derived neurotrophic factor (BDNF) might have been responsible for protective effects against TMT-induced neurotoxicity (Casalbore et al., 2010; Nawa & Takei, 2001). Interestingly, BDNF secretion promotes the up-regulation of synaptic genes like PSD95, SYN, and SNAP25 which in consequence lead to long-term potentiation and synapse formation (Bogen, Haug, Roberg, Fonnum, & Walaas, 2009; Yoshii & Constantine-Paton, 2007). Therefore, BDNF could have resulted in the observed compensatory effect in our study in terms of synaptic density after TMT treatment. Additionally, some authors suggested

that neuronal stem cells and neuronal progenitor cells in the granular layer in the GD and the subventricular zone of the anterior lateral ventricle, where neurogenesis in adults occurs, replace damaged neurons and glia cells after TMT insults (Ogita et al., 2005). The increase in synaptic density in our experiment on day 3 post application can therefore underline that the neurotoxic effect seen clinically on day 1 and 2 and single cell necrosis of neurons do recover and result in a compensating increase of synapses in specific areas of the cortex.

Another important result of the current work was obtained through the power analysis we performed demonstrating that the lowest number of animals would be needed at a TMT dose of 2 mg/kg and by assessing the effect after 72 h. Moreover, the calculated sample sizes between 3 and 10 animals for the respective subregions (Table 3-6) at 72 h indicates that as in the present study with only 3 animals meaningful data can be achieved. In addition, these findings represent important basic data sets to better design and plan the number of animals needed in future preclinical treatment studies and to choose the most suitable timepoint to assess synaptic density by PLA.

Since NF-L represents a well-known biomarker for AD (Sano et al., 2021), we further investigated a potential regulation upon neurotoxic insult by ELISA in the peripheral blood. Interestingly, we observed significant differences for the high dose TMT groups indicating that serum NF-L could serve as a potential biomarker for the detection of TMT-induced toxicity in the CNS. However, the high variability in the animals of the high dose groups (Figure 55) warrants further validation since this might have been caused by stress during the blood sampling (Aasland, Skjerve, & Smith, 2010; S. Kim, Foong, Cooper, Seibel, & Zhou, 2018).

Altogether, measuring synaptic density by the help of the PLA upon neurotoxic insult provides the first detailed analysis of the locoregional distribution of synaptic contacts in the HC and adds another layer of information to the existing studies regarding the functionality of synapses rather than describing expression level changes.

4.5   Outlook

So far for the treatment of AD only drugs ameliorating the symptoms (e.g. donepezil, galantamine and rivastigmine (Cummings, Lee, Ritter, Sabbagh, & Zhong, 2019), and aducanumab (Karran & De Strooper, 2022)), but no preventive or curative medications are available. Synapse loss is one of the earliest markers of AD beginning with a synaptic disfunction years before brain atrophy takes place (Qureshi et al., 2022).

Therefore, many preclinical studies investigating disturbed pathways or new treatment approaches in AD concentrated on the development of robust assays to measure synaptic density. Frequently used techniques have been positron emission tomography (G. F. Chen et al., 2017), electron microscopy (Scheff et al., 2006) and immunohistochemistry (McLeod et al., 2017b). They are endowed with at least one of the following disadvantages: high costs, too laborious, analysis of only small areas preventing high throughput formats, low resolution, and questionable co-localization of synaptic markers. Here, we provide with the PLA an excellent tool circumventing limitations described before in terms of robustness and reliability. Noteworthy, it allows to measure synaptic density in large brain areas with a so far unmet spatiotemporal resolution. Furthermore, even larger numbers of samples can be analyzed. Based on these advantages, PLA bears the potential to speed up future drug development for AD substantially and thus to replace the methods mentioned before to a large extent. Altogether, the PLA could become an important tool to test AD compounds more precise, more comprehensively, more economically and swifter.

Another strength of the present work consists of the power analyses performed in the neurotoxicity and tau models. These represent important basic data sets to better design and plan the number of animals needed in future preclinical treatment studies and to choose the most suitable timepoint to assess synaptic density. Hopefully, this will help to avoid unnecessary high numbers of animals.

5   SUMMARY

With a growing and ageing population, neurodegenerative diseases like Alzheimer's disease (AD) are going to appear more frequently in the next years. Currently approved drugs for the treatment of affected patients only mitigate the symptoms but do not prevent or cure the disease. Molecular mechanisms underlying the disease are still not completely understood, but there are indications that the immune system plays a key role in disease progression. Microglia, the resident immune cells of the brain, quite early in the disease progression prune away synaptic contacts. This loss of synaptic contacts is associated with a cognitive decline. Therefore, it is of great importance to study synaptic contacts since they could serve as an early indicator of the disease or as an efficacy readout in drug development.

Here, we developed a robust and sensitive proximity ligation assay (PLA) -based method to quantify synaptic density on brain tissues of different types of mouse models. This required an optimized pair of antibodies recognizing pre- and postsynaptic markers which have to be in close vicinity to generate a PLA signal. We successfully identified marker pairs to visualize general as well as glutamatergic synapses. Important improvements of the PLA method included a comparison of different tissue preparation methods, buffers, probe coupling, mounting medium, heat distribution during hybridization, liquid barrier preparation, suitable controls, scanning and image analysis parameters.

Upon development of a robust and reliable PLA protocol to determine synaptic density, we assessed synaptic contacts in healthy young and adult C57Bl6/J mice, spatiotemporal changes in large brain areas in two different AD models (Aβ and tau transgenic models), and finally changes in synaptic density after neurotoxic insult by trimethyltin (TMT). Our most important findings were i) a higher number of synaptic contacts in the entorhinal cortex in developing compared to adult brains, ii) a decreased number of synaptic contacts in close vicinity to Aβ plaques, iii) a decreased synaptic density in cortical layer I in 6 months-old tau-transgenic animals, and iv) a dose-dependent increase of synaptic contacts in the hippocampus upon TMT insult after 72 hours. These findings represent important basic data sets on the spatiotemporal distribution of synaptic contacts in healthy and diseased brains and especially provide novel data regarding synapse density in the different cortical layers.

Furthermore, spatiotemporal data on the synaptic density upon neurotoxic insult and the cortical layers in the tau transgenic AD model were used for a detailed power analysis to calculate the sample size of future treatment studies. This might help to avoid unnecessary high numbers of animals in preclinical drug development studies and to determine the most suitable timepoints for the measurement of synaptic contacts. Altogether, the present work established the PLA as a novel important tool to assess synaptic contacts in the frame of AD research. Major advantages are its high precision, robustness, reliability, the possibility to analyze large brain areas, that it is easy to handle and can be used in a more economical way as comparable methods to determine synaptic contacts. Spatiotemporal data on the synaptic density generated by the PLA in non-diseased and diseased brain represent an important data source for future preclinical studies on AD.

6   ZUSAMMENFASSUNG

Mit zunehmend wachsender und alternder Bevölkerung werden in den kommenden Jahren auch neurodegenerative Erkrankungen wie die Alzheimer Krankheit zunehmen. Bisher zugelassene Medikamente zur Behandlung von betroffenen Patienten mildern jedoch nur die Symptome, sind jedoch nicht in der Lage die Krankheit zu verhindern oder zu heilen. Die grundlegenden Mechanismen der Erkrankung sind immer noch nicht vollständig geklärt, wobei es Hinweise gibt, dass das Immunsystem eine wesentliche Rolle im Krankheitsverlauf einnimmt. Mikroglia sind die ortsständigen Immunzellen des Gehirns, welche synaptische Kontakte bereits früh im Krankheitsverlauf reduzieren. Dieser Synapsenverlust steht in Verbindung mit der Abnahme kognitiver Funktionen. Daher ist es von großer Bedeutung, den synaptischen Verlust zu untersuchen, da dieser als Frühindikator der Krankheit und auch als verlässlicher Parameter zur Beurteilung der Sicherheit und Wirksamkeit neuer Medikamente dienen könnte.

In dieser Arbeit wurde daher eine robuste und sensitive Methode basierend auf dem Proximity Ligation Assay (PLA) entwickelt, um die synaptische Dichte auf Hirngewebe verschiedener Mausmodelle messen zu können. Hierfür war ein aufeinander abgestimmtes Antikörperpaar erforderlich, welches als Voraussetzung für ein erfolgreiches PLA-Signal in unmittelbarer Nähe zueinander prä- und postsynaptische Strukturen erkennt. Geeignete Paare für generelle als auch glutamaterge synaptische Marker wurden erfolgreich identifiziert und für geeignet befunden. Zudem wurden am PLA Protokoll wichtige Verbesserungen wie der Vergleich von verschiedenen Gewebeprozessierungen durchgeführt, als auch verschiedene Puffer, Probe-Kopplung, Eindeckmedien, Wärmeverteilung während der Hybridisierungsschritte, verschiedene Flüssigkeitsbarrieren und entsprechende Kontrollen getestet, sowie die Einstellungen für Scan- und Bildanalyse etabliert.

Über die Entwicklung eines robusten und zuverlässigen PLA-Protokolls zur Bestimmung der synaptischen Dichte hinaus, wurden synaptische Kontakte in gesunden jungen und adulten C57Bl6/J Mäusen bestimmt, räumlich und zeitlich aufgelöste Veränderungen in großen Hirnarealen in zwei verschieben (Aβ- und Tau-transgenen) Alzheimer Mausmodellen und Veränderungen der synaptischen Dichte nach der Applikation des neurotoxischen Trimethylzinn (TMT) bestimmt. Zu den wichtigsten Erkenntnissen hierbei zählen i) eine höhere Anzahl an synaptischen Kontakten im entorhinalen Cortex in jungen Mäusen im Vergleich zu adulten, ii) eine Reduktion der synaptischen

Dichte in unmittelbarer Nähe zu Aβ-Plaques und iii) eine stark verringerte synaptische Dichte in der obersten Kortikalisschicht in 6-Monate alten Tau-transgenen Mäusen und iv) eine dosisabhängige Zunahme der synaptischen Dichte 72 Stunden nach der Applikation von Trimethylzinn.

Diese Beobachtungen stellen wichtige Basisdaten zur räumlichen und zeitlichen Verteilung der synaptischen Dichte in gesunden wie erkrankten Gehirnen dar und bieten insbesondere neue Erkenntnisse hinsichtlich der Verteilung der synaptischen Dichte in den kortikalen Schichten im TG4510 Mausmodell. Darüber hinaus wurden die räumlich und zeitlich aufgelösten Daten der synaptischen Dichte der neurotoxischen Studie, sowie die Daten der synaptischen Dichte in den kortikalen Schichten im Tau-transgenen Mausmodell für eine Poweranalyse verwendet, um die Tierzahl für zukünftige Behandlungsstudien zu berechnen.

Zusammengefasst wurde in dieser Arbeit der PLA als neuartiges und wichtiges Werkzeug zur Bestimmung der synaptischen Dichte im Rahmen der Alzheimer Forschung entwickelt. Die wesentlichen Vorteile des PLA ergeben sich durch seine hohe Präzision, Stabilität, Verlässlichkeit, der Möglichkeit große Hirnareale zu analysieren, seiner einfachen Handhabung und der Kosteneffizienz gegenüber vergleichbaren Methoden, um die synaptische Dichte zu bestimmen. Die mit dem PLA generierten räumlich und zeitlich aufgelösten Daten zur Bestimmung der synaptischen Dichte in gesunden und erkrankten Gehirnen stellen wichtige Basisdatensätze für künftige präklinische Alzheimer Studien dar.

7 LITERATURE

Aasland, K. E., Skjerve, E., & Smith, A. J. (2010). Quality of blood samples from the saphenous vein compared with the tail vein during multiple blood sampling of mice. *Lab Anim, 44*(1), 25-29. doi:10.1258/la.2009.009017

Abud, E. M., Ramirez, R. N., Martinez, E. S., Healy, L. M., Nguyen, C. H. H., Newman, S. A., . . . Blurton-Jones, M. (2017). iPSC-Derived Human Microglia-like Cells to Study Neurological Diseases. *Neuron, 94*(2), 278-293.e279. doi:https://doi.org/10.1016/j.neuron.2017.03.042

Ageta-Ishihara, N., Yamazaki, M., Konno, K., Nakayama, H., Abe, M., Hashimoto, K., . . . Kinoshita, M. (2015). A CDC42EP4/septin-based perisynaptic glial scaffold facilitates glutamate clearance. *Nature Communications, 6*, 10090-10090. doi:10.1038/ncomms10090

Ahmari, S. E., & Smith, S. J. (2002). Knowing a nascent synapse when you see it. *Neuron, 34*(3), 333-336. doi:10.1016/s0896-6273(02)00685-2

Alexander, T. (2018). *Volume fluorescence microscopy of mouse brains to examine Alzheimer's disease.* (Master of Science Master Thesis). Hochschule Mannheim,

Almandoz-Gil, L., Persson, E., Lindström, V., Ingelsson, M., Erlandsson, A., & Bergström, J. (2018). In Situ Proximity Ligation Assay Reveals Co-Localization of Alpha-Synuclein and SNARE Proteins in Murine Primary Neurons. *Frontiers in neurology, 9*. doi:10.3389/fneur.2018.00180

Alzheimer, A. (1907). Uber eine eigenartige Erkrankung der Hirnrinde. *Zentralbl. Nervenh. Psych., 18*, 177-179.

Amadeo, A., Pizzi, S., Comincini, A., Modena, D., Calogero, A. M., Madaschi, L., . . . Cappelletti, G. (2021). The Association between α-Synuclein and α-Tubulin in Brain Synapses. *International Journal of Molecular Sciences, 22*(17), 9153. Retrieved from https://www.mdpi.com/1422-0067/22/17/9153

Association, A. s. (2019). 2019 Alzheimer's disease facts and figures. *Alzheimer's & dementia, 15*(3), 321-387. doi:https://doi.org/10.1016/j.jalz.2019.01.010

Bachiller, S., Jiménez-Ferrer, I., Paulus, A., Yang, Y., Swanberg, M., Deierborg, T., & Boza-Serrano, A. (2018). Microglia in Neurological Diseases: A Road Map to Brain-Disease Dependent-Inflammatory Response. *Frontiers in cellular neuroscience, 12*. doi:10.3389/fncel.2018.00488

Bahr, G. F., Bloom, G., & Friberg, U. (1957). Volume changes of tissues in physiological fluids during fixation in osmium tetroxide or formaldehyde and during subsequent treatment. *Exp Cell Res, 12*(2), 342-355. doi:10.1016/0014-4827(57)90148-9

Bancher, C., Jellinger, K., Lassmann, H., Fischer, P., & Leblhuber, F. (1996). Correlations between mental state and quantitative neuropathology in the Vienna Longitudinal Study on Dementia. *European archives of psychiatry and clinical neuroscience, 246*(3), 137-146.

Bashiri, H., Enayati, M., Bashiri, A., & Salari, A.-A. (2020). Swimming exercise improves cognitive and behavioral disorders in male NMRI mice with sporadic Alzheimer-like disease. *Physiology & Behavior, 223*, 113003. doi:https://doi.org/10.1016/j.physbeh.2020.113003

Bittner, T., Burgold, S., Dorostkar, M. M., Fuhrmann, M., Wegenast-Braun, B. M., Schmidt, B., . . . Herms, J. (2012). Amyloid plaque formation precedes dendritic

spine loss. *Acta Neuropathol, 124*(6), 797-807. doi:10.1007/s00401-012-1047-8

Block, M. L., Zecca, L., & Hong, J.-S. (2007). Microglia-mediated neurotoxicity: uncovering the molecular mechanisms. *Nature Reviews Neuroscience, 8*(1), 57-69.

Bloom, G. S. (2014). Amyloid-β and Tau: The Trigger and Bullet in Alzheimer Disease Pathogenesis. *JAMA neurology, 71*(4), 505-508. doi:10.1001/jamaneurol.2013.5847

Bogen, I. L., Haug, K. H., Roberg, B., Fonnum, F., & Walaas, S. I. (2009). The importance of synapsin I and II for neurotransmitter levels and vesicular storage in cholinergic, glutamatergic and GABAergic nerve terminals. *Neurochem Int, 55*(1-3), 13-21. doi:10.1016/j.neuint.2009.02.006

Burgey, C. (2019). *Reevaluation of hippocampal seeding model with AD seeds in hippocampal CA1.* Paper presented at the AbbVie R&D Neuroscience Science Day October 2019, Ludwigshafen, Rhineland-Palatine, Germany.

Butterfield, D. A., & Pocernich, C. B. (2003). The Glutamatergic System and Alzheimer's Disease. *CNS Drugs, 17*(9), 641-652. doi:10.2165/00023210-200317090-00004

Calderon-Garcidueñas, A. L., & Duyckaerts, C. (2018). Chapter 23 - Alzheimer disease. In G. G. Kovacs & I. Alafuzoff (Eds.), *Handbook of Clinical Neurology* (Vol. 145, pp. 325-337): Elsevier.

Caraci, F., Nicoletti, F., & Copani, A. (2018). Metabotropic glutamate receptors: the potential for therapeutic applications in Alzheimer's disease. *Current Opinion in Pharmacology, 38*, 1-7. doi:https://doi.org/10.1016/j.coph.2017.12.001

Carroll, M. C. (2004). The complement system in regulation of adaptive immunity. *Nature Immunology, 5*(10), 981-986. doi:10.1038/ni1113

Casalbore, P., Barone, I., Felsani, A., D'Agnano, I., Michetti, F., Maira, G., & Cenciarelli, C. (2010). Neural stem cells modified to express BDNF antagonize trimethyltin-induced neurotoxicity through PI3K/Akt and MAP kinase pathways. *Journal of cellular physiology, 224*(3), 710-721.

Chen, G.-f., Xu, T.-h., Yan, Y., Zhou, Y.-r., Jiang, Y., Melcher, K., & Xu, H. E. (2017). Amyloid beta: structure, biology and structure-based therapeutic development. *Acta Pharmacologica Sinica, 38*(9), 1205-1235.

Chen, G. F., Xu, T. H., Yan, Y., Zhou, Y. R., Jiang, Y., Melcher, K., & Xu, H. E. (2017). Amyloid beta: structure, biology and structure-based therapeutic development. *Acta Pharmacol Sin, 38*(9), 1205-1235. doi:10.1038/aps.2017.28

Chen, M.-K., Mecca, A. P., Naganawa, M., Finnema, S. J., Toyonaga, T., Lin, S.-f., . . . McDonald, J. W. (2018). Assessing synaptic density in Alzheimer disease with synaptic vesicle glycoprotein 2A positron emission tomographic imaging. *JAMA neurology, 75*(10), 1215-1224.

Chen, M. K., Mecca, A. P., Naganawa, M., Finnema, S. J., Toyonaga, T., Lin, S. F., . . . van Dyck, C. H. (2018). Assessing Synaptic Density in Alzheimer Disease With Synaptic Vesicle Glycoprotein 2A Positron Emission Tomographic Imaging. *JAMA Neurol, 75*(10), 1215-1224. doi:10.1001/jamaneurol.2018.1836

Ching, J., Osborne, A., Eva, R., Prudent, J., & Yu-Wai-Man, P. (2021). Quantifying inter-organelle membrane contact sites using proximity ligation assay in fixed optic nerve sections. *Experimental Eye Research, 213*, 108793. doi:https://doi.org/10.1016/j.exer.2021.108793

Choi, S. W., Guan, W., & Chung, K. (2021). Basic principles of hydrogel-based tissue transformation technologies and their applications. *Cell, 184*(16), 4115-4136.

Colton, C. A., & Wilcock, D. M. (2010). Assessing activation states in microglia. *CNS & Neurological Disorders-Drug Targets (Formerly Current Drug Targets-CNS & Neurological Disorders), 9*(2), 174-191.

Crimins, J. L., Rocher, A. B., Peters, A., Shultz, P., Lewis, J., & Luebke, J. I. (2011). Homeostatic responses by surviving cortical pyramidal cells in neurodegenerative tauopathy. *Acta Neuropathol, 122*(5), 551-564. doi:10.1007/s00401-011-0877-0

Cruz-Martín, A., Crespo, M., & Portera-Cailliau, C. (2010). Delayed stabilization of dendritic spines in fragile X mice. *Journal of Neuroscience, 30*(23), 7793-7803.

Cummings, J., Lee, G., Ritter, A., Sabbagh, M., & Zhong, K. (2019). Alzheimer's disease drug development pipeline: 2019. *Alzheimer's & Dementia: Translational Research & Clinical Interventions, 5*, 272-293. doi:https://doi.org/10.1016/j.trci.2019.05.008

Czirr, E., Castello, N. A., Mosher, K. I., Castellano, J. M., Hinkson, I. V., Lucin, K. M., . . . Wyss-Coray, T. (2017). Microglial complement receptor 3 regulates brain Aβ levels through secreted proteolytic activity. *J Exp Med, 214*(4), 1081-1092. doi:10.1084/jem.20162011

Danielson, E., Perez de Arce, K., Cimini, B., Wamhoff, E.-C., Singh, S., Cottrell, J. R., . . . Bathe, M. (2021). Molecular Diversity of Glutamatergic and GABAergic Synapses from Multiplexed Fluorescence Imaging. *eNeuro, 8*(1), ENEURO.0286-0220.2020. doi:10.1523/ENEURO.0286-20.2020

Darby, I. A., & Hewitson, T. D. (2006). *In situ hybridization protocols* (Vol. 207): Springer.

Dawson, T. M., Golde, T. E., & Lagier-Tourenne, C. (2018). Animal models of neurodegenerative diseases. *Nature Neuroscience, 21*(10), 1370-1379. doi:10.1038/s41593-018-0236-8

Dejanovic, B., Huntley, M. A., De Mazière, A., Meilandt, W. J., Wu, T., Srinivasan, K., . . . Sheng, M. (2018). Changes in the Synaptic Proteome in Tauopathy and Rescue of Tau-Induced Synapse Loss by C1q Antibodies. *Neuron, 100*(6), 1322-1336.e1327. doi:10.1016/j.neuron.2018.10.014

DeKosky, S. T., & Scheff, S. W. (1990). Synapse loss in frontal cortex biopsies in Alzheimer's disease: correlation with cognitive severity. *Ann Neurol, 27*(5), 457-464. doi:10.1002/ana.410270502

DeVos, S. L., Corjuc, B. T., Commins, C., Dujardin, S., Bannon, R. N., Corjuc, D., . . . Hyman, B. T. (2018). Tau reduction in the presence of amyloid-β prevents tau pathology and neuronal death in vivo. *Brain, 141*(7), 2194-2212. doi:10.1093/brain/awy117

Deweerdt, S. (2019). Deep connections. *Nature, 571*(7766), S6-S8.

Di Maio, R., Hoffman, E. K., Rocha, E. M., Keeney, M. T., Sanders, L. H., De Miranda, B. R., . . . Greenamyre, J. T. (2018). LRRK2 activation in idiopathic Parkinson's disease. *Sci Transl Med, 10*(451). doi:10.1126/scitranslmed.aar5429

Domingues, C., AB da Cruz e Silva, O., & Henriques, A. (2017). Impact of cytokines and chemokines on Alzheimer's disease neuropathological hallmarks. *Current Alzheimer Research, 14*(8), 870-882.

Dore, K., Pao, Y., Soria Lopez, J., Aronson, S., Zhan, H., Ghosh, S., . . . Kebschull, J. M. (2020). SYNPLA, a method to identify synapses displaying plasticity after learning. *Proceedings of the National Academy of Sciences of the United States of America, 117*(6), 3214-3219. doi:10.1073/pnas.1919911117

Dorostkar, M. M., Burgold, S., Filser, S., Barghorn, S., Schmidt, B., Anumala, U. R., . . . Herms, J. (2014). Immunotherapy alleviates amyloid-associated synaptic

pathology in an Alzheimer's disease mouse model. *Brain, 137*(Pt 12), 3319-3326. doi:10.1093/brain/awu280

Drew, L. (2018). An age-old story of dementia. *Nature, 559*(7715), S2-S3.

Du, X., Li, J., Li, M., Yang, X., Qi, Z., Xu, B., . . . Deng, Y. (2020). Research progress on the role of type I vesicular glutamate transporter (VGLUT1) in nervous system diseases. *Cell & Bioscience, 10*(1), 26. doi:10.1186/s13578-020-00393-4

Duyckaerts, C., Delatour, B., & Potier, M.-C. (2009). Classification and basic pathology of Alzheimer disease. *Acta Neuropathologica, 118*(1), 5-36. doi:10.1007/s00401-009-0532-1

Eagleson, K. L., Milner, T. A., Xie, Z., & Levitt, P. (2013). Synaptic and extrasynaptic location of the receptor tyrosine kinase met during postnatal development in the mouse neocortex and hippocampus. *Journal of Comparative Neurology, 521*(14), 3241-3259.

El Mestikawy, S., Wallén-Mackenzie, Å., Fortin, G. M., Descarries, L., & Trudeau, L.-E. (2011). From glutamate co-release to vesicular synergy: vesicular glutamate transporters. *Nature Reviews Neuroscience, 12*(4), 204-216. doi:10.1038/nrn2969

Ellington, A. D., & Szostak, J. W. (1990). In vitro selection of RNA molecules that bind specific ligands. *Nature, 346*(6287), 818-822.

Erben, T., Ossig, R., Naim, H. Y., & Schnekenburger, J. (2016). What to do with high autofluorescence background in pancreatic tissues - an efficient Sudan black B quenching method for specific immunofluorescence labelling. *Histopathology, 69*(3), 406-422. doi:10.1111/his.12935

Evans, T. A., Bury, L. A., Huang, A. Y., & Sabo, S. L. (2019). Spatio-temporal dynamics of neocortical presynaptic terminal development using multi-photon imaging of the corpus callosum in vivo. *Scientific Reports, 9*(1), 14028. doi:10.1038/s41598-019-50431-6

Fabrizi, C., Pompili, E., De Vito, S., Somma, F., Catizone, A., Ricci, G., . . . Fumagalli, L. (2016). Impairment of the autophagic flux in astrocytes intoxicated by trimethyltin. *Neurotoxicology, 52*, 12-22.

Falcon, B., Zhang, W., Schweighauser, M., Murzin, A. G., Vidal, R., Garringer, H. J., . . . Goedert, M. (2018). Tau filaments from multiple cases of sporadic and inherited Alzheimer's disease adopt a common fold. *Acta Neuropathologica, 136*(5), 699-708. doi:10.1007/s00401-018-1914-z

Fan, W.-J., Yan, M.-C., Wang, L., Sun, Y.-Z., Deng, J.-B., & Deng, J.-X. (2018). Synaptic aging disrupts synaptic morphology and function in cerebellar Purkinje cells. *Neural Regeneration Research, 13*(6), 1019-1025. doi:10.4103/1673-5374.233445

Finnema, S. J., Nabulsi, N. B., Eid, T., Detyniecki, K., Lin, S.-f., Chen, M.-K., . . . Carson, R. E. (2016). Imaging synaptic density in the living human brain. *Science translational medicine, 8*(348), 348ra396-348ra396. doi:doi:10.1126/scitranslmed.aaf6667

Fredriksson, S., Gullberg, M., Jarvius, J., Olsson, C., Pietras, K., Gústafsdóttir, S. M., . . . Landegren, U. (2002). Protein detection using proximity-dependent DNA ligation assays. *Nat Biotechnol, 20*(5), 473-477. doi:10.1038/nbt0502-473

Gait, M. J. (1984). *Oligonucleotide synthesis*: IRL press.

Gamache, J., Benzow, K., Forster, C., Kemper, L., Hlynialuk, C., Furrow, E., . . . Koob, M. D. (2019). Factors other than hTau overexpression that contribute to tauopathy-like phenotype in rTg4510 mice. *Nat Commun, 10*(1), 2479. doi:10.1038/s41467-019-10428-1

Gaugler, J. E., Kane, R. L., & Kane, R. A. (2002). Family care for older adults with disabilities: Toward more targeted and interpretable research. *The International Journal of Aging and Human Development, 54*(3), 205-231.

Geloso, M. C., Corvino, V., & Michetti, F. (2011). Trimethyltin-induced hippocampal degeneration as a tool to investigate neurodegenerative processes. *Neurochemistry International, 58*(7), 729-738.

Gengler, S., Hamilton, A., & Hölscher, C. (2010). Synaptic plasticity in the hippocampus of a APP/PS1 mouse model of Alzheimer's disease is impaired in old but not young mice. *PLoS One, 5*(3), e9764. doi:10.1371/journal.pone.0009764

Gomes, I., Sierra, S., & Devi, L. A. (2016). Detection of Receptor Heteromerization Using In Situ Proximity Ligation Assay. *Curr Protoc Pharmacol, 75*, 2.16.11-12.16.31. doi:10.1002/cpph.15

Gomes, L. A., Hipp, S. A., Rijal Upadhaya, A., Balakrishnan, K., Ospitalieri, S., Koper, M. J., . . . Rabe, S. (2019). Aβ-induced acceleration of Alzheimer-related τ-pathology spreading and its association with prion protein. *Acta Neuropathologica, 138*(6), 913-941.

Gomez, W., Morales, R., Maracaja-Coutinho, V., Parra, V., & Nassif, M. (2020). Down syndrome and Alzheimer's disease: common molecular traits beyond the amyloid precursor protein. *Aging (Albany NY), 12*, 1011 - 1033.

Gonzalez-Lozano, M. A., Klemmer, P., Gebuis, T., Hassan, C., van Nierop, P., van Kesteren, R. E., . . . Li, K. W. (2016). Dynamics of the mouse brain cortical synaptic proteome during postnatal brain development. *Scientific Reports, 6*, 35456-35456. doi:10.1038/srep35456

Goodwin, L. O., Splinter, E., Davis, T. L., Urban, R., He, H., Braun, R. E., . . . Murray, S. A. (2019). Large-scale discovery of mouse transgenic integration sites reveals frequent structural variation and insertional mutagenesis. *Genome Res, 29*(3), 494-505. doi:10.1101/gr.233866.117

Gottschall, P. E., Ajmo, J. M., Eakin, A. K., Howell, M. D., Mehta, H., & Bailey, L. A. (2010). Panel of synaptic protein ELISAs for evaluating neurological phenotype. *Exp Brain Res, 201*(4), 885-893. doi:10.1007/s00221-010-2182-x

Grillo, F. W., Song, S., Ruivo, L. M. T.-G., Huang, L., Gao, G., Knott, G. W., . . . Little, G. E. (2013). Increased axonal bouton dynamics in the aging mouse cortex. *Proceedings of the National Academy of Sciences, 110*(16), E1514-E1523.

Guerreiro, R., Wojtas, A., Bras, J., Carrasquillo, M., Rogaeva, E., Majounie, E., . . . Younkin, S. (2013). TREM2 variants in Alzheimer's disease. *New England Journal of Medicine, 368*(2), 117-127.

Guo, T., Noble, W., & Hanger, D. P. (2017). Roles of tau protein in health and disease. *Acta Neuropathologica, 133*(5), 665-704. doi:10.1007/s00401-017-1707-9

Hampshire, V. A., & Gilbert, S. H. (2019). Refinement, Reduction, and Replacement (3R) Strategies in Preclinical Testing of Medical Devices. *Toxicologic Pathology, 47*(3), 329-338. doi:10.1177/0192623318797289

Haroon, E., Miller, A. H., & Sanacora, G. (2017). Inflammation, Glutamate, and Glia: A Trio of Trouble in Mood Disorders. *Neuropsychopharmacology, 42*(1), 193-215. doi:10.1038/npp.2016.199

Harry, G. J., Lefebvre days'Hellencourt, C., McPherson, C. A., Funk, J. A., Aoyama, M., & Wine, R. N. (2008). Tumor necrosis factor p55 and p75 receptors are involved in chemical-induced apoptosis of dentate granule neurons. *J Neurochem, 106*(1), 281-298. doi:10.1111/j.1471-4159.2008.05382.x

Hartwell, L. H., Hopfield, J. J., Leibler, S., & Murray, A. W. (1999). From molecular to modular cell biology. *Nature, 402*(6761), C47-C52. doi:10.1038/35011540

Harvey, R. J., Skelton-Robinson, M., & Rossor, M. N. (2003). The prevalence and causes of dementia in people under the age of 65 years. *Journal of neurology, neurosurgery, and psychiatry, 74*(9), 1206-1209. doi:10.1136/jnnp.74.9.1206

Hayashi, M. K., Tang, C., Verpelli, C., Narayanan, R., Stearns, M. H., Xu, R.-M., . . . Hayashi, Y. (2009). The postsynaptic density proteins Homer and Shank form a polymeric network structure. *Cell, 137*(1), 159-171.

He, Z., Guo, J. L., McBride, J. D., Narasimhan, S., Kim, H., Changolkar, L., . . . Lee, V. M. Y. (2018). Amyloid-β plaques enhance Alzheimer's brain tau-seeded pathologies by facilitating neuritic plaque tau aggregation. *Nature Medicine, 24*(1), 29-38. doi:10.1038/nm.4443

Helboe, L., Egebjerg, J., Barkholt, P., & Volbracht, C. (2017). Early depletion of CA1 neurons and late neurodegeneration in a mouse tauopathy model. *Brain Res, 1665*, 22-35. doi:10.1016/j.brainres.2017.04.002

Holtmaat, A., Wilbrecht, L., Knott, G. W., Welker, E., & Svoboda, K. (2006). Experience-dependent and cell-type-specific spine growth in the neocortex. *Nature, 441*(7096), 979-983.

Hong, S., Beja-Glasser, V. F., Nfonoyim, B. M., Frouin, A., Li, S., Ramakrishnan, S., . . . Stevens, B. (2016). Complement and microglia mediate early synapse loss in Alzheimer mouse models. *Science, 352*(6286), 712-716. doi:10.1126/science.aad8373

Hoover, B. R., Reed, M. N., Su, J., Penrod, R. D., Kotilinek, L. A., Grant, M. K., . . . Liao, D. (2010). Tau mislocalization to dendritic spines mediates synaptic dysfunction independently of neurodegeneration. *Neuron, 68*(6), 1067-1081. doi:10.1016/j.neuron.2010.11.030

Hou, Y., Dan, X., Babbar, M., Wei, Y., Hasselbalch, S. G., Croteau, D. L., & Bohr, V. A. (2019). Ageing as a risk factor for neurodegenerative disease. *Nat Rev Neurol, 15*(10), 565-581. doi:10.1038/s41582-019-0244-7

Hromadkova, L., Bezdekova, D., Pala, J., Schedin-Weiss, S., Tjernberg, L. O., Hoschl, C., & Ovsepian, S. V. (2020). Brain-derived neurotrophic factor (BDNF) promotes molecular polarization and differentiation of immature neuroblastoma cells into definitive neurons. *Biochimica et Biophysica Acta (BBA) - Molecular Cell Research, 1867*(9), 118737. doi:https://doi.org/10.1016/j.bbamcr.2020.118737

Hua, J. Y., & Smith, S. J. (2004). Neural activity and the dynamics of central nervous system development. *Nature Neuroscience, 7*(4), 327-332. doi:10.1038/nn1218

Huang, H., Nie, S., Cao, M., Marshall, C., Gao, J., Xiao, N., . . . Xiao, M. (2016). Characterization of AD-like phenotype in aged APPSwe/PS1dE9 mice. *Age (Dordr), 38*(4), 303-322. doi:10.1007/s11357-016-9929-7

Hurst, J. H. (2013). Richard Scheller and Thomas Südhof receive the 2013 Albert Lasker Basic Medical Research Award. *The Journal of Clinical Investigation, 123*(10), 4095-4101. doi:10.1172/JCI72681

Jackson, J. S., Witton, J., Johnson, J. D., Ahmed, Z., Ward, M., Randall, A. D., . . . Ashby, M. C. (2017). Altered Synapse Stability in the Early Stages of Tauopathy. *Cell Rep, 18*(13), 3063-3068. doi:10.1016/j.celrep.2017.03.013

Jarvius, M., Paulsson, J., Weibrecht, I., Leuchowius, K. J., Andersson, A. C., Wählby, C., Söderberg, O. (2007). In situ detection of phosphorylated platelet-derived growth factor receptor beta using a generalized proximity ligation method. *Mol Cell Proteomics, 6*(9), 1500-1509. doi:10.1074/mcp.M700166-MCP200

Jawaid, S., Kidd, G. J., Wang, J., Swetlik, C., Dutta, R., & Trapp, B. D. (2018). Alterations in CA1 hippocampal synapses in a mouse model of fragile X syndrome. *Glia, 66*(4), 789-800. doi:10.1002/glia.23284

Jayasena, S. D. (1999). Aptamers: an emerging class of molecules that rival antibodies in diagnostics. *Clinical chemistry, 45*(9), 1628-1650.

Jellinger, K. A. (2020). Neuropathology of the Alzheimer's continuum: an update. *Free Neuropathology, 1*(0), 32. doi:10.17879/freeneuropathology-2020-3050

Kamboh, M. I., Demirci, F. Y., Wang, X., Minster, R. L., Carrasquillo, M. M., Pankratz, V. S., . . . for the Alzheimer's Disease Neuroimaging, I. (2012). Genome-wide association study of Alzheimer's disease. *Translational Psychiatry, 2*(5), e117-e117. doi:10.1038/tp.2012.45

Kang, S. S., Ahn, E. H., Liu, X., Bryson, M., Miller, G. W., Weinshenker, D., & Ye, K. (2021). ApoE4 inhibition of VMAT2 in the locus coeruleus exacerbates Tau pathology in Alzheimer's disease. *Acta Neuropathologica, 142*(1), 139-158. doi:10.1007/s00401-021-02315-1

Kari, G., Rodeck, U., & Dicker, A. P. (2007). Zebrafish: An Emerging Model System for Human Disease and Drug Discovery. *Clinical Pharmacology & Therapeutics, 82*(1), 70-80. doi:https://doi.org/10.1038/sj.clpt.6100223

Karran, E., & De Strooper, B. (2022). The amyloid hypothesis in Alzheimer disease: new insights from new therapeutics. *Nature Reviews Drug Discovery*. doi:10.1038/s41573-022-00391-w

Katze, M., Korth, M. J., Law, G. L., & Nathanson, N. (2015). *Viral pathogenesis: from basics to systems biology*: Academic Press.

Kettenmann, H., Hanisch, U.-K., Noda, M., & Verkhratsky, A. (2011). Physiology of Microglia. *Physiological Reviews, 91*(2), 461-553. doi:10.1152/physrev.00011.2010

Khalil, M., Teunissen, C. E., Otto, M., Piehl, F., Sormani, M. P., Gattringer, T., . . . Fazekas, F. (2018). Neurofilaments as biomarkers in neurological disorders. *Nature Reviews Neurology, 14*(10), 577-589.

Kim, J., Yang, M., Kim, S.-H., Kim, J.-C., Wang, H., Shin, T., & Moon, C. (2013). Possible role of the glycogen synthase kinase-3 signaling pathway in trimethyltin-induced hippocampal neurodegeneration in mice. *PLoS One, 8*(8), e70356.

Kim, S., Foong, D., Cooper, M. S., Seibel, M. J., & Zhou, H. (2018). Comparison of blood sampling methods for plasma corticosterone measurements in mice associated with minimal stress-related artefacts. *Steroids, 135*, 69-72. doi:10.1016/j.steroids.2018.03.004

Klingberg, A., Hasenberg, A., Ludwig-Portugall, I., Medyukhina, A., Männ, L., Brenzel, A., . . . Gunzer, M. (2017). Fully Automated Evaluation of Total Glomerular Number and Capillary Tuft Size in Nephritic Kidneys Using Lightsheet Microscopy. *Journal of the American Society of Nephrology, 28*(2), 452. doi:10.1681/ASN.2016020232

Klunk, W. E., Bacskai, B. J., Mathis, C. A., Kajdasz, S. T., McLellan, M. E., Frosch, M. P., Hyman, B. T. (2002). Imaging Aβ plaques in living transgenic mice with multiphoton microscopy and methoxy-X04, a systemically administered Congo red derivative. *Journal of Neuropathology & Experimental Neurology, 61*(9), 797-805.

Kopeikina, K. J., Polydoro, M., Tai, H. C., Yaeger, E., Carlson, G. A., Pitstick, R., . . . Spires-Jones, T. L. (2013). Synaptic alterations in the rTg4510 mouse model of tauopathy. *J Comp Neurol, 521*(6), 1334-1353. doi:10.1002/cne.23234

Kowalski, A. (2019). *Development of a quick, robust and chemically-defined differentiation protocol from human induced pluripotent stem cells towards cortical neurons to phenotype Alzheimer's Disease.* (Inauguraldissertation). Medizinische Fakultät Mannheim der Ruprecht-Karls-Universität zu Heidelberg,

Kowalski, K., & Mulak, A. (2019). Brain-Gut-Microbiota Axis in Alzheimer&rsquo;s Disease. *Journal of Neurogastroenterology and Motility, 25*(1), 48-60. doi:10.5056/jnm18087

Kraft, A. D., McPherson, C. A., & Harry, G. J. (2016). Association Between Microglia, Inflammatory Factors, and Complement with Loss of Hippocampal Mossy Fiber Synapses Induced by Trimethyltin. *Neurotoxicity Research, 30*(1), 53-66. doi:10.1007/s12640-016-9606-8

Lashley, T., Schott, J. M., Weston, P., Murray, C. E., Wellington, H., Keshavan, A., . . . Rohrer, J. D. (2018). Molecular biomarkers of Alzheimer's disease: progress and prospects. *Disease models & mechanisms, 11*(5), dmm031781.

Lau, D. H., Hogseth, M., Phillips, E. C., O'Neill, M. J., Pooler, A. M., Noble, W., & Hanger, D. P. (2016). Critical residues involved in tau binding to fyn: implications for tau phosphorylation in Alzheimer's disease. *Acta Neuropathol Commun, 4*(1), 49. doi:10.1186/s40478-016-0317-4

Lee, S., Yang, M., Kim, J., Kang, S., Kim, J., Kim, J. C., . . . Moon, C. (2016). Trimethyltin-induced hippocampal neurodegeneration: A mechanism-based review. *Brain Res Bull, 125*, 187-199. doi:10.1016/j.brainresbull.2016.07.010

Lee, S., Yang, M., Kim, J., Son, Y., Kim, J., Kang, S., . . . Shin, T. (2016). Involvement of BDNF/ERK signaling in spontaneous recovery from trimethyltin-induced hippocampal neurotoxicity in mice. *Brain research bulletin, 121*, 48-58.

Lemprière, S. (2021). Genome-wide association study identifies new risk loci for Alzheimer disease. *Nature Reviews Neurology, 17*(11), 659-659. doi:10.1038/s41582-021-00575-9

Leng, F., & Edison, P. (2021). Neuroinflammation and microglial activation in Alzheimer disease: where do we go from here? *Nat Rev Neurol, 17*(3), 157-172. doi:10.1038/s41582-020-00435-y

Lewerenz, J., & Maher, P. (2015). Chronic Glutamate Toxicity in Neurodegenerative Diseases—What is the Evidence? *Frontiers in Neuroscience, 9*(469). doi:10.3389/fnins.2015.00469

Li, M., Cui, Z., Niu, Y., Liu, B., Fan, W., Yu, D., & Deng, J. (2010). Synaptogenesis in the developing mouse visual cortex. *Brain research bulletin, 81*(1), 107-113. doi:https://doi.org/10.1016/j.brainresbull.2009.08.028

Liu, W., Lin, H., He, X., Chen, L., Dai, Y., Jia, W., . . . Chen, L. (2020). Neurogranin as a cognitive biomarker in cerebrospinal fluid and blood exosomes for Alzheimer's disease and mild cognitive impairment. *Translational Psychiatry, 10*(1), 125. doi:10.1038/s41398-020-0801-2

Liu, Z., Lv, J., Zhang, Z., Wang, B., Duan, L., Li, C., . . . Ming, H. (2021). The main mechanisms of trimethyltin chloride-induced neurotoxicity: Energy metabolism disorder and peroxidation damage. *Toxicology Letters, 345*, 67-76. doi:https://doi.org/10.1016/j.toxlet.2021.04.008

Luna-Viramontes, N. I., Campa-Córdoba, B. B., Ontiveros-Torres, M. Á., Harrington, C. R., Villanueva-Fierro, I., Guadarrama-Ortíz, P., . . . Luna-Muñoz, J. (2020). PHF-Core Tau as the Potential Initiating Event for Tau Pathology in Alzheimer's Disease. *Frontiers in cellular neuroscience, 14*, 247-247. doi:10.3389/fncel.2020.00247

Lundgren, J. L., Ahmed, S., Schedin-Weiss, S., Gouras, G. K., Winblad, B., Tjernberg, L. O., & Frykman, S. (2015). ADAM10 and BACE1 are localized to synaptic vesicles. *Journal of neurochemistry, 135*(3), 606-615.

Lyman, M., Lloyd, D. G., Ji, X., Vizcaychipi, M. P., & Ma, D. (2014). Neuroinflammation: the role and consequences. *Neuroscience research, 79*, 1-12.

Mahoney, Z. X. (2007). *Discs-large homolog 1 (DLG1) and laminins in mouse tissue morphogenesis and maintenance*: Washington University in St. Louis.

Maia, L. F., Kaeser, S. A., Reichwald, J., Hruscha, M., Martus, P., Staufenbiel, M., & Jucker, M. (2013). Changes in amyloid-β and Tau in the cerebrospinal fluid of transgenic mice overexpressing amyloid precursor protein. *Sci Transl Med, 5*(194), 194re192. doi:10.1126/scitranslmed.3006446

Majewska, A. K., Newton, J. R., & Sur, M. (2006). Remodeling of synaptic structure in sensory cortical areas in vivo. *Journal of Neuroscience, 26*(11), 3021-3029.

Makin, S. (2018). The amyloid hypothesis on trial. *Nature, 559*(7715), S4-S4.

Mandelkow, E. (1999). Alzheimer's disease. The tangled tale of tau. *Nature, 402*(6762), 588-589. doi:10.1038/45095

McLeod, F., Marzo, A., Podpolny, M., Galli, S., & Salinas, P. (2017a). Evaluation of synapse density in hippocampal rodent brain slices. *JoVE (Journal of Visualized Experiments)*(128), e56153.

McLeod, F., Marzo, A., Podpolny, M., Galli, S., & Salinas, P. (2017b). Evaluation of Synapse Density in Hippocampal Rodent Brain Slices. *Journal of visualized experiments : JoVE*(128), 56153. doi:10.3791/56153

Merck.(2019). Duolink® PLA Probemaker Guide. Retrieved from https://www.sigmaaldrich.com/DE/de/technical-documents/protocol/protein-biology/protein-and-nucleic-acid-interactions/duolink-probemaker-user-manual

Merck KGaA, D. (accessed: 2021). Duolink® Proximity Ligation Assay. Retrieved from https://www.sigmaaldrich.com/DE/de/products/protein-biology/duolink-proximity-ligation-assay

Michiels, L., Delva, A., van Aalst, J., Ceccarini, J., Vandenberghe, W., Vandenbulcke, M., . . . Laere, K. V. (2021). Synaptic density in healthy human aging is not influenced by age or sex: a 11C-UCB-J PET study. *Neuroimage, 232*, 117877. doi:https://doi.org/10.1016/j.neuroimage.2021.117877

Millipore, E. (2017, 06/2017). Duolink® PLA Fluorescence Protocol. Lit. No. 5325_MSIG Ver. 1.0 2017 - 05325.

Molinuevo, J. L., Ayton, S., Batrla, R., Bednar, M. M., Bittner, T., Cummings, J., . . . Blennow, K. (2018). Current state of Alzheimer's fluid biomarkers. *Acta Neuropathologica, 136*(6), 821-853. doi:10.1007/s00401-018-1932-x

Morris, J. C. (2005). Early-stage and preclinical Alzheimer disease. *Alzheimer Dis Assoc Disord, 19*(3), 163-165. doi:10.1097/01.wad.0000184005.22611.cc

Murmu, R. P., Li, W., Holtmaat, A., & Li, J.-Y. (2013). Dendritic spine instability leads to progressive neocortical spine loss in a mouse model of Huntington's disease. *Journal of Neuroscience, 33*(32), 12997-13009.

Nawa, H., & Takei, N. (2001). BDNF as an anterophin; a novel neurotrophic relationship between brain neurons. *Trends in neurosciences, 24*(12), 683-684.

Nielsen, B. S. (2012). MicroRNA in situ hybridization. In *Next-Generation MicroRNA Expression Profiling Technology* (pp. 67-84): Springer.

Norden, D. M., & Godbout, J. (2013). Microglia of the aged brain: primed to be activated and resistant to regulation. *Neuropathology and applied neurobiology, 39*(1), 19-34.

O'Dell, R. S., Mecca, A. P., Chen, M.-K., Naganawa, M., Toyonaga, T., Lu, Y., . . . van Dyck, C. H. (2021). Association of Aβ deposition and regional synaptic density in early Alzheimer's disease: a PET imaging study with [11C]UCB-J. *Alzheimer's Research & Therapy, 13*(1), 11. doi:10.1186/s13195-020-00742-y

Ogita, K., Nishiyama, N., Sugiyama, C., Higuchi, K., Yoneyama, M., & Yoneda, Y. (2005). Regeneration of granule neurons after lesioning of hippocampal dentate

gyrus: evaluation using adult mice treated with trimethyltin chloride as a model. *Journal of neuroscience research, 82*(5), 609-621.

Olsson, B., Lautner, R., Andreasson, U., Öhrfelt, A., Portelius, E., Bjerke, M., . . . Zetterberg, H. (2016). CSF and blood biomarkers for the diagnosis of Alzheimer's disease: a systematic review and meta-analysis. *The Lancet Neurology, 15*(7), 673-684. doi:https://doi.org/10.1016/S1474-4422(16)00070-3

Orlandi, C., Omori, Y., Wang, Y., Cao, Y., Ueno, A., Roux, M. J., . . . Martemyanov, K. A. (2018). Transsynaptic Binding of Orphan Receptor GPR179 to Dystroglycan-Pikachurin Complex Is Essential for the Synaptic Organization of Photoreceptors. *Cell Reports, 25*(1), 130-145.e135. doi:https://doi.org/10.1016/j.celrep.2018.08.068

Paolicelli, R. C., Bolasco, G., Pagani, F., Maggi, L., Scianni, M., Panzanelli, P., . . . Gross, C. T. (2011). Synaptic pruning by microglia is necessary for normal brain development. *Science, 333*(6048), 1456-1458. doi:10.1126/science.1202529

Patrick, G. N., Zukerberg, L., Nikolic, M., de La Monte, S., Dikkes, P., & Tsai, L.-H. (1999). Conversion of p35 to p25 deregulates Cdk5 activity and promotes neurodegeneration. *Nature, 402*(6762), 615-622.

Perretta, G., Righi, F. R., & Gozzo, S. (1993). Neuropathological and behavioral toxicology of trimethyltin exposure. *ANNALI-ISTITUTO SUPERIORE DI SANITA, 29*, 167-167.

Pikuleva, I. A. (2006). Cytochrome P450s and cholesterol homeostasis. *Pharmacology & Therapeutics, 112*(3), 761-773. doi:https://doi.org/10.1016/j.pharmthera.2006.05.014

Potts, E. M., Coppotelli, G., & Ross, J. M. (2020). Histological-based stainings using free-floating tissue sections. *JoVE (Journal of Visualized Experiments)*(162), e61622.

Qin, Q., Teng, Z., Liu, C., Li, Q., Yin, Y., & Tang, Y. (2021). TREM2, microglia, and Alzheimer's disease. *Mechanisms of Ageing and Development, 195*, 111438. doi:https://doi.org/10.1016/j.mad.2021.111438

Qureshi, Y. H., Berman, D. E., Marsh, S. E., Klein, R. L., Patel, V. M., Simoes, S., . . . Small, S. A. (2022). The neuronal retromer can regulate both neuronal and microglial phenotypes of Alzheimer's disease. *Cell Reports, 38*(3), 110262. doi:https://doi.org/10.1016/j.celrep.2021.110262

Radde, R., Bolmont, T., Kaeser, S. A., Coomaraswamy, J., Lindau, D., Stoltze, L., . . . Jucker, M. (2006). Abeta42-driven cerebral amyloidosis in transgenic mice reveals early and robust pathology. *EMBO Rep, 7*(9), 940-946. doi:10.1038/sj.embor.7400784

Raleigh, V. S. (2019). Trends in life expectancy in EU and other OECD countries. doi:doi:https://doi.org/10.1787/223159ab-en

Ramsden, M., Kotilinek, L., Forster, C., Paulson, J., McGowan, E., SantaCruz, K., . . . Ashe, K. H. (2005). Age-dependent neurofibrillary tangle formation, neuron loss, and memory impairment in a mouse model of human tauopathy (P301L). *J Neurosci, 25*(46), 10637-10647. doi:10.1523/jneurosci.3279-05.2005

Robertson, M. P., & Ellington, A. (1999). In vitro selection of an allosteric ribozyme that transduces analytes to amplicons. *Nature biotechnology, 17*(1), 62-66.

Rochefort, N. L., & Konnerth, A. (2012). Dendritic spines: from structure to in vivo function. *EMBO reports, 13*(8), 699-708.

Rocher, A. B., Crimins, J. L., Amatrudo, J. M., Kinson, M. S., Todd-Brown, M. A., Lewis, J., & Luebke, J. I. (2010). Structural and functional changes in tau mutant mice neurons are not linked to the presence of NFTs. *Exp Neurol, 223*(2), 385-393. doi:10.1016/j.expneurol.2009.07.029

Romoli, M., Mandarano, M., Romozzi, M., Eusebi, P., Bedetti, C., Nardi Cesarini, E., . . . Costa, C. (2019). Synaptic vesicle protein 2A tumoral expression predicts levetiracetam adverse events. *Journal of Neurology, 266*(9), 2273-2276. doi:10.1007/s00415-019-09410-0

Roser, M., Ortiz-Ospina, E., & Ritchie, H. (2013). Life expectancy. *Our World in Data*.

Rudolf, R., Mongillo, M., Rizzuto, R., & Pozzan, T. (2003). Looking forward to seeing calcium. *Nat Rev Mol Cell Biol, 4*(7), 579-586. doi:10.1038/nrm1153

Russell, W. M. S., & Burch, R. L. (1959). *The principles of humane experimental technique*: Methuen.

Sá, F., Pinto, P., Cunha, C., Lemos, R., Letra, L., Simões, M., & Santana, I. (2012). Differences between Early and Late-Onset Alzheimer's Disease in Neuropsychological Tests. *Frontiers in neurology, 3*, 81-81. doi:10.3389/fneur.2012.00081

Sandström, J., Kratschmar, D. V., Broyer, A., Poirot, O., Marbet, P., Chantong, B., . . . Monnet-Tschudi, F. (2019). In vitro models to study insulin and glucocorticoids modulation of trimethyltin (TMT)-induced neuroinflammation and neurodegeneration, and in vivo validation in db/db mice. *Arch Toxicol, 93*(6), 1649-1664. doi:10.1007/s00204-019-02455-0

Sano, T., Masuda, Y., Yasuno, H., Shinozawa, T., Watanabe, T., & Kakehi, M. (2021). Blood Neurofilament Light Chain as a Potential Biomarker for Central and Peripheral Nervous Toxicity in Rats. *Toxicological Sciences, 185*(1), 10-18. doi:10.1093/toxsci/kfab122

Sauerbeck, A. D., Gangolli, M., Reitz, S. J., Salyards, M. H., Kim, S. H., Hemingway, C., . . . Kummer, T. T. (2020). SEQUIN Multiscale Imaging of Mammalian Central Synapses Reveals Loss of Synaptic Connectivity Resulting from Diffuse Traumatic Brain Injury. *Neuron, 107*(2), 257-273.e255. doi:10.1016/j.neuron.2020.04.012

Schafer, D. P., Lehrman, E. K., Kautzman, A. G., Koyama, R., Mardinly, A. R., Yamasaki, R., . . . Stevens, B. (2012). Microglia sculpt postnatal neural circuits in an activity and complement-dependent manner. *Neuron, 74*(4), 691-705.

Schafer, D. P., & Stevens, B. (2010). Synapse elimination during development and disease: immune molecules take centre stage. *Biochemical Society Transactions, 38*(2), 476-481.

Scheff, S. W., Price, D. A., Schmitt, F. A., & Mufson, E. J. (2006). Hippocampal synaptic loss in early Alzheimer's disease and mild cognitive impairment. *Neurobiology of Aging, 27*(10), 1372-1384. doi:https://doi.org/10.1016/j.neurobiolaging.2005.09.012

Scheuner, D., Eckman, C., Jensen, M., Song, X., Citron, M., Suzuki, N., Kukull, W. (1996). Secreted amyloid β–protein similar to that in the senile plaques of Alzheimer's disease is increased in vivo by the presenilin 1 and 2 and APP mutations linked to familial Alzheimer's disease. *Nature Medicine, 2*(8), 864-870.

Schonhaut, D. R., McMillan, C. T., Spina, S., Dickerson, B. C., Siderowf, A., Devous Sr, M. D., . . . Rabinovici, G. D. (2017). 18F-flortaucipir tau positron emission tomography distinguishes established progressive supranuclear palsy from controls and Parkinson disease: A multicenter study. *Annals of Neurology, 82*(4), 622-634. doi:https://doi.org/10.1002/ana.25060

Science, A. I. f. B. (2020a). Developing Mouse Brain. *Mouse, E16.5, Coronal.* Retrieved from https://developingmouse.brain-map.org/experiment/thumbnails/100075063?image_type=hp_yellow

Science, A. I. f. B. (2020b). Developing Mouse Brain. *Mouse, P14, Coronal.* Retrieved from https://developingmouse.brain-map.org/experiment/thumbnails/100014118?image_type=nissl

Science, A. I. f. B. (2021). Allen Brain Atlas. *Mouse, P56, Coronal.* Retrieved from https://mouse.brain-map.org/experiment/thumbnails/100048576?image_type=atlas

Selkoe, D. J. (1996). Amyloid β-protein and the genetics of Alzheimer's disease. *Journal of Biological Chemistry, 271*(31), 18295-18298.

Selkoe, D. J., & Schenk, D. (2003). Alzheimer's disease: molecular understanding predicts amyloid-based therapeutics. *Annu Rev Pharmacol Toxicol, 43*, 545-584. doi:10.1146/annurev.pharmtox.43.100901.140248

Shimojo, M., Takuwa, H., Takado, Y., Tokunaga, M., Tsukamoto, S., Minatohara, K., . . . Higuchi, M. (2020). Selective Disruption of Inhibitory Synapses Leading to Neuronal Hyperexcitability at an Early Stage of Tau Pathogenesis in a Mouse Model. *J Neurosci, 40*(17), 3491-3501. doi:10.1523/jneurosci.2880-19.2020

Siddoway, B., Hou, H., & Xia, H. (2011). Glutamatergic synapses: molecular organisation. *eLS*.

Simon-Chica, A., Fernández, M. C., Wülfers, E. M., Lother, A., Hilgendorf, I., Seemann, G., . . . Schneider-Warme, F. (2022). Novel insights into the electrophysiology of murine cardiac macrophages: relevance of voltage-gated potassium channels. *Cardiovasc Res, 118*(3), 798-813. doi:10.1093/cvr/cvab126

Söderberg, O., Gullberg, M., Jarvius, M., Ridderstråle, K., Leuchowius, K. J., Jarvius, J., . . . Landegren, U. (2006). Direct observation of individual endogenous protein complexes in situ by proximity ligation. *Nat Methods, 3*(12), 995-1000. doi:10.1038/nmeth947

Spalteholz, W. (1914). *Über das Durchsichtigmachen von menschlichen und tierischen Präparaten und seine theoretischen Bedingungen, nebst Anhang: Über Knochenfärbung.* Leipzig: Leipzig, S. Hirzel, 1914.

Sperling, R. A., Aisen, P. S., Beckett, L. A., Bennett, D. A., Craft, S., Fagan, A. M., . . . Phelps, C. H. (2011). Toward defining the preclinical stages of Alzheimer's disease: recommendations from the National Institute on Aging-Alzheimer's Association workgroups on diagnostic guidelines for Alzheimer's disease. *Alzheimers Dement, 7*(3), 280-292. doi:10.1016/j.jalz.2011.03.003

Spires-Jones, T., & Knafo, S. (2011). Spines, plasticity, and cognition in Alzheimer's model mice. *Neural plasticity, 2012*.

Stelzmann, R. A., Norman Schnitzlein, H., & Reed Murtagh, F. (1995). An english translation of alzheimer's 1907 paper,"über eine eigenartige erkankung der hirnrinde". *Clinical Anatomy: The Official Journal of the American Association of Clinical Anatomists and the British Association of Clinical Anatomists, 8*(6), 429-431.

Stephan, A. H., Barres, B. A., & Stevens, B. (2012). The Complement System: An Unexpected Role in Synaptic Pruning During Development and Disease. *Annual Review of Neuroscience, 35*(1), 369-389. doi:10.1146/annurev-neuro-061010-113810

Stevens, B., Allen, N. J., Vazquez, L. E., Howell, G. R., Christopherson, K. S., Nouri, N., . . . Stafford, B. (2007). The classical complement cascade mediates CNS synapse elimination. *Cell, 131*(6), 1164-1178.

Südhof, T. C. (2012). The presynaptic active zone. *Neuron, 75*(1), 11-25. doi:10.1016/j.neuron.2012.06.012

Tang, X., Wu, X., Dubois, A. M., Sui, G., Wu, B., Lai, G., . . . Ren, X. (2013). Toxicity of trimethyltin and dimethyltin in rats and mice. *Bull Environ Contam Toxicol, 90*(5), 626-633. doi:10.1007/s00128-013-0975-x

Tarawneh, R., D'Angelo, G., Crimmins, D., Herries, E., Griest, T., Fagan, A. M., . . . Holtzman, D. M. (2016). Diagnostic and Prognostic Utility of the Synaptic Marker Neurogranin in Alzheimer Disease. *JAMA neurology, 73*(5), 561-571. doi:10.1001/jamaneurol.2016.0086

Terry, R. D., Masliah, E., Salmon, D. P., Butters, N., DeTeresa, R., Hill, R., . . . Katzman, R. (1991). Physical basis of cognitive alterations in Alzheimer's disease: synapse loss is the major correlate of cognitive impairment. *Ann Neurol, 30*(4), 572-580. doi:10.1002/ana.410300410

Tolppanen, A.-M., Solomon, A., Kulmala, J., Kåreholt, I., Ngandu, T., Rusanen, M., . . . Kivipelto, M. (2015). Leisure-time physical activity from mid- to late life, body mass index, and risk of dementia. *Alzheimer's & dementia, 11*(4), 434-443.e436. doi:https://doi.org/10.1016/j.jalz.2014.01.008

Trachtenberg, J. T., Chen, B. E., Knott, G. W., Feng, G., Sanes, J. R., Welker, E., & Svoboda, K. (2002). Long-term in vivo imaging of experience-dependent synaptic plasticity in adult cortex. *Nature, 420*(6917), 788-794.

Tsien JZ, C. D., Gerber D, Tom C, Mercer EH, Anderson DJ, Mayford M, Kandel ER, Tonegawa S. . (1996). Subregion- and cell type-restricted gene knockout in mouse brain. *Cell, 27;87(7)*. doi: 10.1016/s0092-8674(00)81826-7

Tuerk, C., & Gold, L. (1990). Systematic evolution of ligands by exponential enrichment: RNA ligands to bacteriophage T4 DNA polymerase. *Science, 249*(4968), 505-510.

van der Kant, R., Goldstein, L. S., & Ossenkoppele, R. (2020). Amyloid-β-independent regulators of tau pathology in Alzheimer disease. *Nature Reviews Neuroscience, 21*(1), 21-35.

Verkhratsky, A., & Nedergaard, M. (2018). Physiology of Astroglia. *Physiological Reviews, 98*(1), 239-389. doi:10.1152/physrev.00042.2016

Verstraelen, P., Garcia-Diaz Barriga, G., Verschuuren, M., Asselbergh, B., Nuydens, R., Larsen, P. H., . . . De Vos, W. H. (2020). Systematic Quantification of Synapses in Primary Neuronal Culture. *iScience, 23*(9), 101542. doi:https://doi.org/10.1016/j.isci.2020.101542

Wang, J., Gu, B. J., Masters, C. L., & Wang, Y. J. (2017). A systemic view of Alzheimer disease - insights from amyloid-β metabolism beyond the brain. *Nat Rev Neurol, 13*(10), 612-623. doi:10.1038/nrneurol.2017.111

Wattmo, C., & Wallin, Å. K. (2017). Early- versus late-onset Alzheimer's disease in clinical practice: cognitive and global outcomes over 3 years. *Alzheimer's Research & Therapy, 9*(1), 70. doi:10.1186/s13195-017-0294-2

Widrow, B., Kim, Y., Park, D., & Perin, J. K. (2019). Chapter 1 - Nature's Learning Rule: The Hebbian-LMS Algorithm. In R. Kozma, C. Alippi, Y. Choe, & F. C. Morabito (Eds.), *Artificial Intelligence in the Age of Neural Networks and Brain Computing* (pp. 1-30): Academic Press.

Wiley, J. (2021). Alzheimer's disease facts and figures. *Alzheimers Dement, 17*, 327-406.

Wiseman, F. K., Al-Janabi, T., Hardy, J., Karmiloff-Smith, A., Nizetic, D., Tybulewicz, V. L. J., . . . Strydom, A. (2015). A genetic cause of Alzheimer disease: mechanistic insights from Down syndrome. *Nature Reviews Neuroscience, 16*(9), 564-574. doi:10.1038/nrn3983

Wu, H.-Y., Kuo, P.-C., Wang, Y.-T., Lin, H.-T., Roe, A. D., Wang, B. Y., . . . Tai, H.-C. (2018). β-Amyloid induces pathology-related patterns of tau

hyperphosphorylation at synaptic terminals. *Journal of Neuropathology & Experimental Neurology, 77*(9), 814-826.

Wu, T., Dejanovic, B., Gandham, V. D., Gogineni, A., Edmonds, R., Schauer, S., . . . Hanson, J. E. (2019). Complement C3 Is Activated in Human AD Brain and Is Required for Neurodegeneration in Mouse Models of Amyloidosis and Tauopathy. *Cell Reports, 28*(8), 2111-2123.e2116. doi:https://doi.org/10.1016/j.celrep.2019.07.060

Wyss-Coray, T. (2016). Ageing, neurodegeneration and brain rejuvenation. *Nature, 539*(7628), 180-186. doi:10.1038/nature20411

Yang, B., Treweek, J. B., Kulkarni, R. P., Deverman, B. E., Chen, C. K., Lubeck, E., . . . Gradinaru, V. (2014). Single-cell phenotyping within transparent intact tissue through whole-body clearing. *Cell, 158*(4), 945-958. doi:10.1016/j.cell.2014.07.017

Yin, X., Zhao, C., Qiu, Y., Zhou, Z., Bao, J., & Qian, W. (2021). Dendritic/Post-synaptic Tau and Early Pathology of Alzheimer's Disease. *Frontiers in molecular neuroscience, 14*, 671779-671779. doi:10.3389/fnmol.2021.671779

Yoshii, A., & Constantine-Paton, M. (2007). BDNF induces transport of PSD-95 to dendrites through PI3K-AKT signaling after NMDA receptor activation. *Nat Neurosci, 10*(6), 702-711. doi:10.1038/nn1903

Yuan, A., Rao, M. V., & Nixon, R. A. (2012). Neurofilaments at a glance. *Journal of cell science, 125*(14), 3257-3263.

Yudkoff, M., Daikhin, Y., Lin, Z. P., Nissim, I., Stern, J., Pleasure, D., & Nissim, I. (1994). Interrelationships of leucine and glutamate metabolism in cultured astrocytes. *J Neurochem, 62*(3), 1192-1202. doi:10.1046/j.1471-4159.1994.62031192.x

Zhang, F., Gannon, M., Chen, Y., Yan, S., Zhang, S., Feng, W., Wang, Q. (2020). β-amyloid redirects norepinephrine signaling to activate the pathogenic GSK3β/tau cascade. *Science translational medicine, 12*(526), eaay6931. doi:doi:10.1126/scitranslmed.aay6931

Zhao, L. (2019). CD33 in Alzheimer's Disease – Biology, Pathogenesis, and Therapeutics: A Mini-Review. *Gerontology, 65*(4), 323-331. doi:10.1159/000492596

Zhou, F. W., & Roper, S. N. (2010). Densities of glutamatergic and GABAergic presynaptic terminals are altered in experimental cortical dysplasia. *Epilepsia, 51*(8), 1468-1476.

Zhu, F., Cizeron, M., Qiu, Z., Benavides-Piccione, R., Kopanitsa, M. V., Skene, N. G., . . . Komiyama, N. H. (2018). Architecture of the mouse brain synaptome. *Neuron, 99*(4), 781-799. e710.

8 APPENDIX

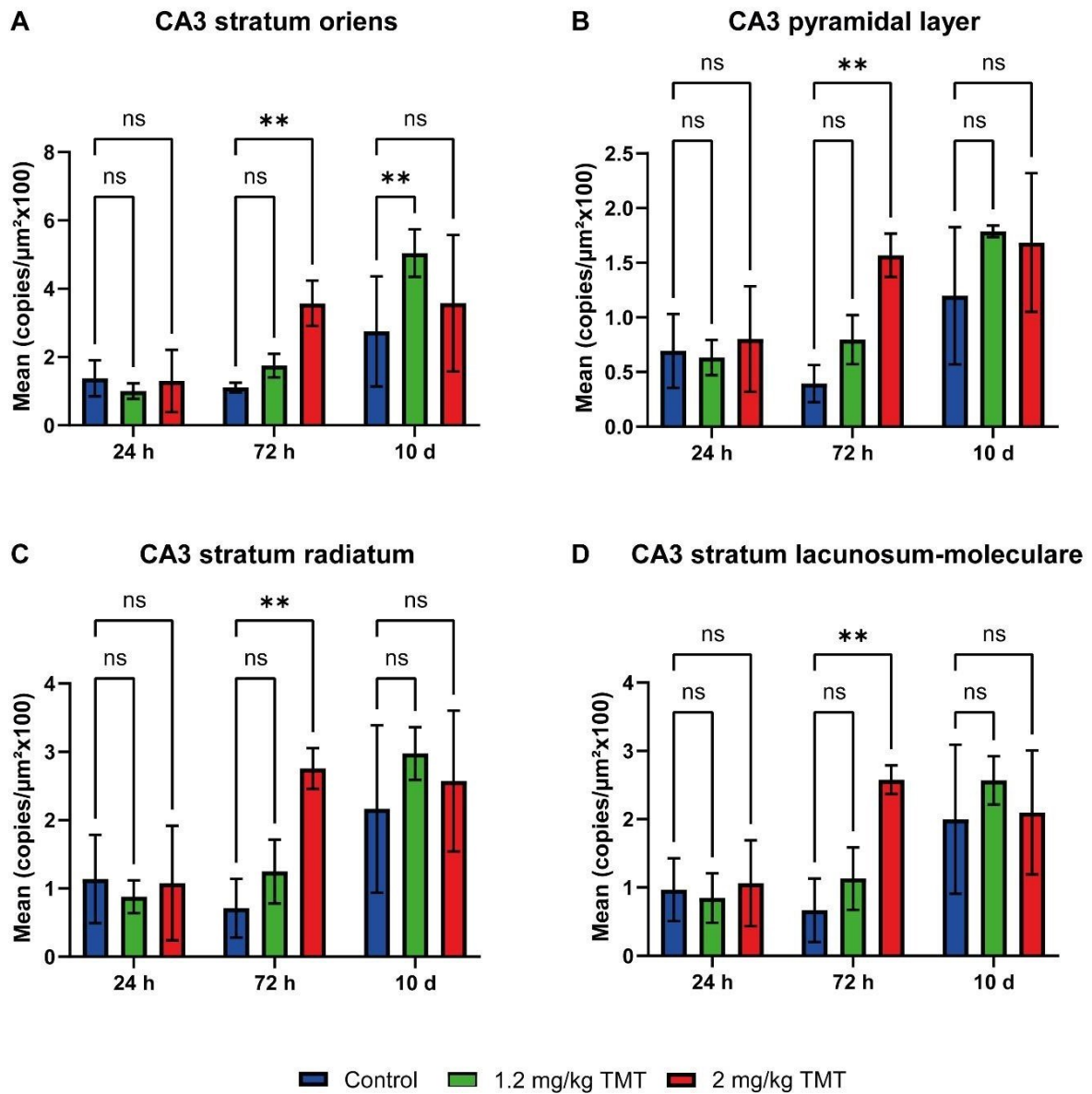## 8.1 Supplementary Data

Hippocampus and CA subregions
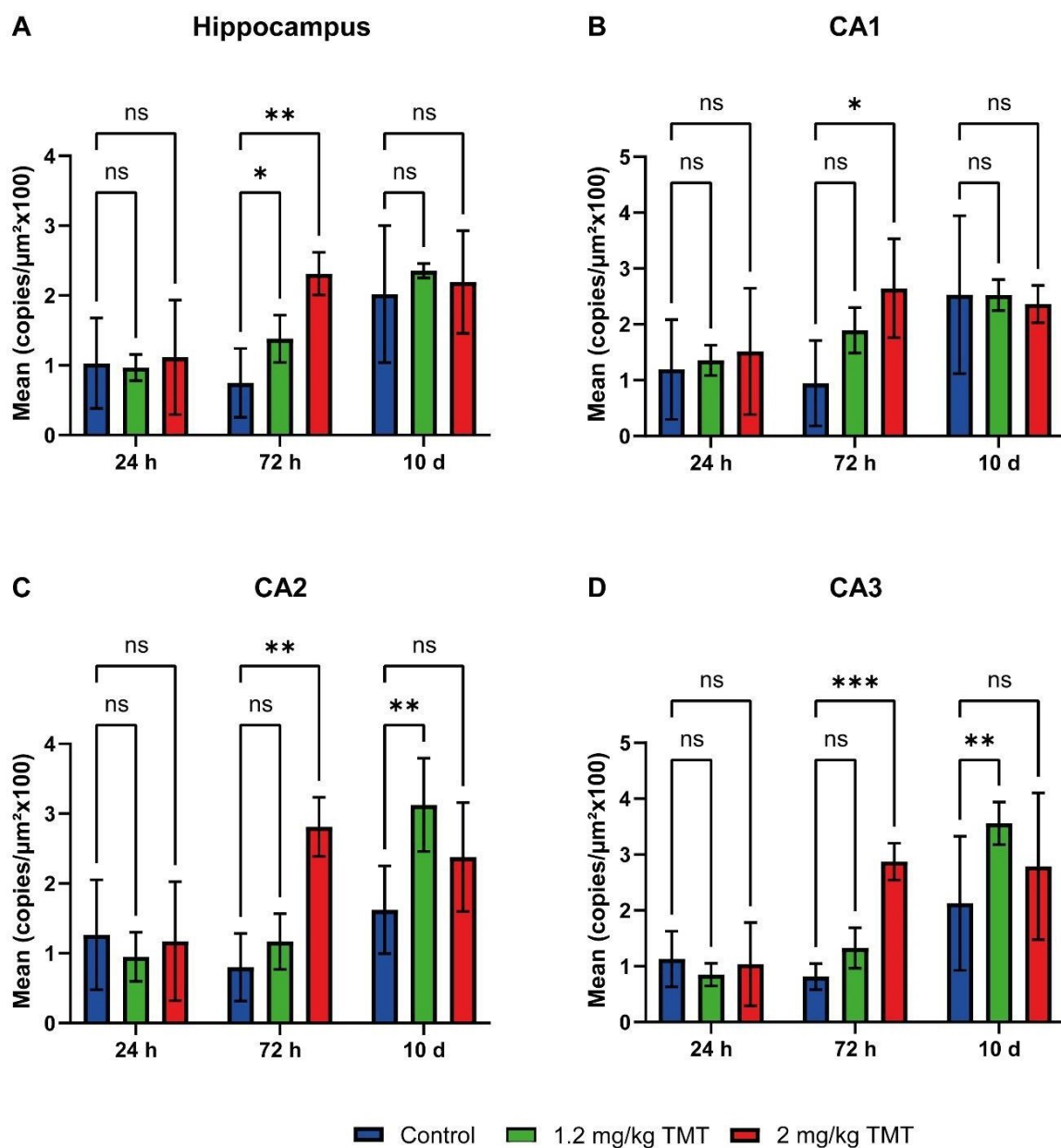
Supplementary Figure 1: **PLA puncta quantification for glutamatergic density in the hippocampus and its subregion, the Ammon's horns (CA).** *Quantification of different dose groups, control (blue), low dose 1.2 mg/kg TMT (green) and high dose 2 mg/kg TMT (red) after 24 h, 72 h and 10 days after TMT application in wt mice in brain areas of the hippocampus (A), CA1 (B), CA2 (C) and CA3 (D).*
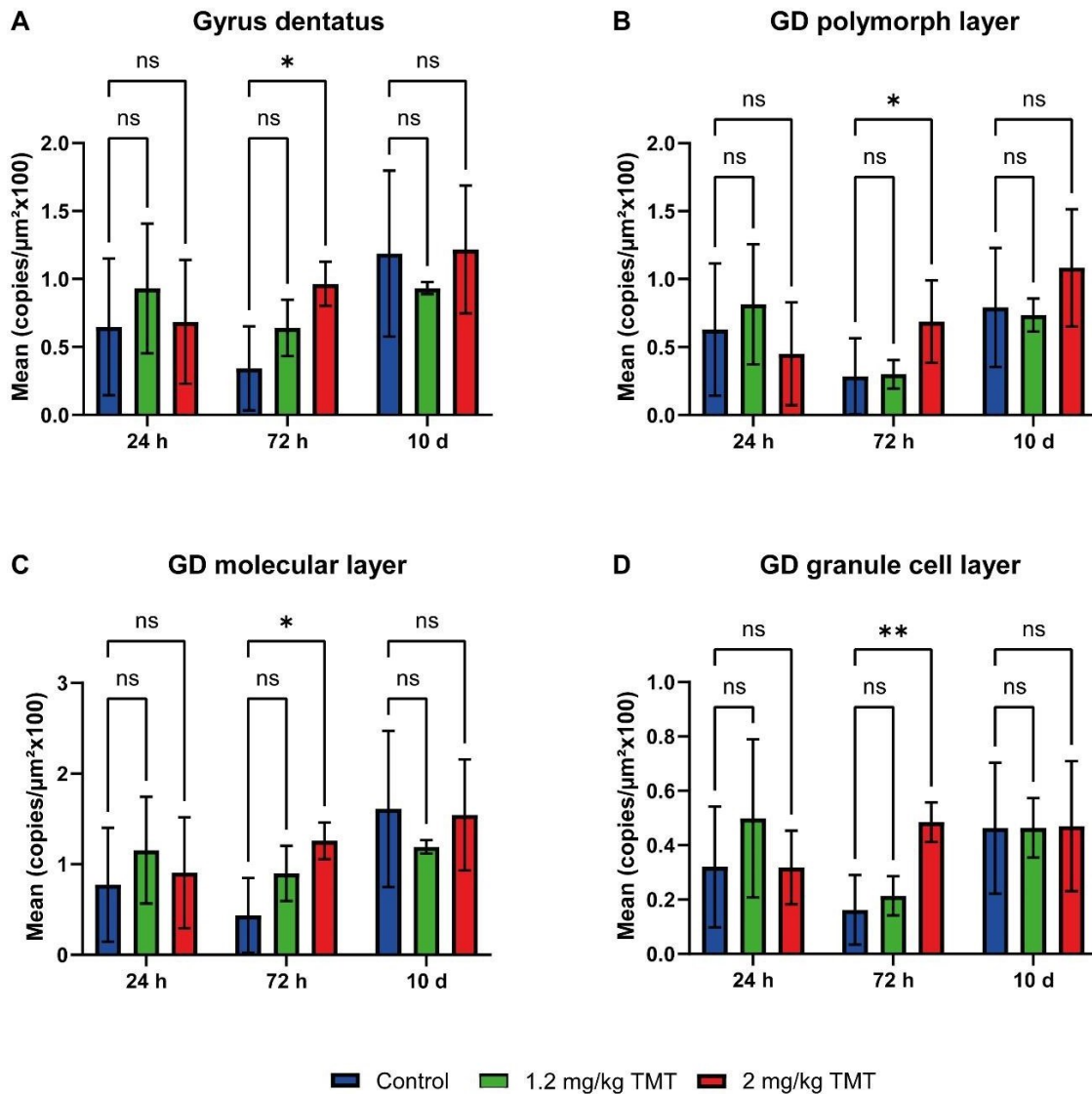
CA2 subgroups
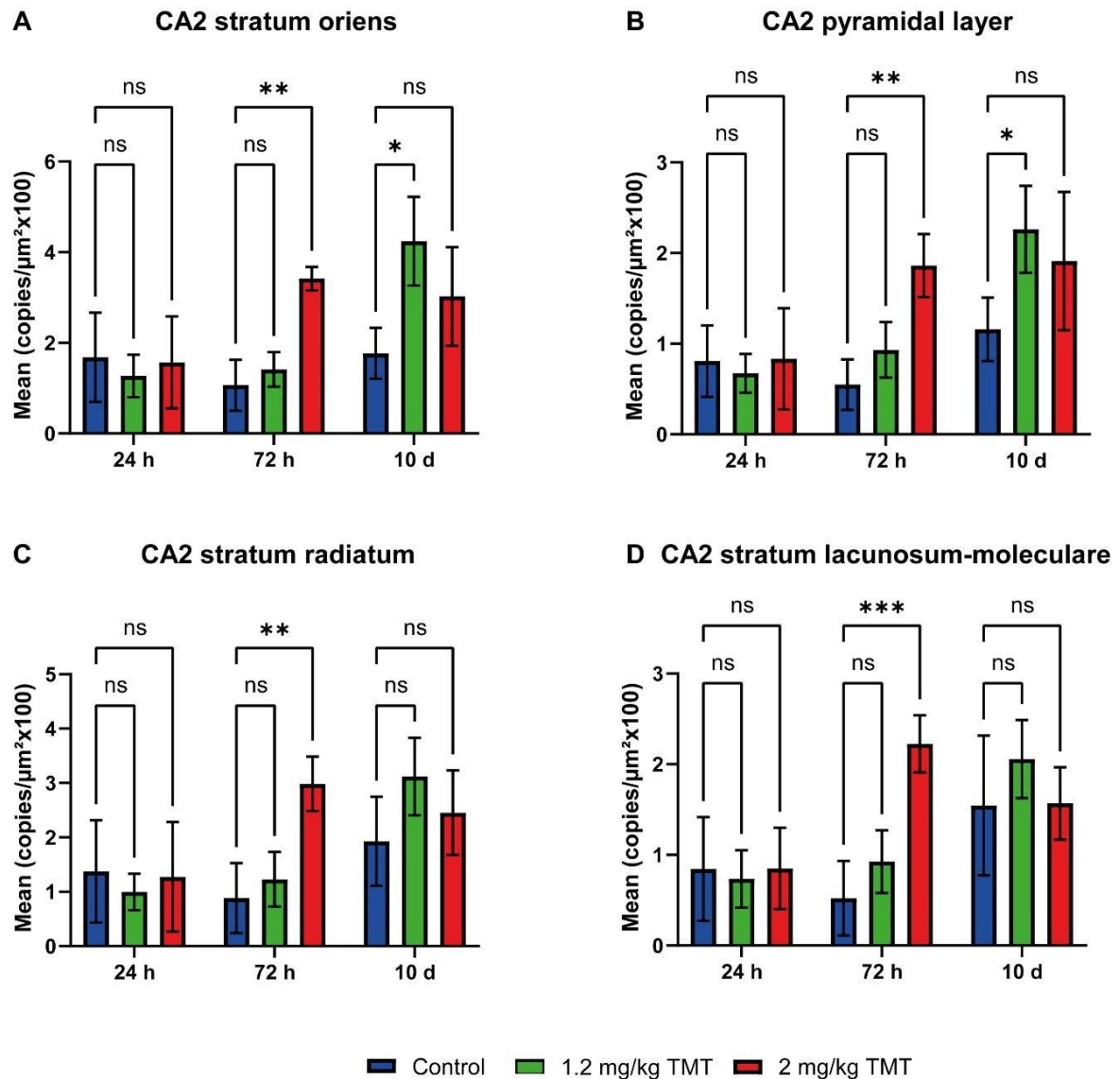
Supplementary Figure 2: **Synaptic density in TMT-treated mice in CA2 subregions.** *Quantification of different dose groups, control (blue), low dose 1.2 mg/kg TMT (green) and high dose 2 mg/kg TMT (red) after 24 h, 72 h and 10 days after TMT application in wt mice in brain areas of the CA2 subregions stratum oriens (A), pyramidal layer (B), stratum radiatum (C) and stratum lacunosum-moleculare (D).*

CA3 subgroups

*Supplementary Figure 3: **Synaptic density in TMT-treated mice in CA3 subregions.** Quantification of different dose groups, control (blue), low dose 1.2 mg/kg TMT (green) and high dose 2 mg/kg TMT (red) after 24 h, 72 h and 10 days after TMT application in wt mice in brain areas of the CA3 subregions stratum oriens **(A)**, pyramidal layer **(B)**, stratum radiatum **(C)** and stratum lacunosum-moleculare **(D)**.*

Gyrus dentatus and subgroups

Supplementary Figure 4: **PLA to quantify synaptic density in control and TMT-treated mice in the area of the gyrus dentatus.** *Quantification of different dose groups, control (blue), low dose 1.2 mg/kg TMT (green) and high dose 2 mg/kg TMT (red) after 24 h, 72 h and 10 days after TMT application in wt mice in hippocampal area gyrus dentatus (GD)* **(A)** *that was further divided and PLA puncta quantified in the areas of the polymorph layer* **(B)***, molecular layer* **(C)** *and granule cell layer* **(D).**

A

B
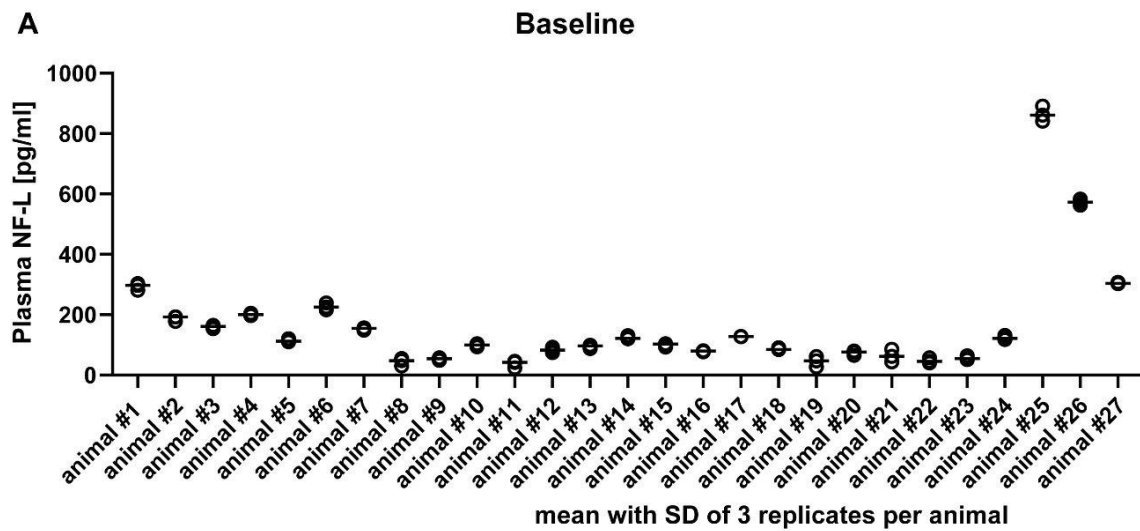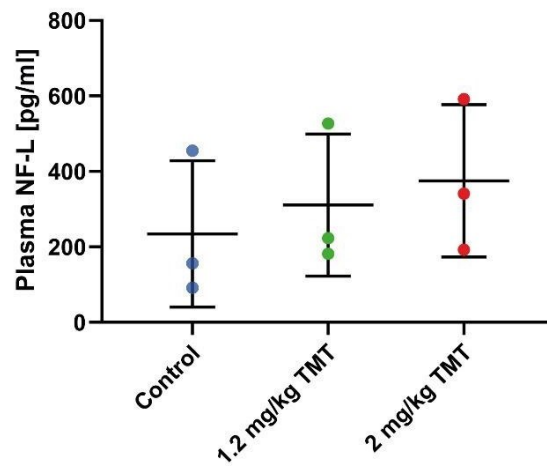
*Supplementary Figure 5: **Plasma NF-L at baseline and 1 h post TMT treatment. (A)** Graph shows three replicates per animal at baseline, blood taken 1 week before TMT treatment. **(B)** Graph shows mean per group of control (blue) and mice treated with 1.2 mg/kg TMT (green) and 2 mg/kg TMT (red) 1 h post TMT application.*

8.2   Presentations and Poster Contributions

Tatjana Mende, Christopher Sliwinski: Proximity ligation assay (PLA) to quantify synaptic density. Presentation at AbbVie Science Day, December 15th, 2021

Marie-Theres Weil, **Tatjana Alexander**, Thomas Jahn: 3D study of Alzheimer`s disease hallmarks using novel imaging technique. Poster presented at AbbVie Celebration of Science, October 24th, 2019

Tatjana Alexander, Marie-Theres Weil, Thomas Jahn, Andreas Popp: Tissue Clearing and Volume Fluorescence Microscopy to Examine Alzheimer's Disease. Poster presented at "17th European Congress of Toxicologic Pathology", September 17th - 20th, 2019, Cologne, Germany

Tatjana Alexander, Marie-Theres Weil, Thomas Jahn, Andreas Popp: Tissue Clearing and Volume Fluorescence Microscopy to Examine Alzheimer's Disease. Poster presented at AbbVie DMPK and PCS Poster Session, August 27th, 2019

9   LEBENSLAUF

PERSONALIEN

Name	Tatjana Mende (geb. Alexander)
Geburtsdatum:	18.03.1989
Geburtsort:	Heidelberg

SCHULISCHER WERDEGANG

2005 – 2009	Willy-Hellpach-Schule Heidelberg
18.06.2009	Abitur

UNIVERSITÄRER WERDEGANG

SS2010 - SS2013	Beginn des Studiums der Pharmazie An der Goethe-Universität, Frankfurt am Main ohne Abschluss
WS2013 – WS2015	Bachelor Bioverfahrenstechnik Frankfurt University of Applied Sciences Bachelorarbeit: Entwicklung eines Lichtscheibenmikroskopie-basierten Verfahrens zur Einzelzellquantifizierung der Gliomzellinvasion auf organotypischen Hirnschnitten
14.12.2015	Bachelor of Engineering (B. Eng.), Note: 2,4
SS2016 – SS2018	Master Biotechnologie / Biomedical Science and Technology Hochschule Mannheim Masterarbeit: Volume Fluorescence Microscopy of Mouse Brains to examine Alzheimer's Disease
16.07.2018	Master of Science (M. Sc.), Note: 1,8

10 ACKNOWLEDGEMENTS

First of all, I want to thank three people without whom this project would not have been possible: I thank Mathias Hafner, Andreas Popp, and Knut Biber for the topic of my doctoral thesis and the opportunity of a cooperation between Hochschule Mannheim and AbbVie in which I could take part in.

Further, I thank Prof. Mathias Hafner for supervising me as my doctoral father, and for advising me with regards to my thesis.

I take this opportunity to express gratitude to Dr. Andreas Popp and Prof. Knut Biber for the supervision of this thesis and for their guidance through the stages of the process.

I would like to thank Dr. Christopher Sliwinski and Dr. Marie-Theres Weil and the people of the histology lab. I enjoyed the opportunities to grow and learn.

Special thanks go to Dr. Michaela Heimann and Dr. Melanie Meister. I will miss our lunch breaks, which were always a comforting source of inspiration and community. I deeply enjoyed our collaborations as well as our discussions.

I would like to thank my friends and family for their constant support throughout my studies and personal life.

Last and most importantly, thank you to my husband Martin for being by my side through this adventurous time.